Advanced Control and Pulse-Width-Modulation Techniques for High-Speed Permanent Magnet Synchronous Machine Drives

By

Shangjian Dai

A thesis submitted in fulfilment of the requirements for the degree of

Doctor of Philosophy

Department of Electronic and Electrical Engineering

Faulty of Engineering

The University of Sheffield

November 2020

Abstract

Due to the limited switching frequency of semiconductor switches, high-speed permanent magnet synchronous machine (PMSM) drives which have high fundamental frequency usually feature low switching-to-fundamental frequency ratios (SFRs). The low SFR could deteriorate both the dynamic response and the steady-state performance of high-speed PMSM drives. Therefore, advanced control and optimal pulse width modulation (PWM) methods for high-speed PMSM drives have been investigated in this thesis.

Firstly, this thesis proposes a novel deadbeat predictive current control (DBPCC) method for high-speed PMSM drives. The proposed method realises deadbeat control of dq axis currents by tracking the associated stator flux vector in the stationary frame and considers the delay and rotor movement effects explicitly. Consequently, the proposed DBPCC exhibits excellent dynamic response at high speeds even with very low SFRs. Moreover, the influences of parametric mismatch and inverter nonlinearity on the proposed DBPCC are derived analytically and verified both by extensive simulations and experiments.

Secondly, three novel methods, i.e. adaptive reference correcting current injection (ARCCI), adaptive harmonic reference correcting current injection (AHRCCI) and transient identification of inductance are proposed to improve the steady-state control accuracy, current harmonic distortion and dynamic response of high-speed PMSM drives with the proposed DBPCC, respectively. By these proposed methods, the near-ideal deadbeat current control of high-speed PMSM drives can be achieved even with inaccurate machine parameters inverter nonlinearity and other non-ideal factors such as back EMF harmonics.

Thirdly, synchronous optimal PMW (SOPWM) with minimised current THD is investigated for high-speed PMSM drives. To derive the optimal pulse patterns and evaluate the resultant current THD of SOPWM efficiently, a computationally efficient optimization algorithm and current THD prediction method are proposed. Moreover, to avoid the overshoot current during mode transition, a fast and smooth SOPWM mode transition scheme is developed as well.

Finally, this thesis proposes a fast dynamic current control with SOPWM for high-speed PMSM drives. The proposed method can achieve current distortions similar to SOPWM in steady states and fast current response in transients as well.

Dedicated to my grandmother Caiyun Shao in loving memory.

Acknowledgement

Table of Acronyms and Symbols

Acronyms

Acronym	Description
3PS	Three-phase symmetry
AHRCCI	Adaptive harmonic reference correcting current injection
ARCCI	Adaptive reference correcting current injection
DBPCC	Deadbeat predictive current control
DC	Direct current
EMF	Electromagnetic force
HWS	Half-waveform symmetry
IGBT	Insulated gate bipolar transistor
IM	Induction machine
IPM	Inserted permanent machine
MOSFET	Metal-oxide-semiconductor filed-effect transistor
MTPA	Maximum torque per ampere
OAA	Optimal activating angles
OFT	Optimal flux trajectory
OPP	Optimal pulse pattern
OSA	Optimal switching angles
OSVP	Optimal switching vector pattern
OSVS	Optimal switching vector sequence
PMSM	Permanent magnet synchronous machine
PWM	Pulse width modulation

Acronym	Description
QWS	Quarter-waveform symmetry
RMS	Root-mean-square
SFR	Sampling to fundamental frequency ratio
SHR	Sampling to harmonic frequency ratio
SiC	Silicon carbide
SOPWM	Synchronous optimal pulse width modulation
SPMSM	Surface mounted permanent magnet synchronous machine
SVM	Space vector modulation
TDD	Total demand distortion
THD	Total harmonic distortion

Symbols

Symbol	Description
d	Current distortion factor
$\boldsymbol{d}_\psi$	Dynamic stator flux error vector
$\boldsymbol{d}_i$	Dynamic stator current error vector
f_{sw}	Switching frequency
i_d	d-axis current
i_q	q-axis current
$\boldsymbol{i}_{dq}$	Stator current vector in the dq frame
I_1, i_1	Fundamental current amplitude

Symbol	Description
I_h, i_h	Harmonic current amplitude
I_{h_6S}	Harmonic current amplitude under six-step operation
I_n	The nth harmonic current amplitude
K_p	Proportional gain
K_i	Integral gain
L_d	d-axis stator voltage
L_q	q-axis stator voltage
L_s	Synchronous inductance
m	Modulation index
M	Switch angle number in the first quarter cycle
n_m	Mechanical speed
N_p	Pulse number
$\boldsymbol{P}$	Pulse pattern
r_P	Apothem of optimal stator flux trajectory
R	Phase resistance
T_e	Electromagnetic torque
u_d	d-axis stator voltage
u_q	q-axis stator voltage
$\boldsymbol{u}_{dq}$	Stator voltage vector in the dq frame
$\boldsymbol{u}_{\alpha\beta}$	Stator voltage vector in the $\alpha\beta$ frame
$\boldsymbol{u}_{sop}^*$	Optimal stator voltage vector reference in the stationary frame

Symbol	Description
$u_{ao,bo,co}$	Phase terminal voltage
V_n	The nth harmonic voltage amplitude
$\boldsymbol{VS}$	Voltage-second input
V_{dc}	DC-link voltage
α_i	The ith primary switching angle
ω_e	Electric angular speed
ψ_m	Permanent magnet flux linkage
ψ_d	d-axis stator flux
ψ_q	q-axis stator flux
$\boldsymbol{\psi}_{dq}$	Stator flux vector in the dq frame
$\boldsymbol{\psi}_{\alpha\beta}, \boldsymbol{\psi}_s$	Stator flux vector in the αβ/stationary frame
$\boldsymbol{\psi}_{sop}^*$	Optimal stator flux vector reference in the stationary frame
θ_{sf}^*	Reference stator flux angle
θ_u^*	Reference stator voltage angle
$\cdot(k)$	Quantity at step k
$\widehat{}$	Estimated quantity
$\star$	Reference quantity

Table of Contents

CHAPTER 1
General Introduction

1.1 Background of High-Speed SPMSM Drives

Electrical machine drives are increasingly demanded in numerous applications, including electrified transportation, domestic appliances, industrial manufacture and etc. It is estimated that 60%~70% of total industrial energy is being consumed on electro-mechanical energy conversion [1]. Among various electrical machine drives, the high-speed electric machine drive has currently become one of the very attractive topics of research, due to its high efficiency and power density.

Employing high-speed electric machine drives can bring many benefits. In the applications such as oil & gas compressors, spindles, turbochargers, air compressor, micro-turbines [2]–[4], direct high-speed drives can eliminate the intermediate mechanical gearbox, consequently the compactness, efficiency, and reliability of the drive system can be enhanced. In the manufacture applications, increase the drive speeds can also help to increase productivity and product quality [4].

On the other hand, with high rated speeds, the power density of the machine drives will increase. The volume and weight of the drive can be reduced for given magnitude of power conversion. This property is very attractive in many applications such as electrified transportation. The future electric traction machines roadmap published by the US Department of Energy targets at the power density of 50kW/L by 2025. To achieve this goal, increasing the operating speed of the drive is regarded as one of the effective ways [5]. Advanced electric machine drives are also highly demanded in the more electric aircraft (MEA) application, where hydraulic, pneumatic and mechanical systems are being replaced by electric machines. Utilization of high-speed electric drives such as high-speed starters/generators [6], [7] can effectively save the weight and space of drives, reduce the fuel consummation and CO_2 emission.

High-speed machines have many different types including induction machine (IM), permanent magnet synchronous machine (PMSM) and switch reluctance machine (SRM). Due to the highest power density and efficiency, PMSMs are currently more favoured in the space-critical and weight-critical applications such as EVs [5] and MEAs [6], [7]. Moreover, due to the stress concertation problem in the thin steel bridges, the application

of interior permanent magnet machines (IPMSM) is limited in high-speed drives [8]. Therefore, surface mounted permanent magnet synchronous machines (SPMSM) are generally more attractive for high-speed drives and hence employed as the investigation objective in this thesis. Although high-speed SPMSM drives exhibits many advantages in power density and efficiency, the high operating speed can pose many challenges on the design and control of the electric drive, which will be introduced in the next section.

1.2 Overview and Challenges of High-Speed SPMSM Drives
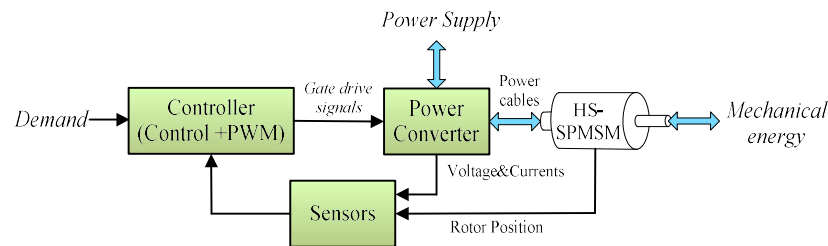
Fig. 1-1 Illustration of the typical structure of a high-speed SPMSM drive

Fig. 1-1 shows the overall structure of a typical high-speed SPMSM drive. It is mainly composed of high-speed SPMSM, power converter, controller, sensors for voltage, current and rotor position. The input demand could be the speed or torque depending on the application. The fundamental functionality of the controller is to generate the gate drive signals for the power converter. It usually consists of the speed control and the torque or current control that generates the reference stator voltages and pulse-width modulation (PWM) which implements the reference stator voltages. However, due to high rotation speeds, the design and implementation of each part in the SPMSM drive will become more difficult than the conventional one.

1.2.1 High-Speed SPMSMs

From the machine side, the high rotational speed will increase the mechanical stress on the rotor of SPMSM and sleeves to retain the permanent magnets (PMs) are required. Different sleeve materials have been compared in [6], [9]. In the high-power high-speed PM starters/generators, the carbon fibre is an attractive choice due to the very low eddy current losses in the sleeve and high yield stress margin [5]–[7]. For the super-high speed PMSM of 500,000 rpm, a non-segmented cylindrical two-pole PM with titanium sleeve are employed to ensure sufficient low stress on the PM [10], [11]. For the out-rotor high-speed machine with the maximum speed of 150,000 rpm, the ferromagnetic ring is used

to provide the mechanical support of PMs, which not only bears the centrifugal force but also functions as the back iron of the rotor [4]. Due to utilization of rotor sleeves and need for large mechanical clearance, a high-speed SPMSM usually has large effective air-gaps.

On the other hand, the skin and proximity effects of conductor will increase the stator winding resistance at high electrical frequency. The iron losses in the stator and rotor will also rise due to the high frequency excitation currents and magnetic fields. Therefore, the increase in the copper loss, iron loss, and rotor frictional loss will pose a challenge for the thermal design of high-speed SPMSMs. Slotless stator design are usually employed for super high speed drives for minimising field distortion [4], [9]–[11]. As each physical domain, including electromagnetics, mechanics and thermal, may reach its limit, the design of high-speed SPMSM becomes a very complex task and requires multi-physics optimal design [12]. Additionally, reliable high-speed bearings are also important and can be very challenging to design and manufacture. The magnetic bearing [13]–[15] is an attractive solution and have been increasingly researched due to the good controllability and dynamics of rotor systems, low mechanical loss at high speeds and low maintenance cost.

1.2.2 Power Converters for High-Speed SPMSMs
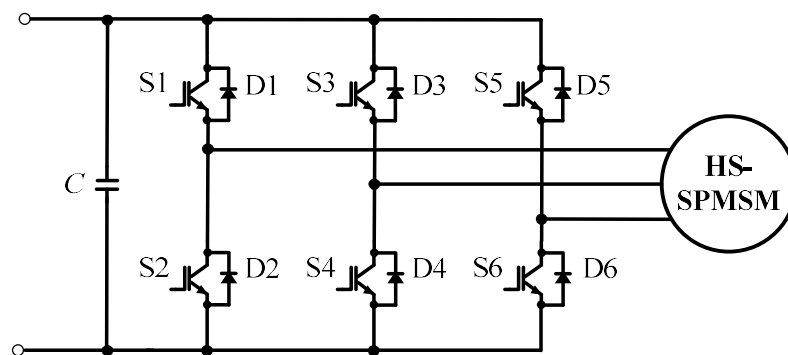
Fig. 1-2 Two-level inverter fed high-speed SPMSM drive

The power electronic converters of high-speed PMSM drives are required to provide high frequency sinusoidal stator currents. The two-level voltage source inverter (VSI) shown in Fig. 1-2, is the most employed topology for PMSM drives. However, as the switching frequency of the power switches are constrained, the switching to fundamental frequency ratios (SFRs) could be low for high-speed PMSM drives. The low SFRs will cause high current ripples and create many problems including high harmonic losses, high torque ripples, high peak currents, etc. The problem caused by low SFRs could be further worsen by the low inductance of high-speed SPMSMs due to the large air gaps and

slotless design of super high-speed PMSM drives [9]–[11]. In order to supress the current distortion, passive current filters are needed, however they will increase the volume and cost of the drive system.

Alternatively, multi-level inverters [16], [17] can be employed to reduce the current harmonics. For example, with three-level neutral potential clamped (NPC) inverters, the switching device voltage rating can be reduced to half and the frequency of output phase terminal voltage increases to double of the switching device. Three-level NPC inverter is attractive in high-power and medium voltage drives. However, compared to its two-level counterpart, the control complexity of three-level inverters increases due to increased numbers of switches meanwhile the reliability is compromised as well.

For super-high speeds with extremely high fundamental frequency, e.g. 8.3 kHz for the high-speed PMSM of 500,000 rpm [10], [11], the cascaded power converter structure is usually employed [18], where a DC/DC converter is introduced before the two-level inverter. The 2-level inverter is always operated at six-step manner while the input DC voltage of the 2-level inverter is regulated to control the magnitude of the excitation current. The cascaded power converter simplifies the control of high-speed PMSMs and requires relative low switching frequency of the 2-level inverter. It is an attractive choice for low-power and super high-speed PMSM drives. However, as it requires an extra DC/DC converter of the similar power rating as the 2-level inverter, the cost and volume of the power converter would increase greatly. Moreover, the six-step operation of 2-level inverter exhibits large current distortions and torque ripples. In order to reduce the torque ripple of cascaded power converter, a modified structure with the quasi current source DC/DC converter has been presented in [4], [19]. The torque ripple can be effectively reduced, however, the losses caused by square-wave current could still be large and a large inductor is needed which can further increase the cost and volume of the cascaded power converter.

Recently with the fast development of WBG semiconductors such silicon carbine (SiC) and gallium nitride (GaN) devices, higher switching frequencies are available [20][21]. Employing high switching frequency device can effectively increase SFRs of a high-speed drive and reduce the current harmonics and the related problems. However, high switching frequency could also lead to many undesired problems, such as intensified parasitic influences and voltage oscillations [22], [23], increased EMI due to high di/dt and dv/dt [24], bearing current and accelerated insulation degradation [25], etc.

1.2.3 Control and PWM for High-Speed SPMSMs

In the conventional SPMSM drives, field oriented control (FOC) and space vector modulation (SVM) are widely employed and can lead to satisfactory performance in the low-speed and medium speed SPMSM drives. However, for high-speed SPMSM drives, the low SFRs will not only deteriorate the transient performance but also increase the current harmonic distortions in steady states. It requires advanced control algorithms and optimal PWM to improve the performance under the constraint of switching frequency. In the following two sections, the state-of-the-art current control and optimal PWM techniques will be reviewed respectively and the problems associated with these techniques will be discussed. In addition, to reduce the cost and increase reliability, sensorless control technology is desirable and widely researched for high-speed SPMSM drives [26]–[29]. However, it is not the focus of this thesis and instead a high-speed resolver sensor with the maximum speed of 40,000 rpm [30] is employed in this thesis.

1.3 State-of-the-art Current Control Techniques of High-Speed SPMSM Drives

The state-of-the-art control of PMSM drives can be broadly categorised into two groups, current vector control (CVC) and direct torque control (DTC), according to the controlled variable i.e. current or torque. As shown in Fig. 1-3, CVC includes the classic field oriented control (FOC) [31]–[34], deadbeat predictive current control (DBPCC) [35]–[37] and finite-control-set model predictive current control (FCS-MPCC) [38]–[40]. DTC also encompasses many different methods including the conventional hysteresis DTC [41], [42], stator field oriented control (SFOC) [43], [44], deadbeat direct torque control (DB-DTC) [45]–[47] and finite-control-set model predictive direct torque control (FCS-MPDTC) [48]–[50]. Although not all of them have been reported to implement on high-speed SPMSM drives, in theory, these different control methods are applicable. Particularly, compared to control of IPMSM, control of SPMSM presents less difficulties due to the following reasons.

- Maximum torque per ampere (MTPA) control can be easily implemented by setting the reference d axis current to 0, i.e. $i_d = 0$ control.
- The electromagnetic torque of SPMSM only consists of the component contributed by the interaction between the permanent magnet flux linkage and the

q axis currents. Accurate and high-bandwidth control of q axis current can directly lead to high-performance torque control.

- The dq axis inductances of SPMSM exhibits less nonlinearity than IPMSM, especially for high-speed SPMSMs with large air gaps. Less variations in the machine parameters contribute to better control performance and facilitate use of model based control methods.
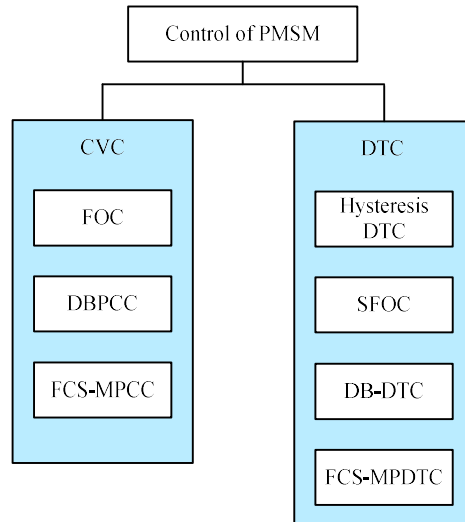
Fig. 1-3 Different control methods for PMSMs

However, control of high-speed PMSM drives can exhibit extra challenges due to the high operating speeds. Firstly, the dq axes cross-coupling effect will become intensified as the speed rises [33]. Accurate and parameter robust dq axis decoupling method is then required. Secondly, at high-speeds, high fundamental frequency entails control with low SFRs, where the large control delay occurs and the control signals are updated in low frequency relative to the fundamental frequency. The dynamic control performance and stability may be problematic at low SFRs [31]–[34]. Additionally, the inverter voltage limit could be reached at high-speeds and flux weakening scheme is needed [51]–[56]. These three issues require particular consideration and measures to address them when selecting and devising the control scheme for high-speed SPMSMs.

Since for SPMSM, control of q axis current can lead to direct regulation of torque and does not require complex flux and torque observers, this thesis particularly focuses on the current control of high-speed PMSM. The state-of-the-art current control methods for high-speed PMSMs will be reviewed in the following sections.

1.3.1 FOC

Ignoring space and time harmonics, the PMSM model in the dq frame can be expressed as (1.1) and (1.2), where u_d and u_d are the dq axis voltages, i_d and i_q are the dq axis currents, L_d and L_q are the dq axis inductances, respectively. R is the phase resistance, ω_e is the electric angular speed, ψ_m is the permanent magnet flux linkage, T_e is the electromagnetic torque. As can be seen form the torque equation, (1.3), control of dq axis currents can realise the torque regulation.

$$u_d = L_d \frac{di_d}{dt} + Ri_d + j\omega_e L_q i_q \tag{1.1}$$

$$u_q = L_q \frac{di_q}{dt} + Ri_q + \omega_e L_d i_d + \omega_e \psi_m \tag{1.2}$$

$$T_e = \frac{3p}{2}\left[\psi_m i_q + \left(L_d - L_q\right)i_d i_q\right] \tag{1.3}$$

For a SPMSM, the dq axis inductances, L_d and L_q are identical and also referred to as the synchronous inductance, L_s. The torque equation of SPMSMs can be simplified as (1.4), which is linear with the q axis current. Hence, control of q axis current can directly lead to torque control. Meanwhile, $i_d = 0$ control is usually employed for MTPA operation of SPMSM drives.

$$T_e = \frac{3p}{2}\psi_m i_q \tag{1.4}$$

1.3.1.1 FOC with dq axes decoupling

From (1.1) and (1.2), it can be clearly seen that the cross-coupling between the dq axis currents become more significant as the speed increases. Therefore, to improve the dynamic control performance, dq axis decoupling is required in FOC otherwise large oscillations in the dq axis currents will occur at high speeds [33]. The feedforward decoupling method is usually employed due to its simplicity. Fig. 1-4 shows the schematics of the conventional FOC for PMSMs, with feedforward decoupling method where K_p and K_i are the proportional and integral (PI) controller gains respectively, s is the Laplace operator. The errors between the reference currents, i_d^*, i_q^* and the actual currents i_d, i_q are fed to the two PI regulators, after which the feedforward decoupling components are added to yield the reference dq axis voltages u_d^*, u_q^*.
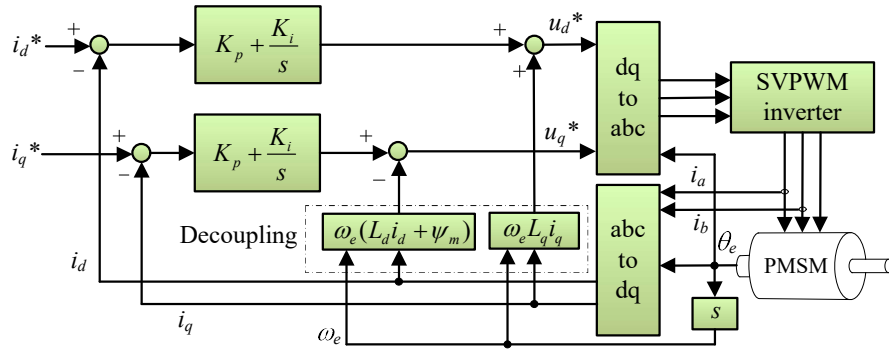
Fig. 1-4 Block diagram of FOC for PMSMs with feedforward decoupling

With accurate machine parameters and sufficient high sampling frequency i.e. large SFRs, the feedforward decoupling components can be regarded same as the actual cross-coupling components in the PMSM. Neglecting the inverter nonlinearity, the actual dq axis voltages, u_d, u_q can be assumed equal to the reference voltages, u_d^*, u_q^*. Hence, the transfer function of the current feedback control in FOC controlled PMSM drive systems can be obtained as shown in Fig. 1-5, where only the q axis current control loop is shown and that of the d axis is the same.
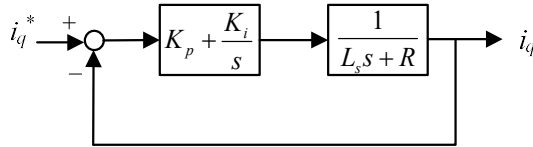
Fig. 1-5 Simplified signal diagram of FOC controlled PMSM drives in the q axis with dq axes decoupled

By proper design of the PI gains, K_p, K_i, given by

$$K_p = \omega_c L_s \tag{1.5}$$

$$K_i = \omega_c R \tag{1.6}$$

the pole associated with the phase resistance and synchronous inductance can be cancelled and the closed-loop transfer function, $G(s)$, of the current feedback control in the dq axis reference system can be derived as

$$G(s) = \frac{\omega_c}{s + \omega_c} \tag{1.7}$$

where ω_c is the designed cut-off frequency of the dq axis current control.

As can be seen from (1.7), FOC controlled PMSM drive system can be approximated as a first-order system and the bandwidth can be adjusted by the PI gains. However, since

the PI gains and the decoupling components are all dependent on the machine parameters, the control performance will deteriorate if the inaccurate machine parameters are used [57]. In order to improve the parameter robustness, an alternative decoupling method based on the complex vector model of PMSM is proposed [33], [57]–[59].

In the complex vector model, current and voltage vectors are represented by complex numbers, with the d axis as the real axis and q axis as the imaginary axis, e.g. $\boldsymbol{i}_{dq} = i_d + j \cdot i_q$, where j is the imaginary operator. The complex vector model of PMSM in the dq frame can be written as

$$\boldsymbol{u}_{dq} = L_s \frac{d\boldsymbol{i}_{dq}}{dt} + R\boldsymbol{i}_{dq} + j\omega_e L_s \boldsymbol{i}_{dq} + j\omega_e \psi_m \qquad (1.8)$$

where $\boldsymbol{u}_{dq}$ and $\boldsymbol{i}_{dq}$ denote the dq axis voltage vector and current vector, respectively.

From (1.8), the complex vector transfer function, $\boldsymbol{G}(s)$, between dq axis currents and voltages of PMSMs can be expressed as

$$\boldsymbol{G}(s) = \frac{\boldsymbol{i}_{dq}}{\boldsymbol{u}_{dq}} = \frac{1}{L_s s + R + j\omega_e L_s} \qquad (1.9)$$

The component $j\omega_e L_s$ in the complex vector transfer function $\boldsymbol{G}(s)$ leads to the complex pole, p_e

$$p_e = -\frac{R}{L_s} - j\omega_e \qquad (1.10)$$

which characterises the dq axis cross-coupling.
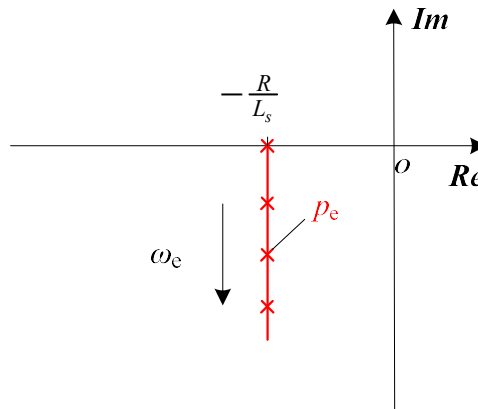
Fig. 1-6 Illustration of pole locus of PMSMs

The pole locus of $G(s)$ is illustrated in Fig. 1-6. As can be seen, the pole, p_e deviate from the real axis as the electrical angular speed ω_e increases. The large imaginary component of the pole indicates intensified oscillation property of the PMSM at high speeds, i.e. strong dq cross-coupling.

Based on the complex vector model and the resultant pole locus described above, the FOC with feedforward decoupling method shown in Fig. 1-4 can be interpreted as bringing the complex pole to the real axis by adding the decoupling terms and the PI controllers are designed to cancel the real pole. Alternatively, the complex PI current controller can be designed as (1.11) to directly cancel the complex pole, where the PI gains, K_p and K_i are the same as expressed in (1.5) and (1.6).

$$G_{\text{PI}}(s) = K_p + \frac{K_i}{s} + \frac{jK_p}{s} \tag{1.11}$$

Fig. 1-7 shows the implementation block diagram of the FOC with complex regulator. As can be seen, the dq de-coupling components are essentially generated by the integral of the current error in the other axis. According to the frequency response function analysis [57], [59], complex PI current regulator performs better than the feedforward decoupling method under parametric mismatch.

Fig. 1-7 Block diagram of FOC for PMSMs with complex PI current regulator

1.3.1.2 Control delay compensation and low SFRs

Fig. 1-8 Typical timing sequence diagram of a digital motor controller

Apart from the increased dq axis cross-coupling, the control delay is another issue of FOC for high-speed PMSMs. Fig. 1-8 shows the typical timing sequence of a digital controller, where at each step the phase currents are sampled and the stator voltage for the next step are calculated. With SVM, the time-step is usually set as same as or double of the switching frequency [60]. In this t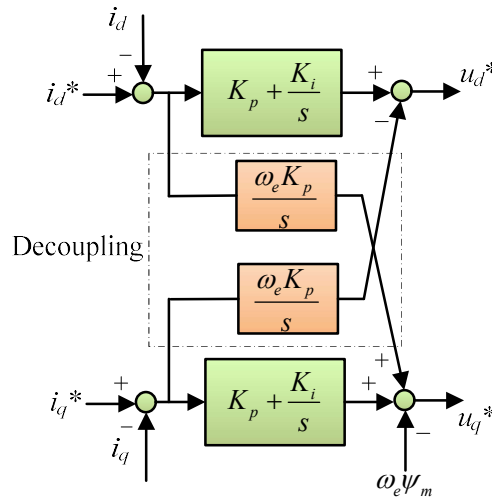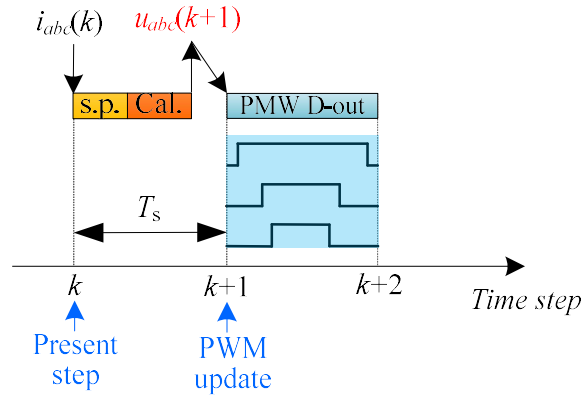hesis, to investigate and improve the control performance under low SFRs, the worst-case scenario is considered i.e. the sampling frequency is set equal to the switching frequency. As can be seen, the control delay consists of both the processing (i.e. sampling and calculation) delay and the PWM delay since the stator voltage or PWM signals can only be updated at the beginning of each step and take one step to complete. For high-speed PMSMs with low SFRs, the control delay can be very large and account for large electrical angles. Consequently, it would cause oscillation and even instability of the PMSM drive system [31], [33]. Therefore, delay compensation is indispensable and extensively researched for high-speed PMSMs.

Currently, the widely employed method is advancing the phase angle of the reference voltage vector by $1.5\omega_e T_s$ [31], where T_s is the sampling time step. This method can effectively improve the dynamic response and the stability of PMSM drives at high speeds. Alternatively, in [33], the delay is modelled as the first-order filter with time constant of $1.5\omega_e T_s$ in the stationary frame. Based on the complex vector transfer function in the dq frame, a delay compensation method is proposed and proves effective for the low SFRs of 30. However, at very low SFRs, these methods would lose effectiveness and the PMSM drive system can become unstable when SFR is lower than 10 [32]. Feedforward decoupling with one-step prediction can help to stabilize the control and achieve low SFR of 4.25 [32], however it requires accurate machine parameters. Thus, directly designed discrete current regulator is preferred for control with low SFRs [61], [62]. It has been

revealed by z-domain analysis that the current control with directly designed discrete current regulator can greatly increase the system stability. According to the simulation analysis [61], the available control bandwidth of FOC is limited to ~5% of the sampling frequency at low SFRs, e.g. ~500 Hz for the sampling frequency of 10 kHz. However, the parameter mismatch and harmonics in the sampling currents at low SFRs are not accounted. These factors may lead to lower control bandwidth settings to ensure the system stability. Therefore, to achieve high control bandwidth of high speed PMSMs with low SFRs, FOC may not be a good choice.

1.3.1.3 Flux weakening operation

Assume the resistive voltage drop is negligible at high speeds, the stator voltage magnitude, u_s at steady states can be calculated by

$$u_s = \sqrt{u_d^2 + u_q^2} = \sqrt{\left(\omega_e L_q i_q\right)^2 + (\omega_e L_d i_d + \omega_e \psi_m)^2} \qquad (1.12)$$

As can be seen, the stator voltage magnitude u_s increases with the speed under $i_d = 0$ control. With a given DC-link voltage, the stator voltage will reach the maximum voltage at a certain speed. Above that speed, the negative d axis current calculated by (1.13) is demanded to maintain the stator voltage within the maximum voltage, V_{max}. As negative d axis current essentially weakens the flux generated by the permanent magnet and the stator flux magnitude, this operation condition is referred to as flux weakening.

$$i_d^* = \sqrt{\left(\frac{V_{max}}{\omega_e}\right)^2 - \left(\frac{L_q}{L_d} i_q^*\right)^2} - \frac{\psi_m}{L_d} \qquad (1.13)$$

Table 1-1 summarises the maximum available stator voltages, V_{max} under different modulation methods. As can be seen, compared to SPWM, SVM can increase the voltage utilization by 15% and hence the operational region by the same extent. Six-step operation can further extend the maximum voltage and operation region by ~10% of that with SVM. However, six-step operation can lead to large current harmonics and reduced efficiency. On the other hand, with SVM, to achieve the same operation region as six-step operation, higher DC-link voltage is required and it will increase the power rating of converter. Therefore, selection between SVM and six-step operation in flux weakening region can be seen as a trade-off between the converter power rating and current harmonic distortion.

Table 1-1 Maximum stator voltage under different modulation methods

SPWM	SVM	Six-step Operation
$\dfrac{V_{dc}}{2}$	$\dfrac{V_{dc}}{\sqrt{3}}$	$\dfrac{2V_{dc}}{\pi}$
1 p.u.	1.15 p.u.	1.27 p.u.

The flux weakening methods for FOC can usually be divided into two categories, i.e. feedforward flux weakening [51], [52], feedback flux weakening [53] and hybrid flux weakening [54]–[56]. In the feedforward flux weakening scheme, the d axis current reference is generated from the machine speed, the torque/q axis current demand, DC-link voltage and machine parameters by the analytical equation, (1.13) or by calibrated look-up-tables (LUTs). This method is simple to implement but the performance is dependent on the accurate machine models or LUTs. On the contrary, in feedback flux weakening method, the d axis current is generated by a PI controller with the difference between the reference stator voltage magnitudes before and after the voltage saturation block as the input. Hence, there is no need for accurate machine parameters with the feedback flux weakening method. In hybrid flux weakening scheme, the d axis current is calculated in the feedforward manner meanwhile corrected by the feedback loop of voltage error. This method compensates the parameter inaccuracy and improves the response time of flux weakening. However, all these three method may suffer from the deteriorated transient performance due to the dq cross-coupling. To address this problem, SFOC [43], [44] with the stator flux magnitude directly regulated is attractive, however the accurate stator flux observer [63]–[71] is required.

It is worth noting that flux weakening operation depends on the design and match of the maximum stator voltage at the base speed and the maximum load with the available DC-link voltage. The base speed is defined as the speed at which the stator voltage under maximum torque per Ampere operation reaches the maximum continuous inverter output voltage for a given DC link voltage. Flux weakening operation is employed for the constant power region above the base speed. However, flux weakening operation is not a distinct requirement for high-speed PMSM drives with high fundamental frequency. Since the machine drive under the study is not designed for field weakening operation, this thesis focuses on control of high-speed PMSMs with high fundamental frequency and low SFRs when flux weakening operation is not required. Nevertheless, application

of the control methods developed in this thesis to flux weakening operation for high speed drives would be an interesting topic for further research.

1.3.2 DBPCC

The concept of deadbeat control is to reach the reference at the next step without error by calculating and applying the desired reference voltages based on the machine model [35], [72]. It can lead to very fast dynamic response and realise high control bandwidth. The reference voltages are usually implemented by SVM, thus it can have excellent steady-state performance as well. DBPCC employs the dq axis current vector as the reference.

Usually, the control time-step is assumed to be sufficient small and the forward Euler approximate method is employed to discretise the PMSM model in (1.1) and (1.2), which can be given by

$$u_d(k) = L_d \frac{i_d(k+1) - i_d(k)}{T_s} + R i_d(k) - \omega_e L_q i_q(k) \tag{1.14}$$

$$u_q(k) = L_q \frac{i_q(k+1) - i_q(k)}{T_s} + R i_q(k) + \omega_e L_d i_d(k) + \omega_e \psi_m \tag{1.15}$$

where (k) and $(k+1)$ denote the corresponding variables at steps k and $k+1$, respectively.

In (1.14) and (1.15), by replacing $i_d(k+1)$ and $i_q(k+1)$ with the reference dq axis currents, i_d^*, i_q^* respectively, the desired/reference dq axis current voltages, $u_d^*(k)$ and $u_q^*(k)$ in step k to achieve i_d^* and i_q^* at step $(k+1)$ can be easily calculated. Transfoming this reference voltages into the stationary frame and they can be implemented by SVM.

However, the predicted voltages $u_d^*(k)$ and $u_q^*(k)$ in step k can only be applied at step $(k+1)$. In order to compensate for the one-step digital processing delay, one-step current prediction is employed in DBPCC [35]–[37]. From (1.14) and (1.15), the dq axis currents in the following step, $\hat{\imath}_d(k+1)$ and $\hat{\imath}_q(k+1)$ can be predicted as

$$\hat{\imath}_d(k+1) = \frac{T_s}{L_d} \left[u_d(k) - R i_d(k) + \omega_e L_q i_q(k) \right] + i_d(k) \tag{1.16}$$

14

$$\hat{\imath}_q(k+1) = \frac{T_s}{L_d}\left[u_q(k) - Ri_q(k) - \omega_e L_d i_d(k) - \omega_e \psi_m\right] + i_q(k) \tag{1.17}$$

With the predicted currents, $\hat{\imath}_d(k+1)$, $\hat{\imath}_q(k+1)$, and the discrete machine model in (1.14) and (1.15), the reference dq axis voltages at step $k+1$, $u_d^*(k+1)$ and $u_q^*(k+1)$ can be calculated by

$$u_d^*(k+1) = L_d \frac{i_d^* - \hat{\imath}_d(k+1)}{T_s} + R\hat{\imath}_d(k+1) - \omega_e L_q \hat{\imath}_q(k+1) \tag{1.18}$$

$$u_q^*(k+1) = L_q \frac{i_q^* - \hat{\imath}_q(k+1)}{T_s} + R\hat{\imath}_q(k+1) + \omega_e L_d \hat{\imath}_d(k+1) + \omega_e \psi_m \tag{1.19}$$

Fig. 1-9 shows the block diagram of the conventional DBPCC. As can be seen, DBPCC consists of two procedures, i.e. one-step current prediction and deadbeat voltage calculation. Based on the discrete model of PMSMs, DBPCC can be readily implemented digitally. Since the reference dq axis voltages, $u_d^*(k+1)$ and $u_q^*(k+1)$ are calculated at step k, the one-step processing delay can be compensated. With the accurate machine parameters, both excellent transient and steady-state performance can be attained.
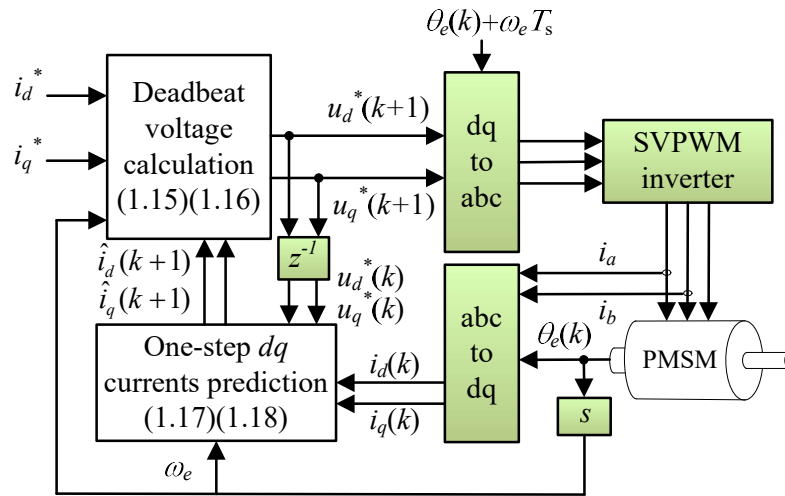

Fig. 1-9 Block diagram of the DBPCC based on the dq frame model of PMSMs

However, with inaccurate parameters and inverter nonlinearity, the performance of DBPCC will deteriorate. Extensive researches have been conducted on the analysis and compensation of the parameter mismatch. The methods can be categorised into two groups, i.e. feedback compensation [73]–[75] and disturbance observer based compensation [37][76]. However, all these methods assumes that the time-step is sufficiently small, which may not apply for high-speed PMSMs with low SFRs.

For high-speed PMSMs, DBPCC can present many problems due to low SFRs. At low SFRs, the rotor movement per time-step calculated by (1.20) in electrical angle can be very large. For example, the SFR of 10 corresponds to a rotor movement of $36°$ in electrical angle. Moreover, since DBPCC effectively consists of two-step prediction, i.e. one-step current prediction and one-step voltage prediction, the rotor movement in the prediction horizon is actually double of (1.20), e.g. $72°$ for SFR=10.

$$\Delta\theta = \frac{360°}{SFR} \tag{1.20}$$

The large rotor movement in the time-step would make the Euler forward approximation in (1.14)~(1.17) inaccurate and consequently lead to deteriorated performances. In [72], the currents in the dq axis cross-coupling terms of the equations for one-step current prediction, i.e. (1.16) and (1.17), and deadbeat voltage calculation, i.e. (1.14) and (1.15) are replaced with the corresponding average currents at steps k and $k + 1$. This measure can help improve the transient performance considering the dq axis currents with DBPCC may change rapidly in two consecutive steps. However, it cannot address the large rotor movement issue at low SFRs. In [35], the rotor movement effect has been compensated by modelling the inverter as a zero-order holder and modifying the dq reference voltage to achieve the same average voltage demanded by those calculated from (1.14) and (1.15). This compensation method is essentially same as the PWM delay compensation method for FOC [31]. However, as will be analysed and discussed in Chapter 2, this type of rotor movement compensation will lose effectively at very low SFRs. Therefore, to address the large rotor movement at high-speeds, a novel stationary frame based DBPCC will be presented in Chapter 2. The analysis and compensation of the parameter mismatch and inverter nonlinearity influences in the proposed DBPCC will also be investigated, which can be found in Chapters 2 and 3.

1.3.3 FCS-MPCC

FCS-MPCC is another type of predictive control [77]–[80]. It has been increasingly gaining interests in the electrical machine controls, due to its simplicity, excellent dynamics and handling capability of addressing the nonlinearity and constraints.
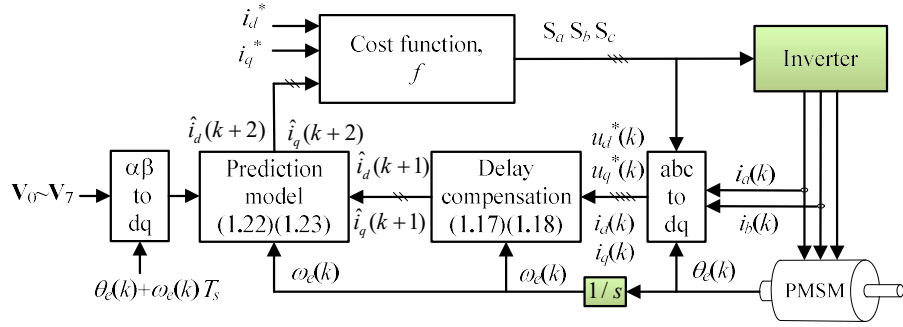
Fig. 1-10 Block diagram of the conventional MPCC

The block diagram of the conventional MPCC method is shown in Fig. 1-10. It mainly consists of three steps [38]. First, to compensate the one-step sampling and calculation delay, the dq currents at the next step, $\hat{\imath}_d(k+1)$ and $\hat{\imath}_q(k+1)$ are predicted by (1.16) and (1.17). Secondly, for a two-level inverter, the inverter voltage vectors only consists 8 possible vectors, i.e. six active vectors ($\mathbf{V}_1 \sim \mathbf{V}_6$) and two zero vectors ($\mathbf{V}_0$ and $\mathbf{V}_7$), as shown in Fig. 1-11.
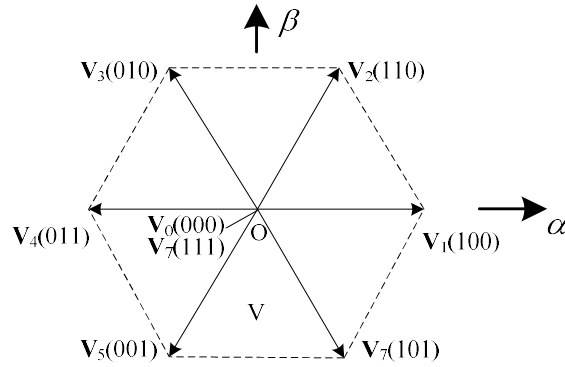

Fig. 1-11 Switching vectors for two-level inverters

Transforming these discrete voltage vectors into the dq frame, the stator currents at step $k+2$ with all possible voltage vectors can be predicted by

$$\hat{\imath}_d(k+2) = \frac{T_s}{L_d}\left[u_d(k+1) - R\hat{\imath}_d(k+1) + \omega_e L_q \hat{\imath}_q(k+1)\right] + \hat{\imath}_d(k+1) \qquad (1.21)$$

$$\hat{\imath}_q(k+2) = \frac{T_s}{L_d}\left[u_q(k+1) - R\hat{\imath}_q(k+1) - \omega_e L_d \hat{\imath}_d(k+1) - \omega_e \psi_m\right] + \hat{\imath}_q(k+1) \qquad (1.22)$$

Subsequently, the cost function, (1.23) can be evaluated for all the predicted dq axis currents in (1.21) and (1.22). The switching vector that minimises the cost function, i.e. current error will then be selected. As the switching vector directly corresponds to the

switching states of the inverter, the PWM block can be eliminated in FCS-MPCC. With the optimal switching vector selected at each step to minimize the current error, excellent dynamic response can be achieved with FCS-MPCC. Besides, the current and voltage constraints can also be met by including them in the cost function [81], [82]. Hence, the flux weakening can potentially be more easily implemented.

$$f = (i_d^* - \hat{\imath}_d)^2 + \left(i_d^* - \hat{\imath}_q\right)^2 \qquad (1.23)$$

The property of the switching frequency with FCS-MPCC is different from the conventional FOC with SVM. The switching frequency of FCS-MPCC is not constant and to obtain similar switching frequency as FOC, high sampling frequency may be required as the switching vectors in the consecutive steps could be the same. On the other hand, as the change of switching vector can only occur at each time step i.e. discretely, the current harmonic distortions with FCS-MPCC could be high. Therefore, extensive modified FCS-MPCC schemes have been proposed in order to improve the steady-state performance of FCS-MPCC. Double switching vectors for each time-step is introduced in [83] and the steady state performance can be enhanced while the good dynamic response is not affected. This method subsequently has been extended to three switching vectors per time-step [84] and multi-switching vectors per time-step i.e. discrete SVM [85]. Steady performance can be improved, however the computation time increased. On the other hand, multi-step prediction can also help to improve the steady state performance of FCS-MPCC [86], [87], however the computation will increase exponentially. In order to solve this problem, the branch and bound method have been proposed to reduce the candidate switching state combinations and hence increase the computational efficiency [88].

Although, the performance of FCS-MPCC have gained remarkable improvement, application of FCS-MPCC for highs-speed PMSMs at low SFRs is still of challenges. To address this issue, the boundary based FCS-MPCC [39], [40] could be a promising technique. In order to reduce the switching frequency, the cost function of FCS-MPCC is modified to include the time duration of different switching vector that can maintain the stator current vector within the defined error boundary [39]. In steady states, the switching vector with the longest time duration is selected so that the switching commutation can be minimised. To achieve fast dynamics, the current error minimisation is still employed in transients when the current error is larger than the defined maximum error. The hysteresis based FCS- MPCC has been successfully applied on high-power IMs with low

SFRs. The sampling frequency for the 50Hz high-power IM drive is selected as 10 kHz. It implies that for high-speed drive with high fundamental frequency, very high sampling and calculation frequency are required. Moreover, the control performance of boundary based FCS-MPCC is heavily dependent on the machine model accuracy since the selection and execution time duration of the switching vector are both predicted. And as the current trajectory prediction horizon varies with the switching vector execution time duration, the prediction with simple Euler extrapolation method may lose effectiveness when one switching vector is active over a long period.

Table 1-2 compares the performance of FOC, DBPCC and FCS-MPCC generally for high-speed PMSM drives. As can be seen, the DBPCC improves the dynamic control performance of the conventional FOC with the steady-state current distortion dependent on model accuracy. It can be implemented in a simple manner. Therefore, DBPCC is an attractive control method for high-speed PMSM drives and will be further investigated and improved in this thesis.

Table 1-2 Comparison of different current vector control methods for high-speed PMSM drives

	FOC	DBPCC	FCS-MPCC
Dynamic Response	Poor	Good	Good
Steady-state Current Distortion	Determined by SVM	Determined by SVM	Poor, but can be optimized.
Sampling Frequency Requirement	Low, same or double of switching frequency	Low, same or double of switching frequency	High

1.4 Reviews of Optimal PWM Techniques with Low SFRs

PWM is an essential part in the electric machine drives. It determines the steady state performance of PMSM drives [60] such as current harmonic distortion, torque ripples, switching losses [89] and common mode voltages [90]–[92], and can also affect the dynamic response [39].

Generally, SPWM and SVM are two mostly widely used. Usually, SPWM is realized by comparing the sinusoidal references with the high-frequency triangular waveform. Due to the degree-of-freedom in selecting the zero sequence voltage in SPWM, many different variations of SPWM have been reported. One category is SPWM with harmonic injection such as THIPWM1/6 [93] and THIPWM1/4 [94] that injects third harmonic harmonics with the amplitude of 1/6 and 1/4 of the fundamental reference respectively.

These PWM methods can enhance the voltage utilization and lead to similar performance as SVM. With SVM, the reference voltage vector derived from the proceeding controller is synthesized by the inverter discrete voltages as illustrated in Fig. 1-11. Alternatively, SVM can be equivalently implemented by SPWM with the zero sequence voltage equal to the minimum of the three reference signals [95] and hence SPWM and SVM are both referred to as carrier based PWM [39], [60]. Since the modulating signals of the above described PWM methods are all continuous with time, they are referred to as continuous PWM (CPWM) [96]. In contrast to CPWM, many different PWM methods with discrete modulating signals can also be derived by adding zero sequence components in SPWM and are named as discontinuous or discrete PWM (DPWM) [95]–[97]. Alternatively, SPWM with zero sequence component injection can also be implemented in the same manner as SVM [95], [97]. Consequently, the differences of various PMW methods reflects in the zero vector partitioning in SVM. Particularly, as the zero vectors are alternatively employed for 60° segments in DPWM, DPWM exhibits less switching frequency and also referred to as bus clamping SVM [98][99]. The frequent used CPWM and DPWM methods are compared analytically in [19]. It can be generally concluded that with the same switching freqeuncy, the SVM is optimal over the low modulation index region until 0.6~0.7, where the modulation index under six-step operation is defined as 1. While DPWM performs better when the modulation index is higher than 0.7. It is worth noting that the general anlysis and comparison in [19] are based on the assumption that the reference voltage vector is fixed over a PWM cycle. It imples the precondiciton of sufficient switching frequency compared to the fundamental freqeucny.

It is widely acknowledged that the conventional carrier based PWMs will lead to abundant harmonic distortions including even and sub harmonics at low SFRs, especially when it is less than 15 [39][100]. The increased current harmonics will further cause high torque ripples, extra conduction losses in a machine drive and temperature rises. Therefore, to mitigate these problems, synchronous PWM methods are usually employed for the electric drives with low SFRs. Generally, synchronous PWM can be classified into two groups, i.e. synchronised carrier based PWM [62], [99], [101], [102] and synchronous optimal PWM (SOPWM).

Synchronised carrier based PWM can be simply implemented on the basis of the conventional carrier based PWM by sampling at certain positions of the reference voltage vector, e.g. $6^{°} + k \cdot 12^{°}$ $(k = 0,1,2,\cdots)$ for the pulse number, N_p=15. As a result, the

derived phase voltage will be symmetrical in a fundamental cycle and then even and triplen harmonics can be eliminated, leading to reduced current THDs. However, only pulse numbers, $N_p = 3 + 6k$ ($k = 0,1,2,\cdots$) are available with the conventional synchronised SVM. Therefore, in [99], [101], the bus clamping SVM methods, i.e. DSVM are considered and switching vector sequences for different pulse numbers are designed. In order to compensate for the sampling position errors and realize smooth transition between different pulse numbers, synchronized PWM with variable time-steps and the reference voltage modification scheme are proposed in [28]. Although symmteric voltage waveforms and current THD reduction can be obtained with synchronized carrier based PWM, the current harmonic distortion can be further reduced by employing SOPWM.

The basic concept of SOPWM is that for a given pulse number, the switching instant of each pulse can be optimised in such way that the resultant fundamental voltage is equal to the reference meanwhile the cost function, e.g. the current THD is minimised [103]–[105]. For different modulation indices and pulse numbers, the optimal pulse patterns (OPPs) can be obtained offline and stored in LUTs for real-time generation of PWM pulses. In steady states, the output voltages would be close to the optimised patterns, which are symmetric and the resultant current THDs are minimised. Alternatively, the cost function of OPPs can also be selected to eliminate certain low harmonics, which corresponds to the selective harmonic elimination PWM (SHEPWM) [106], [107] and current THD minimisation [108]. In addition, to eliminate all the even and triplen harmonics, the OPPs are usually assumed to be of quarter waveform, half waveform and three-phase symmetries. In order to further minimise the current THDs, the symmetries of pulse patterns can be relaxed to feature only half-waveform and three-phase symmetries [109]. But the complexity of offline calculation and the online pulse generation will both increase greatly and it only improves slightly over small ranges of modulation index.

As the steady-state performance of SOPWM relies on the offline obtained OPPs, the calculation of OPPs are of fundamental importance. The formulation of the pulse pattern optimization can be divided to two categories, i.e. time-domain based optimisation [110] and frequency domain based optimisation [103], [111]. The time domain based optimization can lead to polynomial cost functions by the assumption of pure inductive load. It simplifies the OPP calculations. However, the back EMF effect is not considered

in the optimisation and hence the derived OPPs may lose generality for electric machine drives. The frequency domain based method calculates the magnitude of each harmonics by Fourier analysis and then formulate the optimisation problem [103], [111]. It can apply to all different applications including two level inverters and multi-level inverters with inductive loads and electric machine drives. However, the formulation of the pulse pattern optimisation consists of transcendental equations and a nonlinear constraint, therefore the OPPs can only be solved numerically. Varieties of optimization methods including gradient methods [111], genetic algorithm [112], particle swarm optimization [113], etc. have been employed to obtain OPPs. Due to simplicity and generality, the gradient method is currently more widely employed for two-level [103][114][115] and multi-level converters [111] [116][117]. However, in order to obtain the global optimal solution with the gradient methods, the optimization should be repeated substantially more times with different initial values e.g. 25,000 times for three-level converters [111][118]. On the other hand, the trade-off between the current distortion factor and the solution discontinuity requires complex re-optimization procedure and can differ in different applications due to the variation of operating modulation index [111][117]. The optimization and derivation of the OPPs for real-time control of electrical drives can be very time-consuming. Therefore, a computationally efficient optimization algorithm for OPPs will be presented in Chapter 4.

Although the SOPWM exhibits minimised current THDs in steady states, the dynamic performance of SOPWM is not desirable. On the one hand, the transition of SOPWM mode from one pulse number to other as a result of change in fundamental frequency will introduce undesired transients to the system and can result in large overshoot current [105]. The reported transition scheme [119] at certain position can lead to slow mode transition and requires very higher sampling frequency for high-speed drives. To address this problem, a fast and smooth transition scheme of SOPWM mode will be proposed in Chapter 4. On the other hand, the dynamic response of current control with SOPWM is slow. It can be attributed to that the equivalence of OPP to the reference voltage is established in steady states. In transients, the required reference voltage cannot be realised by the retrieved OPP from the LUT. In the applications such as fans where the slow current control response is acceptable, digital filters can be employed to constraint the change rate of the reference voltages and remove the current harmonics in the feedback [120]. However, for high-performance high-speed PMSM drives, fast dynamic current control is required. To address the dynamic problem of the SOPWM, the optimal current

and flux trajectory tracking method have been proposed in [121], [122] and [104], [105] respectively. The concept of this technique is based on real-time modification of the OPPs so that the optimal current or stator flux trajectory associated with OPPs in steady states can be tracked. Since the stator flux can be more accurately estimated by the integration of the phase voltage at high speed or high modulation index, the stator flux tracking method is less machine-parameter-dependent and hence more favoured [30]. However, for a given required stator flux change determined by the dynamic flux error, the switching modification in each phase may not be uniquely determined if switching occurs in each phase and the dynamic flux error could not be fully compensated when there is no or only one phase switching. Hence, the flux tracking performance is dependent on the available number of switching in the three phase OPPs during the control interval. At low pulse numbers, the stator flux is very likely not be able to be tracked due to the lack of switching in certain phases. Since the aforementioned scenarios are not generally covered by the reported flux trajectory tracking method [104], [105], a novel fast dynamic control method with SOPWM will be presented in Chapter 5.

1.5 Scope and Overview of Research

1.5.1 Aim and Objectives

The aim of this thesis is to address the low SFR problems in the control and PWM of the high-speed PMSM drives. The classic and representative 2-level inverter fed high-speed SPMSM drive is employed as the control object. The developed methods and techniques can potentially be extend to the other type of high-speed drives as well. The main objectives of this thesis are summarized below.

1) To develop a novel high-performance high-bandwidth control method for high-speed PMSM drives that can be implemented with low SFRs.

2) To analyse and compensate the influences of practical issues including the inverter nonlinearity and parametric mismatch in the developed control method.

3) To investigate and gain deep understanding on the conventional SOPWM for high-speed PMSM drives, including OPPs optimization, current THD evaluation and optimal stator flux trajectories.

4) To develop a smooth mode transition scheme for SOPWM with different pulse numbers.

5) To develop a novel fast dynamic current vector control with SOPWM for high-speed PMSM drives.

6) To validate the performance of the proposed control and PWM methods on the prototype high-speed PMSM drive.

1.5.2 Main Contributions

Focusing on the development of advanced control and PWM methods for high-speed PMSM drives, the main contributions of this doctoral work are outlined as follows.

1) A robust deadbeat predictive current control method has been proposed for high-speed PMSM drive. Compared to the conventional methods including FOC and DBPCC, the proposed method is hardly affected by large rotor movements in a time-step, which are caused by the high rotating speed and exhibit excellent dynamic response at high speeds even with very low SFRs.

2) The influences of parametric mismatch and inverter nonlinearity of the proposed DBPCC have been analytically analysed and verified by both numerical simulation and experiments. Particularly, the effect of the speed and SFR on the robustness of the proposed DBPCC for high-speed PMSM drives is quantified, whilst such effect is neglected in the conventional analysis.

3) A simple and novel current control error compensation method has been developed for DBPCC. With the proposed method, the average current errors along both d-axis and q-axis caused by inaccurate machine parameters and inverter nonlinearity can be effectively removed.

4) A novel selective current harmonic suppression method has been developed for DBPCC. With the proposed method, all the current harmonics caused by inverter nonlinearity and back EMF harmonics can be eliminated. The proposed method is parameter independent and effective even at high speeds where the ratios between the harmonic frequency and the fundamental frequency are quite low.

5) A novel transient performance improvement method of DBPCC has been proposed based on inductance online adaptation. The proposed method can be readily integrated with the proposed current control error compensation method and current harmonic suppression method. As a result, with the developed method, the nearly ideal deadbeat control can be achieved even with inaccurate machine model i.e. detuned machine parameters and inverter nonlinearity.

6) A computationally efficient pulse pattern optimization algorithm and current THD prediction method have been developed for SOPWM of high-speed PMSM drives.

The proposed methods generally apply for both two-level and multi-level inverters.

7) A fast and smooth SOPWM mode transition scheme for two-level inverter fed high-speed PMSM drives have been proposed based on the general properties of OPPs. The proposed method is very simple and can start the mode transition at any position and realise the transition in 1/6 fundamental cycle smoothly without any overshoot current.

8) A fast dynamic current control with SOPWM has been developed for high-speed PMSMs. With the proposed methods, both low steady-state current harmonic distortions and fast current response can be achieved.

1.5.3 Organization of Thesis

This thesis consists of 6 chapters and the content of each chapter is summarized as follows.

Chapter 1 introduces the background of high-speed machine drives and the low SFR problem in the high-speed machine drive is highlighted. The state-of-art current control methods and the optimal PWM techniques are reviewed for high-speed PMSM drives. Finally, the overall structure of the thesis is briefly introduced.

Chapter 2 proposes a novel stationary frame based DBPCC for high-speed PMSM drives. The proposed method controls dq axis current by tracking the stator flux in the stationary frame and only features two step control delay. The control performance is not affected by the large delay and rotor movement in high-speeds and ideal deadbeat control can be achieved even with extreme low SFRs. On the other hand, as the proposed method relies on the accurate machine model, the influences of the inverter nonlinearity and parameter mismatch on the steady-state performance and transient performance have been both analytically analysed. The proposed method and the analysis are verified by extensive simulations and experiment results on the prototype high-speed PMSM drive.

Based on the analysis of inverter nonlinearity and parameter mismatch in Chapter 2, the proposed DBPCC is furthered improved in **Chapter 3** from three aspects including parameter robustness, harmonic suppression and transient performance. Firstly, to compensate the steady-state control error caused by parameter mismatch and inverter nonlinearity, a novel adaptive reference correcting current injection (ARCCI) method has been proposed. The proposed ARCCI is based on adaptively injecting reference

correcting currents into the reference dq axes currents. By incorporating this method, the proposed DBPCC exhibits similar steady-state performance as that with FOC while achieving significantly faster dynamic response and less cross-coupling between dq axis currents in high speeds. Secondly, the method based on adaptive reference correcting current injection (AHRCCI) is proposed and can effectively suppress all the low-order current harmonics caused by the non-ideal factors such as the inverter nonlinearity and back EMF harmonics. Finally, a novel inductance online identification method is proposed to improve the transient performance deterioration due to the inductance estimation error. This method exploits the transient tracking error caused by inductance mismatch to identify the actual inductance. By employing the identified inductance, the transient performance of DBPCC can be greatly improved and nearly ideal deadbeat current control can be achieved. All the three developed methods in Chapter 3 is parameter independent and can be easily implemented and incorporated in DBPCC for high-speed drives. They are verified by extensive simulation and experiments at both low and high-speeds on the prototype high-speed drives.

In **Chapter 4,** a computationally efficient optimisation procedure has been developed to derive all the OPPs of SOPWM. It can reduce the computation time greatly and provide flexible trade-off between the current distortion factor and the discontinuity number in the derived OPPs. Based on the OPPs, the SOPWM can lead to minimized current THDs via an offline optimisation procedure. A simple harmonic current prediction method has also been proposed to quickly assess the current THDs for high-speed PMSM with SOPWM. Moreover, in order to reduce the dynamic current error caused by the SOPWM mode transition, e.g. pulse number variation, a novel smooth and fast mode transition method has been proposed. The proposed method is based on the general properties of the OPPs and optimal flux trajectory (OFT)s of SOPWM. It can realize a smooth and fast SOPWM mode transition with virtually no dynamic errors. Extensive simulations and experiments have validated the effectiveness of the proposed methods.

In **Chapter 5**, a novel method i.e. pseudo six-step modulation is proposed to address the poor dynamic response of SOPWM based control. The proposed method tracks the optimal flux trajectory associated with SOPWM six-steps per fundamental cycle. Both fast dynamic control of dq axis currents and low current distortions in steady states can be achieved. Moreover, the proposed method can realise fast and smooth pulse number transition and the steady-state current control error caused by the parameter mismatch

and the inverter nonlinearity effects can be compensated. Extensive simulations and experiments have been performed and validated the effectiveness of the proposed method.

Chapter 6 summarises the doctoral work on advanced control and PWM for high-speed PMSM drives, after which the further improvement and possible future research scope are presented.

1.6 List of Publications

1. S. Dai, J. Wang and Z. Sun, "Pseudo Six-Step Modulation with Optimal Flux Tracking for Control of High-Speed Permanent Magnet Synchronous Machines (PMSMs)," 2019 IEEE Energy Conversion Congress and Exposition (ECCE), Baltimore, MD, USA, 2019, pp. 313-320, doi: 10.1109/ECCE.2019.8912637

2. S. Dai, J. Wang, Z. Sun and E. Chong, "An Improved Gradient-Based Optimization Algorithm for Synchronous Optimal Modulation of High-Speed PMSM Drives," 2021 International Electric Machines and Drives Conference (IEMDC), accepted.

3. S. Dai, J. Wang, Z. Sun and E. Chong, "Smooth and Fast Mode Transition of Synchronous Optimal Modulation for Two-Level Inverter Fed High-Speed PMSM Drives," 2021 International Electric Machines and Drives Conference (IEMDC), accepted.

CHAPTER 2

Robust Stationary Frame Based Deadbeat Predictive Current Control for High-Speed PMSM Drives

2.1 Introduction

As introduced in Chapter 1, the control strategies that apply for PMSM drive generally can be also employed to control high-speed PMSM drives, such as conventional FOC [31]–[34], [123] and DTC [41], [42], [124]. However, as the sampling-to-fundamental frequency ratios become extreme low in high speeds, the FOC suffers from poor dynamic response and can even lose stability with SFR less than 10 [32] even if the delay compensation [31] and accurate machine parameters are employed for dq axis decoupling and PI regulator design. Discrete current regulator can be employed to effectively improve the stability of FOC with low SFRs [34], while the current control bandwidth of high speed drives is still limited. On the other hand, DTC can provide very fast dynamic response [125], however, the steady-state performance is inferior as large current and torque ripples exist. By incorporating SVM and PI regulator, the stator flux oriented DTC can greatly improve the steady state performance [43]. However, the dynamic response of the system and the control bandwidth are again limited by the bandwidth of the stator flux observer [66], [67] and the PI regulators for torque and flux control loops. Moreover, as an emerging control technique for electrical machine drives, finite control set (FCS) model predictive control (MPC) exhibit excellent dynamic response [79], but the resultant current/torque ripples are larger than the SVM based control. It is difficult to design hardware filters since the control scheme has varied switching frequency. It can be improved by numerous methods such as employing double or multiple switching vector in a time step [126], but the computational burden can be very intensive, especially with multiple step predictive control [87]. However, the deadbeat control is simpler and can contribute to both fast dynamic response and low current harmonics with constant switching frequency since carried based SVM can be employed [36], [37], [127]–[129]. Compared to deadbeat direct flux and torque control (DB-DTFC), deadbeat predictive current control (DBPCC) [128][129] does not require complicated flux and torque observer and deadbeat control of current can lead to deadbeat torque control accordingly. Moreover, the calculation of the reference voltage vector is simpler and one-step sampling

and calculation delay is compensated in DBPCC. Therefore, DBPCC is very attractive for high-speed SPMSM drives [35].

The conventional DBPCC is usually based on discrete machine model in the dq frame and incorporates two procedures, namely predict the dq axis currents at next sampling step firstly and then calculate the reference voltage vector that can achieve the reference currents. High fidelity and accurate machine models [130] are available and the online identification techniques of machine parameters [131] are well developed. With accurate machine model, the conventional DBPCC can have excellent control performance of high-speed PMSM drives, with the current controlled with only two time-step delay and the steady state current harmonics similar to that with FOC, determined by SVM.

However, in high speeds with low SFRs, the calculated reference voltage vector in the synchronous frame cannot be realized accurately due to a relatively large rotor movement during the control period. As a result, the control performance of conventional DBPCC would deteriorate even with accurate machine parameters. One effective solution is to compensate the rotor movement by modifying the reference voltage vector in the dq frame [35]. Assuming that the reference voltage in the stationary frame equals to the actual voltage, the rotor movement effect during the control can be modelled as the rotation of the reference voltage in the dq frame. To obtain the same average voltage in the dq frame that accounts the effect of rotor rotation, the reference voltage vector fed to the SVM are modified. Actually, this rotor movement compensation method has been widely employed in synchronous PI current regulator based conventional FOC as well [31]. Nevertheless, as will be analysed and demonstrated in this chapter, this kind of rotor movement compensation is not sufficient for high speeds with very low SFRs.

Alternatively, instead of using the dq frame based machine model, the stationary frame based model of PMSM can be employed so that the obtained reference voltage vector is based on the stationary frame and can be more accurately realised by SVM. In [128], the stationary frame based model is employed, however, the rotor movement influence on the back EMF is not considered. As presented in [132], the large rotor movement in high speed can still cause a large prediction error in current using the stationary frame based voltage model of PMSM by linear current approximation. In [133], a stator flux controller is employed to control the phase current of high-speed PMSM. It is not affected by the rotor movement however it requires the LUT between phase current magnitude and phase flux. Moreover, it does not generally apply to current vector control

with any combination of d- and q-axis currents and one-step current prediction is not included. Additionally, disturbance observers can be also employed to compensate the rotor movement caused [37], [134]. However, as the SFRs reduces, the observer [69], [135] may lose stability.

Therefore, in order to address the problem caused by large rotor movement in high speeds, this chapter presents a novel DBPCC scheme for high-speed PMSM drives based on the stator flux vector tracking in the stationary frame. With the proposed method, the reference voltage vector in the stationary frame is directly calculated and can be achieved by SVM. The rotor movement effect and the processing delay are both precisely taken into accounts. The proposed control is not sensitive to the large rotor movement in high speeds while applicable over a wide speed and SFR range. The proposed method has a general structure of dq axis current control and can readily replace the conventional FOC. To gain in-depth understanding, the conventional DBPCCs with and without rotor compensation are analysed both analytically and quantitatively. Consequently, the application ranges of conventional DBPCCs in terms of SFRs are identified. Extensive simulation and experiment results has demonstrated the problem of conventional DBPCCs and validated the effectiveness of the proposed method.

In practical applications, the control performance of DBPCC is still mainly determined by the model accuracy. Thus, it is of great importance to analyse and predict the influence of model inaccuracy. In this chapter, the influence of parameters mismatch and the inverter nonlinearity on the proposed SF-DBPCC are also analytically analysed in both steady states and transients with due account of the sampling frequency and machine speed. The derived analytical equations can serve as a very powerful tool to accurately predict the current control errors of proposed DBPCC under parameters mismatch and inverter nonlinearity in various speeds. Accordingly, a number of key understandings of the parametric mismatch and inverter nonlinearity influence on the control performance of proposed DBPCC have been established for both low speeds and high speeds. Importantly, it shows that with parametric mismatch, the current control error in steady states would increase greatly. The analytical error analysis lays the foundation for the performance improvement of proposed DBPCC under parameter mismatch and inverter nonlinearity.

2.2 Robust Stationary Frame-Based Deadbeat Predictive Current Control

In this section, a novel stationary frame based DBPCC, which is robust to the large rotor movement in high speeds is presented. Firstly, the rotor movement influence on the conventional DBPCCs with and without rotor movement compensation is analysed, after which the principle and implementation of the proposed DBPCC is presented. In section 2.2.4, extensive simulations are conducted and validate the effectiveness of the proposed DBPCC. Besides, a quantitative method based on two time-step current predictor are also proposed for evaluating the rotor movement influence on different DBPCC schemes over the whole speed range, where the critical SFRs are identified for different DBPCCs. In section 2.2.5, the experiment results are presented and analysed to verify the proposed method. Finally, in section 2.2.6, the current control bandwidth and harmonic current control with the stationary frame-based DBPCC are discussed.

2.2.1 Analysis of Synchronous Frame-Based Conventional DBPCCs in High Speeds

The conventional DBPCCs incorporate two procedures, namely predicting the next step currents and calculating the reference voltage vector in the subsequent step to achieve the reference currents. Since they all employ the machine model based on the rotational frame i.e. the dq frame, all the reference stator voltages should be converted into their stationary frame equivalence before being sent to the SVM. According to the principle of SVM, it can implement the calculated reference voltage in the stationary frame correctly, namely, the actual average stator voltage in the stationary frame is identical to the reference voltage. However, as the speed increase due to the large rotor movement in a time-step, the actual average stator voltage in the dq frame would not equal to the reference dq voltage, which fundamentally compromises the deadbeat control in conventional synchronous frame based DBPCC schemes.

In this subsection, firstly the general analytical expression of average stator voltage error in the dq frame are derived, after which conventional DBPCCs with and without the rotor movement compensation are briefly introduced. Finally, the average stator voltage error of the conventional DBPCCs with and without rotor movement compensation are quantified and the influence of large rotor movement in high speeds on the conventional DBPCCs are discussed.

2.2.1.1 Average stator voltage error in the dq frame

Ignoring the resistive voltage drop, the reference average voltage in the stationary frame can be realized correctly by an ideal inverter with SVM and the corresponding stator flux increment in the αβ frame, namely, the voltage-second input, $\boldsymbol{VS}_{\alpha\beta}(k)$, to a motor during the *k*th step in the stationary frame is given by

$$\boldsymbol{VS}_{\alpha\beta}(k) = \int_0^{T_s} \boldsymbol{u}_{\alpha\beta}(t_k + t)dt = T_s\boldsymbol{u}_{\alpha\beta}(k)^* \tag{2.1}$$

where $\boldsymbol{u}_{\alpha\beta}(t_k + t)$ denotes the instantaneous actual stator voltage at the time instant of $t_k + t$ and t_k is the time instant at the beginning of the *k*th step; T_s is the discrete control time-step, which equals to the sampling and PWM updating time-steps; $\boldsymbol{u}_{\alpha\beta}(k)^*$ is the reference stator voltages at step k in the αβ frame.

Corresponding to (2.1), the volt-second input to the motor expressed in the dq frame can be derived as

$$\boldsymbol{VS}_{dq}(k) = \int_0^{T_s} \boldsymbol{u}_{\alpha\beta}(t_k + t) \cdot e^{-j\omega_e t}dt \cdot e^{-j\theta_e(k)} \tag{2.2}$$

where ω_e is the electrical angular speed of rotor rotation, and $\theta_e(k)$ is the electrical rotor angular position at t_k. Therefore, the actual average voltage in the dq frame is given by

$$\boldsymbol{u}_{dq\_av}(k) = \frac{1}{T_s} \int_0^{T_s} \boldsymbol{u}_{\alpha\beta}(t_k + t) \cdot e^{-j\omega_e t}dt \cdot e^{-j\theta_e(k)} \tag{2.3}$$

Further, assuming the reference dq stator voltage in the *k*th step, $\boldsymbol{u}_{dq}(k)^*$, the average stator voltage error in the dq frame in step k can be obtained as

$$\boldsymbol{err}_{udq}(k) = \frac{1}{T_s} \int_0^{T_s} \boldsymbol{u}_{\alpha\beta}(t_k + t) \cdot e^{-j\omega_e t}dt \cdot e^{-j\theta_e(k)} - \boldsymbol{u}_{dq}(k)^* \tag{2.4}$$

2.2.1.2 Conventional DBPCCs with and without rotor movement compensation

In conventional DBPCCs, in order to compensate the one-step processing delay, the reference dq axis voltages in step *k*+1 are calculated based on the one-step predicted current at step *k*+1. Therefore, by assuming that the motor speed does not change during

the two subsequent steps, the conversion between the reference stator voltage in the stationary frame and the synchronous frame for step $k+1$, which is computed at step k, is given as

$$\boldsymbol{u}_{\alpha\beta}(k+1)^* = \boldsymbol{u}_{dq}(k+1)^* \cdot e^{j(\theta_e(k)+\omega_e T_s)} \tag{2.5}$$

where, $\boldsymbol{u}_{dq}(k+1)^*$, $\boldsymbol{u}_{\alpha\beta}(k+1)^*$ are the reference stator voltages in step $k+1$ in the dq and $\alpha\beta$ frames, respectively.

It is worth noting that the reference voltage conversion (2.5) only considers the one-step processing delay and the rotor movement during the PWM implementation process is ignored. Hence, the conventional DBPCC using (2.5) is referred to as conventional DBPCC without rotor movement compensation in this chapter. The scheme is effective for low speed application. However as the speed increases the large rotor movement in PWM implementation period should be compensated.
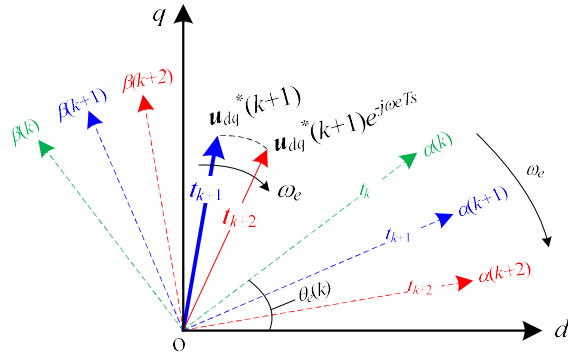
Fig. 2-1 Illustration of the reference stator voltage vector rotation seen in the dq frame in step $k+1$

In conventional FOC, the rotor movement during PWM implementation is also referred to as PWM delay, as it results in an equivalent delay of the stator voltage by half of the PWM updating period. To facilitate analysis, almost all the reported modelling and compensation methods of the rotor movement are based on the approximation that the instantaneous stator voltage equals to the reference stator voltage in the stationary frame [31] or equivalently with a zero-order inverter model in the synchronous frame [34]. Based on this assumption, it implies that the reference voltage in the stationary frame is rotating at the same rotor speed but in the opposite direction viewed from the rotor, as illustrated in Fig. 2-1. Thus, the average voltage in the dq frame can be calculated form the integration of the rotating voltage vector in the dq frame, i.e.

$$\boldsymbol{u}_{dq\_av}(k+1) = \frac{1}{T_s} \int_0^{T_s} \left[\boldsymbol{u}_{\alpha\beta}(k+1)^* \cdot e^{-j(\theta_e(k)+\omega_e T_s)} \right] \cdot e^{-j\omega_e t} dt \tag{2.6}$$

Substituting (2.5) in to (2.6), the relationship between the actual average dq axis voltage and the reference one can be obtained as

$$\boldsymbol{u}_{dq\_av}(k+1) = K(\omega_e T_s) \boldsymbol{u}_{dq}(k+1)^* \tag{2.7}$$

where the coefficient, K is

$$K(\omega_e T_s) = \frac{2\sin(\omega_e T_s/2)}{\omega_e T_s} \cdot e^{-j\omega_e T_s/2} \tag{2.8}$$

As can be seen in (2.7) and (2.8), when the speed is high, K is not identical to 1 which means that the actual average dq axis voltage is not equal to the reference that is produced to achieve deadbeat control. Therefore, the reference voltage conversion in (2.5) should be modified to

$$\boldsymbol{u}_{\alpha\beta}(k+1)^* = \frac{1}{K(\omega_e T_s)} \boldsymbol{u}_{dq}(k+1)^* \cdot e^{j(\theta_e(k)+\omega_e T_s)} \tag{2.9}$$

By simply employing (2.9) instead of (2.5), the conventional DBPCC with rotor movement compensation is obtained. The equivalent rotor movement compensation scheme for dq-axis based DBPCC can also be found in [35]. However, the rotor movement compensation scheme for DBPCC described in (2.9) by only modifying the coordinate transformation is simple and can be implemented easier.

2.2.1.3 Average dq axis stator voltage error and problem of conventional DBPCCs in high-speeds

According to (2.6), by employing the conventional DBPCC with rotor movement compensation, i.e. (2.7) and (2.8), the actual average stator voltage in the dq frame is expected to equal the calculated reference voltage, so that the deadbeat current control can be achieved and the control performance would not be affected by the increasing rotor movement in high speeds. However, this is not the case since the precondition of (2.6) is based on the assumption that the instantaneous stator voltage equals to the reference stator voltage in the stationary frame. In high speeds, this approximation could have large error due to the large harmonic voltage in the time-step with reduced SFRs. In order to identify the error caused by rotor movement in high speeds, the general average dq axis voltage

error derived in (2.4) should be employed. By substituting (2.5) and (2.7) associated with step k into (2.4), the average stator voltage errors in the dq frame can be obtained for conventional DBPCCs without and with compensation as in (2.10) and (2.11), respectively.

$$\boldsymbol{err}_{udq1}(k) = \left[\boldsymbol{u}_{\alpha\beta}(k)^* - \frac{1}{T_s}\int_0^{T_s} \boldsymbol{u}_{\alpha\beta}(t_k + t) \cdot e^{-j\omega_e t}dt\right] \cdot e^{-j\theta_e(k)} \tag{2.10}$$

$$\boldsymbol{err}_{udq2}(k) = \frac{1}{T_s}\int_0^{T_s}\left[\boldsymbol{u}_{\alpha\beta}(t_k + t) - \boldsymbol{u}_{\alpha\beta}(k)^*\right] \cdot e^{-j\omega_e t}dt \cdot e^{-j\theta_e(k)} \tag{2.11}$$

As can been seen in (2.10), without rotor movement compensation, zero voltage error can only be achieved when the speed is low, i.e. $e^{-j\omega_e t}$ is approximated as 1. From (2.11), with rotor movement compensation, if the assumption that the instantaneous stator voltage, $\boldsymbol{u}_{\alpha\beta}(t_k + t)$, in the stationary frame equals to the reference, $\boldsymbol{u}_{\alpha\beta}(k)^*$, is true, zero voltage error can be always guaranteed regardless of speed. However, as the rotor movement increases to relatively large value in high speeds, the harmonic voltage would increase greatly and could lead to large difference between the instantaneous stator voltage, $\boldsymbol{u}_{\alpha\beta}(t_k + t)$ and the reference $\boldsymbol{u}_{\alpha\beta}(k)^*$ in (2.11). The integration in (2.11) over the time-step is not zero and can increase as the voltage vector magnitude increases at high speeds. Consequently, although the rotor movement has been compensated in the conventional DBPCC, a large control error will still occur in high speeds due to the large rotor movement and increased harmonic voltage.
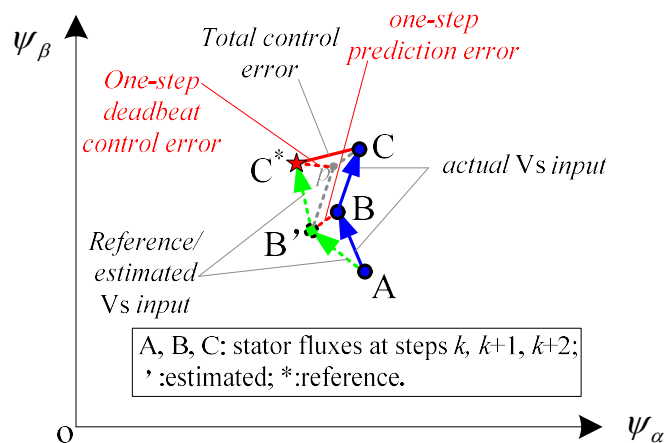
Fig. 2-2 Illustration of the prediction error and control error caused by average voltage error

It is worth noting that apart from causing the realization error of the reference voltage, the average voltage error will also affect the one-step prediction accuracy, since the

voltage used in prediction is different from the actual one. In Fig. 2-2, the stator fluxes in the stationary frame at steps *k*, *k*+1 and *k*+2 are marked as point A, B, C respectively and the superscripts ' and * denote the estimated and reference values, respectively. The blue arrows denote the actual voltage-second inputs to the machine while the green dotted arrow denote the associated reference ones. Line B'B represents the one-step prediction error and line C*C represents the total control error. As seen, the difference between the reference (i.e. estimated) average voltage and the actual one will contribute to both one-step prediction error and one-step deadbeat control error, which finally adds up to form the total control error. Therefore, instead of rotor movement over just one time-step, rotor movements over the two time-steps will influence the control performance of the conventional DBPCC and the control error can be very large in high speeds. To solve this problem, a novel DBPCC robust to the large rotor movement in high speeds is proposed and will be described in next section.

2.2.2 Principle of Proposed Stationary Frame-Based DBPCC

According to the analysis in the previous section, the conventional DBPCC calculates the reference voltage in the rotational frame while its implementation by SVM is based on the stationary frame and would exhibit increasing errors in the average dq axis voltage at high speeds. As a result, the control performance will be much deteriorated due to the large movement in high speeds even though the compensation scheme has been employed. Therefore, in order to reduce the rotor movement influence, a novel stationary frame based DBPCC with flux tracking and accounting the rotor movement explicitly is proposed in this section.

Similar to the conventional DBPCC, the proposed DBPCC consists two steps, i.e. one-step prediction and one-step deadbeat control. However these two steps are both employing the stationary frame based voltage model of the machine, as expressed in

$$\boldsymbol{\psi}_{\alpha\beta} = \int \left(\boldsymbol{u}_{\alpha\beta} - R\boldsymbol{i}_{\alpha\beta}\right)dt \tag{2.12}$$

where $\boldsymbol{\psi}_{\alpha\beta}, \boldsymbol{u}_{\alpha\beta}, \boldsymbol{i}_{\alpha\beta}$ are the stator flux, voltage and current vectors in the stationary frame respectively.

For simplicity, using Euler forward approximation to discretize (2.12) yields

$$\boldsymbol{\psi}_{\alpha\beta}(k+1) = \boldsymbol{\psi}_{\alpha\beta}(k) + T_s\boldsymbol{u}_{\alpha\beta}(k)^* - RT_s\boldsymbol{i}_{\alpha\beta}(k) \tag{2.13}$$

In (2.13), since the stator voltage is usually not easy to be sensed, the associated reference voltages is usually regarded as the actual stator voltages assuming that the inverter drop and nonlinearity can be neglected, which is true in high speeds application. Additionally, employing the reference stator voltages and the Euler forward approximation give accurate estimation of the integration of the actual stator voltages in a time-step regardless of the rotor movement according to the principle of SVM. The error caused by discretization is then only determined by the voltage drop related estimation error, i.e. $\int R\boldsymbol{i}_{\alpha\beta}dt - RT_s\boldsymbol{i}_{\alpha\beta}(k)$, which is negligible in high speeds. The estimation can be improved effectively using the trapezoidal approximation when the resistive voltage drop accounts.

Considering the current model of SPMSM,

$$\boldsymbol{\psi}_{dq} = L_s\boldsymbol{i}_{dq} + \psi_m \tag{2.14}$$

the stator flux at step k in the rotational and stationary frame can be obtained respectively as

$$\boldsymbol{\psi}_{dq}(k) = L_s\boldsymbol{i}_{dq}(k) + \psi_m \tag{2.15}$$

$$\boldsymbol{\psi}_{\alpha\beta}(k) = \left[L_s\boldsymbol{i}_{dq}(k) + \psi_m\right] \cdot e^{j\theta_e(k)} \tag{2.16}$$

Substituting (2.16) into (2.13) gives the predicted stator flux at step k+1,

$$\boldsymbol{\psi}_{\alpha\beta}(k+1) = \left[L_s\boldsymbol{i}_{dq}(k) + \psi_m\right] \cdot e^{j\theta_e(k)} + T_s\boldsymbol{u}_{\alpha\beta}(k)^* - RT_s\boldsymbol{i}_{\alpha\beta}(k) \tag{2.17}$$

The motor speed can be thought as constant due to the relative large mechanical time constant compared to the control time-step, thus the rotor position at step k+1 can be readily calculated as $\theta_e(k) + \omega_e T_s$. Again considering the inverse current model of SPMSM,

$$\boldsymbol{i}_{dq} = \frac{\boldsymbol{\psi}_{dq} - \psi_m}{L_s} \tag{2.18}$$

the *dq* currents at step k+1 can be obtained from (2.17) as

$$i_{dq}(k+1) = \frac{\psi_{\alpha\beta}(k+1) \cdot e^{-j[\theta_e(k)+\omega_e T_s]} - \psi_m}{L_s} \tag{2.19}$$

With (2.17) and (2.19), the one-step prediction of stator flux and current based on the stationary frame can be achieved. Fig. 2-3 shows the block diagram of the stationary frame based one-step prediction. It can be found that the coordinate system transformation of the reference stator voltages is avoided and the rotor movement is explicitly taken into account based on the assumption of constant rotor speed. Hence, the one-step prediction is independent of the rotor movement during the PWM implementation process.
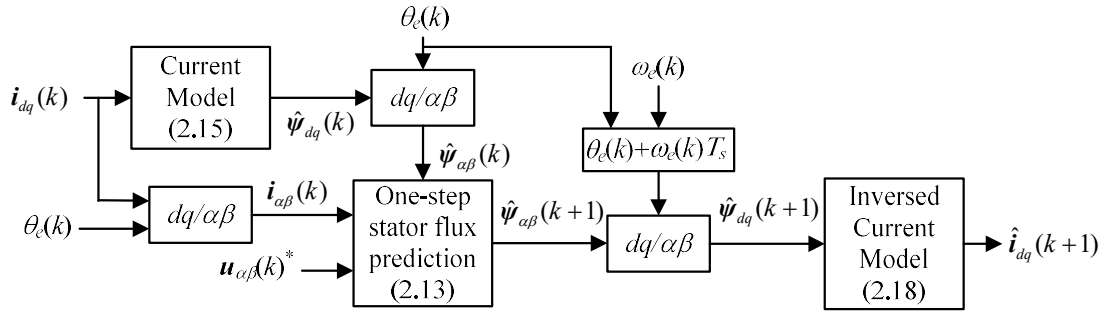
Fig. 2-3 One-step flux and current prediction in proposed SF-DBPCC

Assume the current demands are unchanged over the next two time-steps, i.e. $i_{dq}(k)^* = i_{dq}(k+2)^*$, the reference stator flux in the stationary frame at step $k+2$ is given by

$$\psi_{\alpha\beta}(k+2)^* = \left[L_s i_{dq}(k)^* + \psi_m\right] \cdot e^{j[\theta_e(k)+2\omega_e T_s]} \tag{2.20}$$

Referring back to the stationary frame based voltage model, (2.12) and its discretization, (2.13), the reference stator voltage in the stationary frame can be computed as

$$u_{\alpha\beta}(k+1)^* = \frac{\psi_{\alpha\beta}(k+2)^* - \psi_{\alpha\beta}(k+1)}{T_s} + R i_{dq}(k+1) \cdot e^{j[\theta_e(k)+\omega_e T_s]} \tag{2.21}$$

where $\psi_{\alpha\beta}(k+2)^*$, $i_{dq}(k+1)$ and $\psi_{\alpha\beta}(k+1)$ are provided in (2.17), (2.19) and (2.20), respectively.

As can be seen from (2.21), the reference stator voltage to achieve deadbeat control is obtained directly based on stationary frame. It requires no coordinate conversion and can be implemented by SVM accurately. Hence, the control performance will not be affected by the rotor movement during the PWM implementation process and the

deadbeat tracking of the reference stator flux and currents at step $k+2$ can still be realized in high speeds.

As one-step prediction and one-step deadbeat control in the proposed DBPCC are both performed based on the stationary frame, the rotor movement during the process can be exactly taken in to account by employing (2.17), (2.19) and (2.20). Therefore, the proposed DBPCC is more robust to the rotor movement and expected to improve control performance in the whole speed range including the very high-speed region with very large rotor movement in a time-step and extreme low SFRs.

2.2.3 Implementation of Proposed Stationary Frame-Based DBPCC

Fig. 2-4 shows the block diagram of the proposed DBPCC, the output is the reference stator voltages in the stationary frame with the reference dq axis currents as the input demands. In the figure, ^ denoting the estimated values are used for the state variables dependent on the motor parameters. To improve the linear inductance current model expressed in (2.14), nonlinear current model such as high fidelity PMSM model based on calibrated FE analysis results can be employed [130]. However, for high-speed SPMSM, the machine is almost linear across the operation range due to the relatively large effective air gap. Hence, for simplicity, the linear current model with the measured inductances and PM flux linkage is often sufficient.

To maximize the voltage utilization, hexagon boundary of voltage is used rather than the inscribed circle limit. For simplicity and good performance, the minimum phase error scheme is employed i.e. when the reference voltage vector is outside the boundary, its phase angle is kept unchanged while the length is shortened so that the terminal of the reference voltage vector would locate on the hexagon boundary.

Fig. 2-5 illustrates the high-speed SPMSM drive system with speed control as outer loop and the proposed DBPCC as the inner current control loop. The q-axis current reference is derived from the speed PI regulator and the small current control error in q-axis in steady states can be adjusted via speed control loop. The d-axis reference is set as 0 for the SPMSM however for general application if flux weakening is required, the employed flux weakening scheme can be easily integrated in by changing the d-axis reference accordingly.
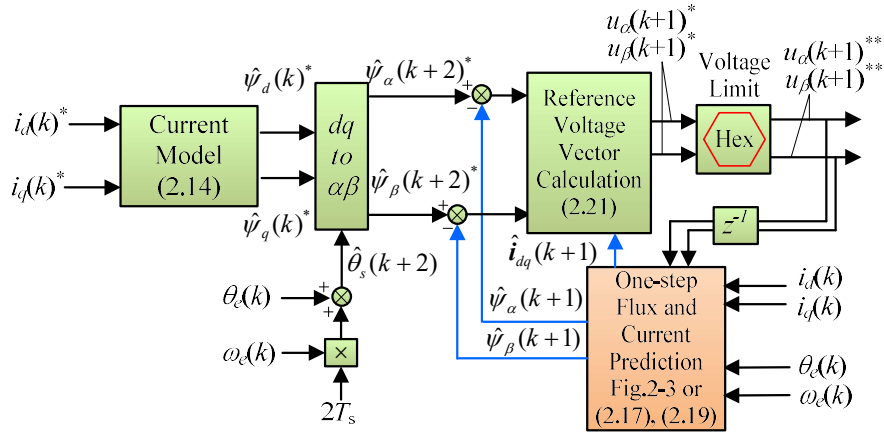
Fig. 2-4 Block diagram of the proposed stationary frame-based DBPCC
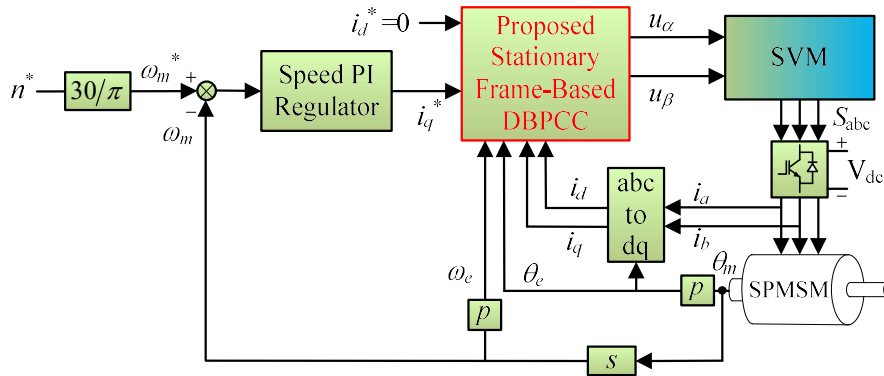
Fig. 2-5 Block diagram of speed regulated SPMSM drive system with the proposed stationary frame-based DBPCC

2.2.4 Simulation Results and Discussions

2.2.4.1 Effectiveness of proposed DBPCC

Extensive simulation has been performed to validate the effectiveness of the proposed DBPCC in various speeds. The parameters of the high-speed motor drives used in the simulation are given in Table 2-1, which are obtained by Finite Element (FE) simulation and calibrated by the measurement of the experiment prototype high-speed PMSM. The parameters are identical to the measured ones presented later in Table 2-3, with the average of the dq-axis inductances employed as the synchronous inductance. In the simulation, the sampling frequency is set to 10 kHz and it is the same as the switching frequency. The resultant SFRs and rotor movement in a time-step at various speeds are presented in Table 2-2. In the simulation, accurate machine parameters and ideal inverter are used. The DC voltage is set as 270V and the moment of inertia of the drive, J is set to 1.5e-5 kg $\cdot$ m^2. The simulation time-step is set as low as 0.1 μs. As shown in Fig. 2-6, the

discretization and timing of the digital control are correctly represented in the MATLAB/Simulink model by zero-holder, delay and discrete integrator blocks. This simulation model configuration is used throughout in this thesis unless specifically stated.

Table 2-1 Parameters of the high-speed PMSM used in simulation

Number of poles pairs	2
Phase resistance	20 mΩ
Synchronous inductance, L_s	129.6 μH
Permanent magnet flux linkage	9.83 mWb
Rated current (1 p.u.)	50 A
Rated torque (1 p.u.)	1.5 Nm

Table 2-2 SFR and rotor movement in a time-step versus motor speed for the 4-pole high-speed SPMSM with sampling frequency of 10 kHz

Speed (rpm)	5 k	10 k	20 k	30 k	40 k	50 k
SFR	60	30	15	10	7.5	6
θ_{sp}	6°	12°	24°	36°	48°	60°
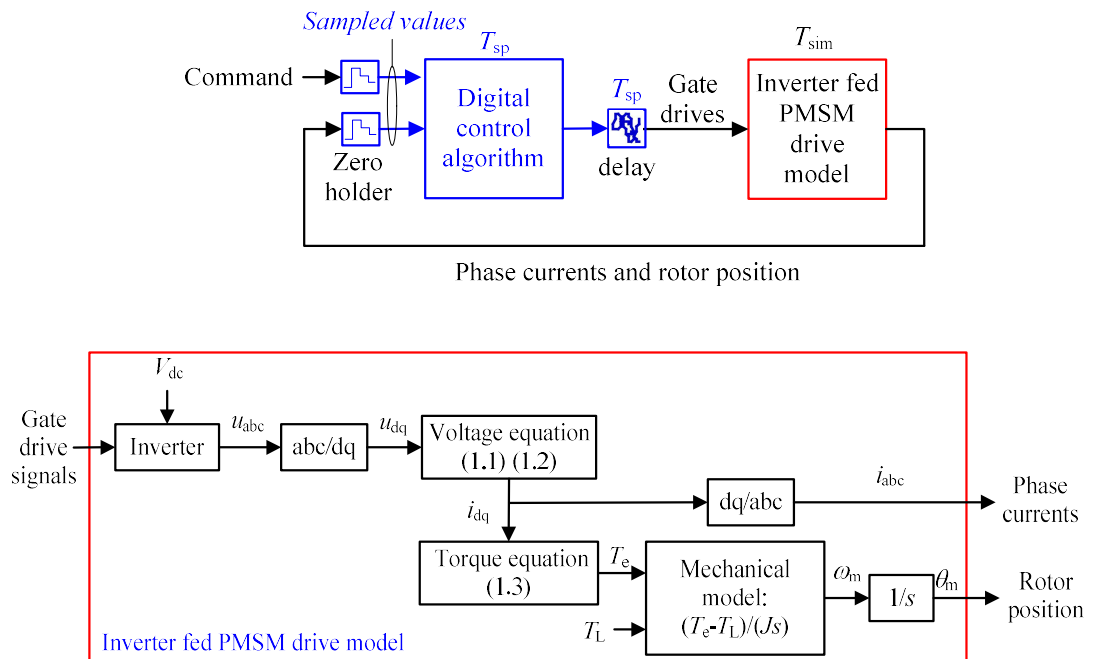
Fig. 2-6 Illustration diagram of MATLAB/Simulink simulation program configuration of digitally controlled inverter fed PMSM drive systems

Acceleration simulations of the high-speed motor from standstill to 50 krpm with constant load torque have been performed to highlight the problems of the conventional DBPCCs with or without rotor movement compensation in high speeds and the

41

effectiveness of the proposed DBPCC. The load torque is set as 0.1 p.u. and the speed control bandwidth is 50 Hz.
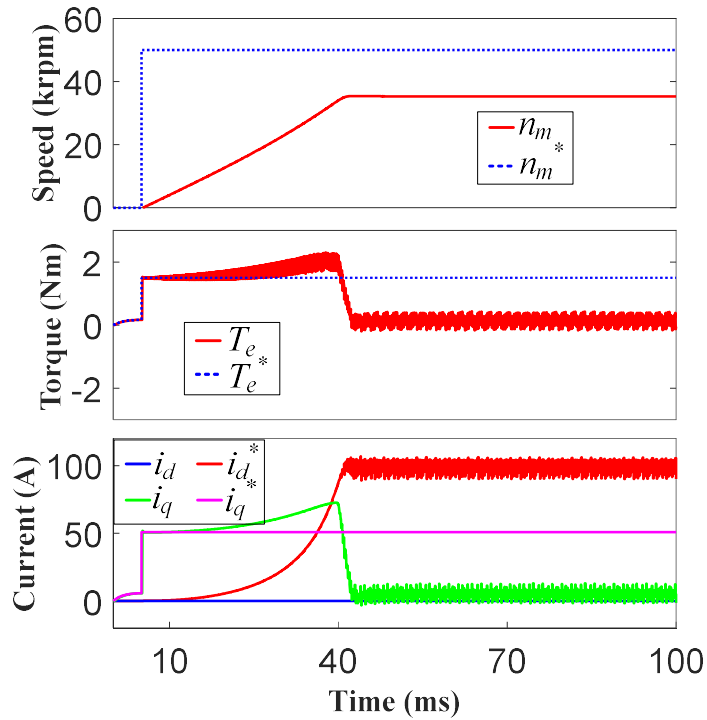
(a)
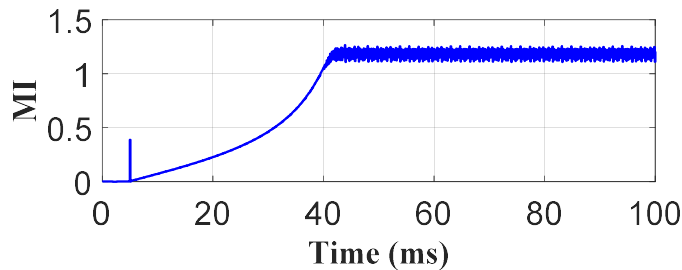
(b)

Fig. 2-7 Simulation Waveforms of the high-speed PMSM accelerating form standstill to 50 krpm under 0.1 p.u. load torque with the conventional DBPCC without rotor movement compensation (a) speed, torque, sampled dq axis current (b) modulation index of reference voltage before hexagon limiter

Fig. 2-7 (a) shows the result of the conventional DBPCC without rotor movement compensation. Since the current switching harmonics are not of interest, only the sampled currents are shown while the switching caused torque ripples can still be observed in the instantaneous torque waveform. As can be seen in Fig. 2-7 (a), the *dq* currents begin to gradually deviate from the reference currents at *t*=10 ms when the motor speed is ~5,000 rpm, the corresponding SFR is 60 and rotor movement in a time-step, $\theta_{sp} = 6°$. At the speed of 10,000 rpm, the current control errors have become noticeable. And as the speed

increases further beyond 20,000 rpm, the *d*-axis current error rises rapidly while the *q*-axis current deviation from the reference is relative small but increases almost linearly with the speed. When at *t*=40 ms, the speed reaches 30,000 rpm, the motor rapidly lose control due to the voltage saturation caused by the large positive *d*-axis current error, as evident in Fig. 2-7 (b). Consequently, the target motor speed, i.e. 50,000 rpm, cannot be realised since the currents are out of control due to voltage saturation.
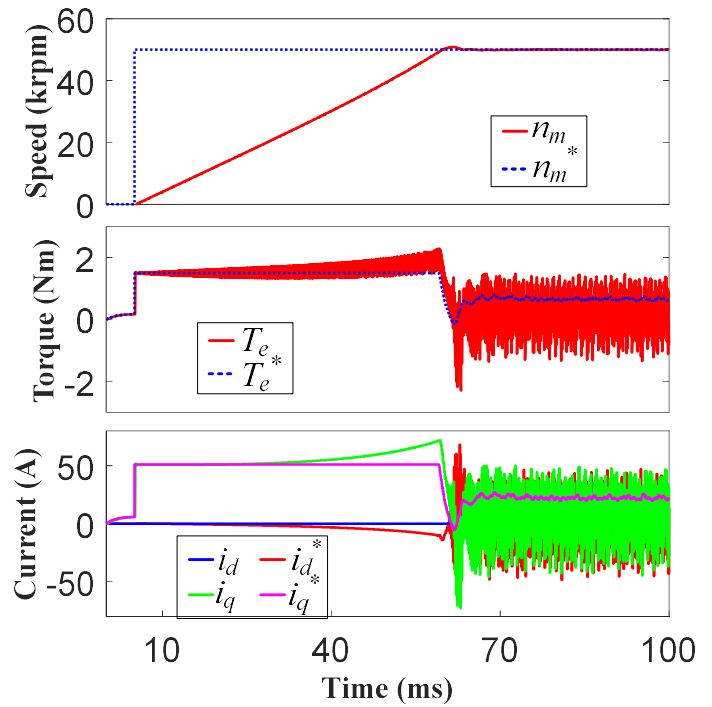
(a)
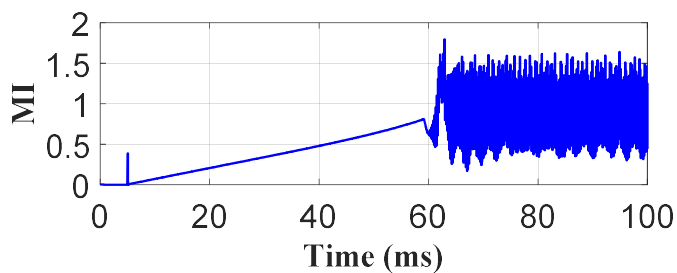
(b)

Fig. 2-8 Simulation Waveforms of the high-speed PMSM accelerating form standstill to 50 krpm under 0.1 p.u. load torque with the conventional DBPCC with rotor movement compensation (a) speed, torque, sampled dq axis current (b) modulation index of reference voltage before hexagon limiter

As can be observed in Fig. 2-8 (a), the rotor movement compensation improves the performance of the conventional DBPCC. Below 20 kprm (SFR=20, $\theta_{sp} = 24°$), the ideal deadbeat current control is achieved while as the speed increases to 30 krpm, the current

errors are obvious and kept increasing with the rising speeds. With the compensation scheme, the reference speed i.e. 50 krpm can be reached. However, when the speed is higher than 48.5 krpm, the *dq* currents and torque exhibit excessive ripples and oscillations because of the voltage saturation excited by the increasing current control error. It is worthy mention that the corresponding SFR where the current errors found to be evident at 30 krpm is 10. It coincides with the fact that in FOC with synchronous PI current control, large oscillations and instability of the current control is reported even with the delay compensation scheme when the SFR is less than 10 [32]. Based on the analysis in section 2.2.1, this can be attributed to the fact that the compensation is based on the assumption that the instantaneous real stator voltages equal to the references. However, this assumption is not valid in high speeds and the reference *dq* axis voltages cannot be realized correctly by SVM.

In contrast, Fig. 2-9 shows the simulation results with the proposed DBPCC as the high-speed machine accelerates form zero speed to 50 krpm. It can be seen in the sampled current waveform that the actual *dq* axis currents can be always in good control and exactly follow the reference currents at any speed. The performance improvement can be clearly recognised when comparing the results in Fig. 2-9 with those presented in Fig. 2-7 and Fig. 2-8, which are obtained in the same condition with the conventional DBPCCs. It is worth noting that the increasing ripples in the torque waveform is because the SFR reduces as the speed rises. However, the speed waveform is hardly affected as the torque ripples are filtered out by the large machine inertial at high speeds.
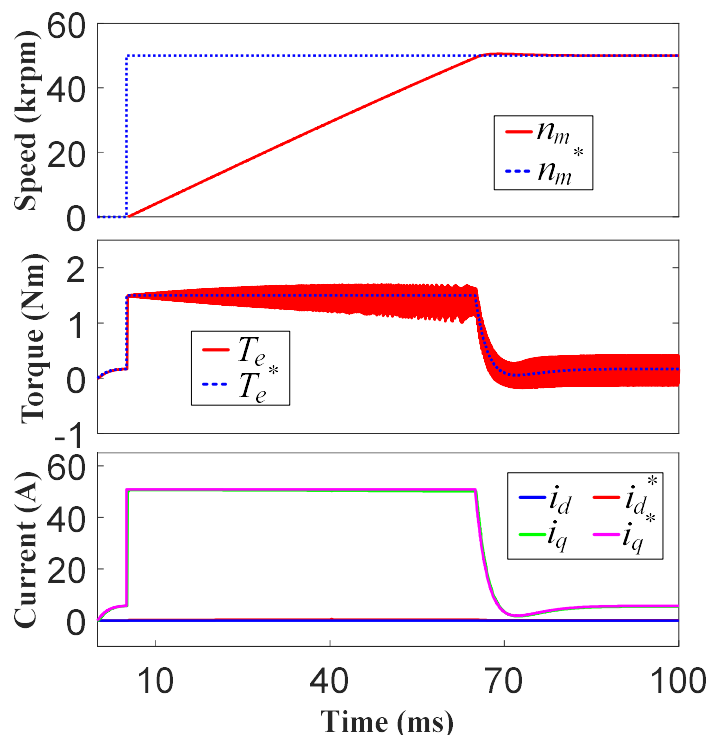
(a)
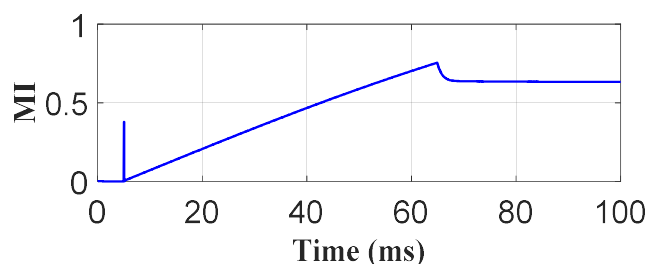
(b)

Fig. 2-9 Simulation Waveforms of the high-speed PMSM accelerating form standstill to 50 krpm under 0.1 p.u. load torque with the proposed DBPCC (a) speed, torque, sampled dq axis current (b) modulation index of reference voltage before hexagon limiter

Fig. 2-10 shows the sampled *dq* axis currents in transients which result with the proposed DBPCC as the *q*-axis current demand stepping from 0 to 25A at 30 krpm, where the SFR equals 10. The desired deadbeat current control is achieved as current demands are tracked without error and with a delay of only two time-step, i.e. 0.2 ms for the sampling frequency of 10 kHz. In Fig. 2-11, the results in the same operation condition employing the conventional DBPCC with rotor movement compensation is presented. As can be seen in Fig. 2-11, large cross coupling between *dq axis* exists during transients with the conventional DBPCC as large *d*-axis current is observed in the transient, even though the rotor movement compensation measure has been taken. Overshoot in *q*-axis also occurs in transient and the current tracking delay approximates to 1.4 ms, much

45

longer than the two time-steps, i.e. 0.2 ms. Moreover, in steady state, nonzero current control errors in both the *d*-axis and *q*-axis are seen. By the comparison of Fig. 2-10 and Fig. 2-11, it confirms that the rotor movement in the conventional DBPCC based on rotational frame is still insufficient for high speeds with low SFRs and the proposed DBPCC is much superior in both transient and steady state performance. For the purpose of comparison, the sampled current waveform in the same conditions using the conventional FOC with delay compensation and feedforward decoupling is also presented in Fig. 2-12. Similar to those shown Fig. 2-11, although the accurate machine parameters are employed, large overshot currents and cross-coupling currents are observed and the setting time is much longer. Therefore, the advantages of employing the proposed DBPCC in high speeds with low SFRs has been confirmed.
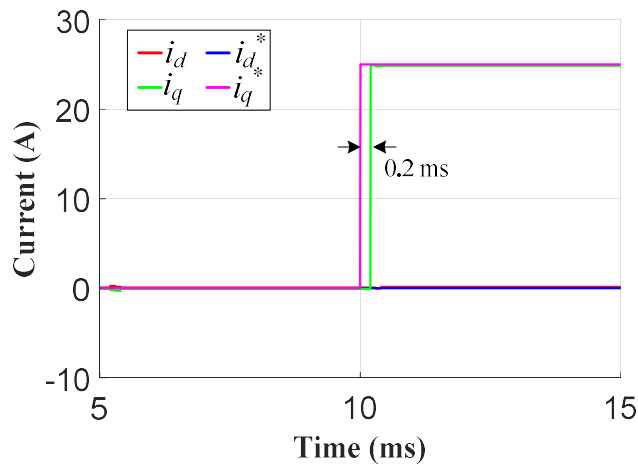
Fig. 2-10 Current control transient waveforms using the proposed DBPCC at 30 krpm (SFR=10)
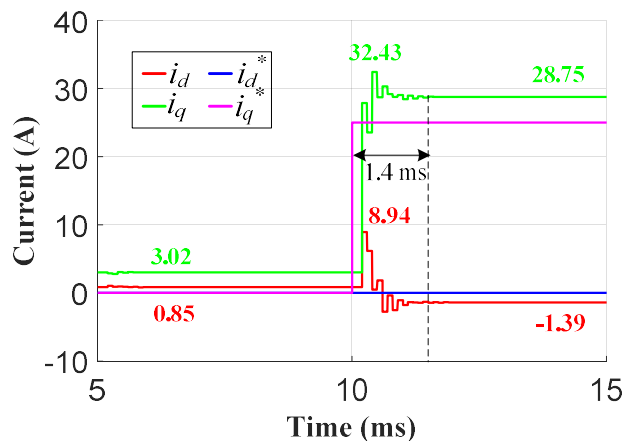
Fig. 2-11 Current control transient waveforms using the conventional DBPCC with rotor movement compensation at 30 krpm (SFR=10)

46
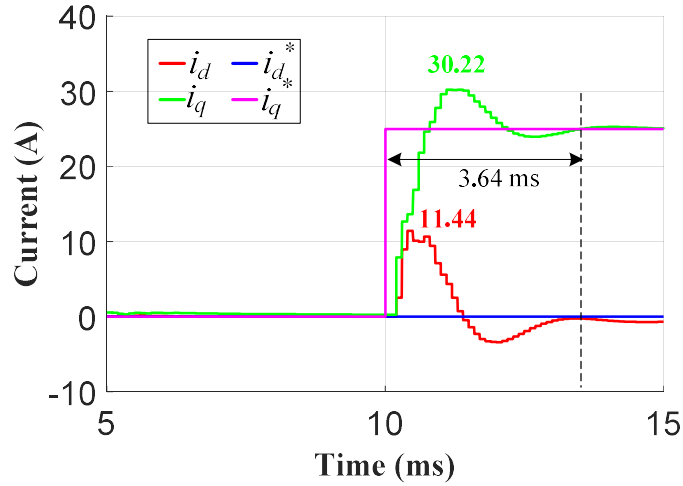
Fig. 2-12 Current control transient waveforms using the conventional FOC with rotor movement compensation at 30 krpm (SFR=10, current control bandwidth of 500 Hz)

2.2.4.2 Quantitative evaluation method of rotor movement influence and critical SFRs

As analysed in section 2.2.1 and demonstrated in the previous subsection, the control error caused by the rotor movement during the PWM implementation process increases greatly in high speeds and as a result, the drive could completely lose control due to the voltage saturation or even trigger overcurrent protection in practice. On the other hand, it is difficult to identify the control error with the conventional DBPCCs in high speeds. In order to evaluate and compare the control errors caused by rotor movement quantitatively for different DBPCC schemes in high-speed region, and generally identify the speed region where the conventional DBPCCs can be applied with large control error, a quantitative evaluation scheme of rotor movement influence for different DBPCC schemes is proposed in this section.
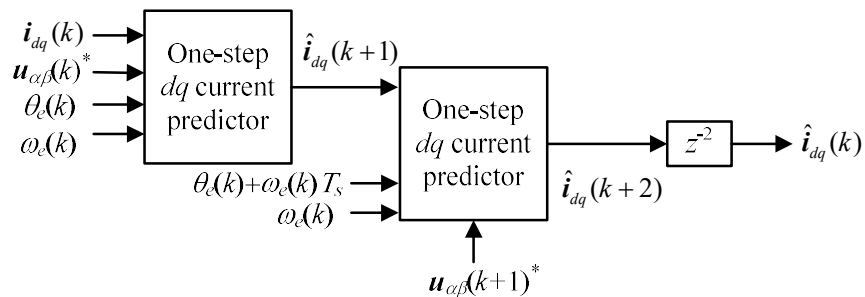
Fig. 2-13 Block diagram of the constructed two-step predictor for rotor movement influence quantitative evaluation in different DBPCC schemes

47
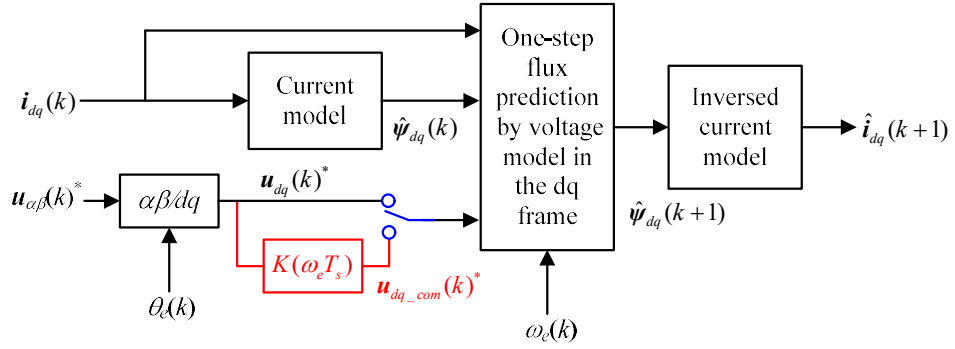
Fig. 2-14 Block diagram of the constituent one-step current predictor in the two-step predictor for conventional DBPCCs with/without rotor movement compensation

The proposed quantitative evaluation method is based on the two-step current predictor associated with different DBPCCs. Fig. 2-13 illustrates the block diagram of the proposed two-step current predictor. It consists of two identical one-step *dq axis* current predictor and cascaded one after the other to predict the *dq* axis currents at the two subsequent steps, to derive the predicted current at the present step. The input stator voltage for the first one-step current predictor, $\boldsymbol{u}_{\alpha\beta}(k)^*$, is calculated at the previous time-step and that for second one-step current prediction, $\boldsymbol{u}_{\alpha\beta}(k+1)^*$, is calculated at the present time-step. The one-step current predictor for the conventional DBPCC is shown in Fig. 2-14. If the rotor movement compensation is employed, $\boldsymbol{u}_{dq\_com}(k)^*$, is used where the coefficient K in the block is calculated according to (2.8). The one-step current prediction for the proposed DBPCC is obtained according to (2.19) or Fig. 2-3.

Because the reference stator voltage is calculated based on the requirement that the predicted currents in the following step would reach the demands, the predicted *dq* axis currents in steady states will be equal to the reference. Hence, instead of using the reference, the predicted current can be employed to compare with the actual sampled currents to define the current control error. Moreover, all the conventional DBPCCs and the proposed DBPCC consists of two steps prediction, one step is to predict the machine states such as the stator flux and current, the other step is to predict the reference stator voltage. Although the two steps prediction are not identical, they are both based on the same machine model and the model errors caused by the rotor movement in the two steps will finally contribute to the control error together. Therefore, the errors between the predicted and the sampled currents can effectively reflect the corresponding error of the DBPCC due to rotor movement in two steps. Furthermore, provided that the exact machine parameters are available and inverter nonlinearity influence is negligible, in other words, no other source of model errors exists, the two-step current prediction error

of the constructed current predictor can serve the purpose to precisely quantify the model error caused by rotor movement during the control.

Since the proposed DBPCC, which can give stable and good current control over the whole speed range, the constructed two-step current predictors of different DBPCCs are implemented simultaneously meanwhile the machine is controlled by the proposed DBPCC. The current prediction errors of the two-step predictors are obtained and utilized to evaluate the resultant model errors in a given DBPCC due to rotor movement in all speeds.
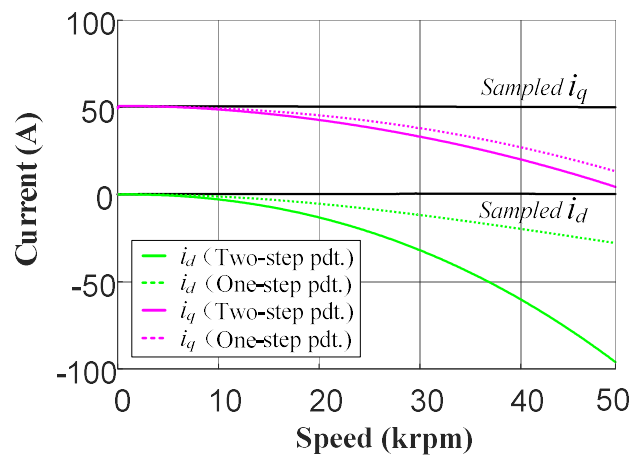
(a)
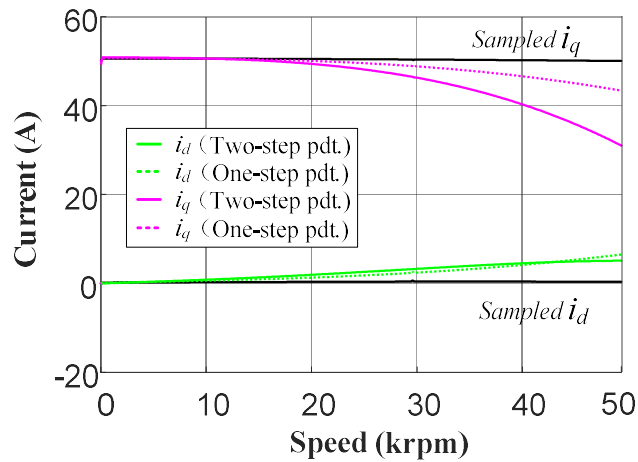
(b)
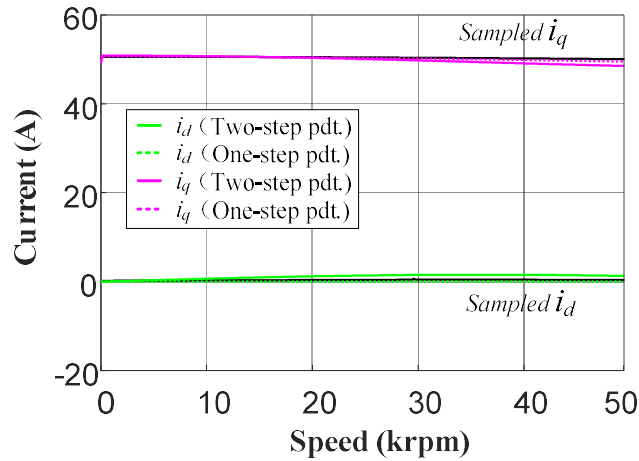
(c)

Fig. 2-15 One-step and two-step current prediction simulation results as the high-speed motor accelerates using the constructed two-step current predictor of (a) conventional DBPCC without rotor movement compensation (b) conventional DBPCC with rotor movement compensation (c) the proposed DBPCC

Fig. 2-15 shows the simulation results of two-step predicted currents of the constructed two-step predictor for three different DBPCCs as the machine is accelerated under the proposed DBPCC from 0 to 50 krpm. The intermedia one-step prediction results are also present, which exhibits less prediction error than the two cumulative predictions due to half rotor movement. It can be found that for the conventional DBPCCs, the increase trend of the two-step prediction error matches well with the current control error rising in Fig. 2-7 and Fig. 2-8, respectively, where the associated DBPCCs actually control the motor.

Table 2-3 summarizes the relative prediction errors of the two-step predictor at various speeds in Fig. 2-15. The nominal current uses the reference q-axis current, which is 50 A in this case. The relative prediction error is defined by the sampled current subtracting the predicted current and then divided by the nominal current i.e. 50A. Fig. 2-16 plots the variations of the relative prediction errors with speed. For comparison, the relative current control errors in Fig. 2-7, Fig. 2-8 and Fig. 2-9 with different DBPCCs at various speeds are depicted in Fig. 2-17, where the relative current control error is calculated by the actual current subtracting the reference current and then divided by the nominal current. The rotor movements in one time-step and SFRs are plotted in Fig. 2-18 with respect to speed.

Table 2-3 Relative two-step prediction errors associate with different DBPCCs at various speeds (simulation results)

	Speed (rpm)	5 k	10 k	20 k	30 k	40 k	50 k
d-axis current prediction error	DBPCC without compensation	0.2%	5.7%	26.4%	63.7%	120.5%	189.4%
	DBPCC with compensation	-0.8%	-1.7%	-3.9%	-6.5%	-9.1%	-10.2%
	Propsoed DBPCC	-0.6%	-1.3%	-2.4%	-3.0%	-3.1%	-2.6%
q-axis current prediction error	DBPCC without compensation	-0.7%	2.4%	14.6%	33.5%	59.9%	90.6%
	DBPCC with compensation	-1.6%	-1.1%	1.2%	7.3%	19.5%	37.8%
	Propsoed DBPCC	-1.3%	-1.2%	-0.9%	0.5%	1.8%	2.9%
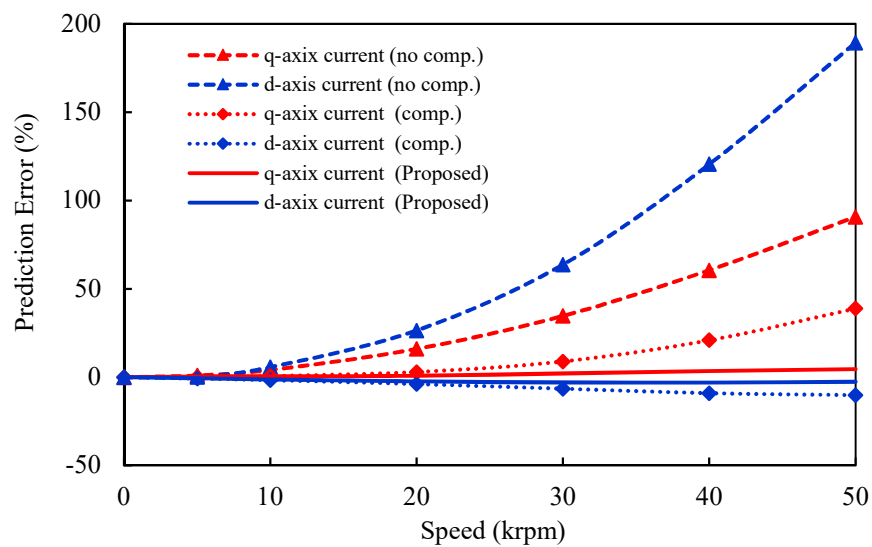
Fig. 2-16 Prediction errors of the two-step predictors associated with different DBPCC schemes, as a function of motor speed
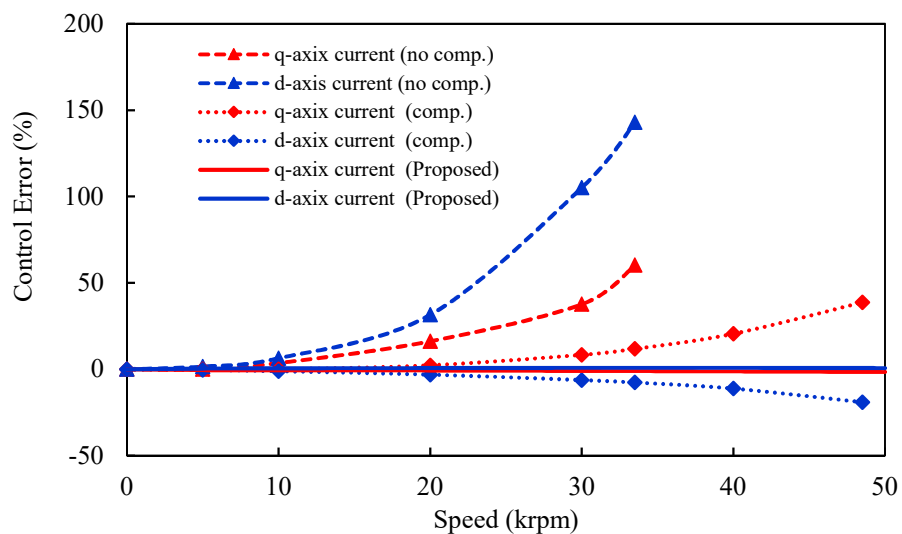
Fig. 2-17 Control errors with different DBPCC schemes, as a function of motor speed (current and voltage unlimited)
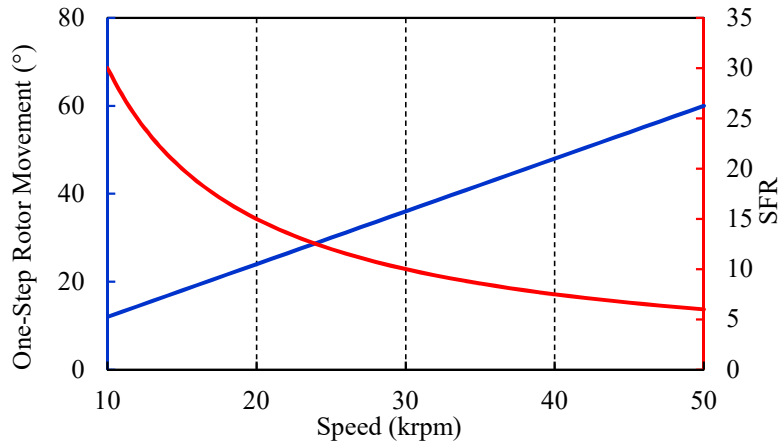
Fig. 2-18　One-step rotor movement and SFR as functions of motor speed

As shown in Fig. 2-16 and Fig. 2-17, without rotor movement compensation, two-step prediction errors and control errors deviate form 0 both around the speed of 10 krpm. With rotor movement compensation, the speed where the prediction and control errors start to increase rises from 10 krpm to 20 kprm. With the proposed DBPCC, the prediction and control errors are both close to zero in the whole speed range. Comparing Fig. 2-16 and Fig. 2-17, it can be seen that both the prediction error and the control error associated DBPCCs increase with speed. However, the two-step prediction errors at high speeds is still possible since the drive is operated by the proposed DBPCC. By decoupling the prediction from control, the influence of rotor movement in the conventional DBPCCs at high speeds can be quantified.
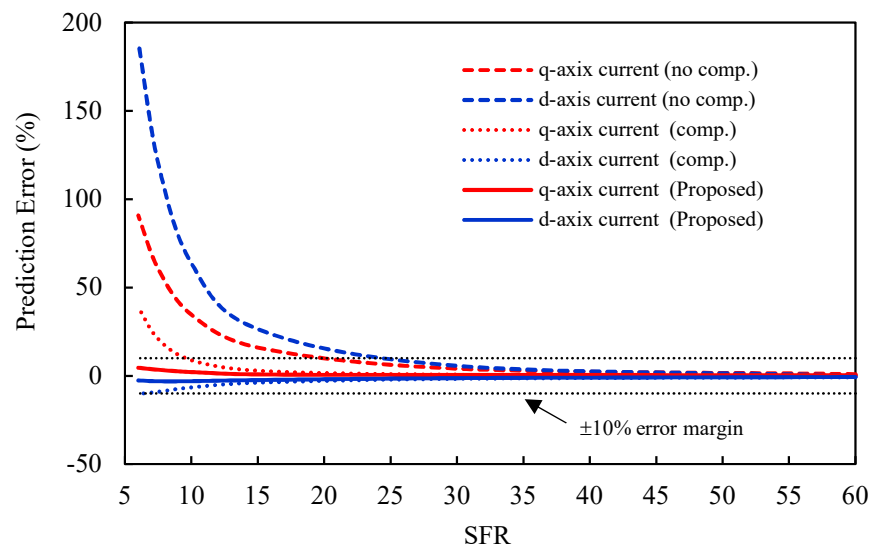
Fig. 2-19　Prediction errors of the constructed two-step predictors associated with different DBPCC schemes, as a function of SFR

Generally, instead of using the absolute speed value, the SFR is employed to identify the high speed and the control difficulty. As can be seen in Fig. 2-18, the rotor movement

52

in a time-step increases linearly with speed while the SFR decreases greatly as the speed increases. Fig. 2-19 shows the two-step prediction errors as a function of SFR. It is evident that as the SFR decreases below a critical value, the prediction errors rise nearly exponentially with the conventional DBPCCs with and without rotor movement compensation. In contrast, the proposed DBPCC has much small prediction errors across the whole SFR range and the increasing error in the low SFR range can be attributed to the estimation error of resistive voltage using simple Euler approximation, which can be effectively improved by trapezoidal approximation.

According to the principle of the deadbeat current control, however, the system would not be unstable as the reference voltage is calculated in an open-loop manner. The model error would only result in current control error in the steady states. However, with the excessive current errors, the voltage and current limits of the system would be reached, causing oscillation and triggering system protection. Therefore, to guarantee the control performance using the conventional DBPCCs, the control errors should be constrained within a small margin. As the two-step prediction error coincides with the control error, the two-step prediction error curves associated with different DBPCCs in Fig. 2-19 can be employed to determine the critical SFRs with predefined error margin.

Table 2-4 shows the critical SFRs for different DBPCCs with various error margins. It can be concluded that to have similar accuracy to the proposed DBPCC, the SFRs with the conventional DBPCC without rotor movement compensation should be higher than 50 and that with rotor movement compensation should be larger than 20. Moreover, it is observed that the critical SFRs of the conventional DBPCC with rotor movement compensation are all close to 10 even with larger error margins. This is due to the exponential increase trend of the associated prediction errors around SFR=10, as shown in Fig. 2-19. For the proposed DBPCC, the prediction error can be always maintained within small error margin of ±5% even when the SFR is reduced to 6. In the results above, the cases with SFR less than 6 is not shown, however in fact, the proposed DBPCC can apply for any SFR higher than 2, which is the extremely unlikely case according to the sampling theorem. It is worth noting that with the proposed DBPCC in very low SFR range, the nonzero prediction error is caused by the simple Euler approximation of resistive voltage drop. The accuracy in the low SFR range can be increased effectively by using trapezoidal approximation. However, use of the Euler approximation over low SFR

range with the proposed DBPCC will not lead to exponential increase of the prediction errors nor oscillation in the system as the errors only relate to the resistive voltage drops.

Table 2-4 Critical SFRs for DBPCCs

	Error Margin	±20%	±15%	±10%	±5%	Error of Propsoed DBPCC±1%
Critical SFR	Conventioanl DBPCC without compensation	18	21	25	32	50
	Conventioanl DBPCC with compensation	8	9	10	12	20
	Proposed DBPCC	<6	<6	<6	<6	<6

2.2.5 Experiment Validation

The proposed method has been tested on the prototype high-speed PMSM drives, whose parameters are shown in Table 2-5. As seen, the actual dq-axis inductances are not identical and slightly different form the synchronous inductance used in the simulation. However, this small difference has little influence on the test results since the "$i_d=0$" control is employed and the d-axis inductance is not influential. As shown in Fig. 2-20 (a), the prototype machine is mounted via an in-line torque transducer onto the dyno motor. For the sake of safety, the whole spin system is enclosed in a spin pit and the concrete lid will be covered during testing. Fig. 2-20 (b) shows the driver for the prototype high-speed machine, which is based on the real-time digital control and simulation platform, OPAL5600. The three-phase IGBT inverter from SEMIKRON (SKiM459GD12E4) is used and placed in the inverter box. The photograph of the overall test rig is shown in Fig. 2-20 (c). Additionally, the high-speed motor driver and high-speed dyno driver have been configured and can be manipulated remotely in OPAL RT-LAB and dSPACE ControlDesk, respectively through internet cables, as shown in Fig. 2-20 (d). Besides, the high-speed spin pit can be monitored in real-time by a camera as well. This experiment test rig is employed throughout this thesis. More information on hardware construction and the power converter used in the experimental prototype can be found in Appendix A. In the testing, the prototype machine is under current control and the speed is regulated by the dyno. The switching frequency and sampling frequency are both 10 kHz. The inverter deadtime is set as 2 μs and the DC-link voltage is 270V.

(a)

(b)

(c)

(d)
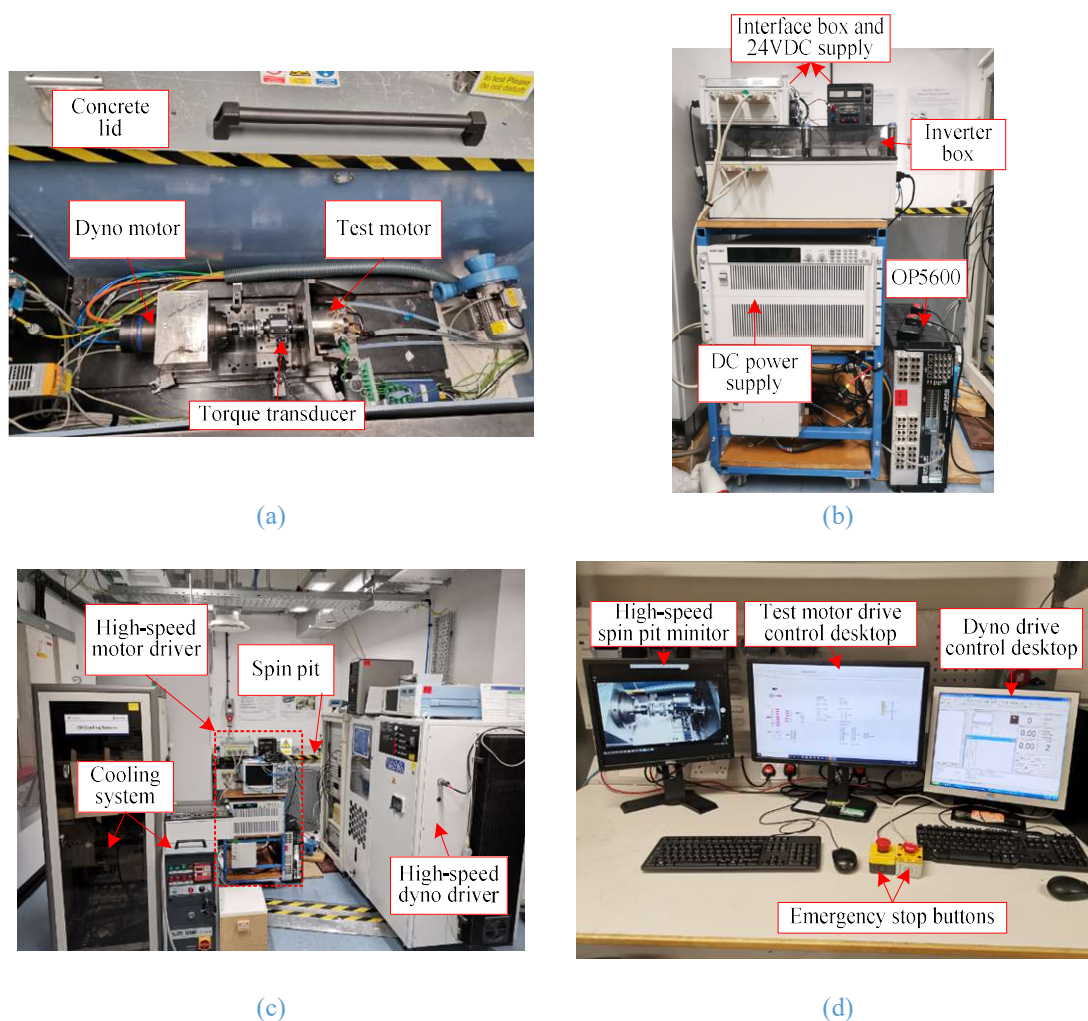
Fig. 2-20 Photos of the test rigs (a) overall view (b) the control centre (c) the high-speed PMSM test bed (d) the motor controller for the prototype high-speed PMSM

Table 2-5 Parameters of the experiment prototype high-speed PMSM

Number of poles pairs	2
Phase resistance	20 mΩ
d-axis inductance	125 μH
q-axis inductance	134.2 μH
Permanent magnet flux linkage	9.83 mWb
Rated current (1 p.u.)	50 A
Rated torque (1 p.u.)	1.5 Nm
Rated speed (1 p.u.)	30,000 rpm

In order to obtain good control performance, accurate machine model should be used. Hence, the measured machine parameters in Table 2-5 are employed in all the DBPCCs. However, the inverter nonlinearity will still cause control error.

(a)   (b)
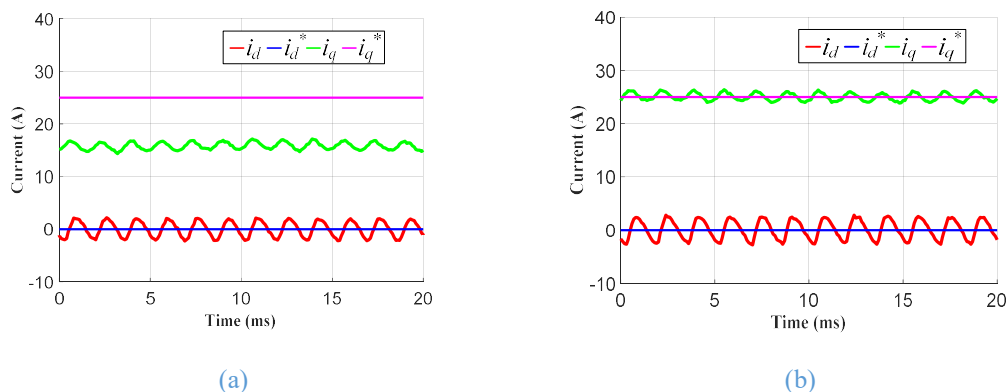
Fig. 2-21 dq axis currents with dead-time of 2 μs and q axis current reference of 25A at 3 krpm. (a) without compensation. (b) with compensation.

(a)   (b)
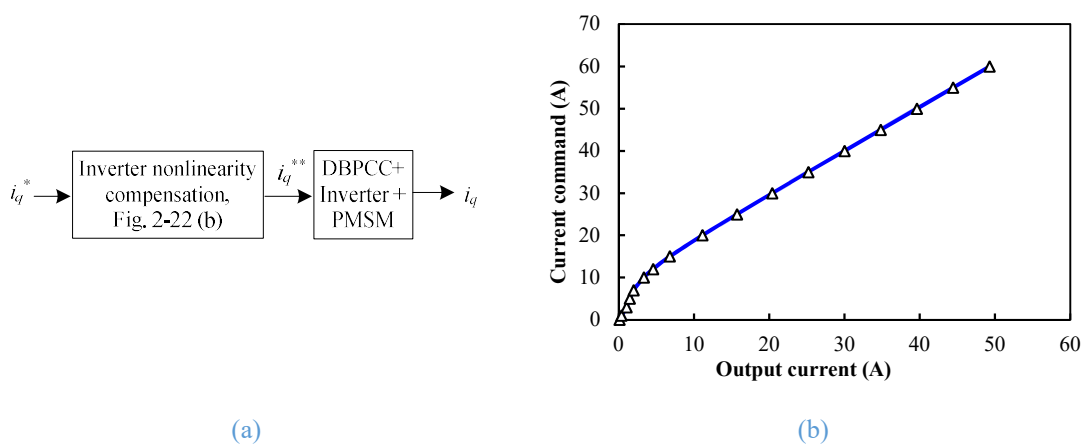
Fig. 2-22 Inverter nonlinearity compensation for DBPCC. (a) control diagram. (b) q axis current demand input to DBPCC as a function of the output q-axis current.

Fig. 2-21 (a) shows the sampled dq axis current in the steady state at 3 krpm with the q axis current reference of 25A with the proposed DBPCC. As can be seen, due to the model error caused by inverter nonlinearity i.e. the inverter voltage drop and deadtime effect, the q axis current have an offset error. The experiments with different q axis current demand have also been performed and Fig. 2-22 (b) plots the relationship between the q axis current demand and the average value of measured output q axis current. To compensate the inverter nonlinearity influence, as shown in Fig. 2-22 (a), the LUT obtained from Fig. 2-22 (b) can be simply added between the input reference and DBPCC controller. As can be seen in Fig. 2-21 (b), after compensation, the current control error caused by inverter nonlinearity can be effectively eliminated. The same tests have been repeated for the conventional DBPCCs, the same amount of q axis current error is observed without compensation while after the compensation is applied, the error can be effectively removed. Thus, this LUT based compensation method for inverter nonlinearity is employed throughout this section.

56

(a)

(b)

(c)
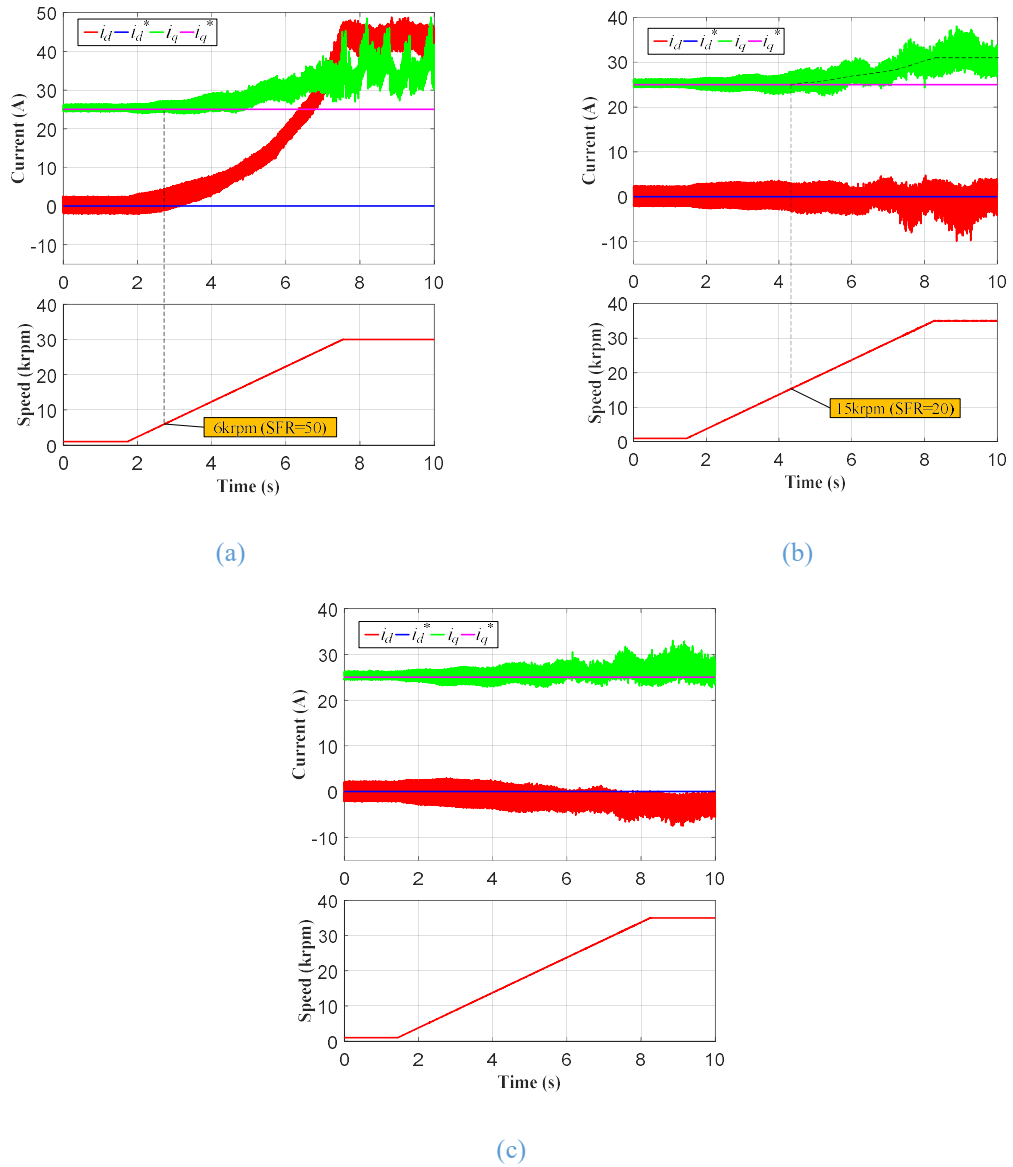
Fig. 2-23 dq axis currents at various speeds (1 krpm~35 krpm) with constant q-axis current reference (25A). (a) Conventional DBPCC without rotor movement compensation. (b) Conventional DBPCC with rotor movement compensation. (c) Proposed DBPCC.

In order to investigate the influence of the operating speed on the control performance of different DBPCCs, the q axis current reference of the prototype high-speed machine is set as constant as 25 A while the machine speed is varied by the dyno. Fig. 2-23 shows the experiment results under different DBPCCs when the machine is accelerated from 1 krpm (SFR=300) to 35 krpm (SFR=8.57) by the dyno. As can be seen, at low speeds with high SFRs, all the control methods exhibits good current control accuracy. However, as the speed rises i.e. the SFR reduces, the current control error with the conventional method rises rapidly. By comparison, the proposed DBPCC control accuracy is hardly affected by the speed. Moreover, as can be seen in Fig. 2-23 (a) and (b), the conventional DBPCC without and with rotor movement compensation deteriorates when the speed is higher than 6 krpm (SFR=50) and 15 krpm (SFR=20), respectively. It confirms the

conclusion derived from the previous quantitative analysis, that to obtain similar control performance, the SFR for the conventional DBPCC without and with compensation should be larger than 50 and 20, respectively.

(a)

(b)

(c)
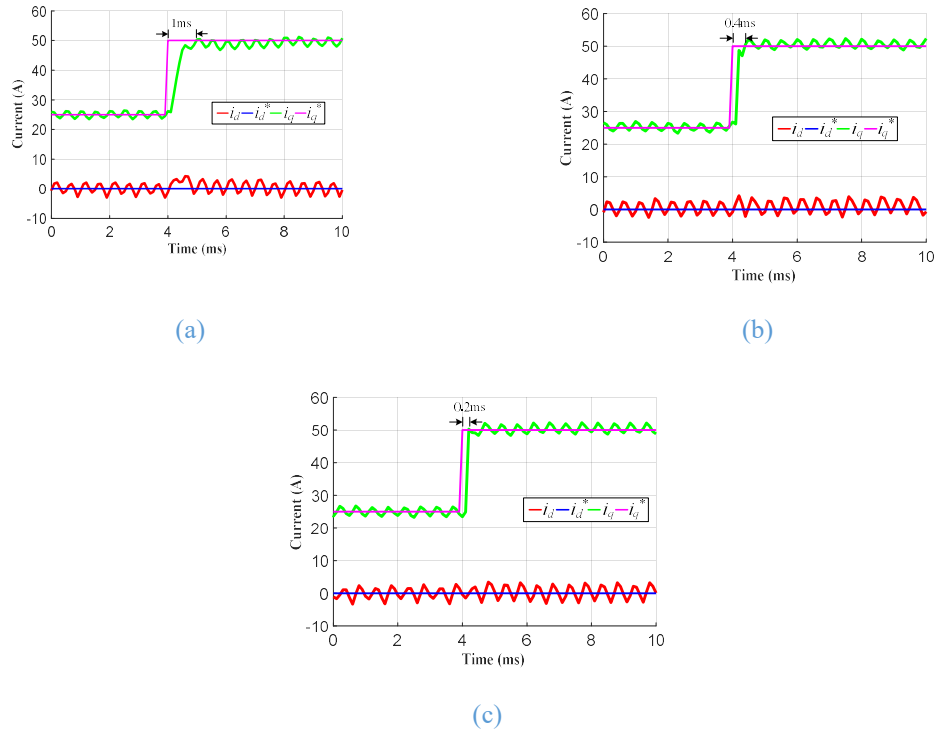
Fig. 2-24 dq axis currents during q-axis current step transients at 10krpm (SFR=30). (a) FOC. (b) Conventional DBPCC with rotor movement compensation. (c) Proposed DBPCC.

Fig. 2-24 shows the current transient control performances with FOC, conventional DBPCC with rotor movement compensation and proposed method at 10 krpm. As can be seen, the DBPCCs exhibits faster current response than FOC. Additionally, since the SFR at 10 krpm with the switching frequency of 10 kHz leads to SFR=30 which is larger than the identified critical SFR for the conventional DBPCC with compensation, the control performance of conventional DBPCC is similar to the proposed method.

(a)

(b)
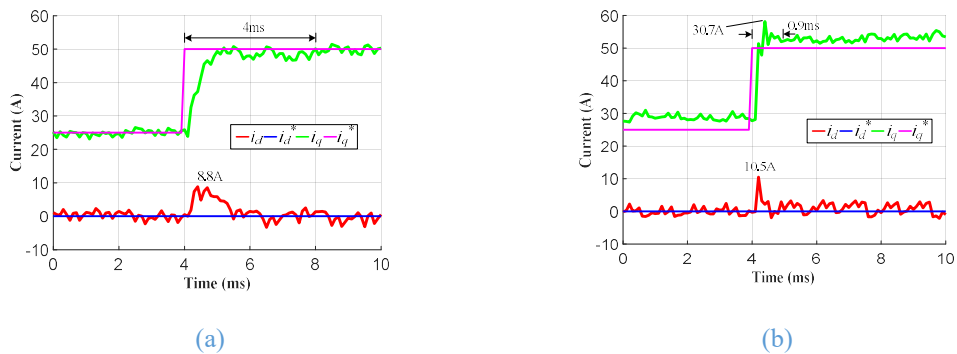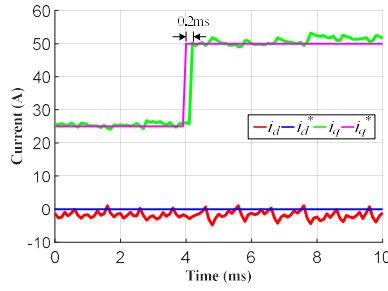
(c)

Fig. 2-25 dq axis currents during q-axis current step transients at 30krpm (SFR=10). (a) FOC. (b) Conventional DBPCC with rotor movement compensation. (c) Proposed DBPCC.
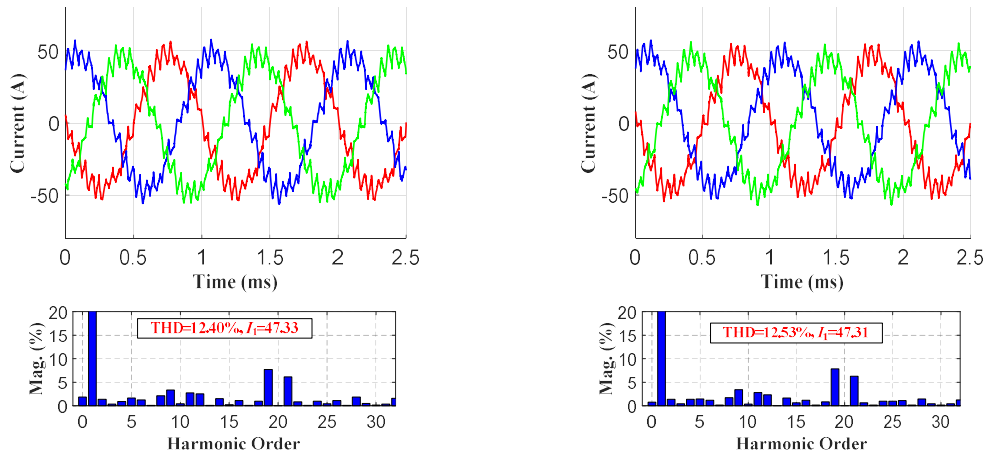
(a)   (b)

Fig. 2-26 Phase currents and current spectrums at the rated condition (30 krpm, 50A). (a) Proposed DBPCC. (b) FOC.

However, as shown in Fig. 2-25 where the current transient control experiments are repeated at the very high speed, i.e. 30 krpm (SFR=10), the control performance of FOC and conventional DBPCC both deteriorate greatly. Although with rotor movement compensation, large cross-coupling between the dq axis can be observed in the conventional DBPCC. However, as can be seen in Fig. 2-25 (c), the deadbeat control of dq axis currents can be still achieved with propose method.

Fig. 2-26 shows the phase currents and the current spectrum with the proposed DBPCC and FOC at the high speed of 30 krpm and rated load current of 50 A. As can be seen, the proposed DBPCC exhibits similar steady-state performance as FOC.

Therefore, the above experiment results have verified the effectiveness of the proposed method at both low speeds and high speeds in terms of both transient and steady-state performance.

2.2.6 Discussion: Current Control Bandwidth and Harmonic Current Control Performance with Proposed DBPCC

Although the proposed SF-DBPCC intrinsically tracks the references via the associated stator fluxes in the stationary frame, the input demands are the reference currents in the dq frame. Hence, the control bandwidth of the proposed DBPCC should be still defined with respects to the synchronous frame, i.e. measured by the frequency response in the dq frame.

Usually, -3 dB in magnitude and 45° delay in phase of the frequency response can be both employed to determine the control bandwidth and the current controllers are designed for a classic first-order system [34]. However, due to the distinctive feature of the deadbeat control, the magnitude of the sampled reference signals can always be tracked with accurate machine model. Therefore, in this chapter, 45° phase delay in the frequency response are employed as the measurement of current control bandwidth for the proposed DBPCC.

With the assumption that the reference current at step $k+2$ equals to step k, the proposed DBPCC features fixed delay, i.e. 2 time-steps. Therefore, the phase delay of the high frequency reference signal with the frequency of f_x is given by

$$PD = 4\pi T_s f_x \tag{2.22}$$

Corresponding to 45° phase delay, the control bandwidth can be determined as

$$f_{bw} = \frac{1}{16T_s} = \frac{f_s}{16} \tag{2.23}$$

where f_s is the sampling frequency.

As can be seen from (2.23), the current control bandwidth of the proposed SF-DBPCC only relates to the sampling frequency. Hence, in some control techniques where the current harmonic injection is employed for performance improvement, the order of the injected harmonic in the dq frame, $n,$ with respect to the fundamental frequency f_1 should satisfy

$$1 < n \le \frac{f_s}{f_1} = \frac{SFR}{16} \tag{2.24}$$

It implies in (2.24) that the controllable current harmonic order in the dq frame decreases as the SFR reduces in high speeds. Therefore, in order to ensure the current harmonic injection ability in high speeds, the sampling frequency should be increased to guarantee that the SFR is sufficient to meet (2.24). In other world, current harmonic injection using the proposed DBPCC with dq axis currents control requires increased sampling and switching frequency in high speeds. The same condition is true if the control is required to reject high order harmonics in the back-emf or caused by other disturbances.
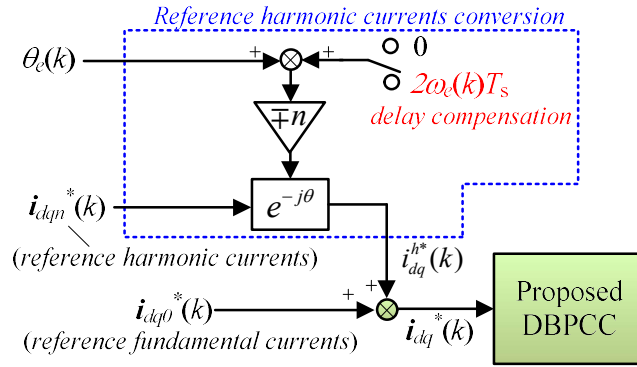
Fig. 2-27 Block diagram of Proposed DBPCC with harmonic current injection control

However, with the proposed DBPCC, the phased delay of current harmonic control can be easily compensated, as shown in Fig. 2-27 where n represents the order of the harmonic in the dq frame to be injected and the sign denotes the rotation direction of the harmonic in the dq frame. For example, when the 5th and 7th current harmonics need to be injected, $\pm n$ should be set as -6 and 6, respectively. Considering the proposed DBPCC has a fixed two steps delay, the harmonic references are transformed to the dq frame with the compensated angle which is the harmonic phase angle advanced by $\mp 2n\omega_e T_s$. As the fixed delay of the DBPCC is compensated, the phase delay of the harmonic current in the dq frame will become zero. It is worth noting that the effective (actual) harmonic reference in the dq frame at step k is equal to that without the phase advancing, i.e., $i_{dqn}^*(k) \cdot e^{-j(\pm n\theta_e(k))}$ and when the amplitudes of the injected current harmonics, $i_{dqn}^*(k)$ varies, it still takes two time-steps to follow the change.
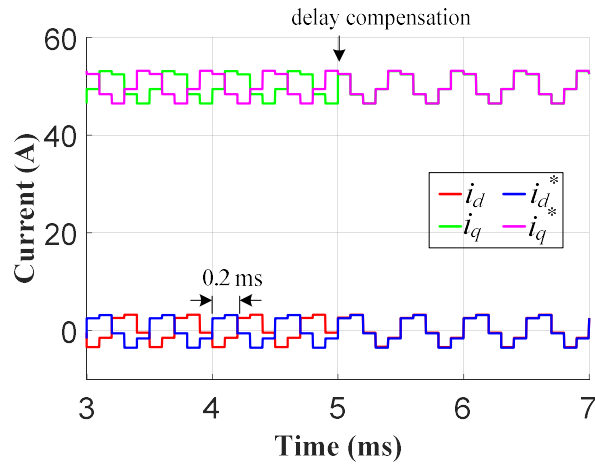
Fig. 2-28 Simulation results of the proposed DBPCC with 5th current harmonic injection control at 10,000 rpm with sampling frequency of 10 kHz

Fig. 2-28 shows the simulation results of the proposed SF-DBPCC with the 5th order current harmonic injection control. The simulation is performed at 10 krpm with sampling frequency of 10 kHz. The frequency of the injected harmonic is 2 kHz in the dq frame. It can be seen in the figure that without the delay compensation, with such low sampling to harmonic frequency ratio (SHR), i.e. 5 in this case, the two time-step delay accounts for 1/5 of the harmonic cycle, i.e. 72°. However, after the delay compensation is triggered, the harmonic current can be followed exactly without delay. Therefore, it can be concluded that with the proposed DBPCC, not only the fundamental current with low SFRs in high speeds but also the harmonic currents with low SHRs can be controlled well.

2.3 Generic Analysis of the Influence of Parametric Mismatch and Inverter Nonlinearity on Stationary Frame Based DBPCC

The robust performance of the proposed DBPCC with respect to large rotor movement in high speeds is obtained assuming ideal inverter and no model error. However, in practice, the control performance of DBPCC is heavily influenced by the accuracy of the machine model and its parameters as well as the inverter nonlinearity. In this section, the influence of parameters mismatch and inverter nonlinearity in the whole speed range with the proposed DBPCC are analysed systematically. In addition, since the resistive voltage drop is relatively small in high speeds and could be identified online in low speeds, the resistance mismatch influence is neglected in the analysis.

2.3.1 Parametric Mismatch Influence in Steady States

2.3.1.1 Analysis of Steady-State Current Control Errors

In this subsection, the current control error in steady states due to parameters mismatch is analytically derived with respects to parametric errors and speed.

Assume that the resistive voltage drop is negligible and the ideal inverter is used, then the real stator flux at step $k+2$ can be expressed as

$$\boldsymbol{\psi}_{\alpha\beta}(k+2) = \boldsymbol{\psi}_{\alpha\beta}(k) + \int_{t_k}^{t_{k+2}} \boldsymbol{u}_{\alpha\beta} dt \tag{2.25}$$

According to the principle of SVM, the integral component on the right hand in (2.25) can be computed by

$$\int_{t_k}^{t_{k+2}} \boldsymbol{u}_{\alpha\beta} dt = T_s\big[\boldsymbol{u}_{\alpha\beta}(k)^* + \boldsymbol{u}_{\alpha\beta}(k+1)^*\big] \tag{2.26}$$

in which, the reference voltages subject to deadbeat control can be calculated from the estimated stator flux variation as

$$\boldsymbol{u}_{\alpha\beta}(k)^* = \big[\widehat{\boldsymbol{\psi}}_{\alpha\beta}(k+1) - \widehat{\boldsymbol{\psi}}_{\alpha\beta}(k)\big]/T_s \tag{2.27}$$

$$\boldsymbol{u}_{\alpha\beta}(k+1)^* = \big[\widehat{\boldsymbol{\psi}}_{\alpha\beta}(k+2)^* - \widehat{\boldsymbol{\psi}}_{\alpha\beta}(k+1)\big]/T_s \tag{2.28}$$

where, $\widehat{\boldsymbol{\psi}}_{\alpha\beta}(k+2)^*$, $\widehat{\boldsymbol{\psi}}_{\alpha\beta}(k)$ are the estimated reference and stator fluxes at steps $k+2$ and k according to the current model with the estimated parameters, respectively.

Therefore, substituting (2.26) combined with (2.27) and (2.28) into (2.25) yields

$$\boldsymbol{\psi}_{\alpha\beta}(k+2) = \boldsymbol{\psi}_{\alpha\beta}(k) + \widehat{\boldsymbol{\psi}}_{\alpha\beta}(k+2)^* - \widehat{\boldsymbol{\psi}}_{\alpha\beta}(k) \tag{2.29}$$

Transforming (2.29) into the *dq* frame at step $k+2$ gives

$$\boldsymbol{\psi}_{dq}(k+2) = \big[\boldsymbol{\psi}_{dq}(k) - \widehat{\boldsymbol{\psi}}_{dq}(k)\big] \cdot e^{-j2\omega_e T_s} + \widehat{\boldsymbol{\psi}}_{dq}(k+2)^* \tag{2.30}$$

Define the steady-state current error, $\triangle \boldsymbol{i}_{dq}$ as

$$\triangle \boldsymbol{i}_{dq} = \boldsymbol{i}_{dq}{}^* - \boldsymbol{i}_{dq} \tag{2.31}$$

Then, according to the current model of PMSM i.e. (2.32), the current error at step $k+2$ can be derived from the corresponding stator fluxes as (2.33).

$$\boldsymbol{\psi}_{dq} = L_s \boldsymbol{i}_{dq} + \psi_m \tag{2.32}$$

$$\triangle \boldsymbol{i}_{dq}(k+2) = \frac{1}{L_s}\left[\boldsymbol{\psi}_{dq}(k+2)^* - \boldsymbol{\psi}_{dq}(k+2)\right] \tag{2.33}$$

Substituting (2.30) into (2.33) using the current model (2.32) with parameter mismatches for the stator fluxes, and assuming the reference current at step $k+2$ equals to the reference sampled at step k, the current error at step $k+2$ can be derived as

$$\triangle \boldsymbol{i}_{dq}(k+2) = \frac{1}{L_s}\Big[\left(\triangle L_s \boldsymbol{i}_{dq}(k)^* + \triangle \psi_m\right) - \left(\triangle L_s \boldsymbol{i}_{dq}(k) + \triangle \psi_m\right) \tag{2.34}$$
$$\cdot\, e^{-j2\omega_e T_s}\Big]$$

where $\triangle L_s$ and $\triangle \psi_m$ are the inductance and PM flux linkage parameter mismatch, defined as $L_s - \hat{L}_s$ and $\psi_m - \hat{\psi}_m$, respectively.

In steady state, the sampled currents in the *dq* frame would be stable and it is reasonable to assume the *dq* currents at steps k and $k+2$ are kept the same, namely

$$\boldsymbol{i}_{dq}(k+2) = \boldsymbol{i}_{dq}(k) \tag{2.35}$$

Denote the constant steady-state current in (2.35) and the associated reference current generally as $\boldsymbol{I}_{dq}$ and $\boldsymbol{I}_{dq}^*$, respectively. Substituting (2.31) and (2.35) into (2.34) obtains the steady-state current as expressed in

$$\boldsymbol{I}_{dq} = \frac{(L_s - \triangle L_s)\boldsymbol{I}_{dq}^* - \triangle \psi_m\left(1 - e^{-j2\omega_e T_s}\right)}{L_s - \triangle L_s \cdot e^{-j2\omega_e T_s}} \tag{2.36}$$

According to the expression of the steady-state current by (2.36), it is seen that with inaccurate machine parameters, the steady-state current will not be equal to the reference and, instead, is a function of the reference current, parameters mismatch, real inductance, motor speed and control time-step. Nevertheless, if the exact inductance and PM flux linkage are employed, i.e. $\triangle L_s = 0$ and $\triangle \psi_m = 0$, the steady-state current (2.36) can be simplified as $\boldsymbol{I}_{dq} = \boldsymbol{I}_{dq}^*$, which indicates the reference current can be tracked without error.

Meanwhile as can be inferred from (2.36), in low speed or with sufficiently high sampling (control) frequency, the one-step rotor movement $\omega_e T_s \approx 0$, which leads to $e^{-j2\omega_e T_s} \approx 1$. As a result, the steady-state current can also be derived as $\boldsymbol{I}_{dq} = \boldsymbol{I}_{dq}^*$

regardless of parameters mismatch. It implies that in low speed with sufficiently high control frequency, the parameters mismatch influence will be less pronounced than in high speeds.

Another finding from (2.36) is that if the parameter mismatch exists only in the PM flux linkage, the current control error is independent of the reference currents and constant at a given speed. However, the current control error increases with speed. On the other hand, the current error caused by the inductance mismatch is dependent on both reference currents and speed.

Moreover, it is worth noting that the factor of 2 in the phase angle of the component $e^{-j2\omega_e T_s}$ in (2.36) can be physically attributed to the two steps prediction characteristic of the proposed DBPCC, i.e. one-step current prediction and one-step reference voltage prediction, in which the parameter inaccuracy will cause combined effect of the final current control error.

2.3.1.2 Numerical Verification

With (2.36), the current control errors under parametric mismatch can be calculated explicitly for all the operating conditions. Fig. 2-29~Fig. 2-31 compare the predicted and simulated results at different scenarios. The parameters of the high-speed PMSM drive listed in Table 2-1 is used in the simulation, and the DC link voltage is set to 100V. The reference q-axis current is set at the characteristic current of the motor, namely $i_q{}^* = \psi_m/L_s$ (75.8 A for the prototype high-speed PMSM motor in Table 2-1) and reference d-axis current is set as 0. To normalise the current control error, the calculated current error value is divided by the characteristic current. The variation of one-step rotor movement in electrical degree is obtained by varying the machine speed while the switching/sampling frequency is kept constant as 10 kHz, e.g. the speed of 10 krpm corresponds to one-step rotor movement of 12 electrical degrees and 50 krpm corresponds to one-step rotor movement of 60 electrical degrees. The normalised estimated parameter is defined as the estimated parameter value divided by the actual value.

The current errors as a function of one-step rotor movement with estimation errors in PM flux linkage and synchronous inductance are plotted in Fig. 2-29 and Fig. 2-30, respectively. Fig. 2-31 shows the current error variation with the relative estimation error of machine parameter. The high extent consistency in the results confirms the accuracy of the analytical equation, (2.36) and the correctness of the analysis above.
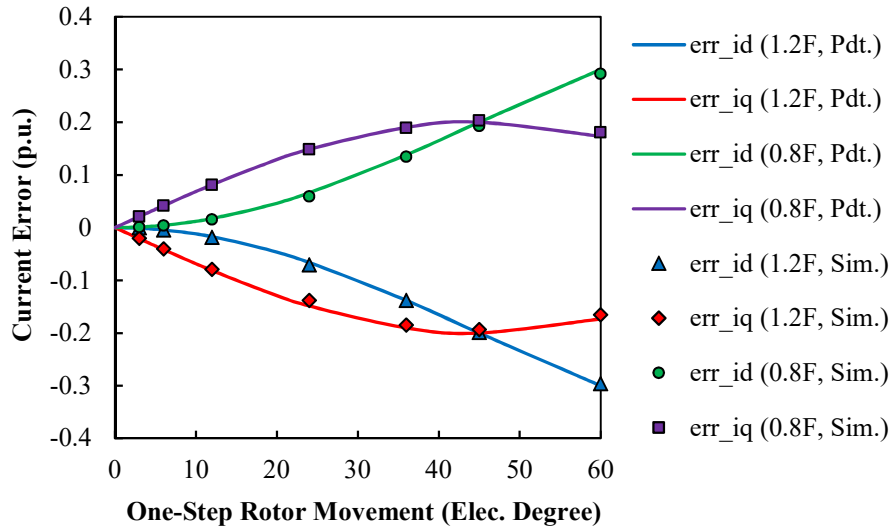
Fig. 2-29 Analytically predicted and numerically simulated current control errors with DBPCC under PM flux linkage mismatch, as a function of one-step rotor movement ($\omega_e T_s$). In the legend, 1.2F and 0.8F denote $\hat{\psi}_m = 1.2\psi_m$ and $\hat{\psi}_m = 0.8\psi_m$, respectively.
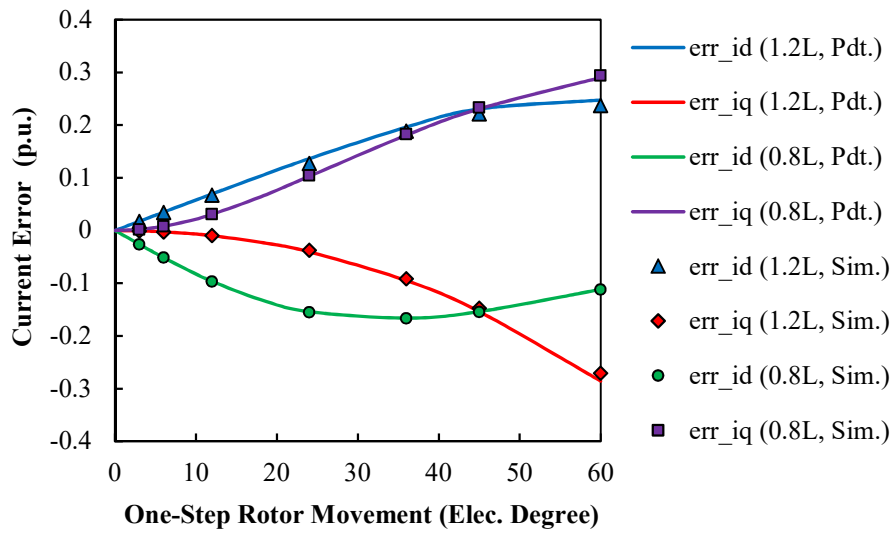
Fig. 2-30 Analytically predicted and numerically simulated current control errors with DBPCC under inductance mismatch, as a function of one-step rotor movement ($\omega_e T_s$). In the legend, 1.2L and 0.8L denote $\hat{L}_s = 1.2L_s$ and $\hat{L}_s = 0.8L_s$, respectively.
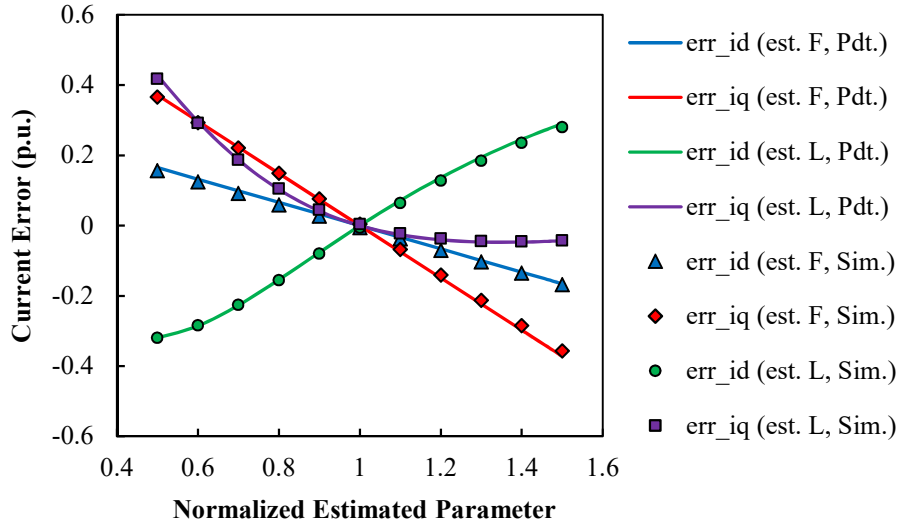
Fig. 2-31 Analytically predicted and numerically simulated current control errors with DBPCC under parameters mismatch with one-step rotor movement of 24 electrical degrees (i.e. SFR=15), as a function of the normalized estimated parameter. In the legend, est. F and est. L denote employing the estimated PM flux linkage and estimated inductance, respectively.

2.3.2 Parametric Mismatch Influence in Transients

2.3.2.1 Analysis of Transient Current Control Error

Ideally, with accurate parameters, the current will be controlled to reach the reference in two time-steps using the proposed DBPCC. However, as discussed previously, the reference cannot be tracked correctly in steady states due to the parameter inaccuracy. Therefore, it is also important to evaluate the transient tracking performance of the DBPCC under parameters mismatch with respect to the resultant steady-state current rather than the actual reference current.

Generally, there can be two categories of the current control transients i.e. transients caused by disturbances and by change in the reference current. However, the change in the reference current can be regarded as an equivalent perturbation caused by a disturbance. Thus, the two types of the transients can be considered as one in the analysis, where the transients are reflected by the difference between the steady-state current associated with the reference and the instantaneous current at the present time. According to (2.36), the steady-state current error, namely, the difference between the reference current I_{dq}^* and the corresponding steady-state current I_{dq} can be expressed as

$$\triangle i_{dq\_ss} = \frac{1}{L_s}\left[\triangle L_s\left(I_{dq}{}^* - I_{dq}\cdot e^{-j2\omega_e T_s}\right) + \triangle \psi_m\left(1 - e^{-j2\omega_e T_s}\right)\right] \tag{2.37}$$

At a transient time-step k, with the sampled current, $i_{dq}(k)$, the current control error after two steps has already been derived in (2.34). Therefore, subtracting (2.37) from (2.34), the current tracking error in transient, namely, the difference between the current at step (k+2) and the steady-state current can be obtained as

$$err_{CT} = I_{dq} - i_{dq}(k+2) = \frac{\triangle L_s\cdot e^{-j2\omega_e T_s}}{L_s}\cdot\left[I_{dq} - i_{dq}(k)\right] \tag{2.38}$$

where $I_{dq} - i_{dq}(k)$ represents the transient in the present current, which can also be caused by the reference changing as explained above. For example, if the reference current changes from I_{dq1}^* to I_{dq2}^*, the associated steady state currents are I_{dq1} and I_{dq2} with steady-state current errors, $\triangle i_{dq\_ss1}$ and $\triangle i_{dq\_ss2}$, respectively. When the present step current, $i_{dq}(k)$ is at the steady-state, i.e. I_{dq1}, then the transient current, $I_{dq} - i_{dq}(k)$ can be expressed as

$$I_{dq} - i_{dq}(k) = I_{dq2} - I_{dq1} = \left(I_{dq2}^* - I_{dq1}^*\right) + \left(\triangle i_{dq\_ss1} - \triangle i_{dq\_ss2}\right) \tag{2.39}$$

By (2.39), it can be seen that the transient current associated with the change in the reference current can be approximated as the reference current variation if the two steady-state current errors are close.

As can be found from (2.38), the transient current, i.e., the current tracking performance is only affected by the inductance parameter mismatch and independent of the PM flux linkage. When the inductance is accurately estimated, i.e. $\triangle L_s = 0$, the current tracking error is 0 and it means all the deviation in the present current from its steady state value can be eliminated in two time-steps, which is exactly the ideal tracking performance of the proposed DBPCC. However, if inaccurate inductance is employed in the two step predictions, the tracking error will not be null and is actually the product of the relative estimation error in inductance, the current deviation at the present step and $e^{-j2\omega_e T_s}$. It implies that in the transient with a step change in the reference, there will be overshoot current with overestimated inductance since a large current deviation will be caused by the suddenly change in the reference current. On the other hand, the current response will be slowed with under-estimated inductance. In contrast with the both, the steady-state error is close to zero at very low speeds while the transient tracking error still

exist. However, at high speeds, the transient overshoot current will occur in both d- and q- axes since the component $e^{-j2\omega_e T_s}$ gives rise to a cross-coupling influence and become more pronounced at higher speeds.

Nevertheless, when the overshoot currents or generally transient tracking errors appear after two time-steps following the reference change, it can be sampled, controlled and reduced quickly within two time-steps, according to (2.38). Generally, after a step change in the reference, the current tracking error at $2n$ time-steps later is given by

$$\boldsymbol{err_{CT}}(n) = \left(\frac{\triangle L_s}{L_s} \cdot e^{-j2\omega_e T_s}\right)^n \cdot \left[\boldsymbol{i_{dq}} - \boldsymbol{i_{dq}}(k)\right] \tag{2.40}$$

As evident in (2.40), the overshoot current will vanish exponentially with increases in steps or time. Hence, although overshoot current will occur when the reference change abruptly, the large overshoot will only last for two time-steps and can be eliminated quite quickly. Moreover, it is also indicated in (2.39) that a small current reference step leads to less current deviation and consequently less overshoot current even with over-estimated inductance.

Additionally, it is worth noting that here the current tracking error is defined as the deviation from the steady-state current, therefore, the actual maximum current deviation with respect to the reference is the sum of the transient current tracking error and the steady-state error.

2.3.2.2 Numerical Verification

According to the derived equation namely (2.38), the transient tracking error under the parameters mismatch can be predicted. In order to validate the prediction accuracy of the analytical equation, extensive numerical simulations have been performed on the prototype high-speed drive as well. In order to the simplify the numerical validation, the simulation is performed at a low speed, i.e. $e^{-j2\omega_e T_s} \approx 1$ while for high speeds the same conclusion can be obtained by calculate the $e^{-j2\omega_e T_s}$ accordingly in (2.38).

Fig. 2-32 shows the simulation results of the q-axis current in transients with different estimated inductance at 3 krpm with sampling/switching frequency of 10 kHz. In the simulation, the d-axis current reference is set as zero and the d-axis current is hardly affected by the transients in the q-axis current and inductance mismatch, thus the waveform is not depicted in the figure.
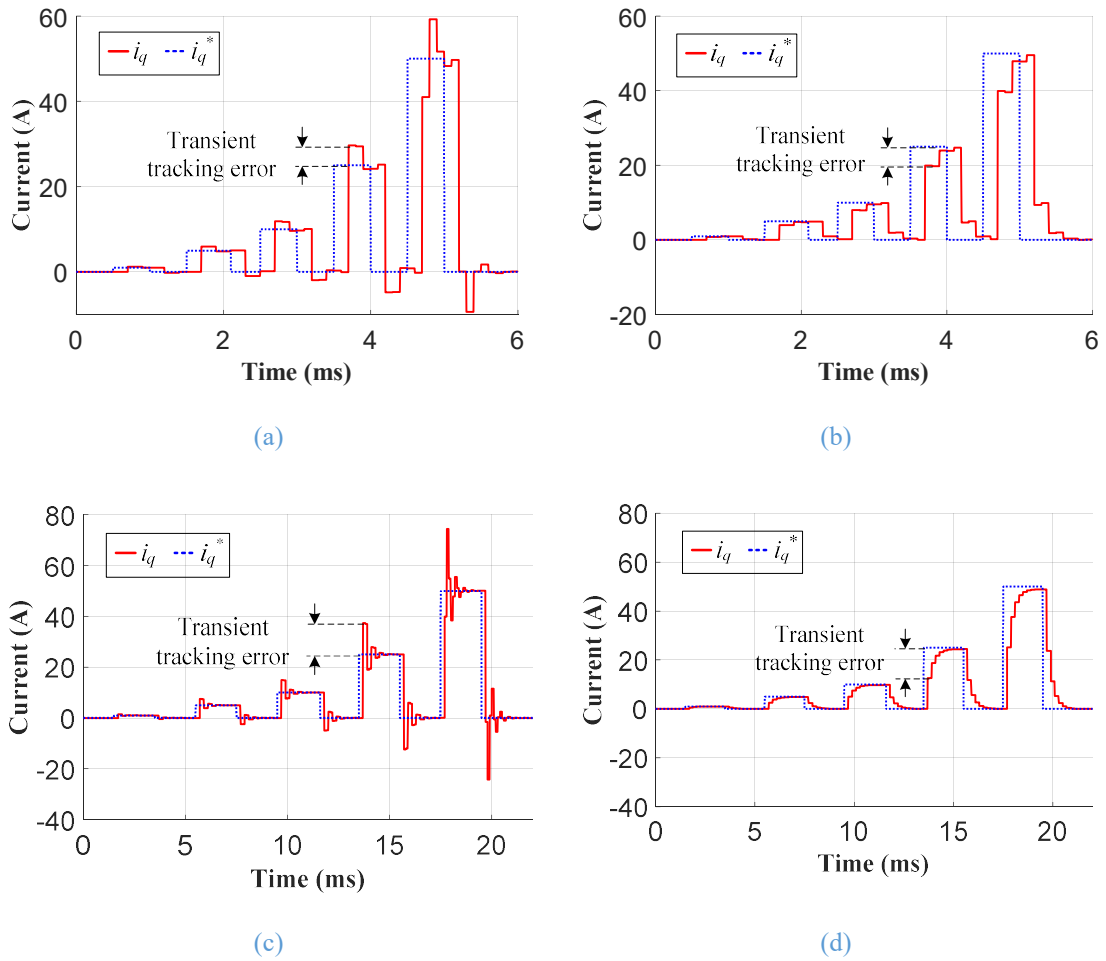
Fig. 2-32 Simulation waveforms of transient tracking errors of SF-DBPCC with different stepping current reference stepping under inductance mismatch (a) $\hat{L}_s = 1.2L_s$ (b) $\hat{L}_s = 0.8L_s$ (c) $\hat{L}_s = 1.5L_s$ (d) $\hat{L}_s = 0.5L_s$
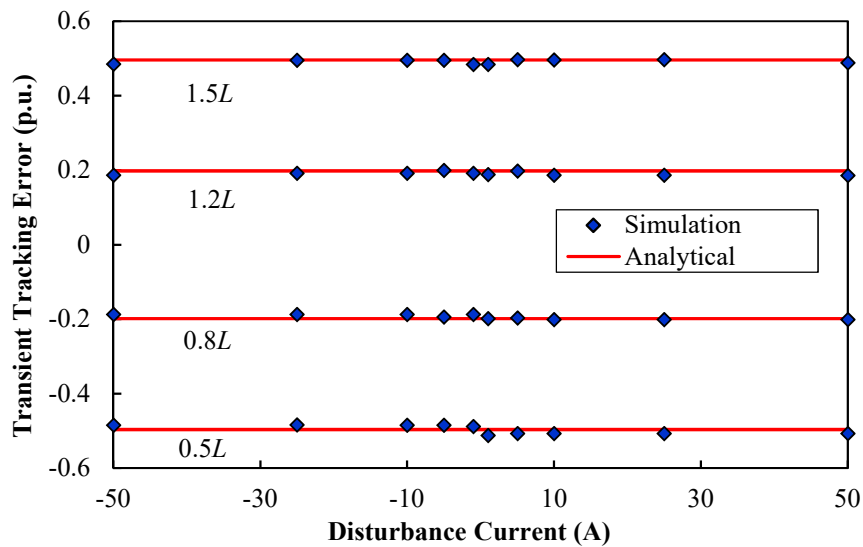
Fig. 2-33 Analytically predicted and numerically simulated transient tracking errors of SF-DBPCC under inductance mismatch at the speed of 3 krpm, f_{sw}=10 kHz (SFR=100) as a function of disturbance current/reference current stepping

70

As can be seen in Fig. 2-32, the q-axis current references are set as a fixed pattern, namely a pulse sequence with the maximum levels of 1A, 5A, 10A, 25A and 50A respectively. As can be seen in Fig. 2-32 (a) and (c), transient tracking errors emerge as overshoot currents after the reference stepping up or down when the inductance is over-estimated. However, with under-estimation of inductance, the transient tracking errors appears undershoots following the transients. It is worthy noting that in Fig. 2-32 (a) and (c), when the current steps from 0 to 50A, a undershoot appears and last for one time-step. It is due to the voltage saturation in such large current change. As in low speed, the steady state current control error is small with inductance mismatch according to (2.47) and the simulation results presented above, thereby the transient disturbance current expressed in (2.40) can simply be approximated as reference current variation. Fig. 2-33 plots the transient tracking errors in Fig. 2-32 obtained with different inductance mismatch in different transient, as a function of the disturbance current i.e. the reference current variation, where the transient tracking errors are normalized against the corresponding disturbance currents. Besides, the analytical predicted transient current tracking errors according to (2.38) are also presented in Fig. 2-33. It can be clearly observed that the numerical simulation results conforms to the analytical prediction. Therefore, it validates the accuracy of the derived equation in (2.38) for the transient tracking errors under parameters mismatch.

2.3.3 Inverter Nonlinearity Influence in Steady States and Transients

2.3.3.1 Inverter nonlinearity caused voltage losses

In order to prevent the shoot-through of the power switches in an inverter leg, dead-time should be inserted between the turn-on and turn-off of the top and bottom switches. As shown in Fig. 2-34, the dead-time and the parasitic voltage drop across the transistor and anti-parallel diode would result in the actual voltage depicted in the red solid line deviating from the ideal voltage in the black dotted line.
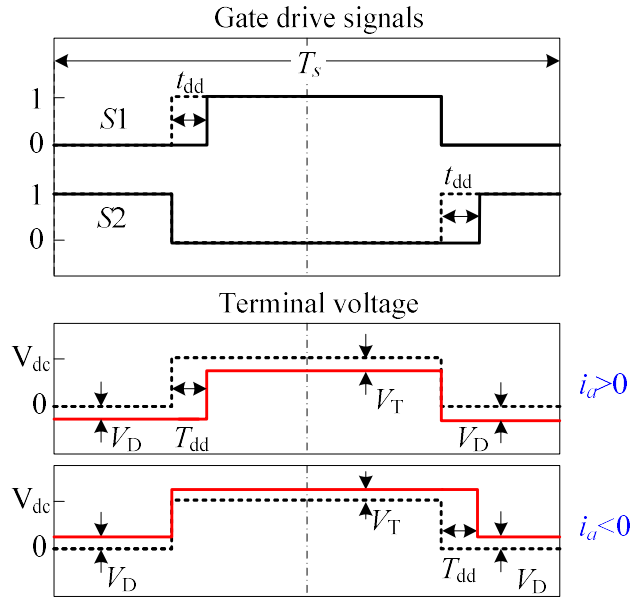
Assume that the parasitic voltage drops, V_T and V_D, are identical and denoted as V_{DT}, then the average voltage loss of the terminal voltage, $V_{inv\_a,b,c}$ in a PWM period due to the dead-time and parasitic voltage drop, known as the inverter nonlinearity is given by

$$V_{inv\_a,b,c} = sign(i_{a,b,c}) \cdot \Delta V \qquad (2.41)$$

where,

$$\Delta V = \frac{1}{T_s}(V_{dc} + V_{DT})T_{dd} + V_{DT} \qquad (2.42)$$

V_{dc} denotes the DC voltage and T_{dd} denotes the equivalent dead-time including the drive signal dead-time and switch turn-on and -off delays.

Assume that the phase current is sinusoidal, then the voltage losses at the three phase terminals can be plot accordingly in Fig. 2-35, which are square waveforms. The resultant phase-to-neutral voltage loss is in a six-step manner.
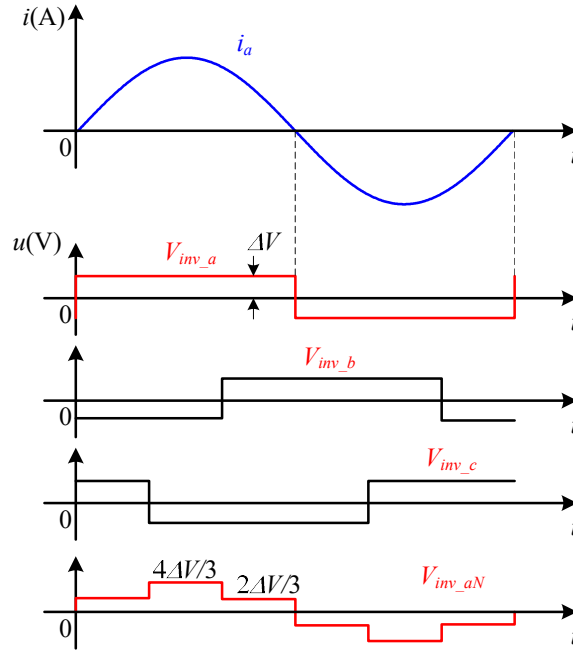
Fig. 2-35 Phase A current, three phase terminals voltage loss and phase A voltage loss due to inverter nonlinearity

The six-step phase voltage loss due to the inverter nonlinearity can be expanded in the form of Fourier series as a function of ΔV. For phase A, this is given by

$$V_{inv\_aN} = \frac{4}{\pi}\Delta V\left(\sin\theta + \sum_{n=6k\pm1}\frac{1}{n}\sin n\theta\right) \tag{2.43}$$

The other two phase voltage losses can be obtained simply by appropriate phase shifting. Convert the three phase voltage losses into the dq frame, and assume i_d=0 control is employed for high-speed SPMSMs, then it can be derived that the average inverter nonlinearity caused voltage loss in the d-axis is equal to 0 while the value in the q-axis is given by

$$V_{inv\_qav} = \frac{4}{\pi}\Delta V = \frac{4}{\pi}\left[\frac{1}{T_s}(V_{dc} + V_{DT})T_{dd} + V_{DT}\right] \tag{2.44}$$

If the parasitic voltage drop of the inverter is negligible, then the average voltage loss due to the dead time in the q-axis can be further simplified as

$$V_{inv\_qav} = \frac{4}{\pi}\Delta V = \frac{4V_{dc}T_{dd}}{\pi T_s} \tag{2.45}$$

Fig. 2-36 shows the simulation results of dq axis voltage loss caused by the inverter nonlinearity with V_{dc}=100 V, f_{sw}=10 kHz and t_{dd}=2 μs, it can be seen that inverter

73

nonlinearity results in the voltage distortions in both d- and q- axes, however, the average voltage loss in the d- axis is zero.
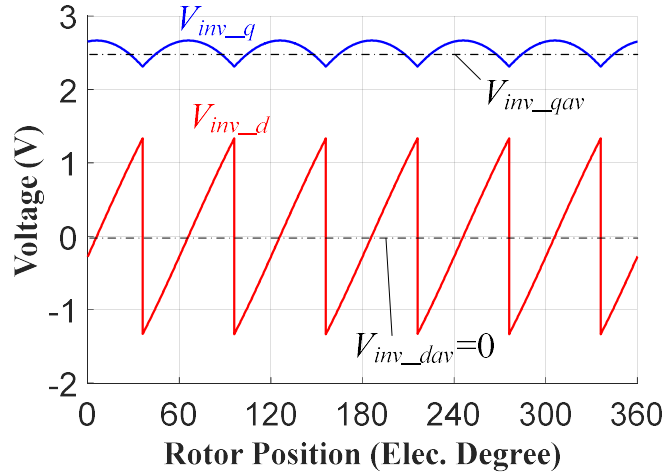
Fig. 2-36 Voltage loss in the d- and q-axes due to inverter nonlinearity with V_{dc}=100 V, f_{sw}=10 kHz and t_{dd}=2 μs

2.3.2.2 *Steady-state current error due to inverter nonlinearity*

As has been shown, the inverter nonlinearity will cause voltage distortions in both d- and q- axes. Accordingly, the voltage distortions will cause both current harmonics and offset control error. In this subsection, the steady-state current control error, namely the average current control error caused by inverter nonlinearity in a general case with parameters mismatch and influence of speed are analytically derived and discussed.

Only the average distortion voltage in the dq frame associated with inverter nonlinearity is considered and the cross-coupling components in the dq frame due to the inverter nonlinearity is ignore provided that they are negligible compared with the fundamental dq axis cross-coupling components. The stator flux at step k+2 in the dq frame represented by (2.30) with ideal inverter can then be modified as

$$\boldsymbol{\psi}_{dq}(k+2) = \left[\boldsymbol{\psi}_{dq}(k) - \widehat{\boldsymbol{\psi}}_{dq}(k)\right] \cdot e^{-j2\omega_e T_s} + \widehat{\boldsymbol{\psi}}_{dq}(k+2)^* \qquad (2.46)$$
$$- 2T_s \boldsymbol{V}_{inv\_dqav}$$

where $\boldsymbol{V}_{inv\_dqav}$ is the average voltage loss vector in the dq frame.

Repeat the same derivation process for the steady-state current in (2.36), by referring to the equations from (2.30) to (2.35) and the average steady-state current considering the

74

influence of both parameters mismatch and inverter nonlinearity can be finally obtained as

$$i_{dq} = \frac{(L_s - \triangle L_s)i_{dq}{}^* - \triangle \psi_m\left(1 - e^{-j2\omega_e T_s}\right) - 2T_s V_{inv\_dqav}}{L_s - \triangle L_s \cdot e^{-j2\omega_e T_s}} \tag{2.47}$$

It can be seen that the inverter nonlinearity will cause a fixed offset current control error independent of the reference current. Moreover, the influence of the inverter nonlinearity is not significantly affected by the speed and the time-step, as the inverter nonlinearity related term in (2.47), $T_s V_{inv\_dqav}$, can be approximated by (2.48) when neglecting the parasitic conducting voltage drops.

$$T_s V_{inv\_qav} = \frac{4V_{dc}T_{dd}}{\pi} \tag{2.48}$$

As can be seen in Fig. 2-37, the analytical equation also provide accurate predictions in the scenarios with inverter nonlinearity, where in the simulation the inverter nonlinearity only includes the dead-time and the switches' parasitic voltage drops are not accounted.
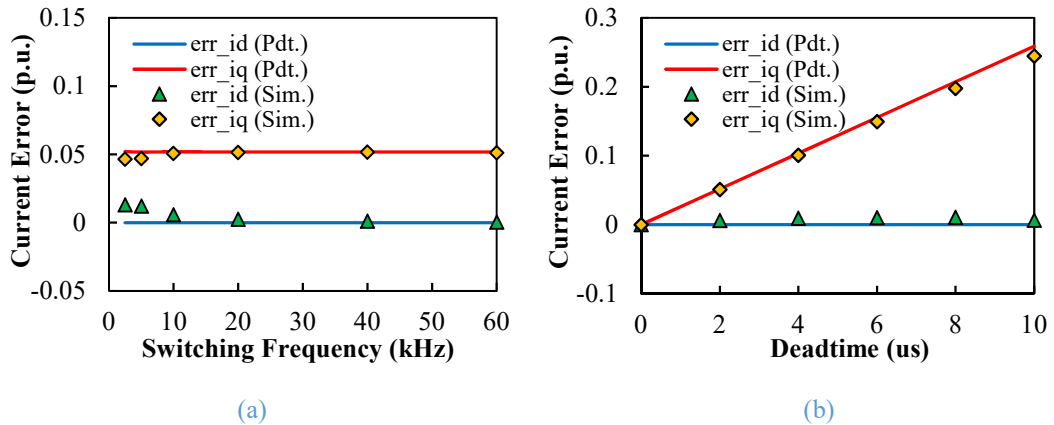
Fig. 2-37 Analytically predicted and numerically simulated current control errors with DBPCC under inverter nonlinearity at 10 krpm, as a function of (a) switching frequency with fixed dead-time of 2us (b) dead-time with constant switching frequency of 10kHz.

It can be found that the current control errors caused by the inverter nonlinearity only relates to the dead-time and not influenced by the switching frequency which can be further extended to the factors, the one-step rotor movement and the motor speed. However, the small discrepancies between the prediction and simulation results can be found at low switching frequencies, i.e. 2.5 kHz and 5 kHz in Fig. 2-37 (a), which corresponds to SFR=7.5 and 15 respectively. It can be attributed to the neglecting of the cross-coupling components in the dq frame relating to the inverter nonlinearity when

deriving (2.46) and the prediction error of the average value of the dead-time caused voltage drop due to the discretization in the actual waveform. Nevertheless, these small prediction error of inverter nonlinearity caused current control error is less important and negligible in high speeds with low SFRs.

2.3.2.2 *Inverter nonlinearity influence in transient*

As can be seen in the steady-state current error expression, (2.47), the average current control error due to the inverter nonlinearity is similar to that caused by PM flux linkage mismatch and independent of the reference and actual currents. The transient current tracking error with the distorted average voltage of the inverter nonlinearity can still be expressed in (2.38), which only relates to the parameter mismatch in the inductance. Therefore, the transient control performance of the proposed DBPCC would not significantly be affected by the inverter nonlinearity.

2.3.4 Summary of Key Understandings of the Parametric Mismatch and Inverter Nonlinearity Influence

In order to assess the influence on the d-axis and q-axis currents, the general expression of the steady-state dq axis current vector (2.47) can be rewritten in the component form as

$$
\begin{cases}
i_d = \lambda_{L1} \cdot i_d{}^* + \lambda_{L2} \cdot i_q{}^* + \lambda_{\psi1} + \lambda_{inv1} \\
i_q = \lambda_{L1} \cdot i_q{}^* - \lambda_{L2} \cdot i_d{}^* + \lambda_{\psi2} + \lambda_{inv2}
\end{cases}
\tag{2.49}
$$

where the coefficients are

$$
\begin{cases}
\lambda_{L1} = \dfrac{a}{a^2 + b^2} \\[2mm]
\lambda_{L2} = \dfrac{b}{a^2 + b^2} \\[2mm]
\lambda_{\psi1} = \lambda_{L1} \cdot c + \lambda_{L2} \cdot d \\
\lambda_{\psi2} = \lambda_{L1} \cdot d - \lambda_{L2} \cdot c \\
\lambda_{inv1} = -\lambda_{L2} \cdot \dfrac{2T_s V_{inv\_qav}}{\hat{L}_s} \\[2mm]
\lambda_{inv2} = -\lambda_{L1} \cdot \dfrac{2T_s V_{inv\_qav}}{\hat{L}_s}
\end{cases}
\tag{2.50}
$$

$$\begin{cases} a = 1 + \dfrac{\triangle L_s}{\hat{L}_s}[1 - \cos(2\omega_e T_s)] \\[2mm] b = \dfrac{\triangle L_s}{\hat{L}_s}\sin(2\omega_e T_s) \\[2mm] c = -\dfrac{\triangle \psi_m}{\hat{L}_s}[1 - \cos(2\omega_e T_s)] \\[2mm] d = -\dfrac{\triangle \psi_m}{\hat{L}_s}\sin(2\omega_e T_s) \end{cases} \qquad (2.51)$$

The key findings on the influences of the parameters mismatch and inverter nonlinearity deduced from the analytical expressions are summarized below.

1) Steady-state current control error caused by parameters mismatch is larger in high speeds than in low speeds. The error is caused by the rotor movement in two time-steps, i.e. $2\omega_e T_s$. For a given $\omega_e T_s$ or SFR, the steady-state current error due to parameter mismatch is constant. As the SFR reduces, the parameters mismatch will cause current control errors in both the q-axis and d-axis.

2) Steady-state current control error caused by PM flux linkage mismatch is independent of the reference current while the error due to inductance mismatch increases as the reference current increases.

3) Dead-time of the inverter causes an offset in the steady-state q-axis current with i_d=0 control. The offset is independent of the motor speed and switching frequency and is a function of the DC-link voltage and dead-time.

4) The transient current tracking performance is not affected by PM flux linkage parameter mismatch and inverter nonlinearity. That is, the steady state can always be reached in two time-steps.

5) Transient overshoot or undershoot currents will occur with inaccurate inductance when the reference current changes in step. The overshoot or undershoot current can be reduced greatly in two-time steps and decays quickly. Small reference changes and inductance estimation errors leads to less overshoot or undershoot currents.

2.3.5 Simulation Results

2.3.5.1 Parameters mismatch influence in steady states and transients at various speeds

(a)   (b)   (c)
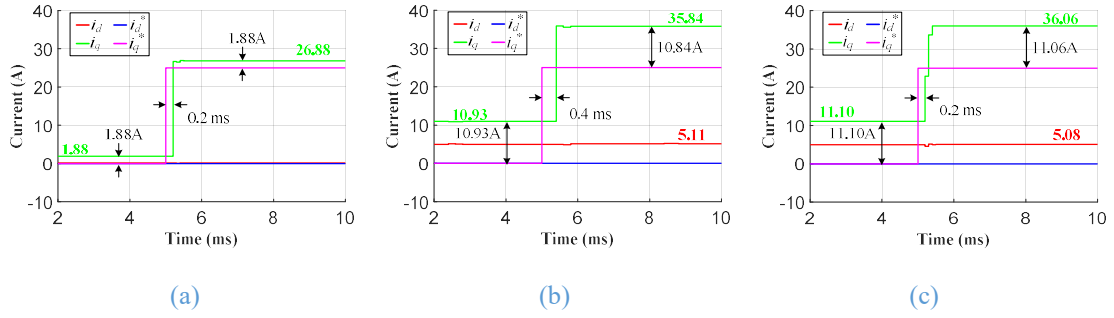
Fig. 2-38 Simulation results of sampled *dq* currents during a step change in q-axis current reference when only PM flux linkage mismatch exists ($\hat{\psi}_m = 1.2\psi_m$) (a) at low-speed of 3,000 rpm, f_{sw}=10 kHz (SFR=100) (b) at high-speed of 10,000 rpm, f_{sw}=5 kHz (SFR=15) (c) at higher-speed of 20,000 rpm, f_{sw}=10 kHz (SFR=15)

(a)   (b)   (c)
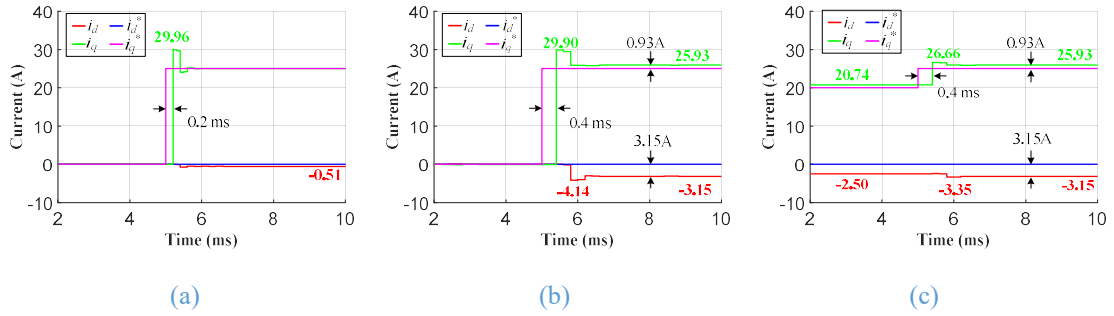
Fig. 2-39 Simulation results of sampled *dq* currents during a step change in q-axis current reference when only inductance mismatch ($\hat{L}_s = 1.2L_s$) exists (a) at low-speed of 3,000 rpm, f_{sw}=10kHz (SFR=100) (b) at high-speed of 10,000 rpm, f_{sw}=5kHz (SFR=15) (c) at high-speed of 10,000 rpm, f_{sw}=5kHz (SFR=15), with a smaller current reference step

(a)   (b)
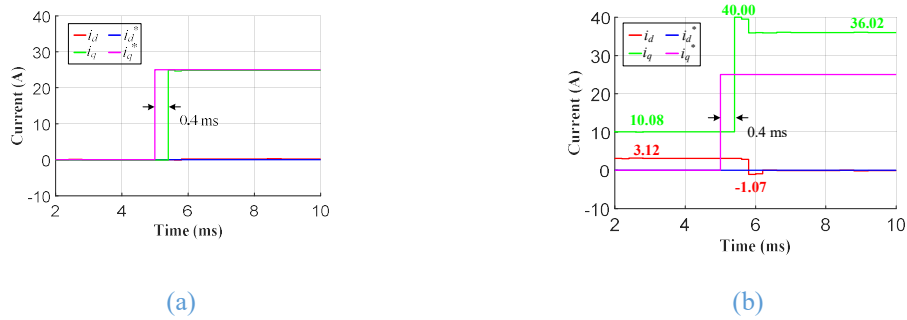
Fig. 2-40 Simulation results of sampled *dq* currents at 10,000 rpm with f_{sw}=5kHz (SFR=15) during a step change in q-axis current reference (a) with accurate parameters (b) with parameters mismatch ($\hat{\psi}_m = 1.2\psi_m$ and $\hat{L}_s = 1.2L_s$)

Fig. 2-38 shows the simulation results only with a mismatch in the PM flux linkage at different speeds. By comparing Fig. 2-38 (a) and (c) under the same conditions except for the operating speed, it can be seen that in low speed, the current control error in steady states only exists in the q-axis, while in high speed, the current control errors increase greatly and can be observed in the d-axis as well. However, with the same SFR, the current control error at 10 krpm has the same value as that in Fig. 2-38 (c) at 20 krpm, which validates that the SFR is the characteristic factor influencing the steady-state current control error when the speed varies. By comparing the steady-state current control

errors with different q-axis current references in Fig. 2-38, it is evident that at a given speed the resultant current control errors due to the PM flux linkage mismatch is constant and independent of the current reference, which validates finding 2). Moreover, it can be observed that although the current errors exist in steady state with the PM flux linkage mismatch, the current transient tracking performance is hardly affected, as the steady state current can be always reached in two time-steps as shown in Fig. 2-38 (a) and (b). It is worth noting that, as shown in Fig. 2-38 (c), the steady state is reached in five time-steps after the reference changes. This is because in such high speed, the sudden change in the q-axis current reference results voltage saturation during the transient. Therefore, all these observations in the simulation results shown in Fig. 2-38 match well with the aforementioned analysis and validate the points summarised in 1), 2) and 4) on the influence of PM flux linkage mismatch in section 2.3.4.

Fig. 2-39 shows the simulation results with only inductance mismatch at both low and high speeds with SFR=100 and SFR=15. As evident in Fig. 2-39 (a) and (b), the current control errors due to the inductance mismatch increase and occur in both the d-axis and q-axis as the speed increases, or effectively as the SFR reduces. By comparing the current control error associated with different reference currents in Fig. 2-39 (b) and (c), it is seen that the errors due to the inductance mismatch is dependent on the reference current as stated in the summary point 2). Moreover, it is seen in both low speed and high speed, overshoot currents occur when the reference currents change, which can be predicted by (2.38). However, as the reference current step reduce, the overshoot current reduces nearly proportionally. In addition, the overshoot currents reduce quickly after two time-steps, which are indicated in (2.38) and stated in the summary point 5).

Fig. 2-40 (b) shows the case with both PM flux linkage and inductance mismatches. It can be seen that the current control errors in transient and steady states are roughly the combined effect of the inductance mismatch and the PM flux linkage mismatch as they are illustrated separately in Fig. 2-38 (b) and Fig. 2-39 (b), respectively. Hence, both overshoot currents in transient and large steady-state current errors are observed. Compared to the ideal performance of the proposed DBPCC as shown in Fig. 2-40 (a), with the parameters mismatches, the control performance of the proposed DBPCC will be significantly deteriorated in high speeds. This suggests that use of accurate parameters or employing compensation scheme for parameters mismatch are crucial for the DBPCC in high-speed applications with low SFRs.

2.3.4.2 *Inverter nonlinearity influence at various speeds*

Fig. 2-41 shows the simulation results with inverter nonlinearity at various speeds, where only the dead-time effect is included in the simulation model. As can be seen, the steady-state errors caused by the inverter nonlinearity are almost independent of the reference currents and speeds. Since the average voltage deviation due to the inverter nonlinearity in the d-axis is zero with i_d=0 control, there is no current offset in the d-axis. Moreover, the transient performance is not affected by the inverter nonlinearity. Hence, the above analysis and the summary points 3) and 4) on the inverter nonlinearity influence are validated by the results in Fig. 2-41. Additionally, it is worth mentioning that these offset errors in the q-axis current can be compensated by the speed closed-lopp control and hence will not be present in a PMSM drive with speed feedback control.

(a)   (b)
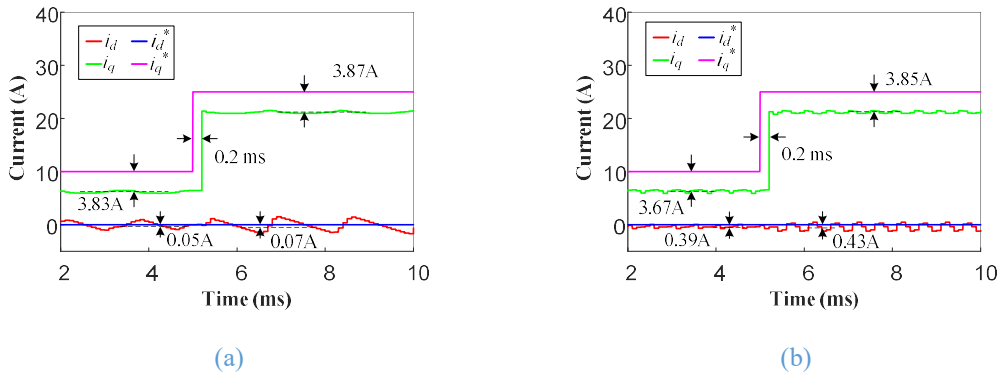
Fig. 2-41 Simulation results of sampled dq currents with t_{dd}=2us and f_{sw}=10kHz (a) at 10,000 rpm (SFR=30) (b) at 3,000 rpm (SFR=100)

2.3.6 Experiment Verification

In order to further validate the analysis and findings relating to the parametric mismatch and inverter nonlinearity, extensive experiments have been performed on the prototype high-speed PMSM, which has already described in section 2.2.5.

Unlike in the simulation where the ideal inverter can be employed, the inverter nonlinearity always exists in the experiment testing. Hence, the influence of the inverter nonlinearity is firstly investigated. Fig. 2-42 (a) and (b) shows the experiment results at the low speed of 3 krpm with different deadtime setting and q axis current reference. As can be seen in Fig. 2-42 (a), the inverter nonlinearity only cause current error in the q axis current and the magnitude of error approximately increase linearly as the deadtime increases. It confirms the analysis and simulation results. In addition, as can be observed from Fig. 2-42 (b), when the load current is larger than 20 A, the current control error

caused by inverter nonlinearity is almost constant, while at light load current the error is relative small. It can be attributed to the parasitic voltage drop property of the used IBGT, which has the same variation as the load current.

(a)   (b)
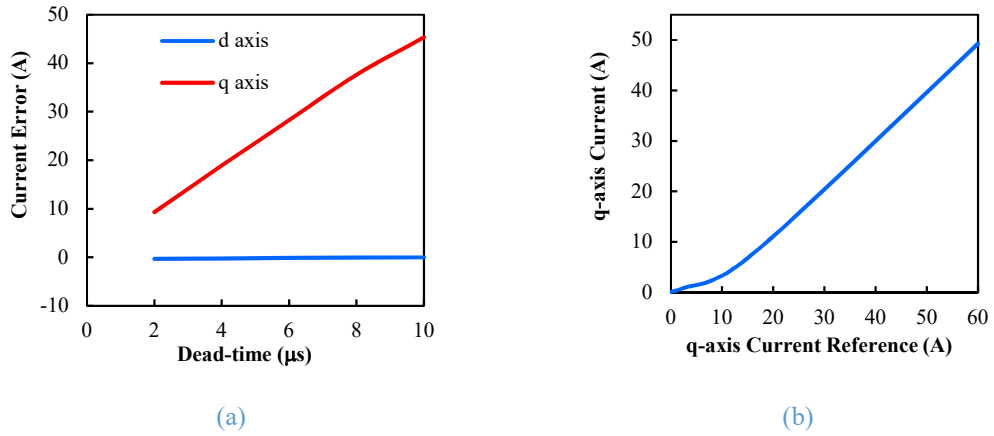
Fig. 2-42 Experiment results of inverter nonlinearity influences under different dead-times and q axis current references. (a) Average current error versus dead-time with q axis current of 50 A. (b) Actual average q-axis current versus q axis current reference with the deadtime of 2 us.

Fig. 2-43 (a) shows the dq axis currents with the q axis current of 25 A and d axis current of 0 A, when the machine speed varies from 1 krpm to 30 krpm. According to the low speed test, i.e. Fig. 2-42 (b), the q axis current with the reference of 25 A is 15.7A. As the speed varies, the dq axis currents can be predicted unchanged based on the previous analysis. Therefore, the test results verify the current control caused by the inverter nonlinearity is almost independent of the speed.

Further, the experiments with parametric mismatch have been performed at various speeds. Fig. 2-43 (b) shows the results with 50% over-estimation of phase resistance and it confirms that the resistance error is less influential in high-speed drives. The results with PM flux linkage and inductance mismatch are shown in Fig. 2-43 (c) to (f). As can be seen, at very low speed, the dq axis currents are almost identical to that with accurate parameters in Fig. 2-43 (a). It confirms that the current control accuracy is less affected by parameter mismatch at low speeds. However, as the speed rises, the current the current error increases. The predicted dq axis current by the derived equation, (2.47) are also plotted. Relative large errors can be observed in Fig. 2-43 (d) and (f), it is because in the prediction, the current error caused by the inverter nonlinearity is assumed constant as that with q axis current of 15.7 A. while when the load current decreases under parameter mismatch, the current error caused by inverter nonlinearity will also varies. However, in general, the experiment results can confirm the correctness of the previous analysis and the derived equation of steady-state current control error, i.e. (2.47).
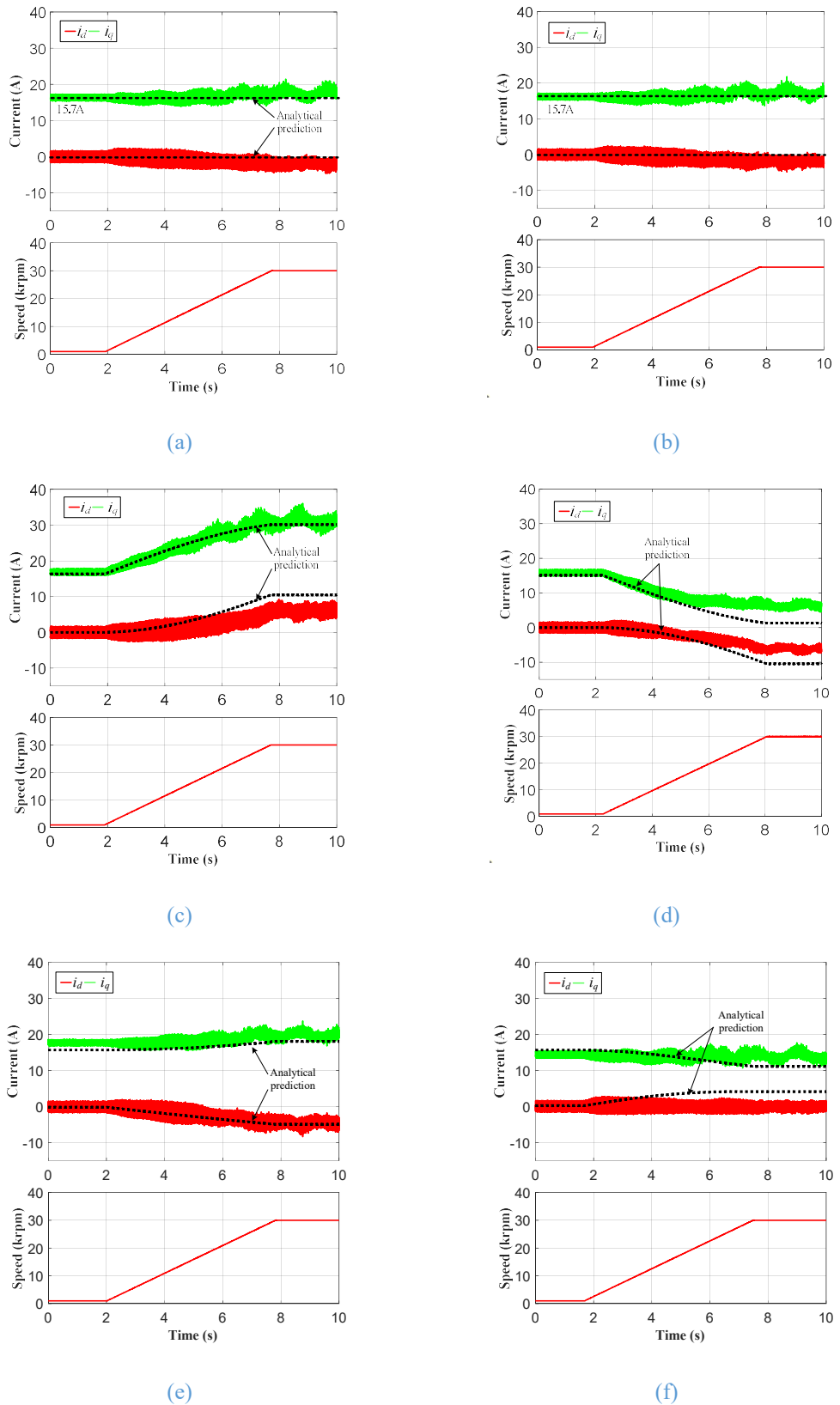
Fig. 2-43 dq axis currents at various speeds (1krpm~30krpm) with constant q-axis current reference (25A) and different machine parameter settings. (a) Accurate machine parameters. (b) 50% over-estimation of phase resistance. (c) 20% over-estimation of PM flux linkage. (d) 20% under-estimation of PM flux linkage. (c) 20% over-estimation of dq-axis inductances. (d) 20% under-estimation of dq-axis inductances.

The influence of inverter nonlinearity and parameter mismatch on the transient performance of proposed DBPCC are also evaluated by experiments. Fig. 2-44 (a), (b) and (c) shows the results at the low speed of 3 krpm with accurate machine parameter, detuned PM flux linkage and detuned inductance respectively. As can be seen, only the inductance mismatch will affect the transient control performance and over-estimation in the inductance will caused overshoot current in the transient.

(a)

(b)

(c)
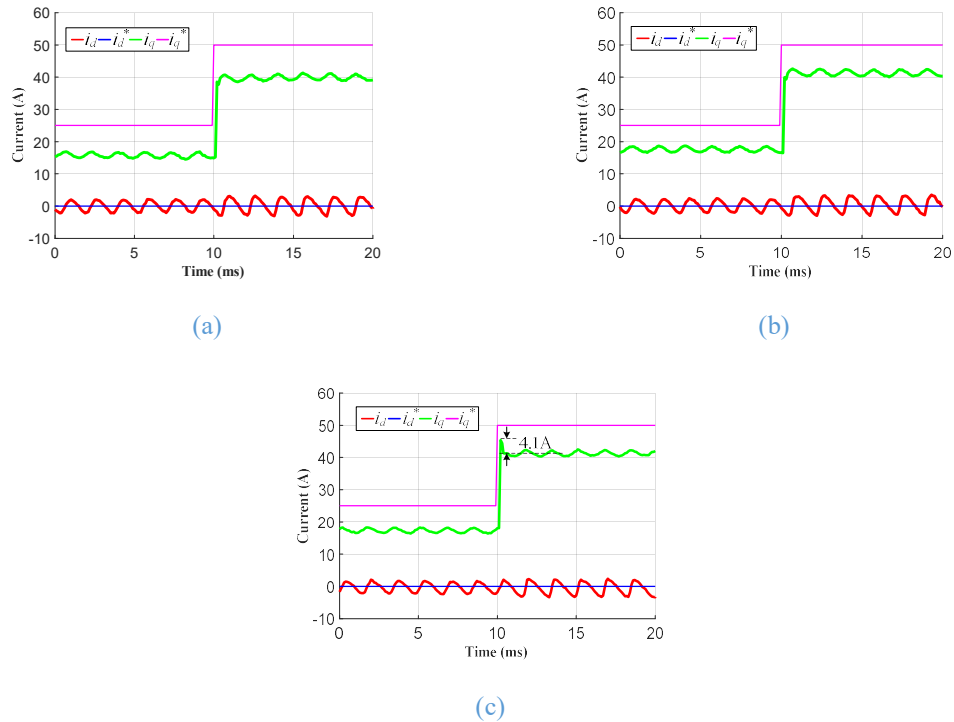
Fig. 2-44 dq axis currents during transients with different machine parameter settings at the low speed of 3krpm. (a) Accurate machine parameters. (b) 20% over-estimation of PM flux linkage. (c) 20% over-estimation of dq-axis inductances.
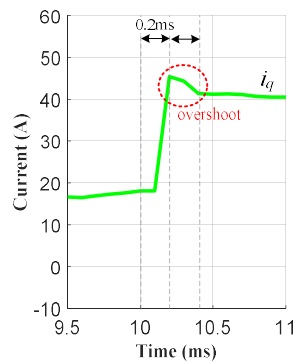
Fig. 2-45 Zoom-in view of the transient q axis current in Fig. 2-44 with 20% over-estimation of dq-axis inductances at 3krpm.

Fig. 2-45 shows the zoom-in view of the transient overshoot q axis current in Fig. 2-44 (c). It verifies the previous analysis that the transient current error caused by inductance mismatch can be effectively reduced after two time-steps, i.e. 0.2 ms in this

case. Fig. 2-46 shows the dq axis currents in the transient with less current step change than that in Fig. 2-44 (c). As expected, the overshoot q axis current reduces and it confirms the previous analysis.
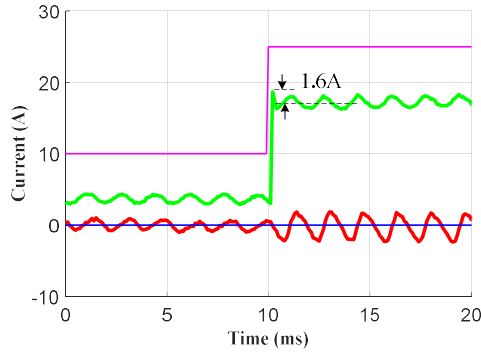
Fig. 2-46 dq axis current during the transient when the q-axis reference changes from 10 to 25A with 20% overestimation of the dq-axis inductances at 3krpm.

The same transient performance tests as Fig. 2-44 have also be performed at the high speed of 30 krpm. As can be seen, similar to the results obtained at the low speed, the inverter nonlinearity and PM flux linkage hardly affect the transient control performance. While it will be influenced by the inductance mismatch.

(a)

(b)

(c)
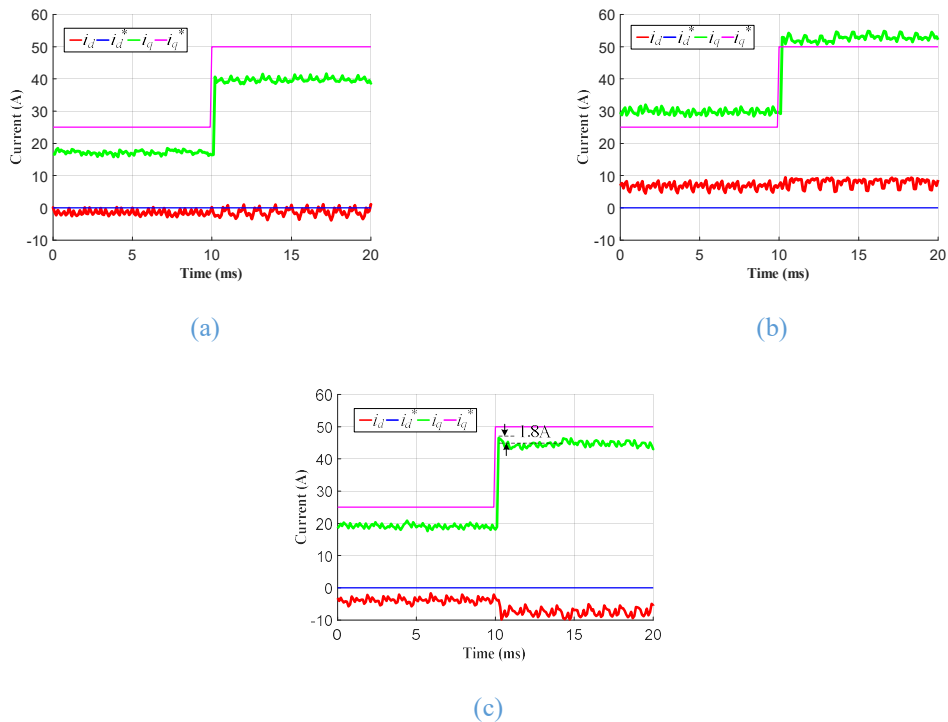
Fig. 2-47 dq axis currents during transients with different machine parameter settings at the high speed of 30 krpm. (a) Accurate machine parameters. (b) 20% over-estimation of PM flux linkage. (c) 20% over-estimation of dq-axis inductances.

2.4 Summary

In this chapter, the rotor movement influence on conventional DBPCCs are analysed analytically and evaluated quantitatively. The problem of conventional DBPCCs in high speeds have been demonstrated. In order to solve the problem caused by large rotor movement in high speeds, the stationary frame based DBPCC is proposed. The proposed method is not affected by the large rotor movement in high-speed and ideal deadbeat control can be achieved even with extreme low SFRs. Extensive simulations and experiments have been performed and verified the effectiveness of the proposed DBPCC.

On the other hand, rigorous analytical expressions of the steady-state current control error and transient current tracking error have been derived for the proposed DBPCC for high-speed PMSM drives. All the key influential factors have been considered, including the parameters mismatch, inverter nonlinearity, sampling frequency and speed. The accuracies of the derived analytical equations have been validated by substantial numerical simulations. The derived analytical equations can serve as a very powerful tool to analyse the parameters mismatch and inverter nonlinearity influence in various speeds. It suggests that with parametric mismatch, the current control error in steady states would increase greatly. The inverter nonlinearity would cause offset error in the q-axis current which is almost independent of speed. The transient performance will be mainly affected by inductance mismatch, resulting in transient overshot or undershoot currents. Extensive simulation and experiments on the prototype high-speed PMSM drives have been performed and confirmed the analysis of parameters mismatch and inverter nonlinearity influence on the proposed DBPCC.

CHAPTER 3
Performance Improvement of Stationary Frame Based Deadbeat Predictive Current Control

3.1 Introduction

As analysed and demonstrated in Section 2.3, the control performance of DBPCC is dependent on the accuracy of the motor parameters and influenced by the inverter nonlinearity. According to the findings established in Section 2.3, the influence of the parameter mismatch on the current control accuracy becomes more significant as the motor speed increases. Therefore, to guarantee the control performance of high-speed PMSM drives with DBPCC, exact motor parameters including inductance and PM flux linkage should be known. However, the actual machine parameters, which relate to operation conditions such as temperature and load current, can hardly be acquired exactly in real applications. It is of great importance to improve the robustness of DBPCC against the parameter mismatch, namely, to mitigate the current control error in the presence of parameter mismatch. Moreover, the inverter nonlinearity would cause an average current offset along the q-axis. Although generally it is true that the effect of the inverter nonlinearity becomes relatively small in high speeds, in scenarios with light loads, the offset error in the current caused by the inverter nonlinearity still accounts for large portion of the total and still needs to be addressed. Thus, in this section, a novel current control error compensation for the proposed DBPCC in high-speed PMSM drives is developed against the parameter mismatch and inverter nonlinearity.

Furthermore, to reduce the current harmonic distortions caused by inverter nonlinearity and non-sinusoidal back EMF and to improve the transient performance under inductance mismatch, two novel methods are proposed for the DBPCC as well.

3.2 Current Error Compensation Based on Adaptive Reference Correcting Current Injection

In this section, a novel current control error compensation for high-speed PMSM drives with the proposed DBPCC is developed. The proposed method is based on injecting correcting components in to the reference *dq* axis current of the DBPCC, named as reference correcting currents (RCCs). An adaptive scheme based on the gradient descend algorithm is also designed to determine the required RCCs, which minimizes the

current control error in real-time. With the proposed adaptive RCC injection (ARCCI) method, the control performance of the DBPCC, more specifically the current control error in steady states, becomes independent of parameter mismatch and inverter nonlinearity in the whole speed range. Furthermore, the implementation of proposed ARCCI is very simple and can be readily integrated to the proposed DBPCC.

The rest of this subsection is arranged as follows. Firstly, the principle of injecting RCCs to compensate the current control error is introduced. Secondly, the proposed adaptive RCC injection or ARCCI scheme is presented, after which the implementation of the DBPCC with the proposed ARCCI is elaborated. Finally, extensive simulation and experiment results validate the effectiveness of the proposed method.

3.2.1 Principle of Current Error Compensation by Reference Correcting Current Injection

According to section 2.3, the parameters mismatch and inverter nonlinearity will give rise to large current control error in steady states in high speeds. In transients, overshoot would occur only with incorrect inductance, but it can be reduced by the DBPCC quickly in two time-steps. Moreover, generally for a given percentage of mismatch, the inductance mismatch causes less steady-state error than that with the PM flux linkage mismatch. Thus the current tracking error in transients is not dealt with in this section and only the steady-state current control error is addressed.

According to the analytical expression (2.49) of the steady-state dq axis currents which result with the DBPCC, the actual currents will not be equal to the reference currents with parameters mismatch and inverter nonlinearity. The concept of the proposed steady-state current control error compensation is to inject two correcting components, referred to as reference correcting currents (RCCs), denoted as $COMP_d$ and $COMP_q$ into the original d-axis and q-axis current references, $i_d{}^*$ and $i_q{}^*$ to obtain new reference currents, $i_d{}^{**}$ and $i_q{}^{**}$ as expressed in (3.1). These modified references will be fed to the proposed DBPCC as its reference inputs.

$$\begin{aligned} i_d{}^{**} &= i_d{}^* + COMP_d \\ i_q{}^{**} &= i_q{}^* + COMP_q \end{aligned} \tag{3.1}$$

Therefore, the steady-state current originally represented in (2.49) will be altered to

$$\begin{cases} i_d = \lambda_{L1} \cdot (i_d^* + COMP_d) + \lambda_{L2} \cdot (i_q^* + COMP_q) + \lambda_{\psi 1} + \lambda_{inv1} \\ i_q = \lambda_{L1} \cdot (i_q^* + COMP_q) - \lambda_{L2} \cdot (i_d^* + COMP_d) + \lambda_{\psi 2} + \lambda_{inv2} \end{cases} \quad (3.2)$$

To nullify the current control error, the desired RCCs can be readily solved as given in

$$\begin{cases} COMP_d^* = A \cdot i_d^* + B \cdot i_q^* + C \\ COMP_q^* = A \cdot i_q^* + B \cdot i_d^* + D \end{cases} \quad (3.3)$$

where the coefficients are

$$A = \frac{\left(\lambda_{L1} - \lambda_{L1}^2 - \lambda_{L2}^2\right)}{\lambda_{L1}^2 + \lambda_{L2}^2}$$

$$B = -\frac{\lambda_{L2}}{\lambda_{L1}^2 + \lambda_{L2}^2} \quad (3.4)$$

$$C = -\lambda_{L1}\lambda_{\psi 1} + \lambda_{L2}\lambda_{\psi 2} - \lambda_{L1}\lambda_{inv1} + \lambda_{L2}\lambda_{inv2}$$

$$D = -\lambda_{L2}\lambda_{\psi 1} - \lambda_{L1}\lambda_{\psi 2} - \lambda_{L2}\lambda_{inv1} - \lambda_{L1}\lambda_{inv2}$$

Injecting the desired RCCs in to the original reference currents, namely substituting (3.3) into (3.2), will ultimately lead to $\boldsymbol{i}_{dq} = \boldsymbol{i}_{dq}^*$ regardless of the parameters mismatch and inverter nonlinearity, which indicates the current control error is eliminated and the control performance of the DBPCC with the desired RCCs is parameter independent. It is worth noting that the analytical expression (3.2) only considers the average current, therefore, in this section zero current control error only refers to zero average error. Indeed, the instantaneous current control error would not be zero as ripples caused by high order harmonics in the back-emf and inverter nonlinearity exist in the currents.

According to the expressions in (3.4) derived from (2.50), the coefficients A, B, C, D are all constant in steady states. Particularly, when the inductance estimation error is zero, A=B=0, which indicates that with accurate inductance, the desired injected RCC is not affected by the reference currents. It can be attributed to the fact that average steady state errors due to the PM flux mismatch and inverter nonlinearity are independent of the reference currents. However, if an inductance mismatch exists, the desired RCC is dependent on dq axis reference currents. In addition, the coefficients in (3.4), (2.50) and (2.51) cannot be computed unless the real parameters are known, which is not the case in

practice. Hence, an online adaptive scheme for the injected RCCs is proposed in next subsection.

3.2.2 Adaptive Reference Correcting Current Injection

An adaptive scheme is designed to generate the desired RCCs in real time which minimizes the current control error.

The objective function to minimize the current control can be defined as

$$J = \frac{1}{2}\left(\boldsymbol{i}_{dq}{}^* - \boldsymbol{i}_{dq}\right)^2 = \frac{1}{2}e_{id}^2 + \frac{1}{2}e_{iq}^2 \tag{3.5}$$

where e_{id}, e_{iq} are the sampled current errors in the d- axis and q-axis respectively.

Substituting $COMP_d{}^*$, $COMP_q{}^*$ into (3.2) yields $\boldsymbol{i}_{dq}{}^*$ and together with (3.2) the current errors can be expressed as

$$e_{id} = \lambda_{L1}\Delta COMP_d + \lambda_{L2}\Delta COMP_q \tag{3.6}$$

$$e_{id} = \lambda_{L1}\Delta COMP_q - \lambda_{L2}\Delta COMP_d \tag{3.7}$$

where,

$$\Delta COMP_d = COMP_d{}^* - COMP_d \tag{3.8}$$

$$\Delta COMP_q = COMP_q{}^* - COMP_q \tag{3.9}$$

Computing the gradient vector of the objective function, J with respect to $COMP_d$ and $COMP_q$ respectively and combining (3.6) ~ (3.9) gives

$$\nabla J_1 = \frac{\partial J}{\partial COMP_d} = -\lambda_{L1}e_{id} \tag{3.10}$$

$$\nabla J_2 = \frac{\partial J}{\partial COMP_q} = -\lambda_{L1}e_{iq} \tag{3.11}$$

According to the gradient descent updating rule, the injected RCC magnitudes, $COMP_d$ and $COMP_q$ are determined by

$$COMP_d(k+1) = COMP_d(k) - \eta\nabla J_1 \tag{3.12}$$

$$COMP_q(k+1) = COMP_q(k) - \eta \nabla J_2 \tag{3.13}$$

where η is the adaptive gain.

According to the expression of λ_{L1} in (2.50) and (2.51), it equals to 1 with accurate inductance and deviates from 1 if the estimated inductance is not equal to the actual. However, it is constant or varies slowly in an inductance mismatch. Therefore, λ_{L1} in the gradient expressions, (3.10) and (3.11), can be approximated as 1. By substituting (3.10), (3.11) into (3.12) and (3.13), the adaptation law is finally derived:

$$COMP_d(k+1) = COMP_d(k) + \eta e_{id}(k) \tag{3.14}$$

$$COMP_q(k+1) = COMP_q(k) + \eta e_{id}(k) \tag{3.15}$$

It has been well known that with large adaptive gain, the adaptation process will be fast, and the current errors can be quickly eliminated. However, if the gain is too high, the transient current control errors may lead to oscillations and large steady state current ripples. Therefore, taking both the convergence speed and steady-state performance into consideration, the adaptive gain, η is selected in the range from 0.005 to 0.05 for the applications in this chapter. Moreover, due to the two time-step delay of the DBPCC, the present current actually corresponds to the reference two time-steps before, thus the dq axis current error, $e_{idq}(e_{id}, e_{iq})$, should be calculated according to the difference between the reference at step k-2 and the present current as

$$e_{idq}(k) = i_{dq}^*(k) \cdot z^{-2} - i_{dq}(k) \tag{3.16}$$

Equations (3.14) and (3.15) determine the injected reference correcting current magnitude in the d-axis and q-axis respectively. Because the injected RCC magnitudes are being updated to minimize the objective function J, which corresponds to the current control error, the adaptive injection of RCC eliminates the current control error in steady states. Again, it is worth noting that the actual instantaneous current error would not be zero due to presence of current ripples, however the average control errors of dq axis currents would exhibit zero error with the proposed adaptive RCC injection (ARCCI) methods.

Additionally, as can be found from the form of (3.14) and (3.15) , the injected RCC magnitudes can be alternatively generated by an integrator with the dq axis current errors as input, namely

$$\boldsymbol{COMP}_{dq}(k) = \frac{K_i T_s}{1 - z^{-1}} \cdot \boldsymbol{e}_{idq}(k) \tag{3.17}$$

where K_i is the integral gain, T_s is the sampling time-step and the corresponding adaptive gain for minimising the objective function, J, is

$$\eta_i = K_i T_s \tag{3.18}$$

When the compensation is implemented in this manner, the integral gain should be set according to the employed sampling frequency to guarantee an appropriate adaptive gain. The simple integration of the current error works can be intuitively understood by the fact that the desired RCCs as expressed in (3.15) are constants in steady states. However, the underpinning principle for the effectiveness of the simple integrator is based on gradient descent of the objection function, J as described above.

Additionally, the current control errors under parameters mismatch and inverter nonlinearity are actually caused by the two predictions of the DBPCC, including one-step current and flux prediction and one-step reference voltage calculation. Since the steady state current error caused by the two predictions are reflected in the sampled currents, which are used as the adaptive gradients, the proposed ARCCI current error compensation scheme is effective even though the next step current and flux are not predicted correctly in the DBPCC when parameter mismatches and inverter nonlinearity exist.

3.2.3 Implementation of Proposed Method

Fig. 3-1 illustrates the simplified block diagram of the proposed ARCCI method with current error minimised in the PMSM drive with the DBPCC. In each step, the dq axis currents are sampled and fed into the ARCCI block, in which the injected RCCs are obtained according to (3.14) and (3.15) and added in to the original reference currents to form the reference inputs to the DBPCC controller.

Fig. 3-2 shows the complete block diagram of the proposed DBPCC with the developed current error compensation strategy, namely ARCCI. The proposed ARCCI mechanism in the figure is alternatively presented in the integrator form, which is equivalent to the one depicted in Fig. 3-1 and the integral gain is set with due consideration of the associated adaptive gain. The stationary frame-based DBPCC is employed here since it is insensitive to the rotor movement and has more robust performance than the conventional synchronous frame-based DBPCC at high speeds.
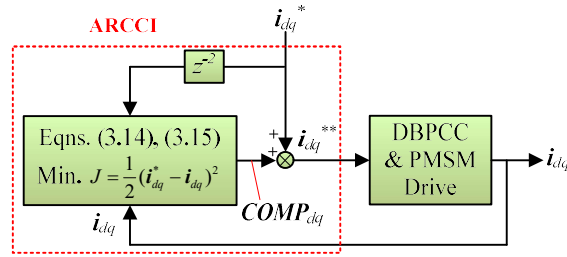
Fig. 3-1 Simplified block diagram of proposed ARCCI method with current error minimized in the PMSM drive with DBPCC
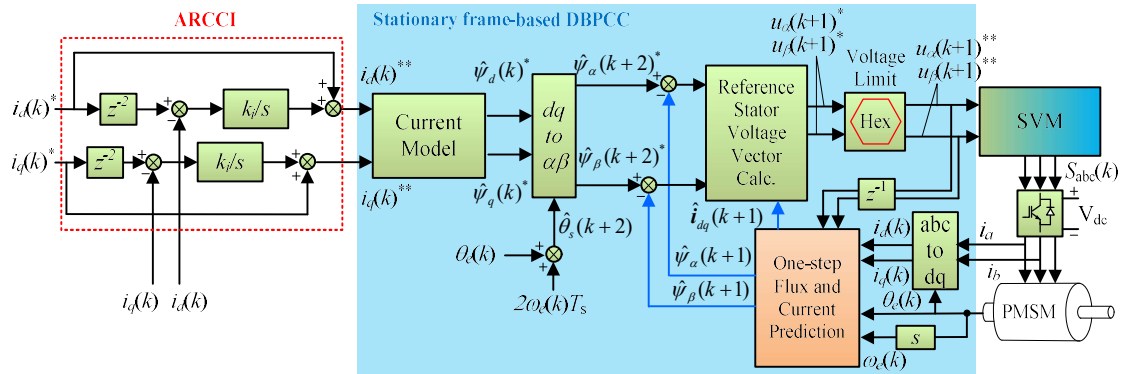
Fig. 3-2 Complete block diagram of stationary frame-based DBPCC with the proposed current error compensation strategy, ARCCI in the form of integrator

3.2.4 Simulation Study and Discussion of Results

Extensive simulations have been performed to study the effectiveness of the developed current control error compensation method. The same prototype high-speed PM machine described in section 2.2.4 is used. The adaptive gain, η, in the proposed method is set to 0.04.

3.2.4.1 *Effectiveness of the proposed method under parameters mismatch and inverter nonlinearity*

Fig. 3-3 ~ Fig. 3-5 show the simulation results without and with the proposed ARCCI at the speed of 10,000 rpm, where the associated SFR is 15 and the q-axis current reference steps from 10 A to 25A at 5 ms. As can be seen in Fig. 3-3 (a), Fig. 3-4 (a) and Fig. 3-5 (b), without current error compensation, the PM flux linkage mismatch, inductance mismatch, and inverter nonlinearity will all cause steady state errors in the dq axis current, especially when the PM flux linkage is estimated incorrectly. However, when the proposed method, ARCCI, is employed, all the steady-state current errors can be eliminated effectively as shown in Fig. 3-3 (b), Fig. 3-4 (b) and Fig. 3-5 (b). Moreover,

the fast dynamic response of the DBPCC is maintained with the proposed method. As shown in Fig. 3-3 (b) and Fig. 3-5 (b), the current reference variations can be tracked with only two time-step delay under the PM flux linkage mismatch and inverter nonlinearity. As can be observed in Fig. 3-4 (b), the overshoot current caused by inductance mismatch can still be reduced greatly in two time-steps and the subsequent residual current errors are the uncompensated current error caused by reference change with the inductance mismatch. It can be removed with the proposed ARCCI. The rate of the error reduction is determined by the adaptive gain.

(a)   (b)
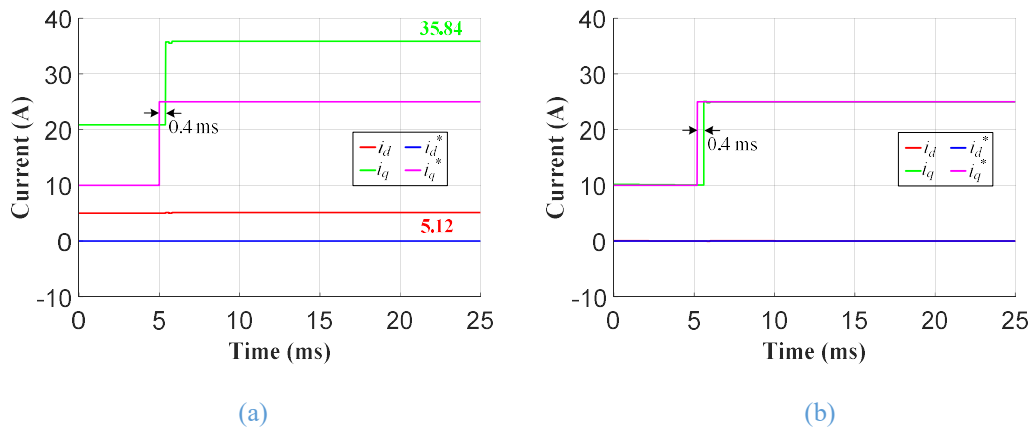
Fig. 3-3 Sampled dq axis currents at 10,000 rpm (f_{sp}=5 kHz, SFR=15) only with PM flux linkage parameter mismatch (1.2ψ_m) (a) without compensation (b) with proposed ARCCI

(a)   (b)
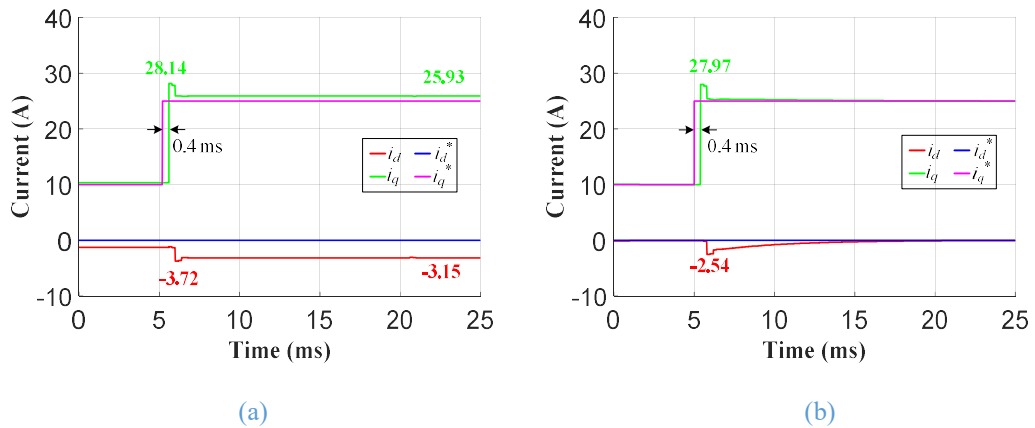
Fig. 3-4 Sampled dq axis currents at 10,000 rpm (f_{sp}=5 kHz, SFR=15) only with inductance parameter mismatch (1.2L_s) (a) without compensation (b) with proposed ARCCI

(a)   (b)
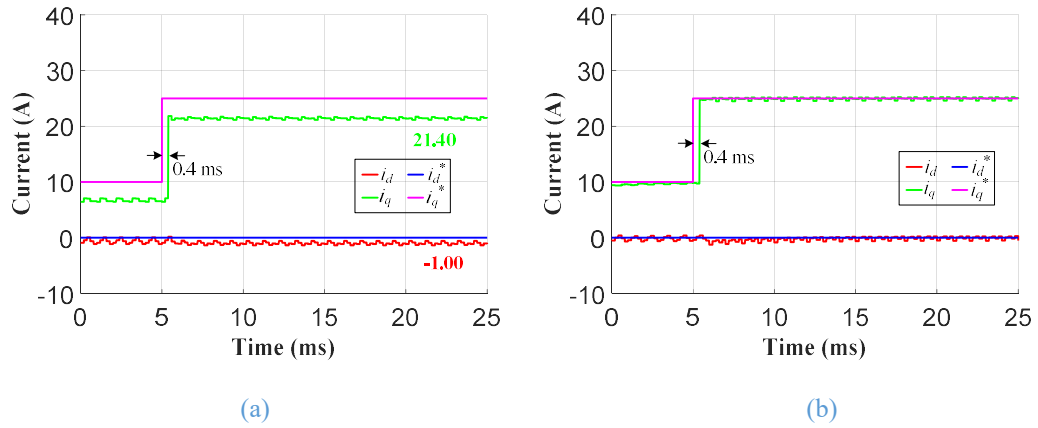
Fig. 3-5 Sampled dq axis currents at 10,000 rpm (f_{sp}=5 kHz, SFR=15) with accurate parameters and inverter nonlinearity (t_{dd} = 2 us) (a) without compensation (b) with proposed ARCCI

Fig. 3-6 compares the results without and with the proposed method when both parameters are estimated incorrectly and the dead-time is present. The q-axis reference is changed from 10 A to 25 A at 5 ms. It can be seen that the proposed method can eliminate all the current control errors in steady states and the transient performance of the DBPCC is maintained albeit there are the short overshoot and undershoot caused by the inductance mismatch. Fig. 3-8 (a) shows the injected RCCs associated with Fig. 3-6 (b) employing the proposed ARCCI. As can be observed, the d-axis and q-axis RCCs are injected into the original reference currents and they change adaptively when the current error varies following the step change in the reference currents with inductance mismatch. As shown in Fig. 3-7, the proposed method is also effective at low speed. Fig. 3-8 (b) shows the injected RCCs at low speed. According to the findings in section 2.3, when the SFR is high at low speed, the steady-state current errors are mainly caused by inverter nonlinearity and independent of the reference currents. Hence, the injected RCCs at low speed does not vary much after the reference current changes. This is different from that shown in Fig. 3-8 (a) at high speed.

Based on the results in Fig. 3-3 ~ Fig. 3-7, it can be concluded that the proposed ARCCI can compensate all the current errors caused by parameters mismatch and inverter nonlinearity at both low and high speeds. As a result, the proposed DBPCC with ARCCI can be regarded as parameter independent since the current control accuracy is not affected by the machine parameters employed in the predictions. It is worth noting that the transient tracking errors i.e. overshoot and undershoot caused by inductance mismatch in transients still exist with the proposed method, however, they are reduced greatly in two time-steps and can be effectively limited by reducing the reference change step, as discussed in section 2.3.

(a)

(b)

(c)

(d)
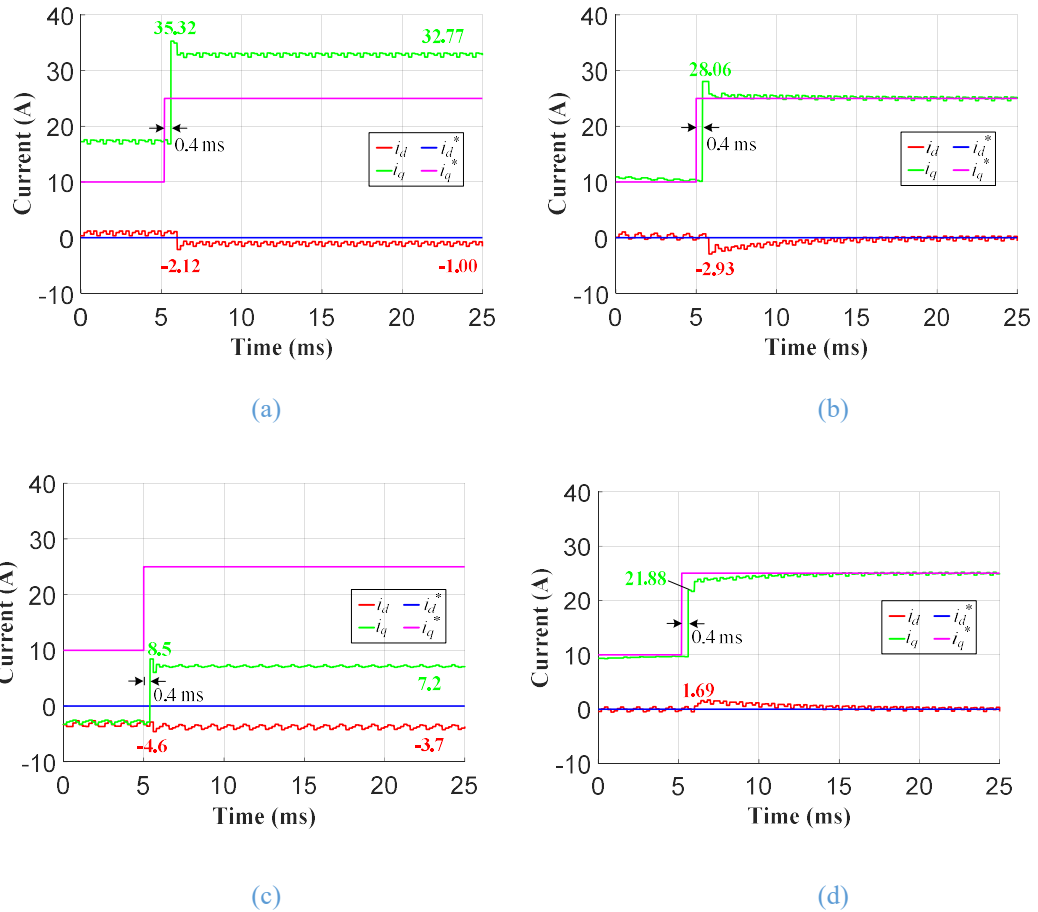
Fig. 3-6 Sampled dq axis currents at 10,000 rpm (fsp=5 kHz, SFR=15) with inaccurate parameters and inverter nonlinearity (a) parametric over-estimation (1.2ψ_m, 1.2L_s, t_{dd} = 2 us), without compensation (b) parametric over-estimation (1.2ψ_m, 1.2L_s, t_{dd} = 2 us), with proposed ARCCI (c) parametric under-estimation (0.8ψ_m, 0.8L_s, t_{dd} = 2 us), without compensation (d) parametric under-estimation (0.8ψ_m, 0.8L_s, t_{dd} = 2 us), with proposed ARCCI

(a)

(b)
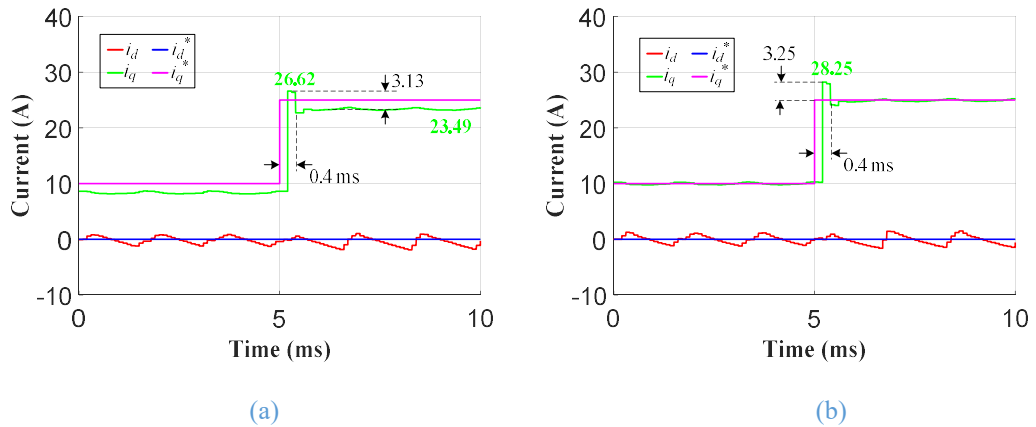
Fig. 3-7 Sampled dq axis currents at 3,000 rpm (f_{sp}=10 kHz, SFR=100) with inaccurate parameters and inverter nonlinearity (1.2ψ_m, 1.2L_s, t_{dd} = 2 us) (a) without compensation (b) with proposed ARCCI

95

(a)   (b)
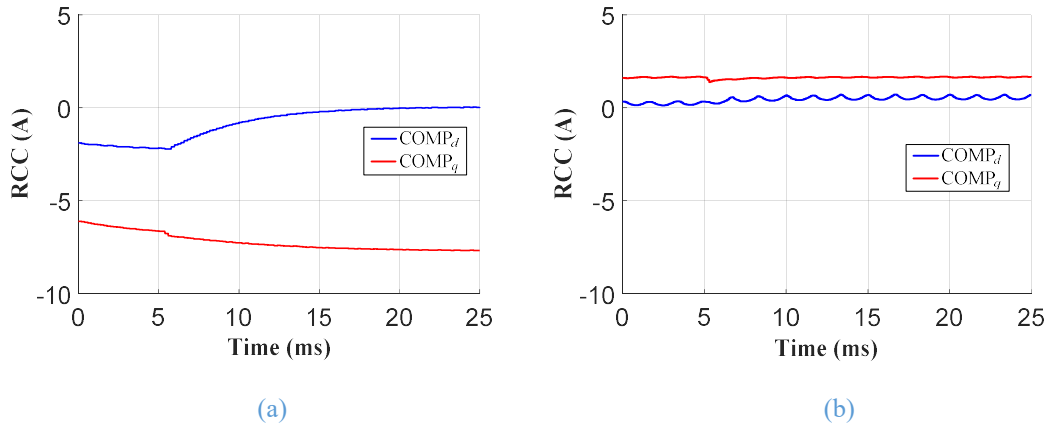
Fig. 3-8 Injected reference correcting currents in the dq axis under parameters mismatch and inverter nonlinearity (1.2ψ_m, 1.2L_s, t_{dd} = 2 us) (a) at 10,000 rpm (f_{sp}=5 kHz, SFR=15) (b) at 3,000 rpm (f_{sp}=10 kHz, SFR=100)

3.2.4.2 *Performance comparison between proposed DBPCC with ARCCI and FOC*

In order to compare the performance of the proposed DBPCC with ARCCI and the conventional FOC, the simulations employing FOC with feedforward decoupling and delay compensation are performed as well. Fig. 3-9 (a)~(c) shows the results with FOC at high speed of 10,000 rpm (SFR=15), with accurate parameters, 20% over-estimated and 20% under-estimated parameters, respectively, which correspond to those in Fig. 3-5 (b), Fig. 3-6 (b) and (d), respectively. By comparing the results, it is evident that the proposed DBPCC with ARCCI has superior transient performance, less cross-coupling between the d-axis and q-axis currents, smaller overshoot currents, no oscillation and faster tracking response.

Fig. 3-9 (d) shows the results with the FOC at low speed of 3,000 rpm with 20% over-estimated parameters. Compared with that shown in Fig. 3-9 (b) under the same condition at high speed, the current control performance is less sensitive to the parameter mismatch and much better with no cross-coupling effect in the d-axis current and the q-axis current being tracked in 0.8ms. However, compared to the result obtained in the same condition using the proposed DBPCC with ARCCI in Fig. 3-7, the proposed DBPCC has faster dynamic response, The references are met in only four time-steps i.e. 0.4 ms including the two time-steps for overshoot current reduction. Therefore, considering the performance over the whole speed range, it can be concluded that the proposed DBPCC with ARCCI excels in transient performance over the conventional FOC.
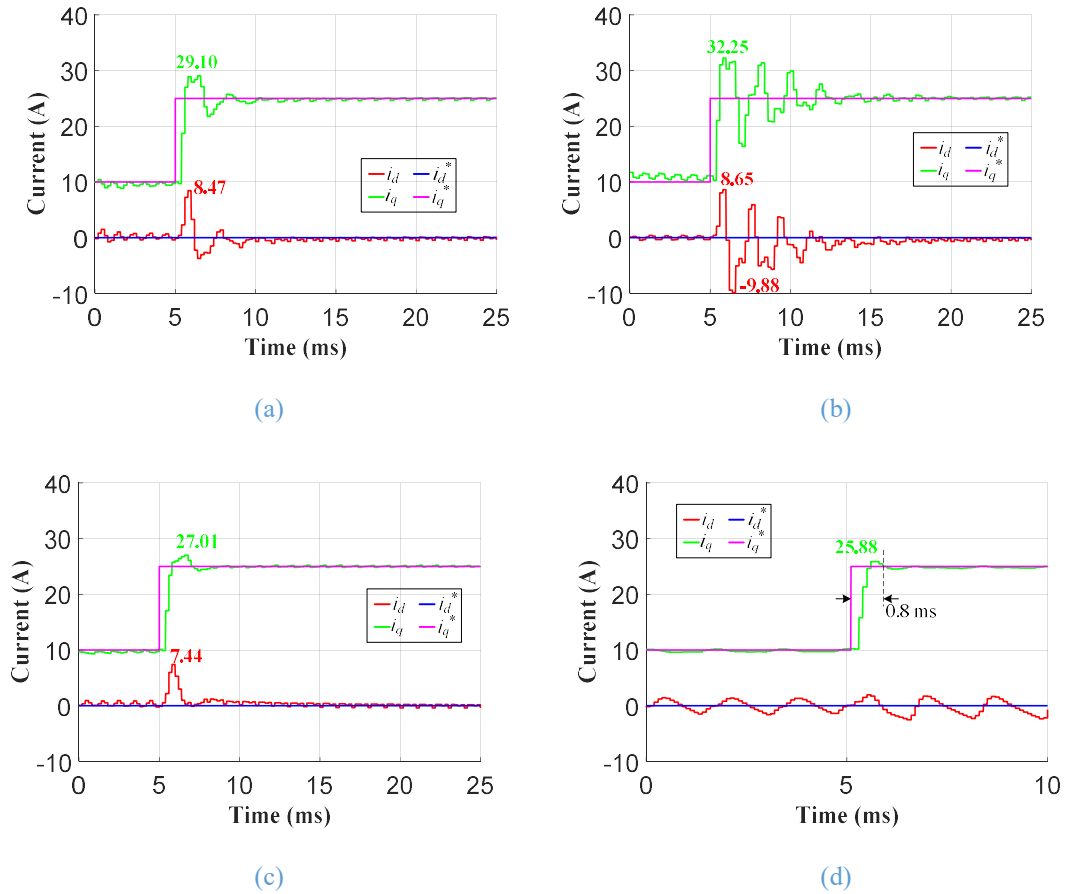
Fig. 3-9 Sampled dq axis current under inverter nonlinearity (t_{dd} = 2 us) using connectional FOC with current bandwidth of 500 Hz, at 10,000 rpm (f_{sp}=5 kHz, SFR=15) (a) accurate parameters (b) parametric over-estimation (1.2 ψ_m, 1.2L_s) (c) parametric under-estimation (0.8 ψ_m, 0.8L_s) (d) at 3,000 rpm (f_{sp}=10 kHz, SFR=100), parametric over-estimation (1.2 ψ_m, 1.2L_s)

3.2.4.3 Steady-state performance of proposed DBPCC with ARCCI

Fig. 3-10 and Fig. 3-11 shows the phase current and their spectrum when the proposed DBPCC with ARCCI and FOC are applied separately to the drive at high speed and low speed with q-axis current reference of 25 A. As can be seen, the proposed DBPCC with ARCCI has similar steady state current waveforms as those with the FOC. However, by comparing the current spectra, the proposed DBPCC with ARCCI exhibits lower 5th and 7th current harmonics in low speeds, which can be attributed to its better current control bandwidth. Hence, the proposed DBPCC with ARCCI also has better steady-state performance than the FOC.

(a)   (b)
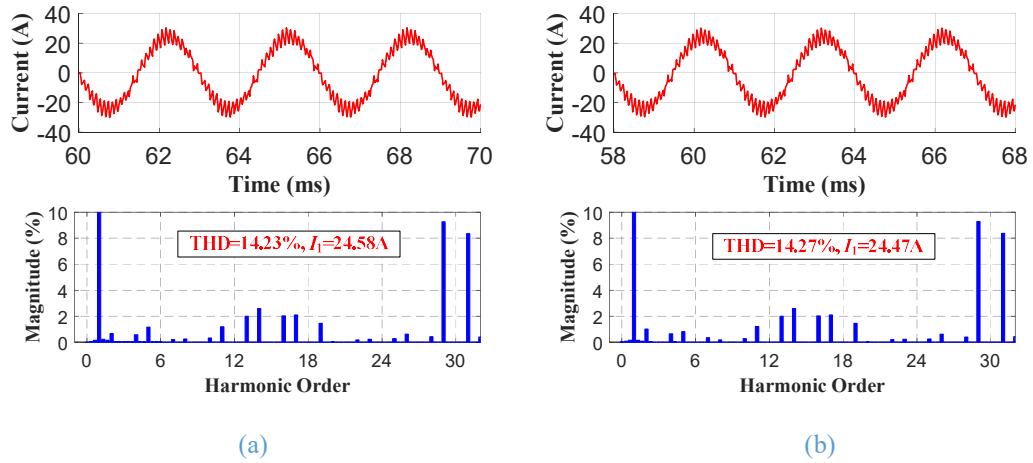
Fig. 3-10 Phase current and its spectrum at 10,000 rpm (SFR=15) with parameters under-mismatch and inverter nonlinearity (1.2 ψ_m, 1.2L_s, t_{dd} = 2 us) (a) with proposed ARCCI (b) with FOC

(a)   (b)
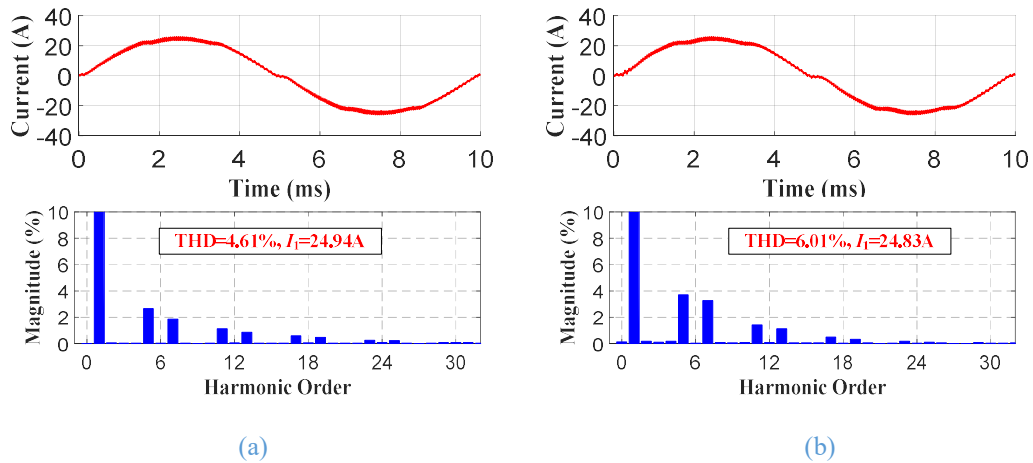
Fig. 3-11 Phase current and its spectrum at 3,000 rpm (SFR=100) with parameters under-mismatch and inverter nonlinearity (1.2 ψ_m, 1.2L_s, t_{dd} = 2 us) (a) with proposed ARCCI (b) with FOC

3.2.5 Experiment Verification

Extensive experiments have been performed to validate the effectiveness of the proposed method. The same test rig described in chapter 2 is used. In the experiments, the speed of the prototype high-speed machine is controlled by the dyno and the current control of the prototype high-speed machine is tested. The switching/sampling frequency is set to 10 kHz, the dead-time in the IGBT inverter is 2 μs, and the DC voltage is 270 V. The adaptive gain in the proposed method, η, is also set to 0.04 in the experiments.

Fig. 3-12 (a) shows the dq axis currents at the low speed of 3,000 rpm (SFR=100) with the dead-time of 2 μs and calibrated parameters. It can be seen that when the ARCCI is not applied, a steady-state current control error of ~10 A, mainly caused by the inverter

nonlinearity, exists in the q-axis current. However, when the ARCCI is activated, as shown in Fig. 3-12 (b), the current control error has been effectively compensated.

Fig. 3-13 (a) shows the dq axis currents at the low speed of 3,000 rpm (SFR=100) with the dead-time of 2 μs and inaccurate parameters deliberately introduced in the prediction model. Compared with Fig. 3-12 (a), the parametric mismatch causes an increase in the q-axis current by ~2 A. The current control error appears to be slightly reduced. As shown in Fig. 3-13 (b), when the proposed ARCCI is applied, the current errors caused by the parameters mismatch and inverter nonlinearity have been eliminated.

(a)   (b)
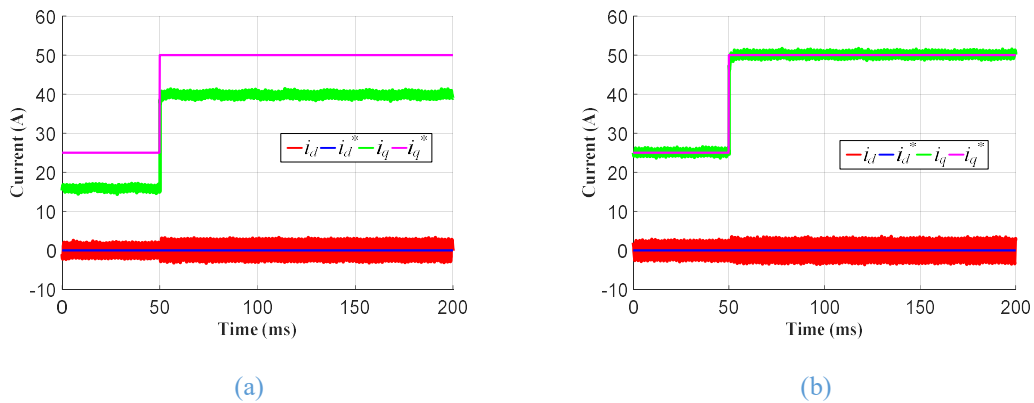
Fig. 3-12 Experiment results of dq axis currents at the low speed of 3,000 rpm (SFR=100) with accurate parameters and dead-time of 2 us (a) without proposed method (b) with proposed ARCCI. Green/purple: sampled/reference q-axis current, red/blue: sampled/reference d-axis current.

(a)   (b)
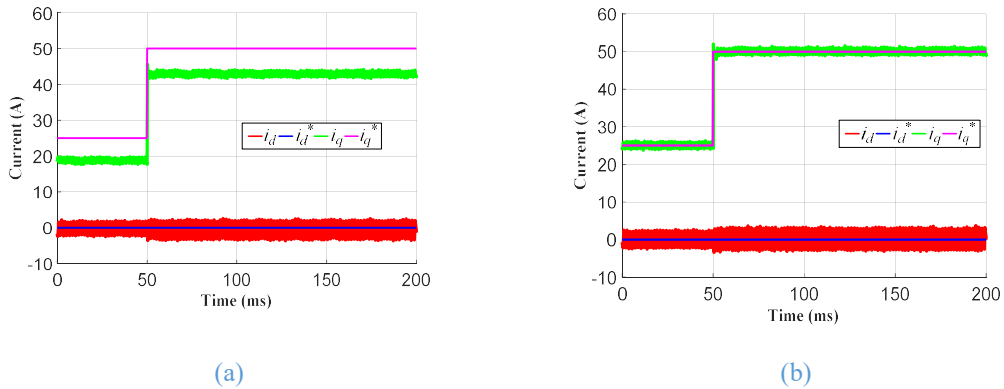
Fig. 3-13 Experiment results of dq axis currents at the low speed of 3,000 rpm (SFR=100) with inaccurate parameters ($1.2\psi_m$, $1.2L_s$, $0.5R_s$) and dead-time of 2 us (a) without proposed method (b) with proposed ARCCI. Green/purple: sampled/reference q-axis current, red/blue: sampled/reference d-axis current.

Fig. 3-14 shows the results at the high speeds of 30,000 rpm (SFR=10) without and with deliberate parametric mismatch but the proposed ARCCI is applied. As can be seen in Fig. 3-14 (a), the current errors of ~10A due to the inverter nonlinearity are similar to that seen in the low speed. However, the current control error due to the parametric mismatch increases at the high speed in Fig. 3-14 (b), compared with that at the low speed

in Fig. 3-12 (a). However, as shown in Fig. 3-15 (a), when the proposed compensation method is activated, it can effectively reduce all the current errors caused by the parametric mismatch and inverter nonlinearity.

(a)   (b)
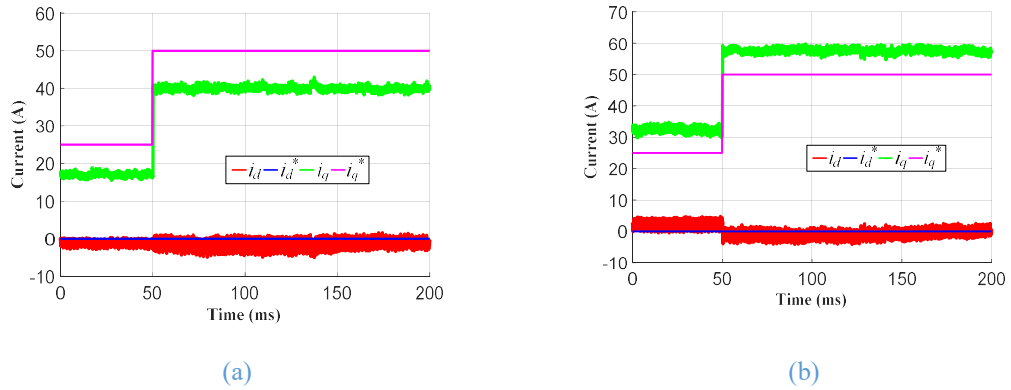
Fig. 3-14 Experiment results of dq axis currents at the high speed of 30,000 rpm (SFR=10) with dead-time of 2 us and (a) accurate parameters (b) inaccurate parameters (1.2ψ_m, 1.2L_s, 0.5R_s). Green/purple: sampled/reference q-axis current, red/blue: sampled/reference d-axis current.

(a)   (b)
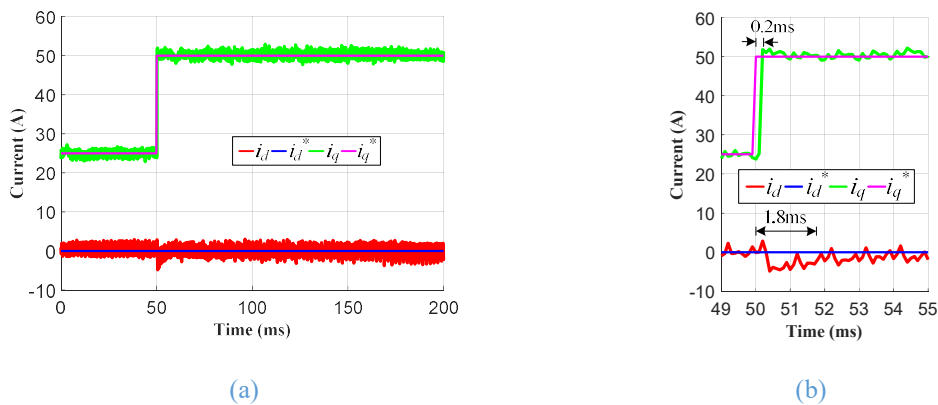
Fig. 3-15 Experiment results of dq axis currents at the high speed of 30,000 rpm (SFR=10) with dead-time of 2 us and inaccurate parameters (1.2ψ_m, 1.2L_s, 0.5R_s) using the proposed method (a) the waveform in transient and steady states (b) the waveform in the transient. Green/purple: sampled/reference q-axis current, red/blue: sampled/reference d-axis current.

Fig. 3-16 shows the experiment results using the conventional FOC with the same parametric mismatch at the high speed of 30,000 rpm. As can be seen, since the SFR is very low, the control performance of FOC deteriorates greatly. By comparison with the results under the same condition in Fig. 3-15, the proposed DBPCC with ARCCI has faster dynamic control of current and less cross-coupling between dq axis, although under the presence of parametric mismatch.

(a)   (b)
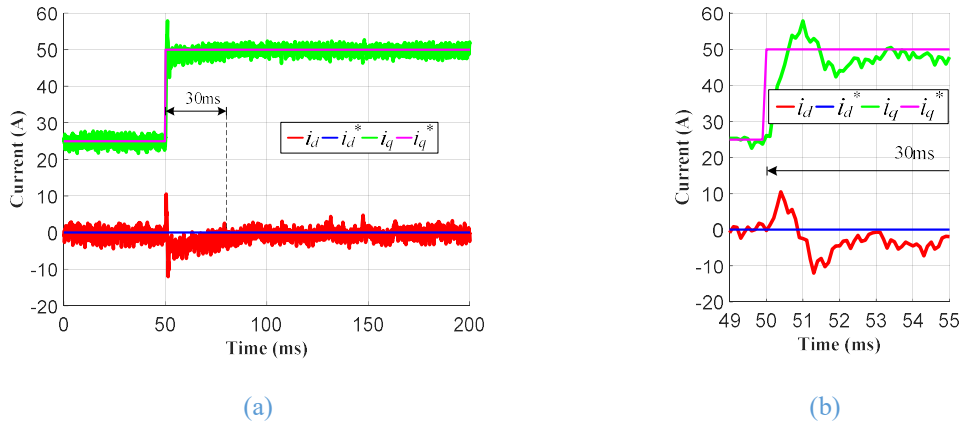
Fig. 3-16 Experiment results of dq axis currents at the high speed of 30,000 rpm (SFR=10) with dead-time of 2 us and inaccurate parameters ($1.2\psi_m$, $1.2L_s$, $0.5R_s$) using FOC with the current control bandwidth of 500 Hz (a) the waveform in transient and steady states (b) the waveform in the transient. Green/purple: sampled/reference q-axis current, red/blue: sampled/reference d-axis current.

Fig. 3-17 and Fig. 3-18 compare the phase currents of the proposed DBPCC with ARCCI and FOC at the low speed and high speed, respectively. It is evident that with the proposed method, the fundamental component of phase currents can be effectively controlled very close to the q-axis current reference. Compared with the results obtained with the FOC, the current harmonic distortion at the low speed with the proposed DBPCC with ARCCI is slightly lower. It is because the DBPCC has higher bandwidth and can suppress some low order current harmonics caused by inverter nonlinearity. At high speeds, the steady-state performances of the proposed DBPCC with ARCCI and FOC are similar. Therefore, the experiment results have demonstrated that the proposed DBPCC with ARCCI has the advantage of fast dynamic response and comparable steady-state performance with the FOC.
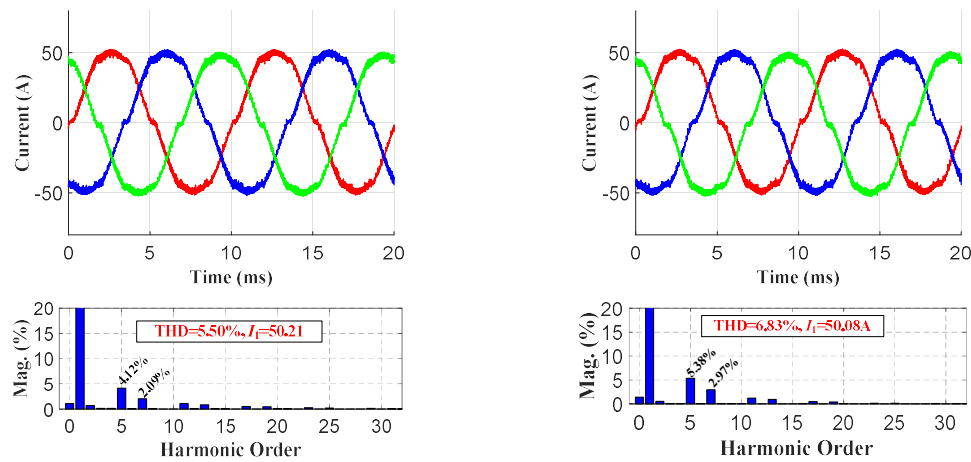
Fig. 3-17 Experiment results of phase currents (i_q^*=50 A) and the current spectrum with dead-time of 2 us and inaccurate parameters ($1.2\psi_m$, $1.2L_s$, $0.5R_s$) at 3,000 rpm (SFR=100). (a) Proposed DBPCC with ARCCI. (b) FOC. Red/blue/green: phase A/B/C current.
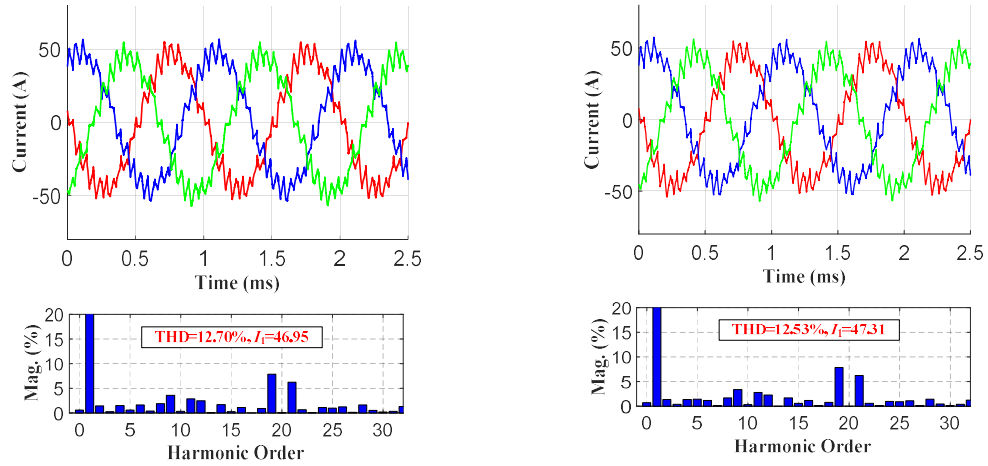
Fig. 3-18 Experiment results of phase currents (i_q^*=50 A) and the current spectrum with dead-time of 2 us and inaccurate parameters ($1.2\psi_m$, $1.2L_s$, $0.5R_s$) at 30,000 rpm (SFR=10). (a) Proposed DBPCC with ARCCI. (b) FOC. Red/blue/green: phase A/B/C current.

3.3 Selective Current Harmonics Suppression Based on Adaptive Harmonic Reference Correcting Current Injection

In this section, a novel selective current harmonics suppression method is proposed. The proposed method is based on injecting harmonic reference correcting currents adaptively into the reference currents of the DBPCC. It can effectively eliminate all the low-order current harmonic distortion caused by inverter nonlinearity and back EMF harmonics.

3.3.1 Current harmonics Induced by Inverter Nonlinearity and Non-sinusoidal Back EMF in DBPCC

Inverter nonlinearity and non-sinusoidal back EMF can both cause harmonic currents in the motor due to the voltage distortions they introduce. Hence, their effects can be together represented by the total voltage harmonic distortion in the motor. Denote the distorted voltage vector caused by all non-ideal factors in the dq frame as $\boldsymbol{V}_{dst\_dq}$ and its nth order harmonic component in the dq frame as $\boldsymbol{V}_{dst\_dqn}^h$.

Based on the nth order harmonic reference frame, the nth order harmonic related variables can be represented. Generally, the voltage equation in the steady states is given as

$$V_{dqn} = (R \pm jn\omega_e L_s) \cdot i_{dqn} \tag{3.19}$$

where, V_{dqn} and i_{dqn} are the voltage vector and current vector in the nth order harmonic reference frame, respectively. $\pm$ corresponds to the rotation direction of the harmonic reference frame, namely, positive for the same rotation direction as the fundamental dq frame and negative for the opposite direction. For example, for the 5$^{\text{th}}$ and 7$^{\text{th}}$ harmonics in the stationary frame, both of them can be 6$^{\text{th}}$ harmonic in the dq frame while the speed of rotation of their harmonic reference frame is $-6\omega_e$ and $6\omega_e$, respectively.

So the nth order harmonic current in the dq frame caused by the voltage distortion due to the inverter nonlinearity and non-sinusoidal back EMF can be obtained as

$$i^h_{dst\_dqn} = \frac{1}{R \pm jn\omega_e L_s} V^h_{dst\_dqn} \tag{3.20}$$

By coordination transformation of (3.20), the associated current harmonic in the stationary frame and the phase current harmonics can finally be derived. It can be easily found that selective harmonic suppression in phase current is equivalent to curb the corresponding current harmonic in the dq frame.

3.3.2 Proposed Selective Current Harmonics Suppression by Adaptive Harmonic Reference Correcting Currents Injection

Considering a general case with any injected harmonic voltage and the voltage distortion caused by inverter nonlinearity and non-sinusoidal back EMF, the actual harmonic current in the aforementioned n^{th} order harmonic reference frame, i^h_{dqn} can be obtained as

$$i^h_{dqn} = \frac{1}{R \pm jn\omega_e L_s} \left(V^{h*}_{dqn} + V^h_{dst\_dqn} \right) \tag{3.21}$$

where V^{h*}_{dqn} is the injected reference harmonic voltage, which corresponds to the reference harmonic current, i^{h*}_{dqn} represented as

$$i^{h*}_{dqn} = \frac{1}{\hat{R} \pm jn\omega_e \hat{L}_s} V^{h*}_{dqn} \tag{3.22}$$

where, ^ denotes the estimated value.

Substituting (3.22) into (3.21), the general expression for the nth order harmonic current, $\boldsymbol{i}_{dqn}^h$ can be derived as

$$\boldsymbol{i}_{dqn}^h = \lambda \cdot \boldsymbol{i}_{dqn}^{h*} + \frac{1}{R \pm jn\omega_e L_s} \boldsymbol{V}_{dst\_dqn}^h \tag{3.23}$$

where the parameter mismatch related coefficient λ is

$$\lambda = \frac{\hat{R} \pm jn\omega_e \hat{L}_s}{R \pm jn\omega_e L_s} \tag{3.24}$$

As can be found from (3.23), normally if harmonic current injection is not employed, i.e. $\boldsymbol{i}_{dqn}^{h*} = 0$, the actual current harmonic is only caused by the inverter nonlinearity and non-sinusoidal back EMF as expressed in (3.20). If the reference current harmonics given in (3.22) is directly injected into the reference currents, the actual harmonic current shown in (3.23) will be affected not only by the parameters mismatch but also by the voltage distortions caused by the non-ideal factors. However, if a correcting component, $\boldsymbol{RCC}_n$ is added into the reference injected current harmonic, the current harmonic expressed in (3.23) can be altered as

$$\boldsymbol{i}_{dqn}^h = \lambda \cdot \left(\boldsymbol{i}_{dqn}^{h*} + \boldsymbol{RCC}_n\right) + \frac{1}{R \pm jn\omega_e L_s} \boldsymbol{V}_{dst\_dqn}^h \tag{3.25}$$

From (3.25), the desired correcting component that results in the actual harmonic current being the same as the reference can be derived as

$$\boldsymbol{RCC}_n = \frac{1-\lambda}{\lambda} \cdot \boldsymbol{i}_{dqn}^{h*} - \frac{1}{\hat{R} \pm jn\omega_e \hat{L}_s} \boldsymbol{V}_{dst\_dqn}^h \tag{3.26}$$

Since the correcting component is added to correct the actual harmonic current, the correcting component is referred to as harmonic reference correcting current (HRCC) and the compensation method to minimise the current harmonics as harmonic reference correcting current injection (HRCCI). As has been shown in section 2.2.6, the proposed DBPCC with harmonic current injection control can track the injected harmonic reference in two time-steps. Thus, the harmonic $\boldsymbol{RCC}_n$ can be directly injected into the reference dq axis current by coordinate transformation of (3.26).

Without loss of generality, a normal case with zero reference harmonic current is considered. In order to suppress the nth order current harmonic, the desired harmonic RCC

in (3.26) to be injected needs to be determined by the harmonic voltage distortion. However, in practice, the actual distortion voltage can hardly be known with accuracy. Hence, it is impossible to obtain the desired injected harmonic RCC according to (3.26) for real-time control of PMSM drives. To circumvent this problem, an adaptive algorithm is designed to calculate the desired injected harmonic RCC online.

The objective function to minimize the selective n^{th} order harmonic current in the dq frame can be defined as

$$J_{hn} = \frac{1}{2}\left(i_{dqn}^{h*} - i_{dqn}^{h}\right)^2 = \frac{1}{2}\left(e_{idqn}^{h}\right)^2 \qquad (3.27)$$

where the reference harmonic current i_{dqn}^{h*} is 0 and e_{idqn}^{h} are the harmonic current control error in the reference harmonic frame.

With the expression of i_{dqn}^{h} in (3.25), the gradient vector of the objective function, J_{hn} against $\boldsymbol{RCC}_n$ can be obtained as as

$$\nabla J_{hn} = -\lambda e_{idqn}^{h} \qquad (3.28)$$

As shown in (3.24), the parameters mismatch related coefficient λ is proportional to the inductance mismatch by neglecting the resistance and constant in steady states. Hence it can be simply approximated as 1 and this approximation will not affect the gradient direction. According to the gradient descent updating rule, the injected harmonic RCC magnitudes, $\boldsymbol{RCC}_n$ is thus determined by

$$\boldsymbol{RCC}_n(k+1) = \boldsymbol{RCC}_n(k) + \eta e_{idqn}^{h} \qquad (3.29)$$

where η is the adaptive gain, which determines the convergence speed of tracking the desired injected harmonic RCC magnitude in (3.26).

To determine the harmonic RCC, the harmonic current control error in the reference harmonic frame, e_{idqn}^{h}, should be obtained. Usually, the harmonic extraction scheme [136] may be employed. However, such harmonic extraction process would affect the dynamic response and significantly increase system complexity. In the proposed adaptive harmonic RCC injection, the harmonic current error information is required to calculate the gradient. However, instead of using the pure current harmonic error of the nth order to calculate the adaptive gradient in (3.28), the harmonic current error is simply obtained by

transforming the current error in the dq frame, e_{idq}, into the nth order rotating reference frame. Further, to account the two time-steps of delay of the proposed DBPCC, the dq axis current error, e_{idq}, is determined by the difference between the reference at the $(k-2)^{\text{th}}$ step and actual currents at the present step. Therefore, the harmonic current error at the kth step is derived as

$$e_{idqn}^{h}(k) = e_{idq}(k) \cdot e^{jn\theta_e} = \left[i_{dq}^{*}(k) \cdot z^{-2} - i_{dq}(k)\right] \cdot e^{jn\theta_e(k)} \qquad (3.30)$$

The updating scheme of the injected harmonic RCC in the reference harmonic frame is given by

$$RCC_n(k+1) = RCC_n(k) + \eta e_{idqn}^{h}(k) \cdot e^{jn\theta_e(k)} \qquad (3.31)$$

Further, by considering the rotation of the harmonic reference frame in the dq frame over the two time-steps as discussed in section 2.2.6, finally the harmonic RCC injected to the dq frame can be obtained as

$$RCC_{dqn}(k+1) = RCC_n(k+1) \cdot e^{-jn(\theta_e(k)+2\omega_e T_s)} \qquad (3.32)$$

According to (3.32), the proposed adaptive harmonic RCC injection (AHRCCI) is actually adding the sinusoidal correcting component associated with the nth harmonic in the dq frame. It has been suggested that adaptive linear neuron method based on the dq frame can alternatively be employed to calculate the weighting coefficients of sinusoidal varying correcting component [137]. However, the proposed adaptive algorithm in this chapter based on the harmonic reference frame is much simpler and can be extended to any selective order harmonic suppression by just changing the harmonic order, *n*. Furthermore, as the harmonic reference frame rotation due to rotor movement is taken into account, the adaptive searching is not affected rotor movement, or independent of speed, while still being effective in the scenarios with low sampling-to-harmonic frequency ratios (SHRs).

3.3.3 Implementation of Proposed Method

The general implementation structure of the proposed selective harmonic current suppression scheme based on AHRCCI is shown in Fig. 3-19. For any n^{th} order harmonic, only the phase angle factor, $\mp n$, needs to be changed according to the selective harmonic order in the dq frame. For example, to eliminate the current harmonics caused by the inverter nonlinearity which are mainly 5th and 7th harmonics in phase currents, the phase

angle factor, $\mp n$ are to be set to -6 and 6, respectively. This also applies for the 5th and 7th harmonics caused by the non-sinusoidal back EMF. If higher order harmonics are also of interests such as 11th and 13th harmonics in phase currents, only $\mp n$ is equal to -12 and 12 accordingly. Finally, in order to suppress multiple current harmonics, the derived harmonic RCCs are summed and added to the dq axis current reference. Moreover, in Fig. 3-19, a high-pass-filter of the current error, formed by subtracting the low-pass-filter output from the original error is employed to minimise the influence of DC offset error in the dq frame. The bandwidth of the LPF can be simply set as a low constant value or a fractional of the fundamental frequency. In addition, given that non-sinusoidal back EMF voltage distortion is proportional to speed and change slowly compared with the control time-step and the inverter nonlinearity caused voltage distortion is of constant magnitude, the adaptive gain can be generally a constant value between 0.005 and 0.05.
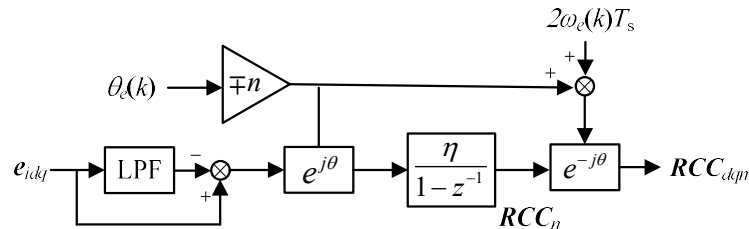
Fig. 3-19 General configuration of the proposed adaptive harmonic RCC injection (AHRCCI) to suppress the nth current harmonics in the dq frame

Fig. 3-20 shows the overall control structure of a PMSM drive with DBPCC using the proposed AHRCCI to suppress the selective current harmonics. In the control structure, the average current control error compensation proposed in section 2.4 is also included which can be regarded as fundamental ARCCI. The numbers of the adaptive harmonic RCC injection blocks are determined by the harmonic orders to be suppressed and they share the identical structure as shown in Fig. 3-19. The ultimate reference current delivered to the DBPCC block is the sum of the original dq reference and the injected RCCs. The detail control structure of the developed DBPCC can be found in Fig. 2-4 in section 2.2.4, and hence omitted here.
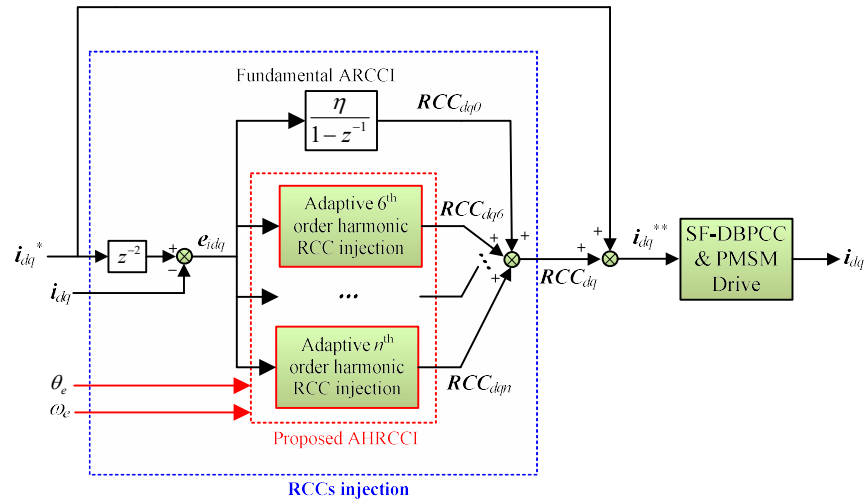
Fig. 3-20 Simplified block diagram of the SF-DBPCC regulated PMSM drive system with the selective harmonic suppression based on the proposed AHRCCI

3.3.4 Simulation Studies and Discussions

In order to validate the proposed selective current harmonic suppression scheme based on AHRCCI in various conditions, numerous simulations have been performed for the prototype high-speed PMSM drive, whose parameters are given in Table 2-1 in section 2.2.4. In the simulations, the inverter dead-time, which is the main cause of the low-order harmonics in the phase currents, and other parameters are the same as those described in section 3.2 unless otherwise stated. The adaptive gain for the fundamental current compensation is set to 0.02 and that for harmonic current compensation is set as 0.01.

3.3.4.1 *Steady-state performance of proposed method*

To validate the effectiveness of selective current harmonic suppression performance of the proposed AHRCCI in steady states, the high-speed machine is operated at 6,000 rpm with the sampling/switching frequency of 20 kHz and the dead-time of 4 μs in the simulation. The fundamental frequency is 200 Hz and the SFR equals to 100, while the frequencies and SHRs associated with different order current harmonics are listed in Table3-1. The SHR associated with the 7th order harmonic current in the stationary frame harmonic is 14.3 while that with 24th current harmonic is only 4, which means there are only four samplings in a harmonic cycle and is difficult to suppress.

Table3-1 Frequencies and SHRs of harmonics at 6,000 rpm with SFR=100 (fundamental frequency of 200Hz and sampling frequency of 20 kHz)

Harmonic order	5th	7th	11th	13th	17th	19th	23th	25th
Freqency in stationary frame (kHz)	1	1.4	2.2	2.6	3.4	3.8	4.6	5
SHR	20	14.3	9.1	7.7	5.9	5.3	4.3	4
Harmonic order in the dq frame	6		12		18		24	

(a)

(b)

(c)

(d)
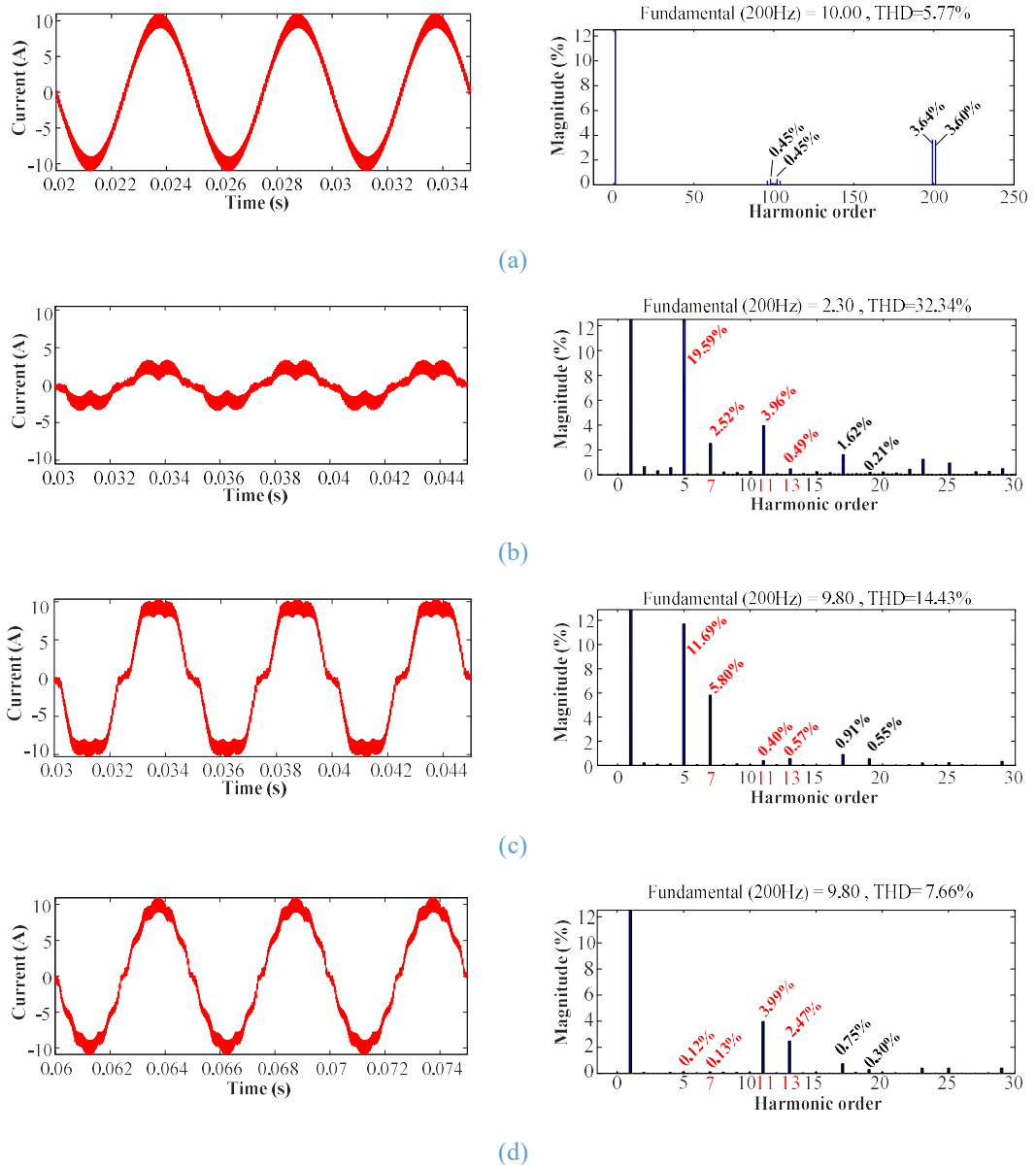
Fig. 3-21 Phase currents and harmonic spectrum distribution at 6,000 rpm with sampling/switching frequency of 20 kHz, dead-time of 4 us and q-axis current reference of 10A (a) ideal case without dead-time (b) without any compensation (c) with only fundamental compensation (d) with selective current harmonics (5th and 7th orders) suppression using proposed method

Fig. 3-21 shows the simulation results of the phase currents and their harmonic spectrum distributions with the q-axis current reference of 10A under different control

schemes. As can be seen in Fig. 3-21 (a), without the dead-time, the phase current is roughly sinusoidal and only exhibits switching harmonics, the dominant components of which are around the twice of the switching frequency, namely 199th and 201st orders. Nevertheless, with the dead-time of 4 us in Fig. 3-21 (b), not only the fundamental current reduces greatly by 77% but also the apparent low-order current harmonics i.e. mainly 5th and 7th orders occur. The current THD increases from the ideal value without dead-time, 5.77% to 32.34%. In Fig. 3-21 (c), the current control error compensation scheme proposed in section 3.2 has been applied and, consequently, the fundamental current magnitude reaches the target within 0.2A error margin. However, the phase current is much deteriorated and the large 5th and 7th harmonics can be observed in the current spectrum. In Fig. 3-21 (d), the proposed AHRCCI scheme is employed to suppress the 5th and 7th order current harmonics. It can be clearly observed in the corresponding current harmonic spectrum that the dominant 5th and 7th order current harmonics are significantly reduced from 11.69% and 5.80% to 0.12% and 0.13%. As a result, the phase current waveform become closer to the sinusoidal shape. Therefore, the effectiveness of the proposed method has been confirmed.

As evident in the current harmonic spectrum with only 5th and 7th order current harmonics suppression in Fig. 3-21 (d), the 11th and 13th order current harmonic increase compared with that without current harmonic suppression. It is because the current ripples, mainly in the forms of 5th and 7th order harmonics are reshaped by AHRCCI and consequently exist as higher order harmonics. Thus, higher order current harmonic suppression schemes are further included in the proposed method. As discussed before, the proposed method can be readily extended for any order harmonic suppression by just changing the coefficient in the general structure in Fig. 3-19. Fig. 3-22 (a)~(c) shows the results with current harmonic suppression up to 13th, 19th and 25th, respectively. It can be seen that the corresponding higher order harmonics can also be effectively suppressed and the current waveform with the current THD of 6.01% in Fig. 3-22 (c) is almost similar to that with the current THD of 5.77% in Fig. 3-21 (a) with an ideal inverter. It is worth noting that the associated SHR for the 25th order harmonic suppression is only 4. By comparison of Fig. 3-22 (c) and (d), the proposed method with 25th order current harmonic suppression can still reduce its magnitude from 0.68% to 0.14% even with such low SHR. Although such high order current harmonic suppression is of less importance in real applications, it verifies the effectiveness of the proposed method in very low SHR

application, which can be a common case in high speed operations where SFRs are already low.

(a)

(b)

(c)
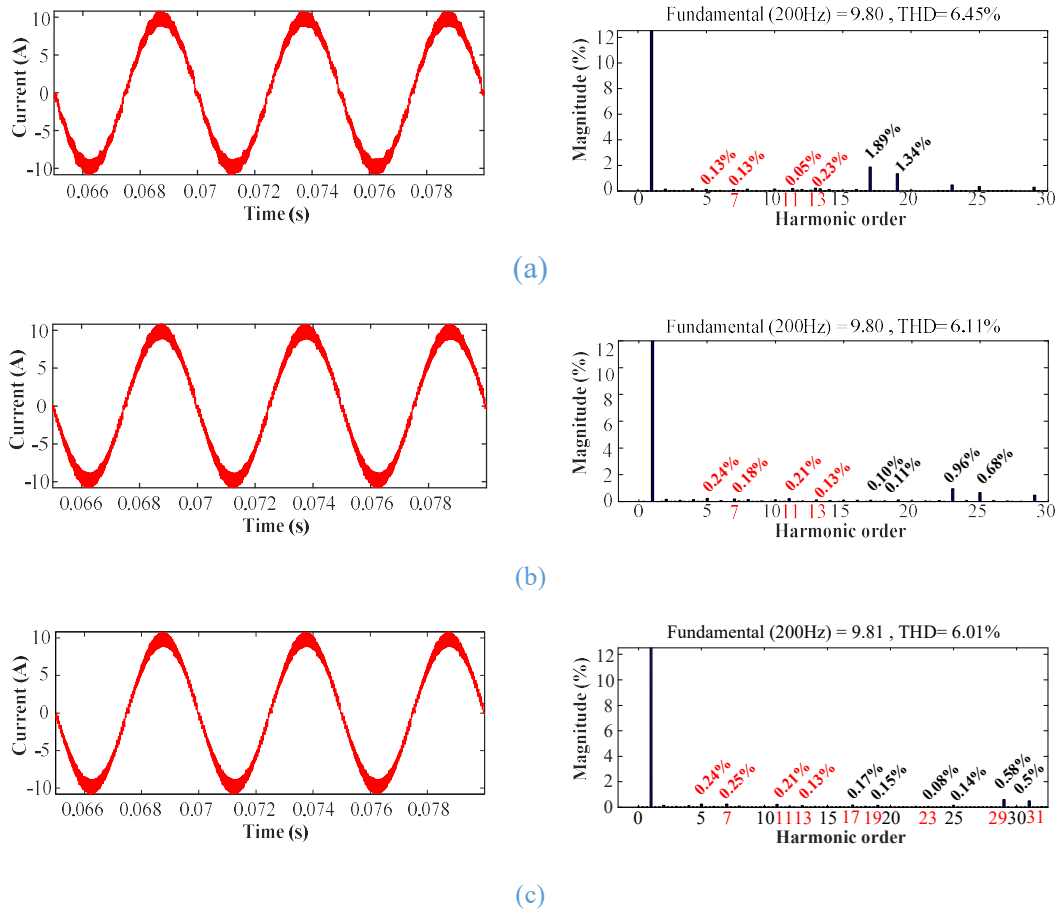
Fig. 3-22 Phase currents and harmonic spectrum distribution using proposed method at 6,000 rpm with sampling/switching frequency of 20 kHz and dead-time of 4 us, with multiple selective current harmonics suppression, (a) 5th, 7th, 11th, 13th orders (b) 5th, 7th, 11th, 13th, 17th, 19th orders (c) 5th, 7th, 11th, 13th, 17th, 19th, 21st, 25th orders

Fig. 3-23 compares the current THD and the fundamental current in Fig. 3-21 and Fig. 3-22 using different compensation schemes, where the compensation scheme 0 represents without any compensation, 1 denotes with only fundamental compensation, 2~5 denotes with fundamental compensation and selective current harmonics suppression, up to 7th, 13th, 19th and 25th respectively. It can be seen that fundamental compensation can effectively reduce the control error of the fundamental due to the dead-time effect, and 5th and 7th orders harmonic suppression improves the THD greatly. The further improvement of higher current harmonic suppression is relatively small. However, since the inclusion of high orders harmonic current suppression method can be very easily implemented using the proposed method, it is still beneficial to have multiple order harmonic suppression in a general perspective. Additionally, if the actual machine has 2nd

harmonic in the back EMF, for example in a consequent pole PM machine, the 2nd order harmonic current suppression may also need to be added.
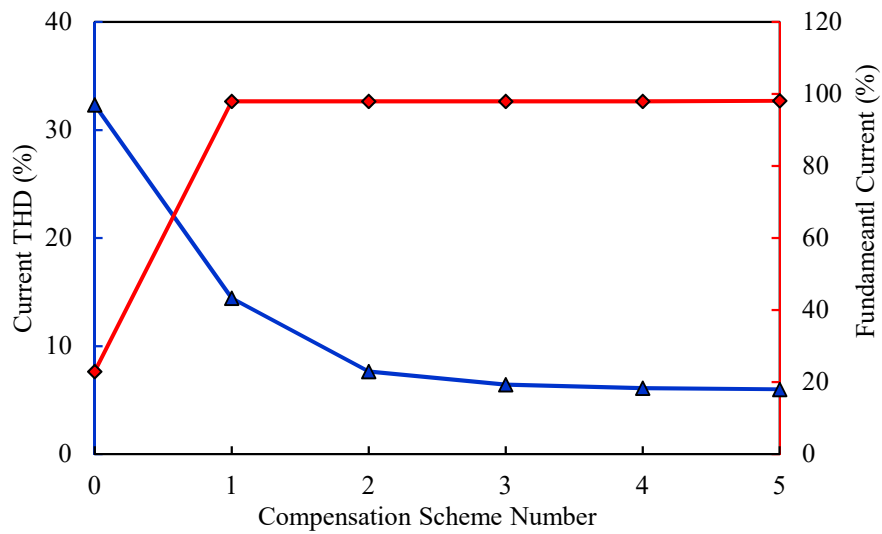
Fig. 3-23 Comparison of current THD and fundamental current under inverter dead-time using different compensation schemes.

3.3.4.2 *Transient performance of proposed method*
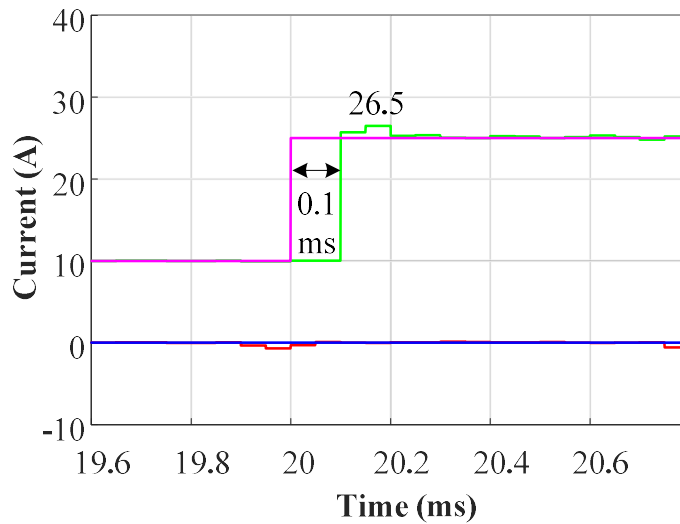
Fig. 3-24 Transient performance with proposed method when the q-axis current steps from 10A to 25A at 6,000 rpm with sampling/switching frequency of 20 kHz and dead-time of 4 us

Fig. 3-24 shows the sampled current waveform during the transient when the reference q-axis current changes form 10 A to 25 A and the harmonic suppression scheme up to the 25th orders is applied successively. It can be observed that the reference currents can be tracked very quickly in the transient just in two time-steps i.e. 0.1 ms, and the

steady state can be reached by four time-steps, i.e. 0.2 ms with just a small overshoot current, i.e. 1.5 A in this case.

3.3.4.3 Parameters independence of proposed method
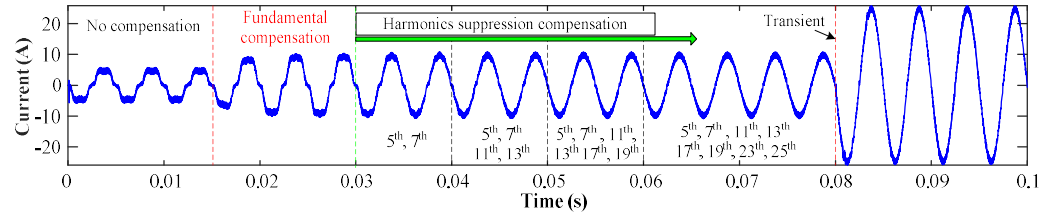
(a)
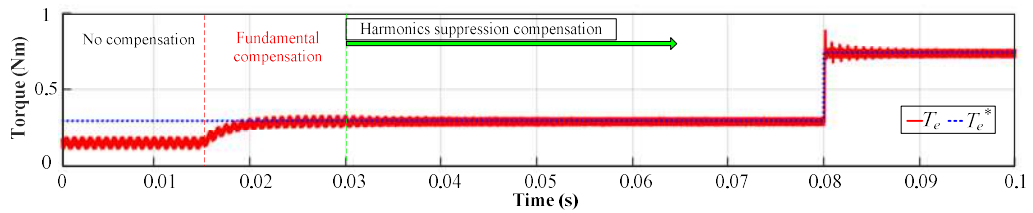
(b)
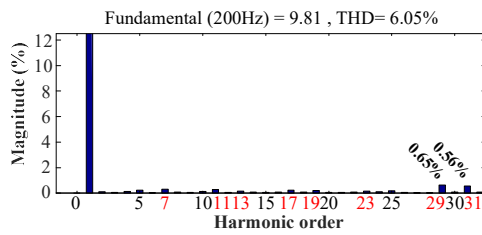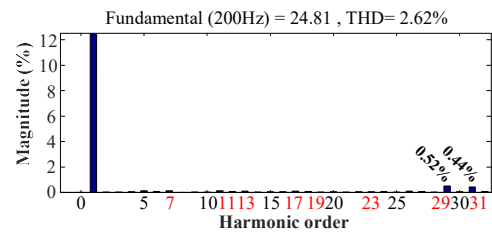
(c)   (d)
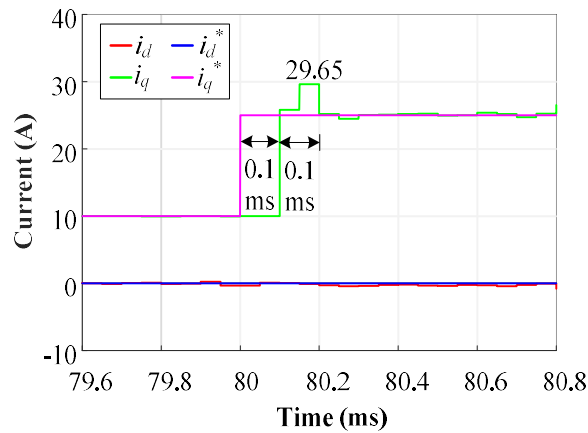
(e)

Fig. 3-25 Simulation results with parameters mismatch and dead-time ($\hat{\psi}_m = 1.2\psi_m$, $\hat{L}_s = 1.2L_s$, $t_{dd} = 2$us) using proposed method at 6,000 rpm with sampling/switching frequency of 20 kHz (a) phase current (b) electromagnetic torque (c) phase current harmonic spectrum associated with the steady state between 0.06s~0.08s (d) phase current harmonic spectrum associated with the steady state between 0.08s~0.1s (e) sampled d-axis and q-axis currents in the reference stepping transient

In order to validate the influence of the parameter mismatch with the proposed method, the simulation with inaccurate parameters are performed. Fig. 3-25 shows the simulation results with 20% over-estimation in both PM flux linkage and inductance. It can be found in Fig. 3-25 (a) that as the fundamental compensation and harmonic suppression schemes are gradually engaged in, the phase currents become closer to the ideal waveform with an ideal inverter. From Fig. 3-25 (b), the resultant torque ripples also reduces as the proposed harmonic suppression scheme is employed. The low order harmonics in the current harmonic spectrums at two different steady states i.e. with q axis reference current of 10 A and 25 A are both effectively eliminated as shown in Fig. 3-25 (c) and (d). Moreover, as shown in Fig. 3-25 (e), the transient response with the proposed method is very fast and only large overshoot current in the q-axis current are observed compared to that with accurate parameters in Fig. 3-24, which can be attributed to the inductance mismatch as analysed in section 2.3. Therefore, it can be concluded that the control performance with the proposed method is parameter independent.

3.3.4.4 The effectiveness of the injected RCCs

Fig. 3-26 (a) and (b) shows the injected RCCs in the dq frame corresponding to the steady state between 0.06s and 0.08s in Fig. 3-25 (a). It can be observed that the DC RCCs and different harmonic orders RCCs are effectively generated by the proposed method and finally adds up to form the total injected RCCs, of which the waveforms are found similar to the typical voltage distortion waveforms caused by the inverter nonlinearity in the dq frame. Fig. 3-26 (c) shows the spectrum of the total injected RCCs in the d-axis and q-axis. It mainly consists of the DC component and 6th, 12th, 18th, 24th order harmonics in the dq frame and coincides with the phase current harmonic spectrum in Fig. 3-25 (c), where the fundamental current has been compensated and the 5th, 7th, 11th, 13th, 17th, 19th, 23rd, 25th order harmonics in the stationary frame have all been supressed.

(a)

(b)

(c)
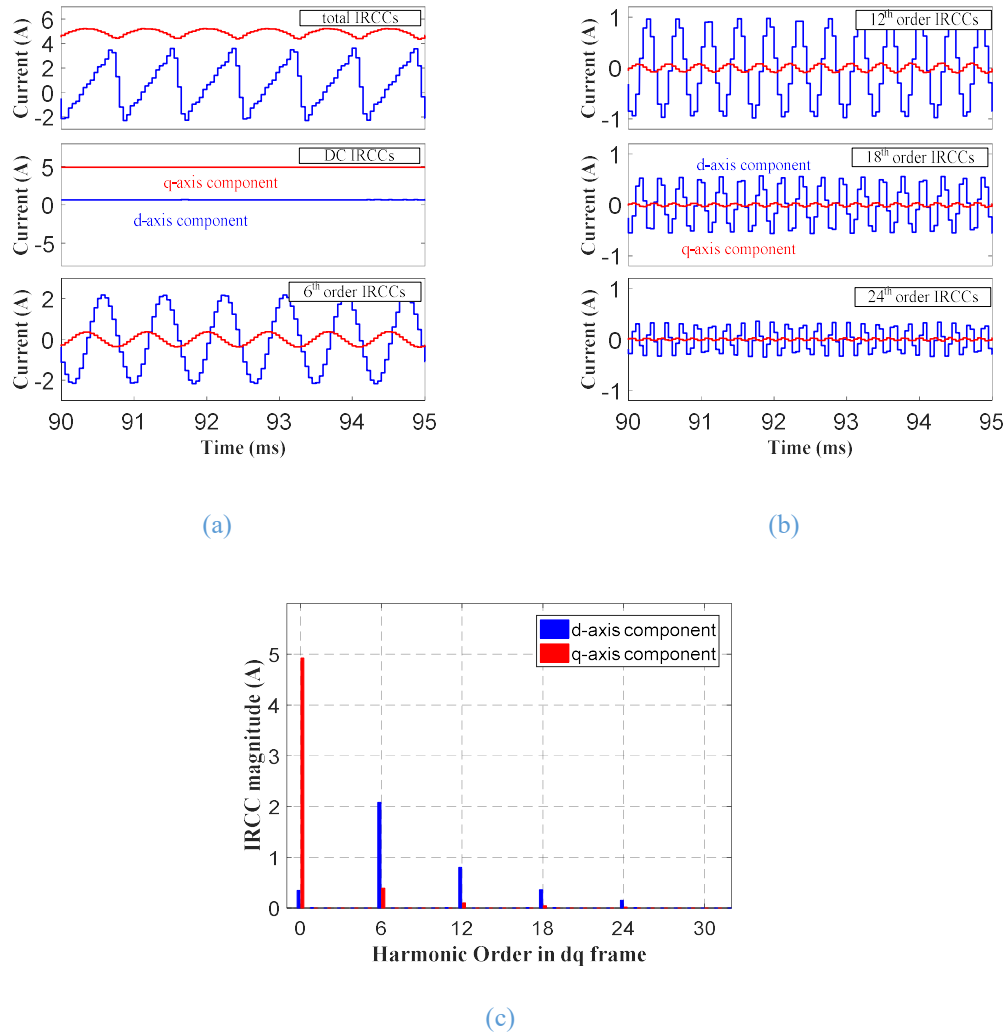
Fig. 3-26 The injected RCCs with selective current harmonic suppression up to 25th order in the steady state between 0.06s~0.08s in Fig. 3-25 (a) the total injected RCCs, DC RCCs and 6th order RCCs in the dq frame in time domain (b) the injected 12th, 18th and 24th orders RCCs in the dq frame in time domain (c) the spectrum of the total injected RCCs in the dq frame

3.3.4.5 Application of proposed method in high speeds with finite SFRs

As demonstrated in the above subsection, the proposed method can even effectively suppress the high order harmonic with the SHR of 4 in low speeds. In high speeds, as the fundamental frequency increases i.e. the SFR reduces, the SHR associated with the same order harmonic will decrease accordingly compared with those in low speeds. Therefore, the current harmonics that can be suppressed in high speeds will be limited to low orders. Table 3-2 lists the SFR and SHRs associated with different order harmonics of the prototype machine at the speed of 10,000 rpm for 3 sampling frequencies.

Table 3-2 SFRs and SHRs with different sampling frequencies at 10,000 rpm (333.33 Hz)

Sampling frequency (kHz)	5	10	20
SFR	15	30	60
SHR5	3	6	12
SHR7	2.14	4.28	8.6
SHR11	1.36	2.7	5.5
SHR13	1.15	2.3	4.6

Fig. 3-27 (a) and (b) show the simulation results at 10,000 rpm with and without the dead-time effect respectively. As can be seen in the figures, the fundamental current reduces and low order harmonics such as 5th and 7th occur in the current spectrum due to the dead-time, which also contributes to the increase of the current THD from 16.64% to 27.11%. However, it can be seen in Fig. 3-28 that as the proposed method with harmonic current suppression is applied, the dominant 5th and 7th harmonic current mainly caused by the dead-time have been eliminated effectively. Moreover, since the higher order harmonic current suppression up to 25th order is also included i.e. higher order harmonic RCCs are injected as well, the harmonics such as 11th, 13th, 17th, 19th, 23rd, 25th order harmonics in the phase current are also suppressed albeit being less significant. Finally, with the proposed method, the current distortion caused by the dead-time has been evidently reduced . The resultant current THD is 17.03%, close to the ideal case of 16.64%. It is worth noting that the residual low order current harmonics in Fig. 3-28 such as 2nd and 4th order are caused by the asynchronous switching with SVM in high speeds, which can also be observed in the ideal case, Fig. 3-27 (a).

As shown in Fig. 3-29, the effectiveness of the proposed method can be more clearly observed in the sampled dq axis current waveforms. Before t=15 ms, no compensation scheme is employed so that the dq axis currents not only has offsets in magnitude but also ripples due to the dead-time. Between t=15 ms and 30 ms, only the fundamental compensation proposed in section 2.4 is employed, the magnitude offset errors in the dq axis currents have been compensated while the ripples, which correspond to the low order current harmonics, still exist. However, after t=30 ms, the proposed method with current harmonic suppression is active, the ripples in the dq axis current have been effectively reduced, and finally the sampled currents closely follow the references. Therefore, it can be generally concluded that with the proposed method, most low order harmonics in the sampled currents can be suppressed even though when the SHFs are extreme-low. It is worth noting that the low-order current harmonics caused by asymmetrical switching in high speeds when the SFR is relatively low cannot be suppressed since they are not

reflected in the sampled currents with the synchronous sampling scheme. However the other harmonic currents due to dead-time and back EMF distortion can be suppressed effectively.

(a)   (b)
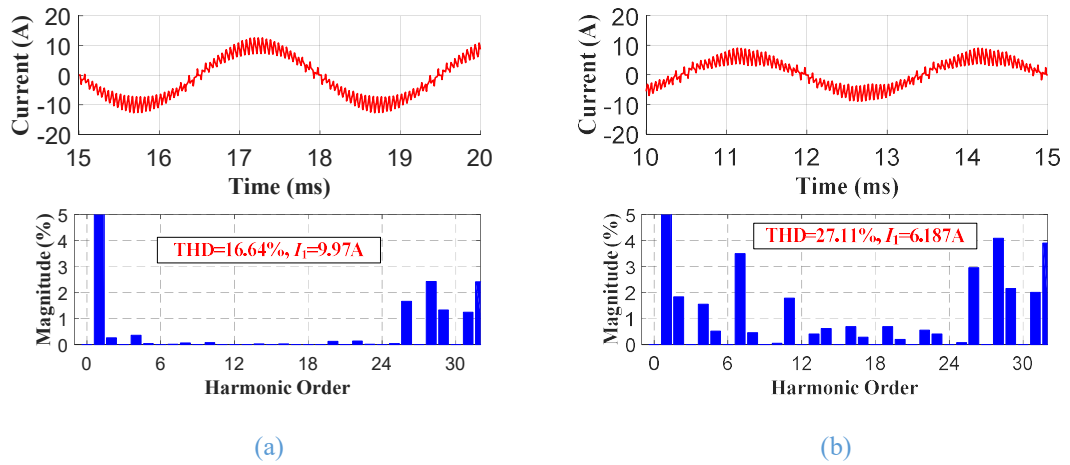
Fig. 3-27 Simulation results of the phase current and phase current harmonic spectrum at 10,000 rpm with sampling/switching frequency of 10 kHz (a) ideal case without dead-time (b) with the dead-time of 2 us

(a)   (b)
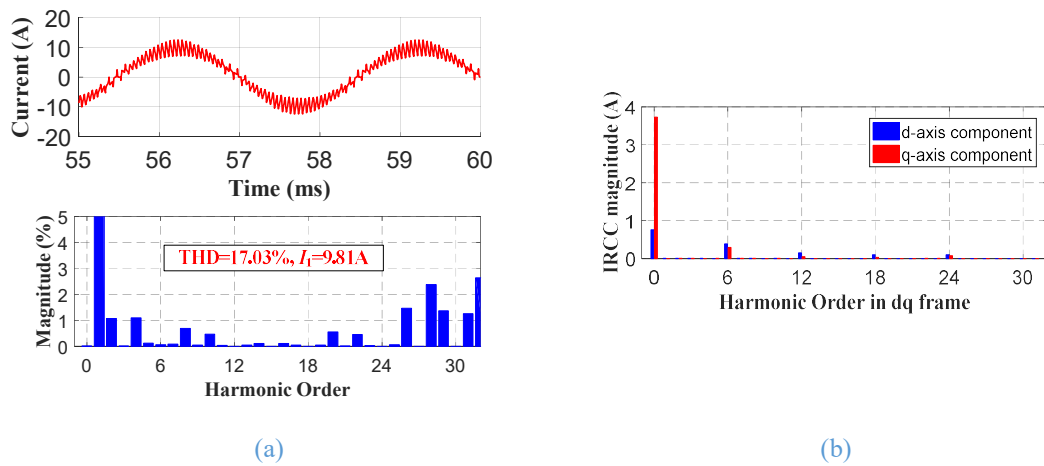
Fig. 3-28 Simulation results at 10,000 rpm with using the proposed method with current harmonic suppression up to 25th order (a) the phase current and its harmonic spectrum (b) injected RCCs spectrum
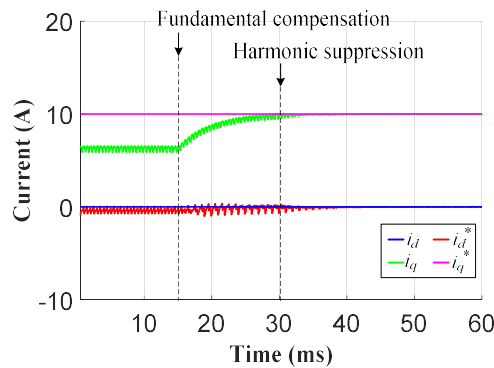
Fig. 3-29 The sampled d-axis and q-axis currents

117

3.3.4.6 Non-sinusoidal back EMF induced current harmonics distortion and suppression

In order to validate the effectiveness of the proposed method on suppressing the non-sinusoidal back EMF induced current harmonics, the simulations with non-sinusoidal back EMF have also been conducted. In this simulation, the main harmonics in the back EMF of the prototype 6/4 high-speed SPMSM i.e. 5th and 7th order harmonics are considered. The magnitudes of the 5th and 7th order harmonic back EMFs are set to 3.71% and 1.14% respectively, according to the measurement result on the prototype machine as shown in Fig. 3-31. In order to focus only on the influence of the back EMF harmonics, an ideal inverter without dead-time is used in the simulation.

Fig. 3-30 (a) shows the phase current and its harmonic spectrum at 10,000 rpm with the same conditions as those in Fig. 3-27 (a), where the motor with sinusoidal back EMF is employed. The 5th and 7th voltage harmonics in the back EMF have caused obvious 5th and 7th current harmonics in the phase current. Moreover, by comparing to the results in Fig. 3-27 (a) with dead-time and sinusoidal back EMF, the 5th and 7th current harmonics are larger with the non-sinusoidal back EMF in high speeds. However, as can be seen in Fig. 3-30 (b), the proposed method can effectively suppress these low-order current harmonics caused by the non-sinusoidal back EMF. It is worthy of mention that as listed in Table 3-2, the SHFs associated with the 5th and 7th harmonics at 10,000 rpm with sampling frequency of 10 kHz are only 6 and 4.128 respectively. The results confirm again that the proposed method is effective in high speeds with both low SFRs and SHRs.

(a)   (b)
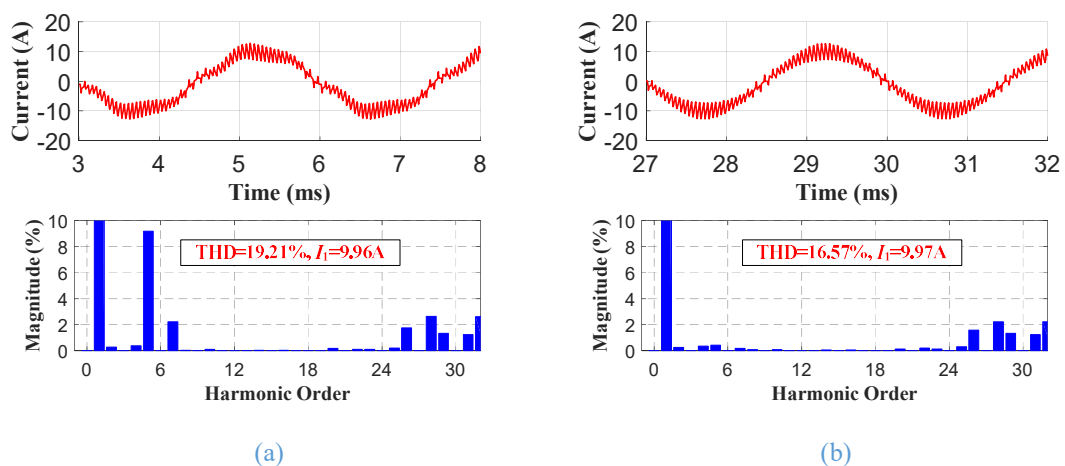
Fig. 3-30 Simulation results of the phase current and its harmonic spectrum at 10,000 rpm with non-sinusoidal back EMF and without dead-time (a) without the proposed method (b) with the proposed method

<div align="center">(a)</div>

<div align="center">(b)</div>
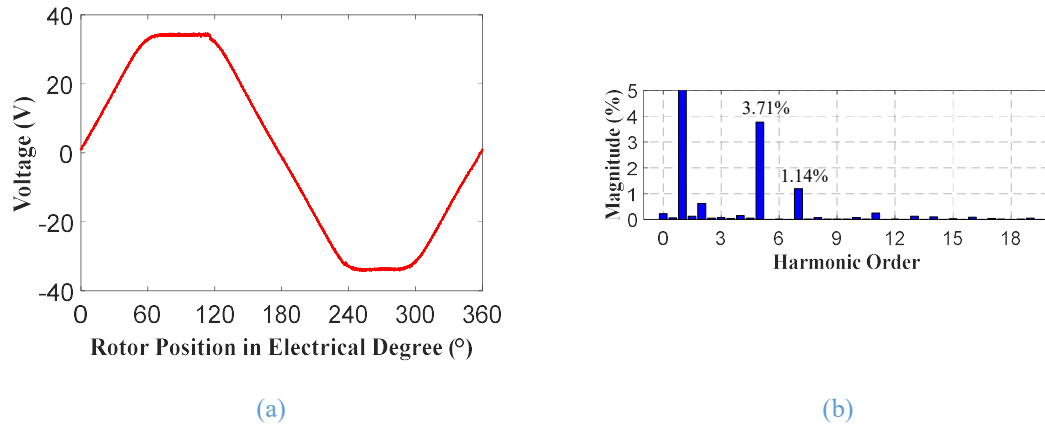
Fig. 3-31 Measured line-to-line back EMF of prototype high-speed PMSM at 10,000 rpm (a) waveform (b) harmonic spectrum

3.3.5 Experiment Verification

The proposed selective current harmonic suppression method has also been validated by numerous experiments on the prototype high-speed machine drive. The switching/sampling frequency is set to 10 kHz, the dead-time is set to 2 μs, and the DC link voltage is 270 V. The proposed DBPCC with the current error compensation method developed in section 3.2 is used as the basic control method. In order to validate the parameter independence of the proposed method, the inaccurate machine parameters are employed intentionally with $\hat{\psi}_m = 1.2\psi_m$, $\hat{L}_d = 1.2L_d$, $\hat{R}_s = 0.5R_s$ in all the experiments, where ψ_m, L_d, and R_s are the calibrated parameters based on measurements. Additionally, to supress all the low order current harmonics up to 25th order, the proposed method includes RCC injection of multiple harmonic orders i.e. 3, 6, 12, 18, and 24 in the dq frame. It is worth noting that if only certain order current harmonic is of interest, only the corresponding harmonic RCC injection is needed.

Fig. 3-32 compares the phase currents and their current spectra without and with the proposed method at the low speed of 3,000 rpm. The term "without the proposed method" means that the DBPCC only with fundamental ARCCI and without the AHRCCI. As can be seen, without the proposed method, the phase currents are greatly distorted, with the 5th and 7th current harmonic distortions of 13.30% and 3.61%, respectively, and the current THD of 16.7%. However, with the proposed method, the phase currents are close to sinusoidal, and the 5th and 7th harmonic current distortions are reduced to 1.03% and 0.31%. Moreover, since multiple harmonic RCC injection is employed in the proposed

method, all the low-order current harmonics below 25th order are effectively rejected and the current THD is reduced to 9.30%.

(a)   (b)
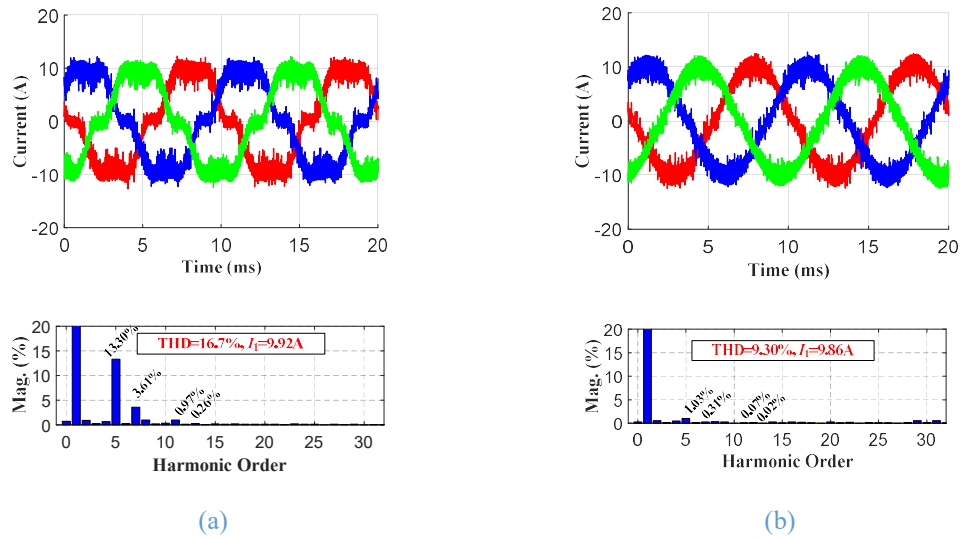
Fig. 3-32 Experiment results of the phase current (i_q^*=10 A) and its harmonic spectrum at 3,000 rpm with dead-time of 2 us (10 A) (a) without the proposed method (b) with the proposed method. Red/blue/green: phase A/B/C current.

(a)   (b)
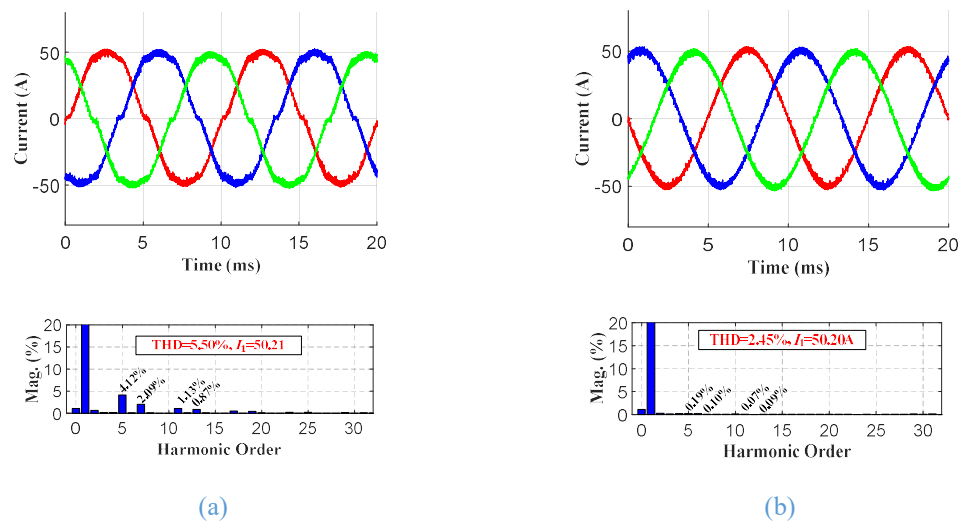
Fig. 3-33 Experiment results of the phase current and its harmonic spectrum at 3,000 rpm without dead-time of 2 us (i_q^*=50 A) (a) without the proposed method (b) with the proposed method. Red/blue/green: phase A/B/C current.

As can be seen in Fig. 3-33, the effect of the harmonic suppression of the proposed control is also evident with higher load currents. In this case, the reference current magnitude has been increased to the rated current of 50 A. The current THD is reduced due to the increase of the fundamental current. However, without the proposed method, the 5th harmonic current distortion is still as high as 4.12%. Whilst, with the proposed method, the 5th harmonic current distortion can be reduced to 0.19%. Moreover, all the

low order harmonics can be effectively suppressed by the proposed method and as a result, more than half reduction in the current THD can be achieved.

Fig. 3-34 shows the results at the high speed of 20,000 rpm. As can be seen, the proposed method can still effectively suppress the 5th harmonic, although with very low SHR5 of 3. It is worth noting that compared to results shown in Fig. 3-32 (b) at the low speed, the higher current THD in Fig. 3-34 (b) is caused by the reduction of the switching-to-fundamental frequency ratio at the high speed, which is 15 for the speed of 20,000 rpm in the experiment. The harmonics around the 15th and 30th orders in the current spectrum are the switching sideband harmonics.

| (a) | (b) |
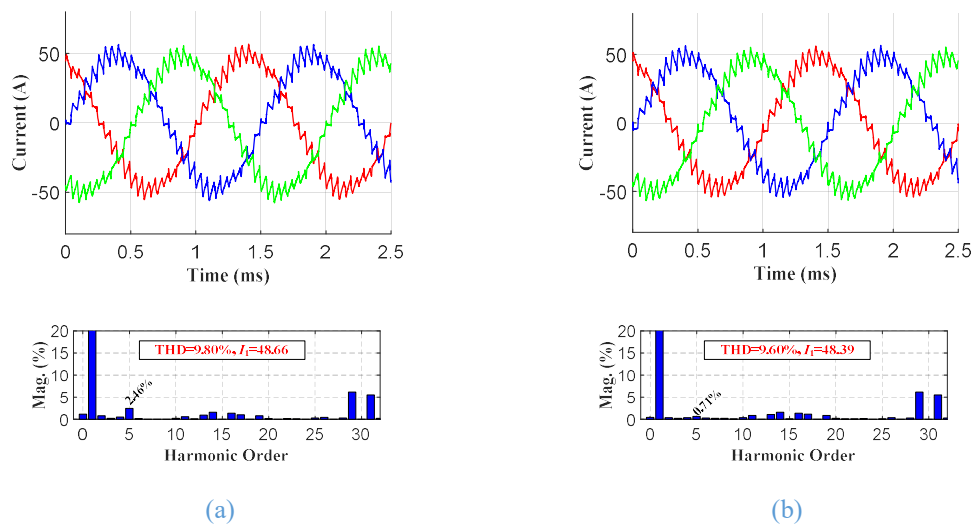
Fig. 3-34 Experiment results of the phase current ($i_q{}^*$=50 A) and its harmonic spectrum at 20,000 rpm without dead-time of 2 us (a) without the proposed method (b) with the proposed method. Red/blue/green: phase A/B/C current.

Fig. 3-36 shows the sampled dq axis currents in the transient with the proposed method when the q-axis reference current steps from 25 A to 50 A at the low speed and the high speed respectively. Compared to the results without the proposed method in Fig. 3-35, the fast dynamic response of the proposed DBPCC is still maintained with the harmonic suppression method at both low speed and high speed. Only slightly overshoot currents are observer due to the inductance mismatch. Moreover, in steady states, almost no current ripples are observed. Therefore, even though the inaccurate parameters are employed throughout the experiments, the excellent performances of the proposed method in both steady states and transients have been demonstrated.

(a)   (b)
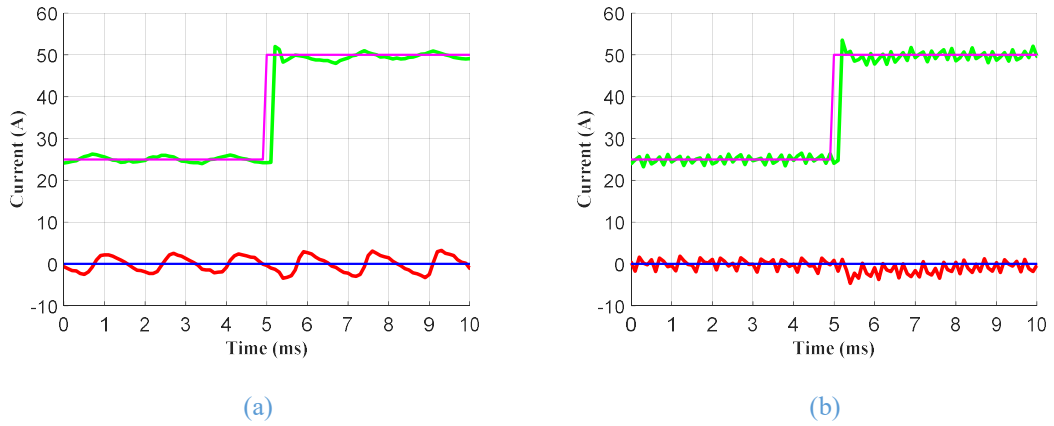
Fig. 3-35 Experiment results of the dq axis current in transient without the proposed method (a) at the low speed of 3,000 rpm (b) at the high speed of 20,000 rpm. Green/purple: sampled/reference q-axis current, red/blue: sampled/reference d-axis current.

(a)   (b)
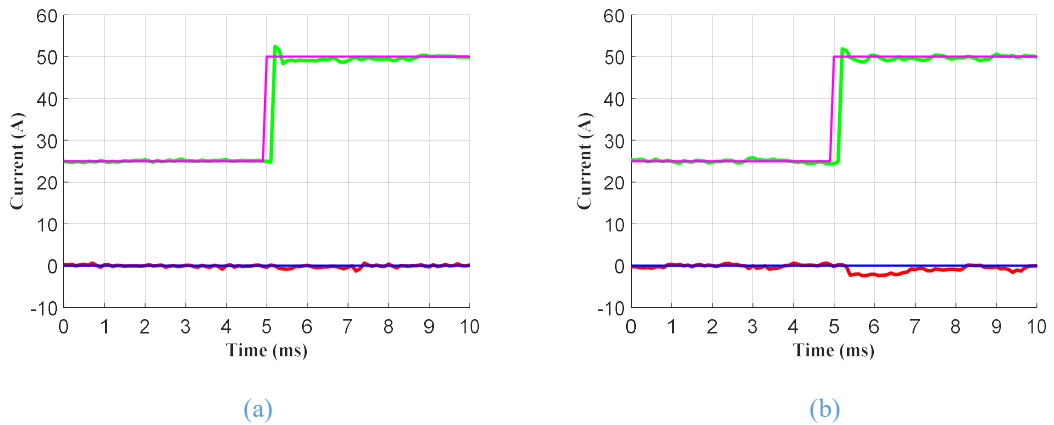
Fig. 3-36 Experiment results of the dq axis current in transient with the proposed method (a) at the low speed of 3,000 rpm (b) at the high speed of 20,000 rpm. Green/purple: sampled/reference q-axis current, red/blue: sampled/reference d-axis current.

3.4 Transient Performance Improvement by Inductance Online Identification

As analysed in section 2.3, the inductance mismatch will not only cause current control error in steady states but also give rise to transient tracking errors. The proposed current error compensation scheme based on ARCCI can eliminate the current errors in the steady states caused by the parameter inaccuracy including inductance mismatch. Moreover, the proposed method based on AHRCCI can effectively suppress the selective current harmonics. Hence, the steady-state performance of the proposed DBPCC has been greatly improved, which is independent of machine parameter and low-order harmonics. However, the transient performance of the proposed DBPCC is still affected by inductance estimation error. High overshoot current may be caused by large over-

122

estimation of inductance and the dynamic current response will be slowed by under-estimation of inductance. Therefore, in this section, a simple transient performance improvement method is proposed to solve the problem caused by inductance inaccuracy in transient. The proposed method exploits the current tracking error information in transient to identify the inductance online. The estimated inductance can be effectively updated every time after the reference changes. The identification process of the inductance does not involve any signal injection and is non-intrusive. Moreover, no complicated observer and extra hardware is required. Extensive simulation and experiment results have validated the effectiveness of the proposed method at both low speeds and high speeds.

3.4.1 Transient Tracking Error under Parametric Mismatch

In section 2.3, the transient tracking error has been analytically obtained in (2.38). It is caused by inductance mismatch but is independent of the PM flux linkage estimation error. Similarly, the transient tacking error of the proposed DBPCC with compensation and selective current harmonics suppression scheme can be derived.

The steady-state current error, namely, the difference between the reference current i_{dq}^* and the corresponding steady-state current i_{dq} has originally been expressed in (2.37). On this basis, the steady-state current error with the RCC injection can be obtained as

$$\triangle i_{dq\_ss} = \frac{1}{L_s}\left[\triangle L_s\left(i_{dq}^* - i_{dq}\cdot e^{-j2\omega_e T_s}\right) + \triangle\psi_m\left(1 - e^{-j2\omega_e T_s}\right)\right]$$
$$+ RCC_{dq\_ss}$$

(3.33)

where RCC_{dq_ss} is the steady-state injected reference correcting current vector.

At a given step k, the current error at step k+2 with the RCC injection, which has been expressed in (2.34) for the case without the RCC injection, can be derived as

$$\triangle i_{dq}(k+2) = \frac{1}{L_s}\left[\left(\triangle L_s i_{dq}^*(k) + \triangle\psi_m\right) - \left(\triangle L_s i_{dq}(k) + \triangle\psi_m\right)\right.$$
$$\left. \cdot e^{-j2\omega_e T_s}\right] + RCC_{dq}$$

(3.34)

where RCC_{dq} is the injected reference correcting currents at step k and can be assumed unchanged during the transient due to the small adaptive gain.

With the current error compensation and harmonic suppression, RCC_{dq_ss} is adaptively adjusted so that the steady-state current error in (3.33) equals to zero. Hence, with the RCC injection, the transient current tracking error is different from that expressed in (2.38) and should be expressed in (3.34). Assume that at step k, the steady state current, i.e. the reference current i^*_{dq1}, has been reached and this reference doesn't change at step k. Since the steady state are maintained, the transient current error at step k+2, which can be obtained as (3.35) according to (3.34), is equal to 0.

$$err_{CT1} = \triangle i_{dq}(k+2) \tag{3.35}$$

$$= \frac{1}{L_s}\left[(\triangle L_s i^*_{dq} + \triangle \psi_m) - (\triangle L_s i_{dq}(k) + \triangle \psi_m)\right.$$
$$\left. \cdot e^{-j2\omega_e T_s}\right] + RCC_{dq} = 0$$

Similar to (3.35), if at step k, the reference current changes from i^*_{dq1} to i^*_{dq2}, the transient current tracking error, err_{CT} is given as

$$err_{CT2} = \frac{1}{L_s}\left[(\triangle L_s i^*_{dq2} + \triangle \psi_m) - (\triangle L_s i_{dq}(k) + \triangle \psi_m) \cdot e^{-j2\omega_e T_s}\right] \tag{3.36}$$
$$+ RCC_{dq}$$

Further, substituting (3.35) into (3.36) yields

$$err_{CT2} = \frac{\triangle L_s}{L_s} \cdot \left(i^*_{dq2} - i^*_{dq1}\right) \tag{3.37}$$

As can be seen from (3.37), the transient current tracking error of the proposed DBPCC with the RCC injection is only proportional to the inductance estimation error and the change in the reference current. The reference current variation can easily be known, therefore the inductance estimation error can be calculated from the transient current tracking error, which is defined as the difference between the new reference current, i^*_{dq} and the actual current at step k+2, $i_{dq}(k+2)$. Additionally, since the transient stator voltage is active from step $k+1$, the current at step $k+1$, $i_{dq}(k+1)$ is nearly identical to that at step k, $i_{dq}(k)$ in steady states. Hence the same transient tracking error will be obtained at steps $k+3$ by replacing $i_{dq}(k)$ with $i_{dq}(k+1)$ in (3.36), namely

$$err_{CT2} = i^*_{dq2} - i_{dq}(k+2) = i^*_{dq2} - i_{dq}(k+3) \tag{3.38}$$

3.4.2 Proposed Inductance Online Identification Method to Improve Transient Performance

According to (3.37), the inductance estimation error ratio, namely the ratio between the inductance estimation error and the real inductance can be expressed as

$$r = \frac{\triangle L_s}{L_s} = \frac{\boldsymbol{err}_{CT2}}{\boldsymbol{i}^*_{dq2} - \boldsymbol{i}^*_{dq1}} \tag{3.39}$$

Considering that the inductance estimation error is given by

$$\triangle L_s = L_s - \hat{L}_s \tag{3.40}$$

Thus, the real inductance can be obtained as

$$L_s = \hat{L}_s + \frac{r}{1 - r} \cdot \hat{L}_s \tag{3.41}$$

According to (3.41) and together with (3.38) and (3.39), it becomes apparent that the real inductance can be identified after a transient with reference current change. More specifically, the reference current change in q-axis can used to identify the q-axis inductance and that in the d-axis to identify the d-axis inductance. Therefore, in order to improve the transient performance in the presence of inductance mismatch, the estimated inductance can be updated each time when the transient tracking error is recorded, according to (3.38), (3.39) and (3.41).

Fig. 3-37 shows the block diagram of the proposed inductance online identification method to improve the transient performance with q-axis inductance mismatch based on (3.38), (3.39) and (3.41), where Δi_{tr} is the threshold set to recognize the transient, r_{max} is the limit set to constrain the absolute value of the calculated inductance estimation error ratio, η is a correction factor of the identified inductance estimation error, ΔL_{max} is the maximum correction of the estimated inductance, S_{sat_v} is the voltage saturation signal with 0 denoting the voltage is saturated and 1 denoting the voltage is not saturated. In this chapter, Δi_{tr}, r_{max}, η, ΔL_{max} are set to 5 A, 1, 1 and $0.5\hat{L}_q$, respectively.

The q-axis estimated inductance will be updated after the reference variation is larger than the set threshold Δi_{tr} and if the stator voltage in the previous time-step is not saturated. From (3.38), the transient current tracking error can be either calculated using the actual current at two time-steps or three time-steps after the transient occurs at step k.

However, considering the stator voltage associated with the current at step $k+3$ is less likely saturated than that for step $k+2$, thus in Fig. 3-37, the transient tracking error at step $k+3$ is employed and the inductance identification process is also executed step $k+3$. Initially, the nominal value of the motor inductance can be simply employed. When a reference change in the q-axis higher than the set threshold is detected, subsequently the real inductance will be identified and the estimated inductance will be updated as illustrated in Fig. 3-37. In steady states or when the reference current variation is within the threshold, the estimated q-axis inductance is kept as the value recently identified. When the transient improvement method is triggered, the identified inductance is employed instead of the nominal inductance. It is worth mentioning that in Fig. 3-37, the estimated inductance error, $\triangle \hat{L}_q$ is directly calculated from the transient tracking error, thus the obtained inductance may keep changing at each transient and wobbles around the real inductance value. An integrator with small gain can be added to eliminate this inductance identification error. In this case, the effective steps tracking the real inductance are counted by the number of transients. Therefore, a number of transients are required to achieve the final stable identification of the inductance. Nevertheless, as indicated by (3.37), small inductance deviation will not deteriorate the transient performance greatly, the direct calculation manner of inductance identification shown in Fig. 3-37 is acceptable in real applications and employed in this chapter.
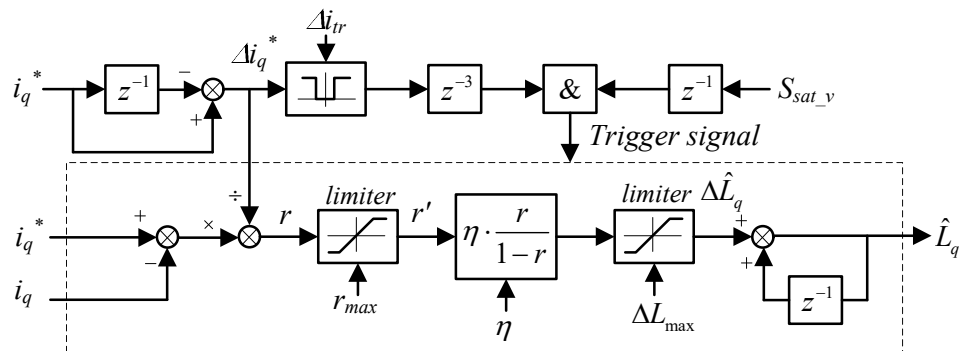
Fig. 3-37 Block diagram of the proposed inductance identification method to improve the transient performance

For the SPMSM without field weakening, the d-axis current reference is usually set to 0, hence the estimation error in the d-axis inductance will not affect the transient performance and only the q-axis inductance identification is necessary. However, the proposed method also applies for the d-axis inductance identification by just replacing it with the identified d-axis quantities in Fig. 3-37. It is also worth noting that the proposed method only leverages the parasitic current tracking error caused by inductance mismatch

and require simple operation and just the current information, which is already available in the control. Therefore, the proposed method is nonintrusive and adds almost no extra cost to the system.

3.4.3 Implementation of Proposed Inductance Online Identification Method in DBPCC

As shown in Fig. 3-38, the proposed inductance online identification method can readily be integrated to the proposed DBPCC with RCC injection methods in Fig. 3-20. After the identified inductance is employed, the transient tracking errors caused by the inductance mismatch are expected to be nearly eliminated. As a result, together with the steady-state current error compensation (namely fundamental ARCCI) proposed in section 3.2, i.e. and the selective current harmonics suppression method (namely AHRCCI) proposed in section 3.3, the ideal deadbeat current control can be realized in practice even with inaccurate information of machine parameters, inverter nonlinearity and non-sinusoidal back EMF of motor.
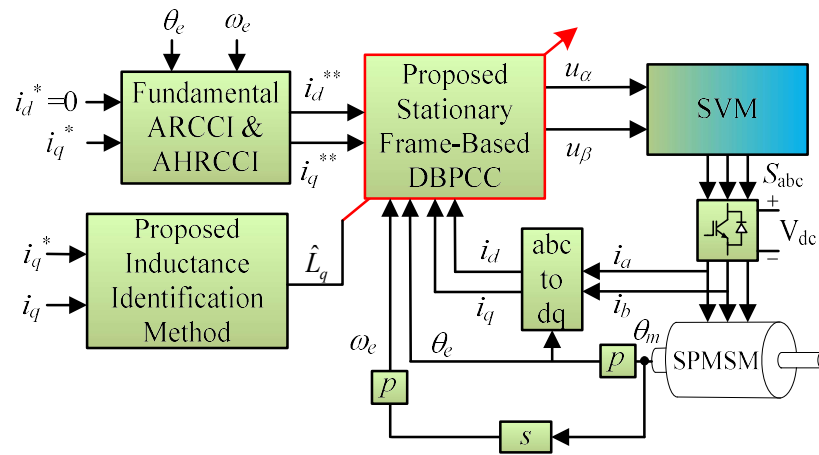
Fig. 3-38 Block diagram of the SPMSM drive system using stationary frame-based DBPCC with fundamental ARCCI, AHRCCI and the proposed inductance identification method

3.4.4 Simulation Study and Discussions

In order to validate the proposed transient improvement method with inductance online identification, extensive simulations have been performed at both low speed and high speed on the prototype high-speed PMSM. In the simulation, the machine parameters are detuned deliberately with $\hat{\psi}_m = 1.2\psi_m$ and $\hat{L}_s = 1.2L_s$. The inverter dead-time is set

as 2 μs. In order to amplify the transient performance deterioration caused by q-axis inductance mismatch, the q-axis inductance is further detuned as $1.5L_s$.

(a)   (b)
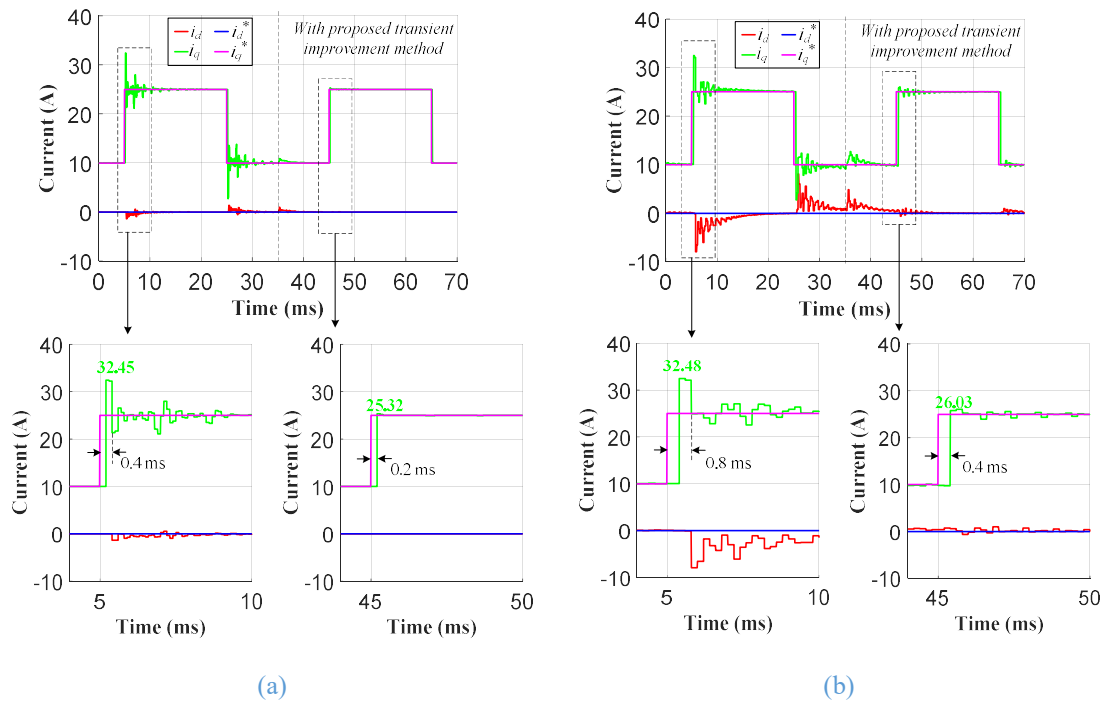
Fig. 3-39 dq axis currents (simulation) in transients and steady states with q-axis inductance mismatch $(1.5L_q)$ (a) at the low speed of 3,000 rpm (SFR=100) (b) at the high speed of 10,000 rpm (SFR=15)

Fig. 3-39 (a) shows the simulation results at the low speed of 3,000 rpm with the switching/sampling frequency of 10 kHz (SFR=100). When $t < 35$ ms, the proposed inductance identification is implemented but the updated inductance is not fed into the proposed BDPCC, i.e. the nominal q-axis inductance of $1.5L_s$ is still employed in the predictions of the deadbeat control. As can be seen, large transient overshoot currents occur when the q-axis reference steps up and down. However, when the use of the newly identified inductance is triggered in the control at t =35 ms, the transient performance is greatly improved and almost ideal deadbeat current control is achieved. From Fig. 3-40 (a), it can be observed that the torque spikes during transients are eliminated after the proposed method is employed. Fig. 3-41 (a) shows the change of the normalised q-axis inductance during the identification process. The step changes in the q-axis reference current when $t < 35$ ms enables the proposed online identification of the inductance. Consequently the estimated inductance is updated and becomes close to the real value every time a transient is detected. At $t = 35$ ms, when the identified inductance is fed into the control, the transient performance is greatly improved.

Fig. 3-39 (b), Fig. 3-40 (b) and Fig. 3-41 (b) show the simulation results at the high speed of 10,000 rpm. In order to study the identification scheme with lower SFR, the sampling/switching frequency is set to 5 kHz, which corresponds to SFR=15. It can be seen that the similar results are obtained as those in the low speed. When the updated inductance is used, the transient control performance is markedly improved.

(a)

(b)
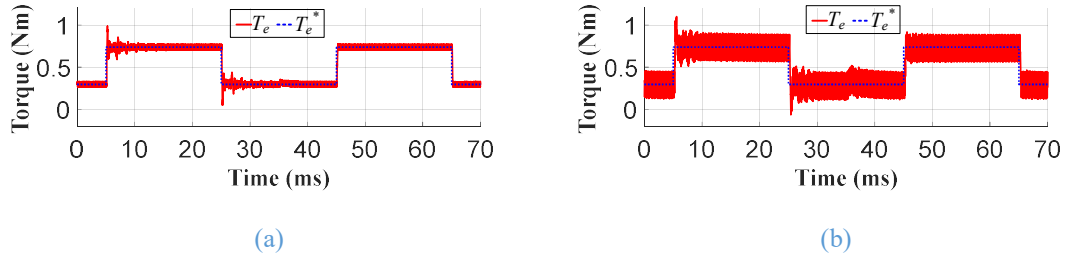
Fig. 3-40 Torque waveform (simulation) in transients and steady states with q-axis inductance mismatch ($1.5L_q$) (a) at the low speed of 3,000 rpm (SFR=100) (b) at the high speed of 10,000 rpm (SFR=15)

(a)

(b)
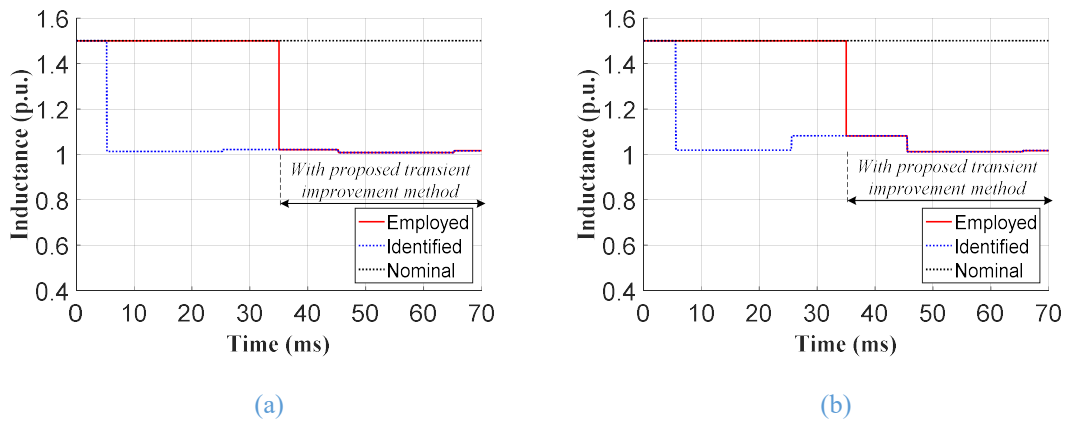
Fig. 3-41 The associated q-axis inductances in Fig. 3-39 (a) at the low speed of 3,000 rpm (SFR=100) (b) at the high speed of 10,000 rpm (SFR=15)

Moreover, as can be seen in Fig. 3-39 (a) and (b), the proposed method does not affect the steady-state performance enhancing methods proposed in section 3.2 and section 3.3, since the adaptive RCC injection methods operates with the steady state errors while the identification scheme operates on the transient error triggered by changes in the reference.

3.4.5 Experiment Results

In order to validate the effectiveness of the proposed method experimentally, the proposed transient improvement method has also been tested on the prototype high-speed PMSM drives. In the experiments, the inaccurate machine parameters are also employed intentionally with $\hat{\psi}_m = 1.2\psi_m$, $\hat{L}_d = 1.2L_d$, $\hat{R}_s = 0.5R_s$. The inverter dead-time is set to 2 μs and the switching/sampling frequency is set to 10 kHz. The q-axis inductance

varies between $0.5L_q$ and $1.5L_q$ in different experiments, where L_q is the measured q-axis inductance value. The proposed current error compensation and selective current harmonics suppression schemes described in section 3.2 and section 3.3 are employed as the basic control in all the experiments.

(a)　　　　　　　　　　　　　　　　(b)
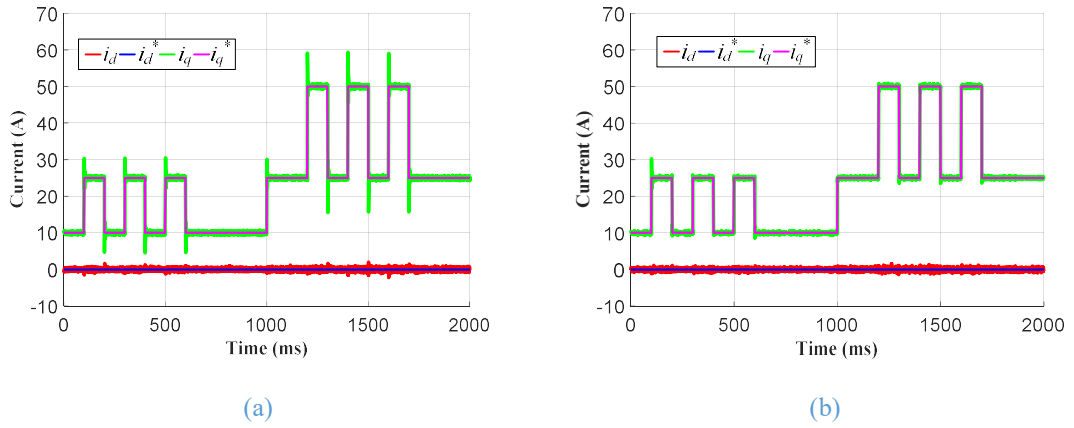
Fig. 3-42 Measured dq axis currents in transients and steady states with q-axis inductance mismatch ($1.5L_q$) at the low speed of 3,000 rpm (SFR=100) (a) without proposed method (b) with propose method. Green/purple: sampled/reference q-axis current, red/blue: sampled/reference d-axis current.

(a)　　　　　　(b)　　　　　　(c)　　　　　　(d)
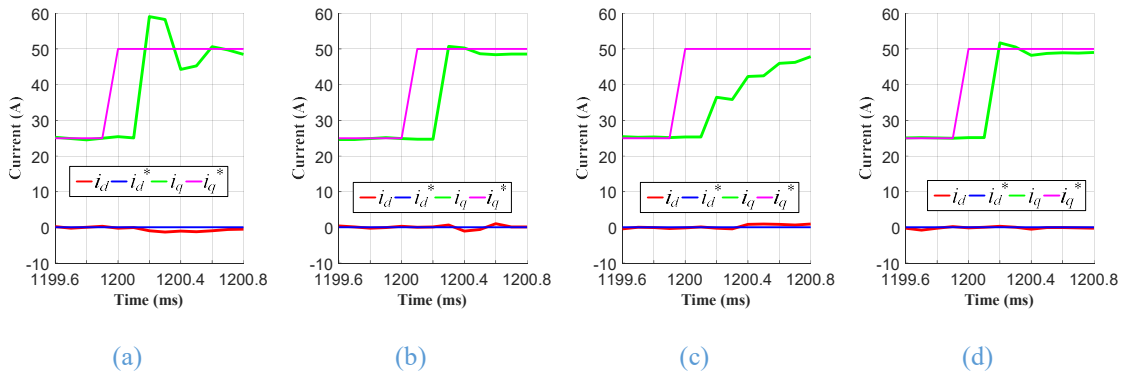
Fig. 3-43 Measured dq axis currents in transients with q-axis inductance mismatch at the low speed of 3,000 rpm (SFR=100) (a) $1.5L_q$, without proposed method (b) $1.5L_q$, with propose method (c) $0.5L_q$, without proposed method (b) $0.5L_q$, with propose method. Green/purple: sampled/reference q-axis current, red/blue: sampled/reference d-axis current.

Fig. 3-42 (a) shows the dq axis current waveforms without the proposed transient improvement method namely the nominal q-axis inductance is employed, which is set to $1.5L_q$. Without the proposed inductance identification method, large overshoot currents are observed when the reference current has a step change. However, as shown in Fig. 3-42 (b), with the proposed transient improvement method, the transient overshot currents can be effectively eliminated. The zoom-in waveforms in the transients associated with Fig. 3-42 (a) and (b) are shown in Fig. 3-43 (a) and (b), the transient performance improvement can be clearly noticed with the proposed method. The results with the nominal q-axis current detuned as $0.5L_q$ without and with the proposed method are also

plotted in Fig. 3-42 (c) and (d). As can be seen, with the under-estimated inductance, the dynamic response of the current is slow while with the proposed method, the nearly ideal deadbeat current control can be achieved.
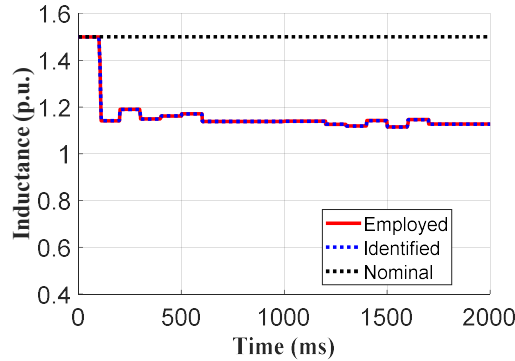
Fig. 3-44 Identified q-axis inductance at the low speed of 3,000 rpm (SFR=100) under q-axis inductance mismatch (1.5L_q) with the transient improved method
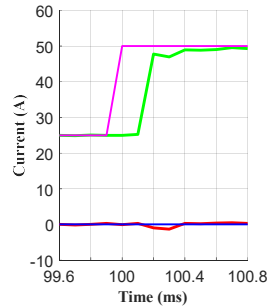
Fig. 3-45 Measured dq axis currents in transients without proposed method using measured q-axis inductance (L_q) at the low speed of 3,000 rpm (SFR=100). Green/purple: sampled/reference q-axis current, red/blue: sampled/reference d-axis current.

Fig. 3-44 shows the identified q-axis inductance variation associated with the test shown in Fig. 3-42 (b) with the proposed transient improvement method. The inductance value is normalized with the measured q-axis inductance, L_q. As can be seen, although the nominal inductance is detuned as 1.5L_q, the actual q-axis inductance has been identified as about 1.15L_q with the proposed inductance online identification method and updated every time when the reference current steps. The identified inductance is 15% larger than the statically measured inductance value. This may be attributed to the measurement error since a small transient current tracking error is observed after two time-steps in Fig. 3-45 when the control uses the measured. Of course, the other factors such as inverter nonlinearity and back-EMF distortions which may influence the identification cannot be completely ruled out as the ARCCI compensation and harmonic suppression is not perfect. The real machine inductance may be between the measured

and the online identified values. However, this small difference in the q-axis inductance will not deteriorate the transient performance greatly as compared with Fig. 3-45.

Fig. 3-46 and Fig. 3-47 show the results at the high speed of 30,000 rpm (SFR=10). The similar conclusions can be obtained as those in the low speed. Particularly, at high speeds, the inductance mismatch would cause large cross-coupling between dq axis and deteriorate the transient performance. However, with the proposed method, the transient performance can be improved significantly with only small dq axis cross-coupling can be observed, due to the small error in the identified inductance. Fig. 3-48 shows the identified inductance associated with Fig. 3-46 (b), it can be seen that the similar q-axis inductance as that at the low speed, i.e. $\sim1.15L_q$ is being identified and the value is updated every times when a transient is recognized, where slight variation is observed.

(a)　　　　　　　　　　　　　　　(b)
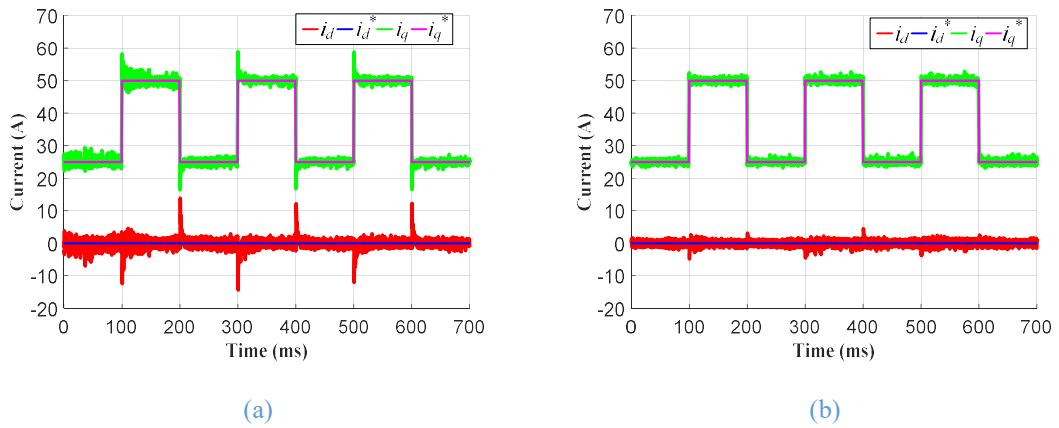
Fig. 3-46 Measured dq axis currents in transients and steady states with q-axis inductance mismatch (1.5L_q) at the high speed of 30,000 rpm (SFR=10) (a) without proposed method (b) with proposed method. Green/purple: sampled/reference q-axis current, red/blue: sampled/reference d-axis current.

(a)　　　　　　(b)　　　　　　(c)　　　　　　(d)
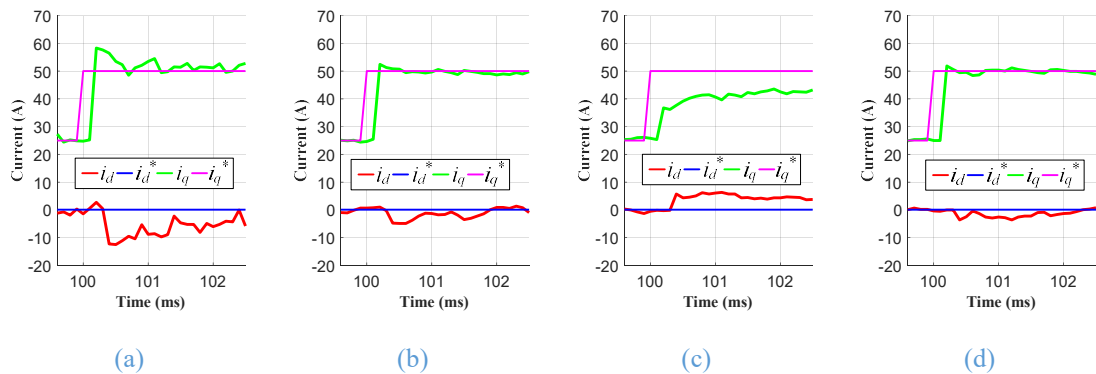
Fig. 3-47 Measured dq axis currents in transients with q-axis inductance mismatch at the high speed of 30,000 rpm (SFR=10) (a) 1.5L_q, without proposed method (b) 1.5L_q, with propose method (c) 0.5L_q, without proposed method (b) 0.5L_q, with propose method. Green/purple: sampled/reference q-axis current, red/blue: sampled/reference d-axis current.
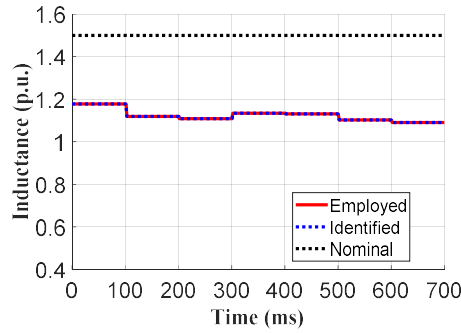
Fig. 3-48 Identified q-axis inductance at the high speed of 30,000 rpm (SFR=10) with the transient improved method under q-axis inductance mismatch ($1.5L_q$)

The phase currents in steady states with the proposed transient improvement method are essentially the same as that only with current error compensation and selective current harmonics suppression, which have been shown in Fig. 3-32 (b), Fig. 3-33 (b) and Fig. 3-34 (b).

Therefore, these experiment results have validated the effectiveness of the proposed transient improvement method in all the scenarios with parametric mismatch at both low speed and high speeds. Moreover, as the current error compensation method and selective current harmonics suppression method are employed simultaneously, the proposed DBPCC with the ARCCI/AHRCCI and inductance identification methods can provide near-ideal deadbeat current control performance in both transient and steady state, even though accurate machine parameters are not known and the inverter nonlinearity and non-sinusoidal back EMF exist in PMSM drives.

3.5 Summary

In this chapter, three novel methods have been developed to improve the steady-state and transient performances of high-speed PMSM drives with the proposed DBPCC.

Firstly, the method based on ARCCI is developed to compensate the average current control errors caused by parameters mismatch and inverter nonlinearity. The proposed method is based on adaptively injecting reference correcting currents into the reference dq axis currents of the proposed DBPCC and can be realized by two delay blocks and two integrators in the dq frame. By incorporating this method, the proposed DBPCC exhibits similar steady-state performance as that with FOC while achieving significantly faster dynamic response. This proposed method can be easily implemented and applicable at high speeds with low SFRs.

Secondly, the method based on AHRCCI is introduced to suppress the low-order current harmonics caused by the inverter nonlinearity and back EMF harmonics. The proposed method is essentially based on reference correcting current injection into the harmonic frames and can be implemented mainly by integrators and coordinate transformation operations. The proposed method is parameter independent and does not require complex extraction of the current harmonics. Since the harmonic control delay is considered, the proposed method can effectively suppress sampled current harmonics of high frequency as well and applicable over a wide SHR range and at high speeds. Moreover, the proposed method can be easily implemented and has a general structure for any order harmonic suppression so that multiple current harmonic suppression can be achieved with the proposed method.

Finally, the transient improvement method with inductance online identification is developed for the proposed DBPCC. The method leverages the transient tracking error caused by inductance mismatch to identify the actual inductance. By employing the identified inductance, the transient performance can be greatly improved. The developed method can be easily integrated to the proposed DBPCC with the ARCCI and AHRCCI. As a result, nearly ideal deadbeat current control can be achieved with both excellent transient and steady-state performance. The proposed method is parameter independent and effective at both low speeds and high speeds.

Additionally, extensive simulations and experiments have been performed and the results have validated the effectiveness of all the proposed methods.

CHAPTER 4

Synchronous Optimal PWM for High-Speed PMSM Drives with Minimised Current Distortions

4.1 Introduction

In the previous chapters, the high performance deadbeat predictive current control (DBPCC) has been developed for high-speed PMSMs. It can lead to robust and fast current control even with low sampling-to-fundamental frequency ratios (SFRs). Meanwhile, the undesirable low-order harmonics can be suppressed effectively by the proposed adaptive harmonic reference correcting current injection (AHRCCI) method. However, the switching harmonics cannot be dealt with by these techniques and they will increase greatly in high speeds when SFRs is relatively low. Similarly, for the conventional SVM based FOC, the reported selective current harmonic suppression methods cannot reduce the switching harmonics as well. These switching harmonics due to the low switching-to-fundamental frequency ratios, also known as low pulse numbers will be dominated at high speeds and they are essentially determined by the employed PWM scheme in steady states. Therefore, in order to reduce the current harmonic distortion at high-speeds with low pulse numbers, the improved PWM schemes should be employed.

For the electrical drives with low pulse numbers, synchronous PWM methods are usually employed, which exhibits symmetrical phase voltages and can cancel all the even and triplen current harmonics. Compared to its counterparts, such as synchronized SVM [102] [99] and selective harmonic elimination (SHE) PWM [106], synchronous optimal PWM (SOPWM) [103] [104] [105] is more attractive for electrical drives, as the total current harmonic distortions (THD) can be minimized. With SOPWM, the steady-state switching harmonics are determined by the optimal pulse patterns (OPPs) obtained from the offline optimization. Hence, the acquisition of OPPs and the offline pulse pattern optimization are important.

The pulse pattern optimization is a convex problem with both linear and nonlinear constraints. It can exhibit many local minima and can be very complex to solve for high-pulse number scenarios, as the solution dimensions increase greatly as the pulse number

gets higher. Varieties of optimization methods including gradient method [111], intelligent algorithms such as genetic algorithm [112] and particle swarm optimization [113], and time-domain based optimization [110] have been reported. Among these methods, due to simplicity and generality, the gradient method is currently more widely employed for two-level [103][114][115] and multi-level converters [111] [116][117]. However, in order to obtain the global optimal solution with the gradient methods, the optimization should be repeated substantially more times with different initial values e.g. 25,000 times for three-level converters [111][118]. On the other hand, the trade-off between the current distortion factor and OSA discontinuity requires complex re-optimization procedure and can differ in different applications due to the variation of operating modulation index [111][117]. The optimization and derivation of the OPPs for real-time control of electrical drives can be very time-consuming.

Therefore, a computationally efficient optimization procedure based on the gradient method is proposed in this chapter. The proposed method includes the analytical gradient of the nonlinear constraint and both predictive and random initial values. The proposed method can reduce the calculation time of the OPPs greatly. Moreover, both the global optimal solution and the associated sets of the continuous optimal solution can be obtained for the whole modulation index range. The optimal switching angles can be flexibly selected according to the specific requirements on the OSA discontinuity numbers and maximum current distortion in different applications. No tedious and complex re-optimizations are required. The proposed method also applies to other converter topologies including multi-level inverters. The numerical optimization results and extensive time-domain simulation results on a prototype high-speed SPMSM drive have been obtained and verified the effectiveness of the proposed method. Moreover, the effectiveness of OPPs based SOPWM on the current harmonic distortion reduction of the high-speed PMSM drives has been validated.

Further, in variable-speed drives, the pulse number of SOPWM, i.e. SOPWM mode, will change when speed varies if the attainable switching frequency is limited to a fixed value. This change can cause undesirable transients and may result in large current errors during the transition [105]. To address this problem, the transition of the SOPWM mode, i.e. pulse number usually takes place at the zero degrees of the reference voltage in each phase [119]. However, this method requires transition at specific positions of applied voltage and can result in slow responses. A different smooth transition scheme has been

reported for SHEPWM based on the zero current harmonics at 90°. However, this method does not apply to SOPWM because the low-order current harmonics such as 5th and 7th are not equal to zero as that in SHEPWM. An alternative to realize the smooth mode transition is to modify the OPPs in real-time to track the optimal flux trajectory [104] [105]. However, this method requires complex flux observers and online switching calculation process. Therefore, in this chapter, a novel mode transition method has been proposed for SOPWM. Based on the general property of SOPWM, the proposed method can start the mode transition at any position and complete the transition within 1/6 fundamental cycle. The smooth and fast mode transition can be achieved between any two SOPWM modes including different pulse numbers, pulse types and continuous sets of OSA. Moreover, the proposed transition is very simple and almost add no cost to the drive system.

4.2 Pulse Pattern Optimization and Implementation of SOPWM for Inverter-Fed High-Speed PMSM Drives

This section is arranged as follows. Firstly, the basic principle of the pulse pattern optimization of SOPWM is introduced, after which the optimization problem is analysed. Subsequently, a computationally efficient optimization procedure for pulse pattern optimization is proposed. In section 4.2.4, by applying the proposed method, all the optimal pulse patterns are obtained and presented. In section 4.2.5, the implementation of the OPPs based SOPWM for high-speed PMSM drives is described. Extensive simulations are performed in section 4.2.6. As follows, a fast prediction method for the current harmonics of the motor drive using SOPWM is presented. As demonstrated, it can be a very efficient tool for evaluating current switching harmonic distortions of high-speed PMSMs with SOPWM. Finally, real-time hardware-in-the-loop tests and experiment results are given in section 4.2.8.

4.2.1 Pulse Pattern Optimization of SOPWM

4.2.1.1 Symmetric Pules Patterns and Associated Harmonics

Fig. 4-1shows the equivalent circuit of a two-level inverter fed high-speed SPMSM drive system, in which the motor is modelled as a three-phase R-L-back EMF load. When in high speeds with limited switching frequency, i.e. low pulse number, the phase terminal voltages, u_{ao}, u_{bo}, u_{co} can exhibit high harmonics and consequently lead to high current

harmonics in a high-speed motor. In addition, as the switching frequency is not much higher than that of the fundamental component, large sub- and low- order harmonic voltages and currents would be present in the motor. Therefore, to eliminate the sub- and even- current harmonics, the phase terminal voltages usually employ symmetric patterns, i.e. half waveform symmetry (HWS) and quarter waveform symmetry (QWS), as shown in Fig. 4-2 by example of pulse number N_p=5. Besides, to eliminate the triplen harmonics, the three phase symmetry (3PS) should be maintained as well, namely the terminal voltages of phases B and C are obtained by shifting the phase A voltage in Fig. 4-2 by ±120° respectively [60]. It is worth noting that the SOPWM with only HWS and 3PS can be employed as well and can contribute to lower current THDs at some operation conditions owing to more switching angles to be optimized [116][109]. However, its real-time implementation will become complex. Thus, in this thesis, the widely used QWS, HWS and 3PS pulse pattern are employed for SOPWM.
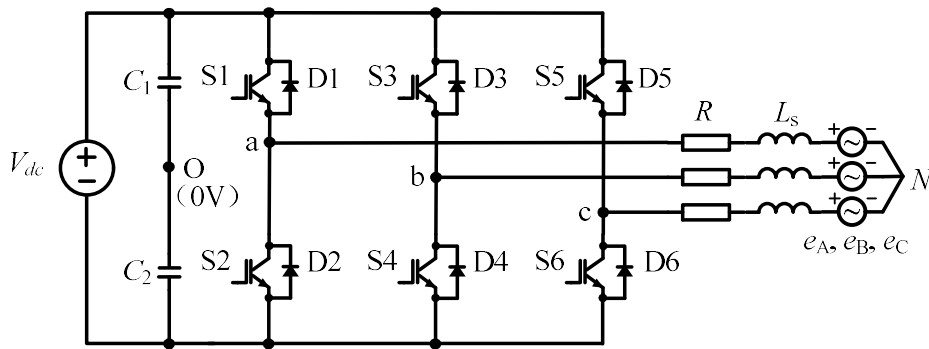
Fig. 4-1 Equivalent circuit of a two-level inverter fed three-phase high-speed SPMSM drive

(a)

(b)
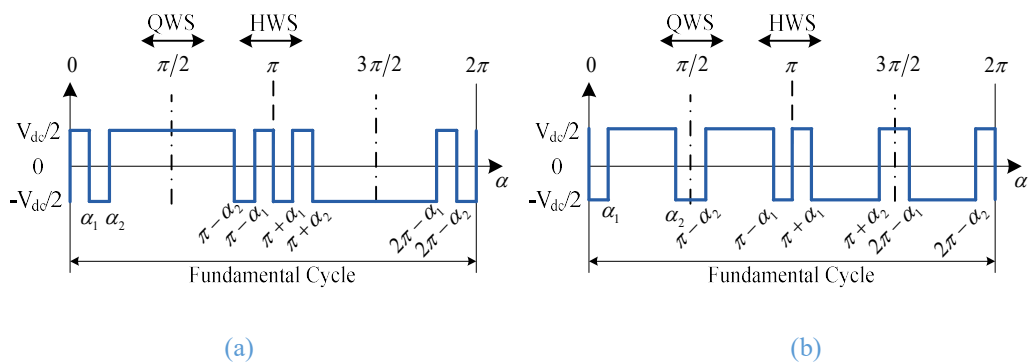
Fig. 4-2 Synchronous and symmetric terminal voltage of phase A for two-level inverters with N_p=5. (a) Type A (b) Type B

As shown in Fig. 4-2, with voltage patterns of QWS, HWS and 3PS, the three phase voltages can be determined by the switching angles in the first quarter cycle of phase A, termed as primary switching angles. For 2-level inverters, two pulse structures, i.e. Type A and Type B exist, with Type A features a rising edge (positive transition) at the zero

position whilst Type B has a falling edge (negative transition). For the both pulse pattern, the pulse number in a fundamental cycle is derived as $N_p=2M+1$, where M is the switching angle number in the first quarter cycle of phase A. Hence, the SOPWM for two-level inverters can only be implemented with the odd pulse number, i.e. 3, 5, 7, $\cdots$. Further, for real-time control of electric machines, the pulse number is usually selected as the maximum permisssiable odd number according to the fundamental frequency and the maximum switching frequency. The pulse number will vary with the operating speed for a given constraint of switching frequency. Also, the switching frequency with SOWPM is not constant across the operating speed range but always within the given constraint.

By Fourier decomposition of the phase terminal voltage and considering the three-phase symmetry, the fundamental and each order harmonic amplitudes of the phase-to-neutral voltage can be obtained as the function of primary switching angles in (4-1).

$$V_n = \pm \frac{2V_{dc}}{n\pi} \cdot \left[1 + 2 \cdot \sum_{i=1}^{M} (-1)^i \cos(n\alpha_i) \right] \quad (n = 1,5,7,\cdots) \quad (4\text{-}1)$$

where, α_i denotes the ith primary switching angles; the sign $\pm$ corresponds to Type A and Type B pulse patterns, respectively; n is the harmonic order, V_1 denotes the fundamental voltage amplitude, $V_n(n>1)$ denotes the voltage amplitude of the nth harmonic. It is seen that all the even and triplen harmonics are not present because of the symmetries of the switching waveform.

The associated phase fundamental and harmonic current magnitudes, I_1 and I_n can be obtained respectively as

$$I_1 = \frac{V_1 - V_{emf}}{\sqrt{(\omega L)^2 + R^2}} \quad (4\text{-}2)$$

$$I_n = \frac{V_n}{\sqrt{(n\omega L)^2 + R^2}} \quad (n = 5,7,\cdots) \quad (4\text{-}3)$$

where, V_{emf} denotes the back EMF amplitude, ω denotes the fundamental electrical angular speed, L is the synchronous inductance of SPMSM, and R is the phase resistance.

4.2.1.2 Pules Pattern Optimization Problem Formulation

As the fundamental phase voltage and current have been formulated in (4-1), (4-2) and (4-3), the primary switching angles, α_i can be optimally determined in such way that

the current THD is minimized meanwhile the fundamental voltage/current matches the reference. Other objectives such as selective harmonic elimination [106] and switching losses [138] can be employed. However, current THD minimization can reduce the overall current distortion in high-speed PMSMs, and thus is employed in this thesis.

As can be seen in (4-3), the current harmonic relates to specific operation conditions such as speed and the machine parameters. In order to represent the current distortion generally, the distortion factor, d is usually used instead of current THD in current distortion optimization and comparison [39]. It is defined as the corresponding root-mean-square (RMS) harmonic current, I_h expressed in (4-4) normalized by the RMS harmonic current, I_{h_6S}, under the six-step operation in the same condition expressed in (4-5). The distortion factor, d is represented in (4-6), where the V_{n*} denotes the normalized harmonic voltage, i.e. the value of V_n in (4-1) normalized with respect to the fundamental voltage under six-step operation, $2V_{dc}/\pi$. Based on (4-1) and (4-6), it can be seen that the distortion factor, d, is only dependent on the primary switching angles, α_i. It is worth noting that the constant, 4.64% in (4-5) and (4-6) corresponds to the weighted THD of voltage (WTHD0) under six-step operation.

$$I_h = \sqrt{I_n^2} = \frac{\sqrt{\sum \left(\frac{V_n}{n}\right)^2}}{\omega L} \tag{4-4}$$

$$I_{h\_6S} = 4.64\% \cdot \frac{2V_{dc}}{\pi \omega L} \tag{4-5}$$

$$d = \frac{I_h}{I_{h\_6S}} = \frac{\sqrt{\sum \left(\frac{V_{n*}}{n}\right)^2}}{4.64\%} \tag{4-6}$$

In this chapter, the modulation index, m is defined as the reference voltage magnitude normalized by the fundamental voltage under six-step operation. Given that minimising d is equivalent to minimising the term inside the root operation in (4-6), the pulse pattern optimization problem, i.e. the primary switching angle optimization can be formulated as (4-7) ~ (4-9), where m^* is the reference modulation index, and the sign $\pm$ in (4-9) correspond to Type A and Type B pulse patterns respectively.

$$min. \quad J(\alpha_i) = \sum \left(\frac{V_{n*}}{n}\right)^2 = \sum_{n=5,7,11,\cdots} \frac{1}{n^2} \cdot \left[1 + 2 \cdot \sum_{i=1}^{M}(-1)^i \cos n\alpha_i\right]^2 \tag{4-7}$$

$$s.t. \quad 0 < \alpha_1 < \alpha_2 < \cdots < \alpha_M < \frac{\pi}{2} \tag{4-8}$$

$$s.t. \quad \pm\left(1 + 2 \cdot \sum_{i=1}^{M}(-1)^i \cos \alpha_i\right) = m^* \tag{4-9}$$

As can be seen, the optimization problem has a nonlinear equality constraint i.e. (4-9) and encompasses transcendental components in both the objective function. It is a nonconvex optimization problem and cannot be solved analytically. To solve the optimisation problem, the simple gradient-based method is usually employed [111] and can compute all the solutions numerically.

4.2.2 Insights into Pulse Pattern Optimization Problem

To gain insights to the pulse pattern optimization problem, the case with pulse number of N_p=5 i.e. M=2 prime switching angles are visualized in Fig. 4-3. The cost function contour is plotted over the feasible region pertinent to the inequality constraints, (4-8), with the colour indicating the cost function value. As can be seen, many local minima exist if the modulation index constrain, i.e. (4-9) is not imposed. When the desired modulation index is taken into account, the dimension of the feasible solution space is reduced by 1. In this case of M=2, the admissible switching angles is limited on a curved line, as depicted by black dotted line. Then the optimal switching angles (OSAs) associated with different modulation indices are obtained by computing the minimum cost function values along these lines, respectively. It can be seen in Fig. 4-3 that the optimal solution trajectory against the modulation index for Type A pulse pattern has two parts and is not continuous over the whole modulation index range. This is due to the nonconvex nature of the optimization problem. As shown in Fig. 4-4, the derived results for Type A pulse patterns have shown the discontinuity characteristic of the optimal switching angles and optimal distortion factor against the modulation index.
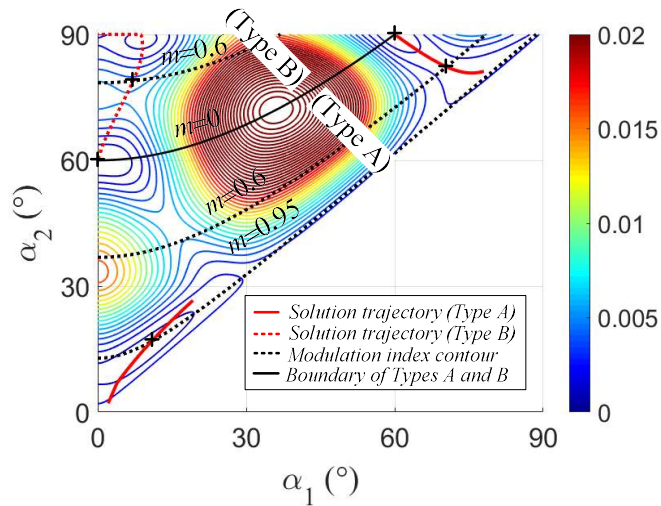
Fig. 4-3 The contour map of cost function $J(\alpha_i)$ for pulse pattern optimization and optimal solution trajectories against the modulation index, with switching angle number, $M=2$ ($N_p=5$). The optimal solutions associated with $m=0, 0.6, 0.95$ are indicted by plus symbols.

Additionally, one can find from (4-7) ~ (4-9) that the formulation of the pulse pattern optimization problem for Type A and Type B only differs in the modulation index constrain, (4-9). It effectively implies that when optimize Type B pulse patterns, the optimal switching angles are found along different curved lines from those for Type A, which stratify the desired modulation index requirements. This has been illustrated in Fig. 4-3 where the optimal solution trajectory for Type B is depicted by dotted red line. Furthermore, for higher pulse numbers, the optimization problem will exhibit the similar properties with the solution space of M dimensions and the constraint hyper-plane of M-1 dimensions.

(a)

(b)
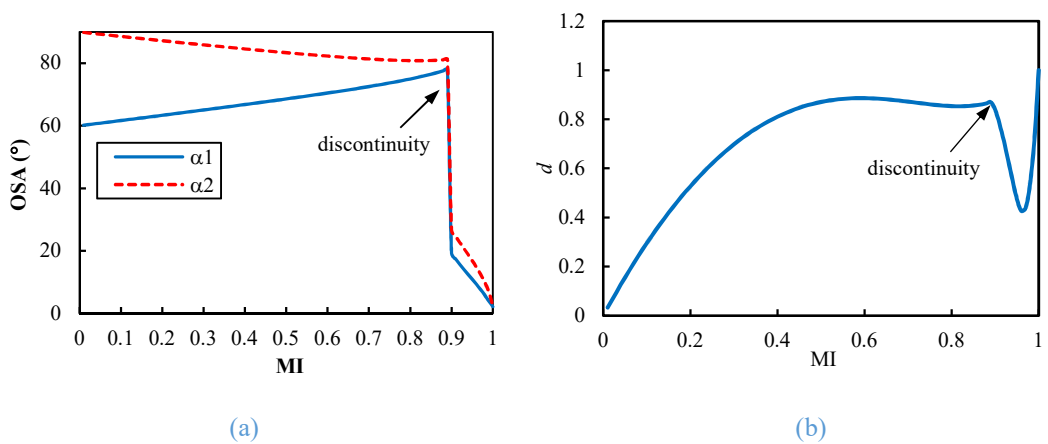
Fig. 4-4 Optimization results for Type A pulse patterns ($M=2$, $N_p=5$). (a) optimal switching angles (b) optimal distortion factor, d

4.2.3 An Improved Procedure for Pulse Pattern Optimization

4.2.3.1 Analytical gradient of the nonlinear constraint

It has been found in the optimization process that the gradient method can fail to find the local optimal solution for high pulse numbers if the initial value is not set appropriately. Hence, an excessive large number of repeats of optimization is needed to circumvent this problem, such as 25,000 times suggested in [111][118].

Based on the insights gained previously into the optimization problem, the problem can be attributed to the fact that the nonlinear constraint dictates an (*M*-1) dimension hyperplane which becomes very complex as the pulse number increases. Consequently, the linearization of the nonlinear constraint or numerically calculated gradient in the employed gradient method cannot guarantee that the solution iteratively changed along the feasible region so fail to search for the valid optimal solution. On the basis of this understanding, instead of using the numerically computed gradient by the gradient solver, the analytical gradients of the nonlinear constrain, (4-9) should be provided, as expressed in (4-10) ~ (4-12). In (4-10), the nonlinear equality constraints are rewritten in the form of $C_{eq} = 0$, where $\mp$ corresponds to Type A and Type B respectively. The element in the gradient vectors, (4-11) is provided in (4-12), where $i = 1,2,\cdots,M$.

$$C_{eq} = 1 + 2 \cdot \sum_{i=0}^{M} (-1)^i \cos \alpha_i \mp m^* = 0 \tag{4-10}$$

$$\nabla C_{eq} = \left[\frac{\partial C_{eq}}{\partial \alpha_1} \quad \frac{\partial C_{eq}}{\partial \alpha_2} \quad \cdots \quad \frac{\partial C_{eq}}{\partial \alpha_M} \right]^T \tag{4-11}$$

$$\frac{\partial C_{eq}}{\partial \alpha_i} = (-1)^i \cdot 2 \sin \alpha_i \tag{4-12}$$

With the analytical gradient of the nonlinear constraint, acquisition of the local optimal solution in each optimization can be guaranteed, independent of the pulse number and insensitive to the initial value setting. The repeat times of an optimization with random initial value can be greatly reduced to less than 100 even for high pulse number of 15, which will be demonstrated in section 4.2.4. As a result, the total computation time required for the pulse pattern optimization for all the pulse numbers and types over the whole modulation will decrease significantly.

4.2.3.2 Proposed computationally efficient optimization procedure

In this section, a computationally efficient optimization procedure is proposed. To obtain global optimal solutions, the optimization is performed in two rounds for a given pulse number and type.
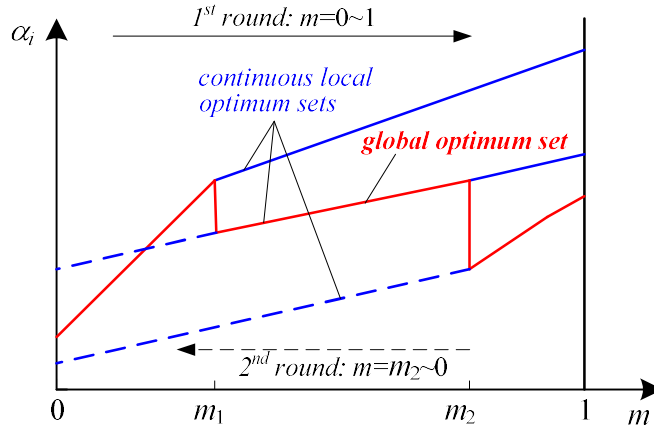
Fig. 4-5 Illustration of deriving the global optimal solutions and all the sets of continuous local optimal solutions during the optimization process. Solid lines denote the results obtained in the 1st round optimization while the dotted lines denote the results obtained in the 2nd round.

As illustrated in Fig. 4-5, the first round of the optimization starts at $m=0$ with a step of 0.01. At each modulation index, the optimization employs the gradient method with the analytical gradient of the nonlinear constraint so that a local minimum solution can be always obtained. At each modulation index, the optimization is performed with the global optimal solution at the previous modulation index as the initial values, referred to as predictive initial values. Moreover, the optimization is repeated with randomly set initial values as well. By comparison, record the best result as the global optimal solution for that modulation index.

As shown in Fig. 4-5, at some modulation indices, e.g. m_1, the OSA discontinuity would inevitably occur. In this case, record both the global optimal solution and the local optimal solution (referred to as the continuous local optimum) which is derived with the predictive initial values. In subsequent optimisations, the predictive initial values include both the global optimum and the continuous local optimum at the previous modulation index. Likewise, when the second OSA discontinuity occurs, record not only the global optimal solution but also all the continuous local optimal solutions obtained with the predictive initial values. As a result, the solutions represented in solid lines in Fig. 4-5 can be obtained in the 1st round optimization.

The 2nd round optimization starts at the highest modulation index where OSA discontinuity occurs. The modulation index then decreases by a step of 0.01and the optimisation repeats with the global optimal solutions at the adjacent modulation index to the right as predictive initial values. After the 2nd round optimization, all the solutions in the dotted lines in Fig. 4-5 can be acquired. Together with the results of the 1st round optimization, both the global optimal OSAs and the associated continuous sets of OSAs over the entire modulation index range can be obtained.

The flow chart of the proposed optimization procedure is shown in Fig. 4-6.
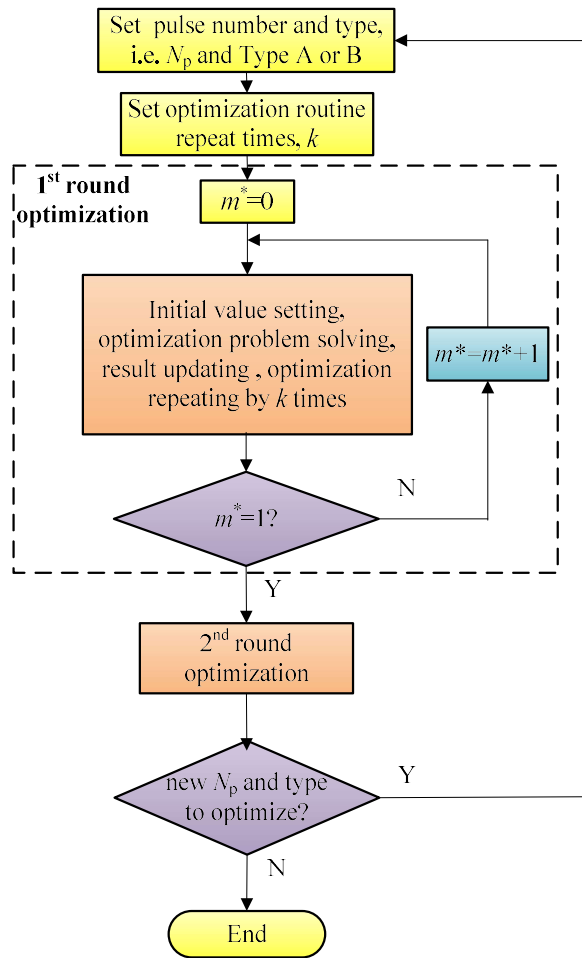
Fig. 4-6 The flow chart of proposed optimization procedure

With the proposed optimization procedure, the trade-off between the current distortion factors and the discontinuity of optimal switching angles can be readily made meanwhile it doesn't require tedious and time-consuming re-optimization as for the conventional optimization procedure [111][118]. By ways of example, the global optimal and sets of continuous local optimal solutions are shown in Fig. 4-7 (a) for the case with pulse number N_p=11 and Type A. For visibility, only the optimal switching angle, α_1 is

displayed. As can be seen, the global solution depicted in solid purple line consists of five parts, which correspond to the five sets of continuous optimal solution, respectively. By allowing small compromise in the current distortion, sets 1, 2 and 5 can be used to construct the optimal solution over the whole modulation index range, depicted in solid red line. It reduces the discontinuity number of the optimal switching angles from 4 to 2. However, if the pulse number varies only in a specific modulation index range e.g. $m=0.4\sim0.8$, one can only employ set 2 and the maximum deviation of the current distortion from the global optimal, which can be seen from Fig. 4-7 (b), is ~0.06 at $m=0.4$.

(a)   (b)
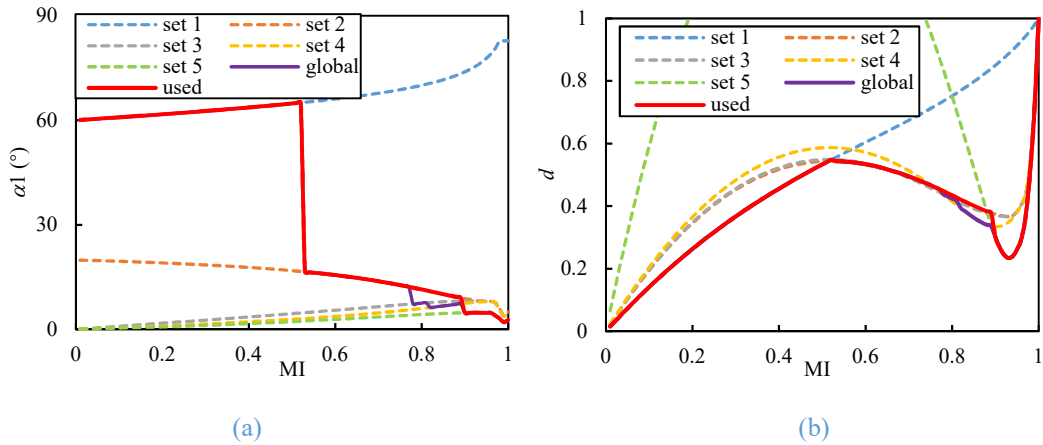
Fig. 4-7 The global optimal solution, sets of continuous local optimal solution, and the constructed optimal solution to use (N_p=11, M=5, Type A) (a) optimal switching angle, α_1. (b) optimal current distortion factor, d.

4.2.3.3 Application in Multi-Level Inverters

The QWS pulse pattern of SOPWM for three-level inverters exhibits only one pulse type, which is shown in Fig. 4-8 by the example with the prime switching angle number M=4 i.e. the corresponding pulse number N_p=2M=8.
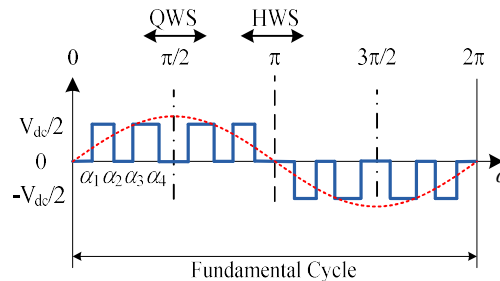
Fig. 4-8 Synchronous and symmetric terminal voltage of phase A for three-level inverters with M_α=4 and N_p=8.

146

The cost function and constraints for the pulse pattern of three-level inverters can be formulated in (4-13) ~ (4-15) and the gradient of the nonlinear constraint is given in (4-16). As can be seen, these expressions have the similar form as the two-level inverter, thus the optimization problem of three-level inverters will feature the same property as discussed previously for the two-level inverter.

$$min. \quad J(\alpha_i) = \sum \left(\frac{V_{n*}}{n}\right)^2 = \sum_{n=5,7,11,\cdots} \frac{1}{n^2} \cdot \left[\sum_{i=1}^{M}(-1)^i \cos n\alpha_i\right]^2 \qquad (4\text{-}13)$$

$$s.t. \quad 0 < \alpha_1 < \alpha_2 < \cdots < \alpha_M < \frac{\pi}{2} \qquad (4\text{-}14)$$

$$s.t. \quad -\sum_{i=1}^{M}(-1)^i \cos \alpha_i = m^* \qquad (4\text{-}15)$$

$$\frac{\partial C_{eq}}{\partial \alpha_i} = (-1)^i \cdot \sin \alpha_i \qquad (4\text{-}16)$$

For multi-level inverters with the voltage levels more than 3, there can be more possibilities of pulse type, e.g. 5 for five-level inverters [111]. Nevertheless, the pulse pattern optimization problem for each type is similar to that of two-level and three level inverters. Therefore, the proposed optimization procedure can apply to multi-level inverters as well, by modifying the cost function, constraints and the analytical gradient of nonlinear constraint accordingly.

4.2.4 Computation and Results of OPPs

The proposed optimization procedure has been employed to compute all the optimal switching angles for two-level inverters with pulse number ranging from 3 to 15 and both Type A and Type B pulse patterns. The number of repeats, k, for the optimization at a modulation index with given pulse number and type is set as $10+5M$, which increases for high pulse number cases and equals to 45 for $N_p=15$. The total computation time is approximately 1.5 h by MATLAB 2016b on a quadcore 3.3GHz PC.

In order to validate if the employed number of repeats is sufficiently high to find the global solution, the optimization for $N_p=15$ with Type A has also been performed with a larger number of repeats, i.e. $k=500$. As shown in Fig. 4-9, the same optimal solutions have been obtained over the whole modulation index range. However, the corresponding computation time increases by 12 times, from 0.3 h to 3.6 h. If the number of repeats is

25,000 as reported in [118], the computation time would be at least 180 h, which is more than 550 times greater than that of the proposed method.

Additionally, as can be seen in Fig. 4-10, with the proposed optimization procedure and k=45, the global optimal solution for N_P=15 with Type A can be found in one repeat over the majority range of modulation index. Large numbers of repeats are only observed at the modulation indices where discontinuities occur in the global optimal switching angles. Therefore, the effectiveness and fast optimization speed of the proposed optimization procedure has been confirmed.

(a)   (b)
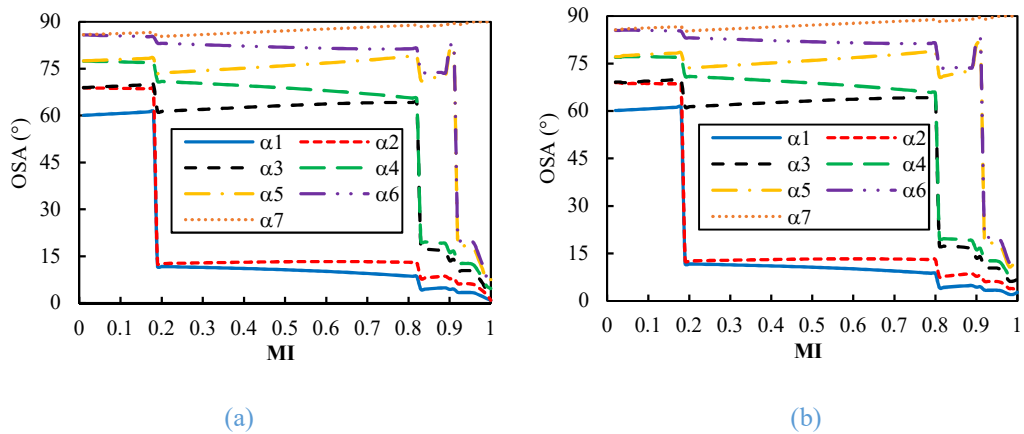
Fig. 4-9 The global optimal solutions obtained with different repeat times of optimization k for N_P=15 and Type A. (a) k=45 (b) k=500
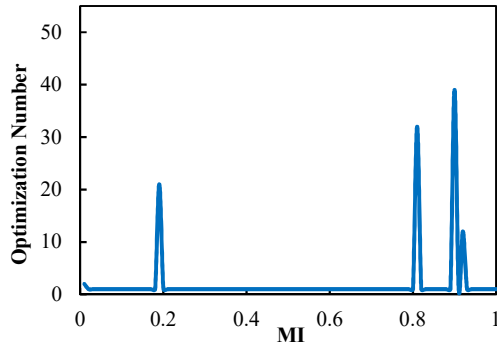
Fig. 4-10 Number of repeats to find the global optimal solution at different modulation indices with k=45 for N_P=15 and Type A.

By the proposed optimization procedure, all the global OSAs and the associated sets of continuous OSAs have been obtained for different pulse numbers and types. The trade-off between the OSA continuity and optimal current distortion has been made generally with the maximum compromise of 0.05 in current distortion factor. Hence, the derived OSAs will exhibit least discontinuity with acceptable small compromise in the current

distortion factor, as has been demonstrated in Fig. 4-7 (b). Fig. 4-8 shows all the derived optimal switching angles for pulse patterns of Type A.

(a)

(b)

(c)

(d)

(e)

(f)
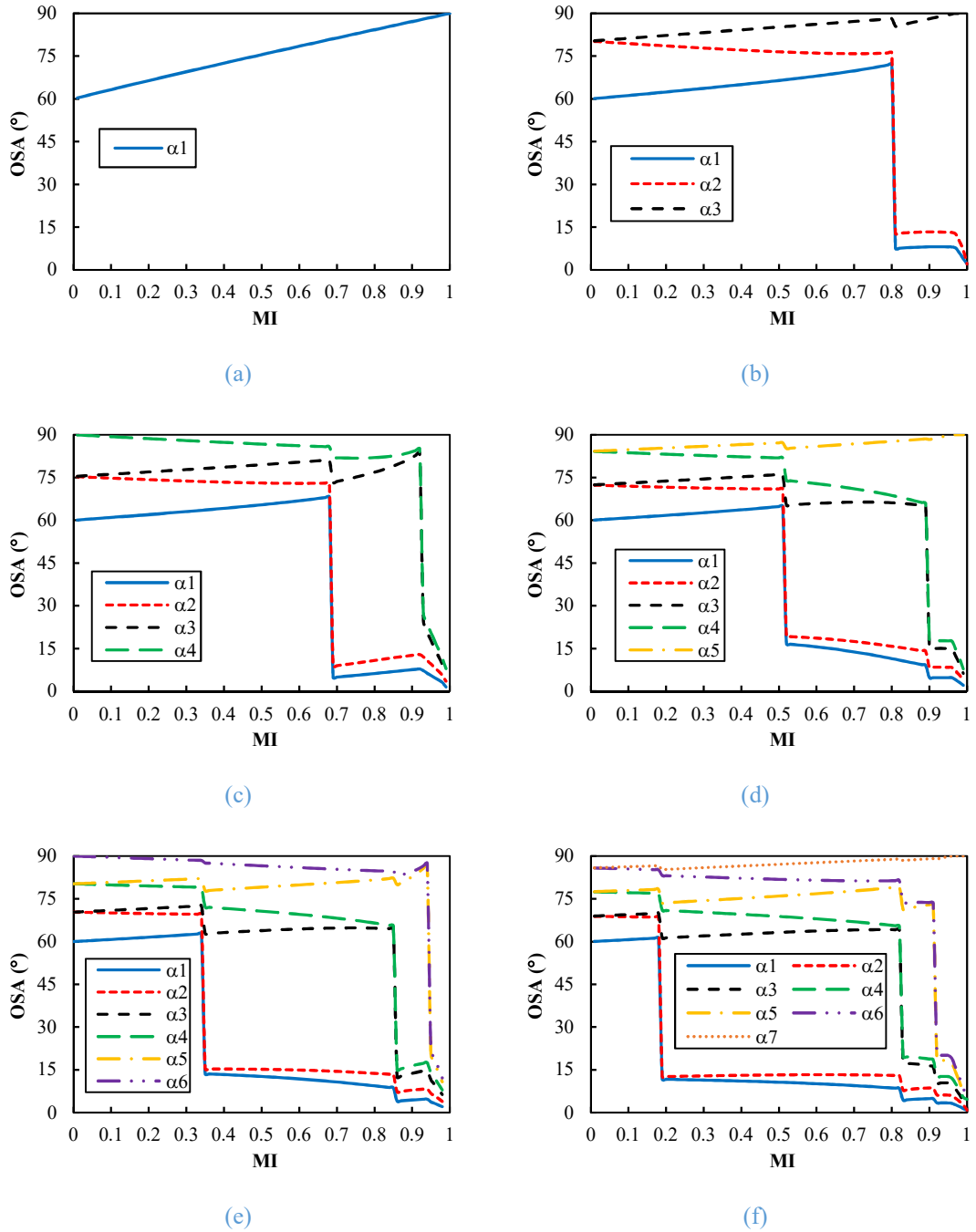
Fig. 4-11 Optimal switching angles for two-level inverters with pulse pattern of Type A. (a) M=1, N_p=3. (b) M=3, N_p=7. (c) M=4, N_p=9. (d) M=5, N_p=11. (e) M=6, N_p=13. (f) M=7, N_p=15. The OSAs for M=2, N_p=3 is shown in Fig. 4-4.

Similarly, the optimal results for Type B can also be obtained. Fig. 4-12 compares the optimal distortion factor with pulse patterns of Type A and Type B. As can be seen, for a given pulse number, the optimal distortion factor with Type A is less than that with Type B over the majority range of modulation index. However, it is worth noting that lower current distortion factors can be obtained with Type B over certain modulation index

149

ranges, e.g. m=0.9~1 for N_p=3. As shown in Fig. 4-13, the combination of the OSAs associated with Type A and B will inevitably cause more discontinuity, which will result in undesired transients in real-time control of drive [105]. However, as evident in Fig. 4-12, the improvements that can be achieved by employing both Type A and Type B decrease as the pulse number increases. Thus, in order to reduce the OSA discontinuity, Type A can be generally employed for all the pulse numbers while Type B can be incorporated in for low pulse numbers subjective to the specific application.
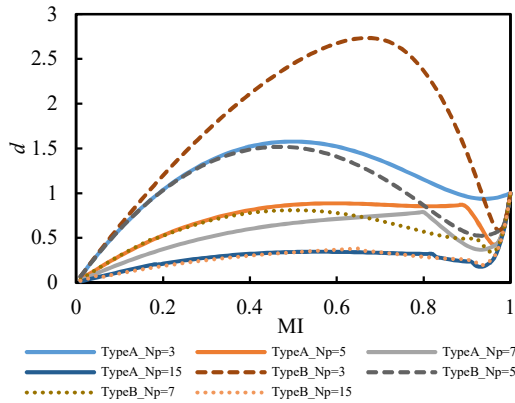
Fig. 4-12 Comparison of optimal current distortion factors of OPPs with Type A and Type B under different pulse numbers
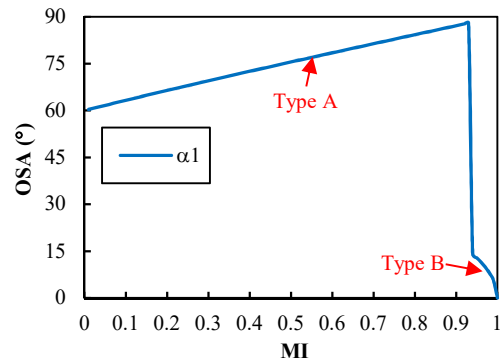
Fig. 4-13 Derivation of the OSAs over the whole modulation index range by combination of the OSAs for Type A and Type B (M=1, N_p=3)

Fig. 4-14 summarizes the optimal current optimal distortion factors associated with the derived OSAs where the switching angles shown in Fig. 4-13, Fig. 4-4 and Fig. 4-8 (b)~(f) are employed respectively for different pulse numbers. These sets of OSAs can be employed as the general OSAs for two-level inverters. The associated OSA discontinuity numbers over the whole modulation index are 1 for N_p=3~7, 2 for N_p=9,11 and 3 for N_p=13,15.
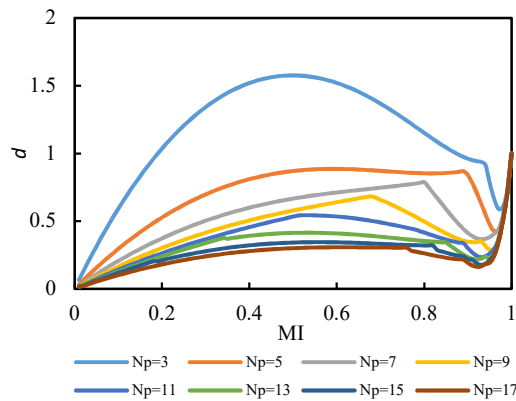
Fig. 4-14 Optimal distortion factor d as a function of modulation index under different pulse numbers

4.2.5 Implementation of OPPs based SOPWM

The offline optimized OSAs and the associated pulse type determine the OPPs and can be stored in look-up-tables for the real time motor control. Fig. 4-15 shows the implementation block diagram of SOPWM, where the input is the reference voltage vector and the outputs are the gate drive signals. The gate drive signals of SOM can be generated by comparing the reference phase voltage angle with the OSAs. Therefore, the conversion of a voltage vector to its magnitude and angle, and high-speed comparators and integrator are required. These processes need to be executed at very high rate and can be implemented on a FPGA. By contrast, the reference phase angles, $\varphi_{uA}{}^*$, $\varphi_{uB}{}^*$, $\varphi_{uC}{}^*$ and the OPPs are being updated at a low rate, the same as the sampling frequency, T_s. Additionally, to compensate the sampling and calculation delay, the reference voltage angle is forwarded by $\omega_e T_s$.
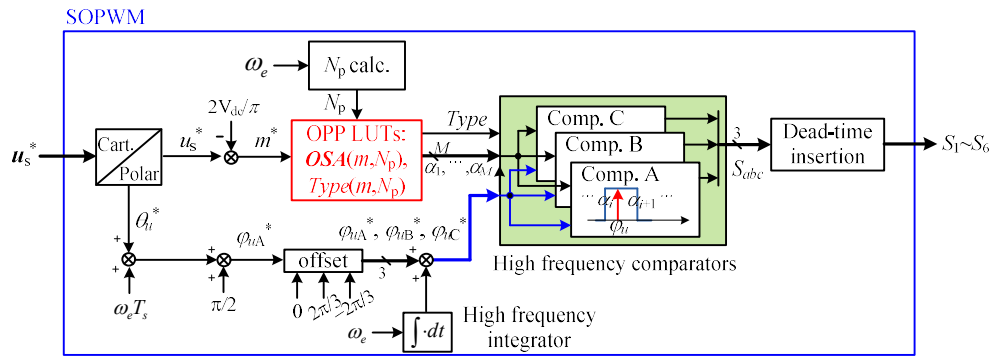
Fig. 4-15 Block diagram illustration of the real-time implementation of SOPWM

The pulse number, N_p, is determined by the electrical speed, ω_e, so that the associated switching frequency would not surpass the maximum permissible switching frequency, f_{sw_max}, according to

$$\frac{1}{N_p + 1} \leq \frac{\omega_e}{2\pi f_{sw\_max}} \leq \frac{1}{N_p} \tag{4-17}$$

When the pulse number is larger than 15, SVM is employed as the improvement in the current distortion is negligible with SOPWM.

Fig. 4-16 shows the schematic of the SOPWM implemented in the high-speed SPMSM drive system with FOC. As can be seen, it has the similar structure with SVM based FOC and the transitions between the two can be made according to the speed. At low speed where the ratio of the maximum switching frequency to the fundamental frequency is greater than 15, SVM will be employed. However, the transition from SVM

to SOPWM or vice versa can incur undesired transients. Additionally, the system dynamic performance deteriorates when SOPWM is used because the optimization of OPPs is based on steady-state states. The problem can be eased by avoiding step changes of dq axis current references and adding filters to the input reference voltage vector of SOM [120] or simply reducing the bandwidth of the current PI regulator. These measures, however, are not applicable to high-speed SPMSM drives where high current control bandwidth and high dynamic response are crucial. The fast dynamic control with SOPWM will be investigated in the next chapter.
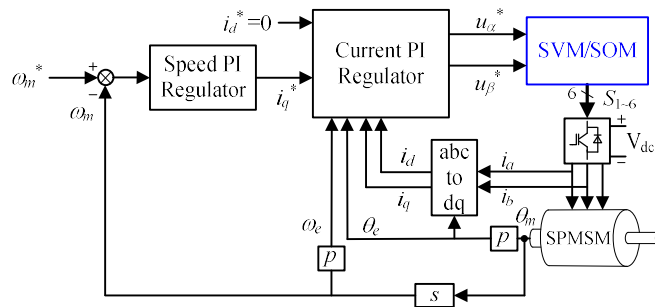
Fig. 4-16 Block diagram of the high-speed PMSM drive system with SVM or SOPWM

4.2.6 Simulation Study

To verify the improvement of current harmonic distortion using SOPWM, extensive simulation has been performed on the high-speed prototype SPMSM in MATLAB/SIMULINK, whose parameter are given in section 2.1. In the simulation, the DC voltage is set to 200 V and the inverter nonlinearity influence is not considered. In the transients with step changes in the q axis current, FOC with SVM and high current control bandwidth of 500 Hz is employed. Subsequently when the steady state is reached, the PWM scheme is switched from SVM to SOPWM and the current control bandwidth of FOC is also reduced to a low value, i.e. 100 Hz, to constrain the system dynamic and generating a smooth reference voltage vector. The sampling frequency is set to twice the switching frequency in both the PWM schemes. The high-speed motor is operated in the constant speed of 30,000 rpm, corresponding to the fundamental frequency of 1 kHz, with current control. The switching frequency and the q-axis current demands have been varied to simulate the scenarios with different pulse numbers and modulation indices and i_d=0 control is used throughout the simulation. The harmonic current, I_h is calculated from the product of the current THD and fundamental current.

(a)   (b)
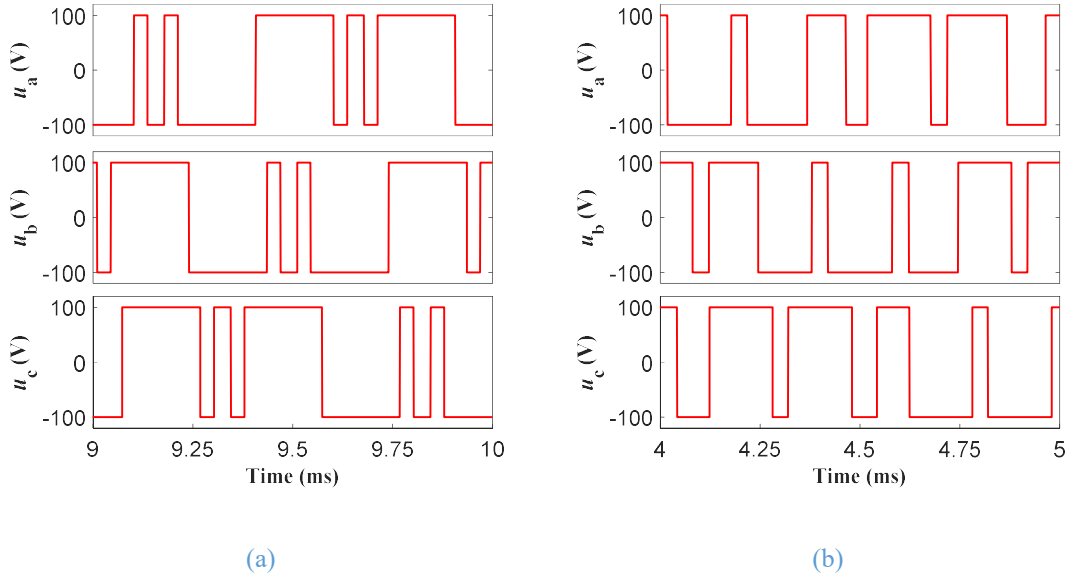
Fig. 4-17 The three-phase terminal voltages at 30,000 rpm with m=0.59 and f_{sw}=5 kHz (N_p=5) (a) SOM (b) SVM

(a)   (b)
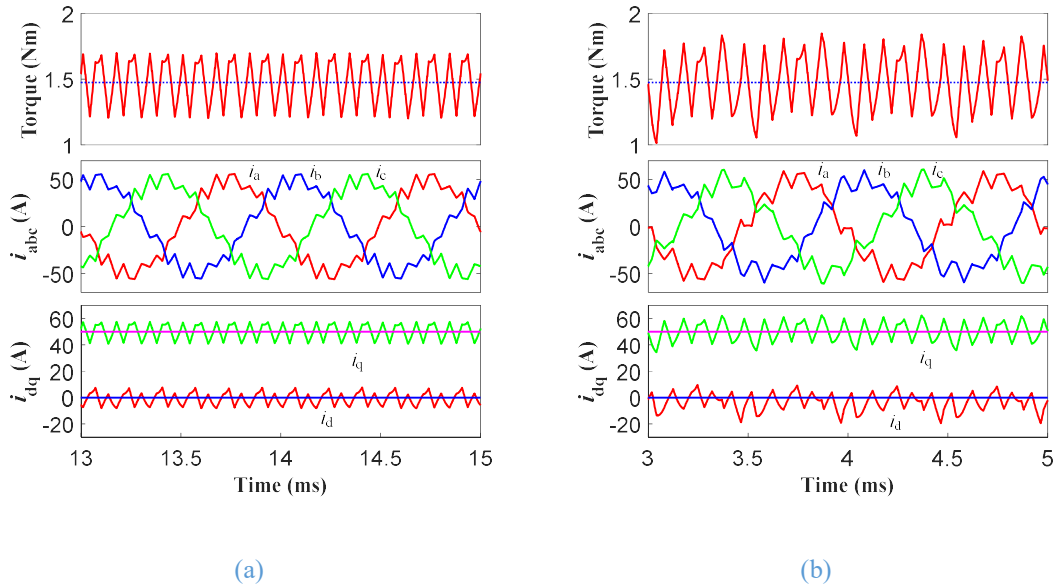
Fig. 4-18 The torque, phase currents, dq axis currents at 30,000 rpm with m=0.59 and f_{sw}=5 kHz (N_p=5) (a) SOM (b) SVM

(a)   (b)
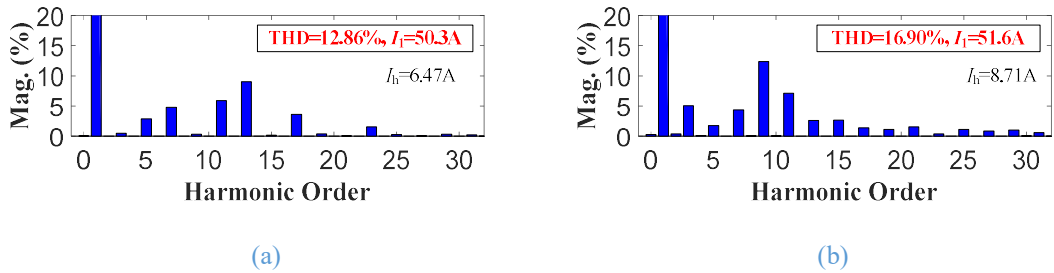
Fig. 4-19 Phase A current spectrum at 30,000 rpm with m=0.59 and f_{sw}=5 kHz (N_p=5) (a) SOM (b) SVM

153

Fig. 4-17~Fig. 4-19 shows the simulation results with the q axis current demand of 50 A (m=0.6) and the pulse number N_p=5, i.e. f_{sw}=5kHz. As can be seen in Fig. 4-17 (a), with SOPWM, the three phase terminal voltages feature QWS, HWS and 3PS and as a result, all the even and triplen current harmonics are eliminated in the phase current spectrum shown in Fig. 4-19 (a). Compared to the results with SVM in the same condition, the high-speed motor under SOPWM exhibits less current THD and current ripples in Fig. 4-18. It is worth noting that the triplen current harmonics such as 3rd and 9th in Fig. 4-19 (b) with SVM is because the three-phase voltage waveforms are not symmetrical with SVM under the scenario with low pulse numbers.

Fig. 4-20 (a) and (b) compare the phase currents, phase terminal voltage and current harmonic spectrum under the two modulation schemes with the q axis current reference of 115A (m=0.88) and the pulse number N_p=9, i.e. f_{sw}=9kHz. As can be observed, the harmonic currents decrease with the increased switching frequency compared to the case with N_p=5. The SOPWM is still better than SVM, with more than half of the harmonic currents being reduced. Moreover, as demonstrated in Fig. 4-20 (c), to achieve the similar current THD as the SOM at this operating point, the switching frequency of SVM has to be nearly doubled, to 20 kHz.

(a)   (b)   (c)
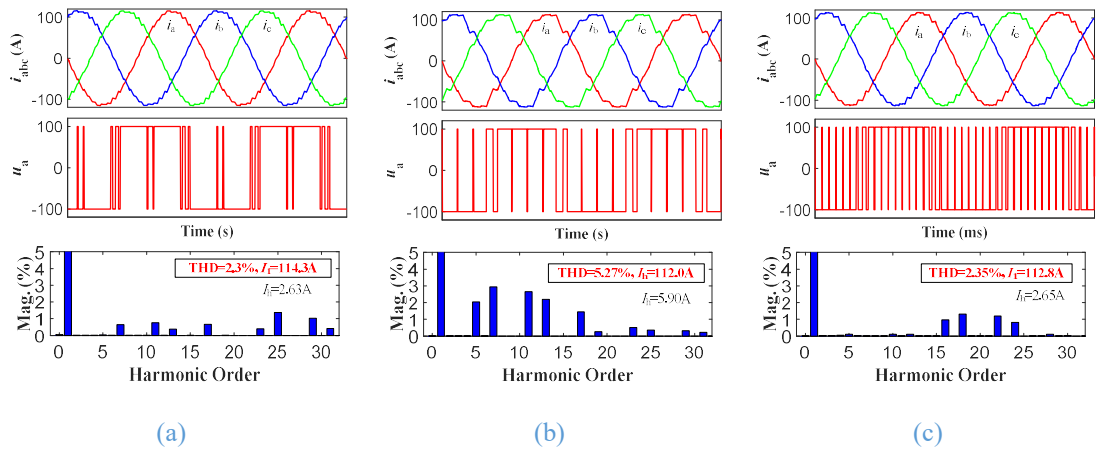
Fig. 4-20 Phase currents, phase A terminal voltage and current spectrum at 30,000 rpm with m=0.88
(a) SOM with f_{sw}=9kHz (N_p=9) (b) SVM with f_{sw}=9kHz (c) SVM with f_{sw}=20kHz

The influence of the modulation index and pulse number have been investigated as well. As can be seen in Fig. 4-21 (a), with a given pulse number, the improvement of the current harmonic distortion by SOM become more remarkable in high modulation index range. It is due to the fact that the harmonic current with SVM increase at high modulation index [95] while that with SOM will decrease or maintain after the modulation index reaches a given value before rising again in over-modulation region, which is essentially

governed by the optimal current distortion factor curves in Fig. 4-14. On the other hand, as evident in Fig. 4-21 (b), at a certain modulation index, the differences of the two PWM schemes with respect to the current harmonic distortion become less pronounced with high pulse numbers. Therefore, the SOM is more attractive for operation with high-modulation indices and small pulse numbers. This characteristic matches well with the high-speed PMSM drives, of which the modulation index is high at high speeds with high fundamental frequency.

(a)   (b)
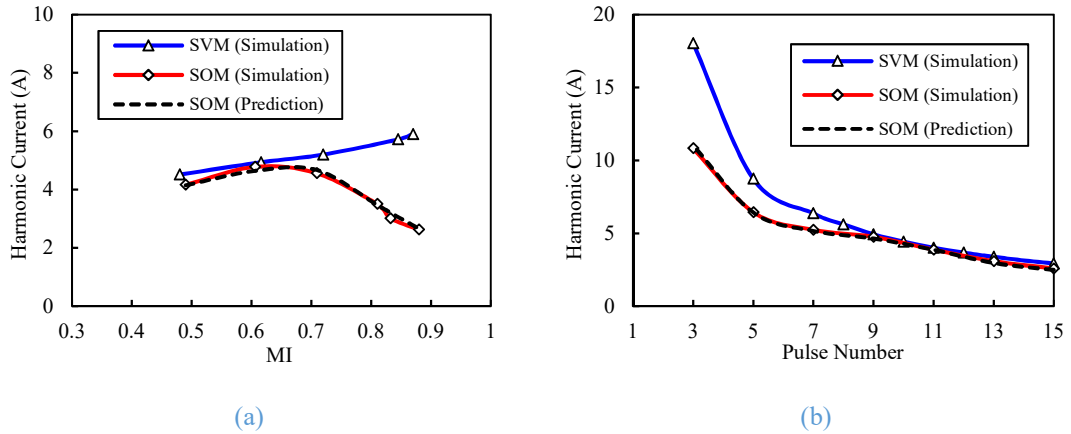
Fig. 4-21 Phase harmonic current, I_h as a function of (a) modulation index with N_p=9 (b) pulse number at m=0.6

4.2.7 Fast Prediction of Switching Harmonic Current with SOM

As the switching-to-fundamental frequency ratio is very low in high-speed PMSMs, it would lead to excessive and unacceptable current distortions. As discussed and verified previously, SOM can provide the minimum current THDs. Therefore, evaluation of the harmonic currents of high-speed PMSMs under SOM can give the information of the achievable lowest current distortion for the employed power converter hardware. It can provide a design reference if the hardware schemes are required to improve, such as design modification of the motor and adoption of passive filters, multi-level inverters and high switching frequency SiC MOSFETs.

Usually, the current harmonic distortion of the motor drive can be obtained by time-domain simulation. However, it requires substantial simulations to cover all the possible scenarios and the complex procedure needs to be repeated when the parameters of the

high speed drive change. To this end, a simple harmonic current prediction method for the high-speed drive under SOM is developed in this subsection.

The optimal current distortion factor d defined in (4-6) is independent of the machine parameter and only determined by the voltage pulse patterns. It is effectively a function of pulse number and modulation index, denoted as $d(m, N_p)$ and can be plotted in Fig. 4-14. Therefore, according to the definition (4-6), the actual steady-state harmonic current I_h of any drive employing the OPPs can be derived as

$$I_h = d(m, N_p) \cdot I_{h\_6S} \qquad (4\text{-}18)$$

where the harmonic current under the six-step operation, I_{h_6S} can be derived as (4-19), which relates to the DC-link voltage, machine inductance, L_s and electrical speed ω_e.

$$I_{h\_6S} = \frac{9.28\% V_{dc}}{\pi \omega_e L_s} \qquad (4\text{-}19)$$

For the high-speed SPMSM with i_d=0, the q axis current can be derived from the electromagnetic torque, T_e as

$$i_q = \frac{2T_e}{3p\psi_m} \qquad (4\text{-}20)$$

The fundamental stator voltage magnitude can be obtained as

$$u_s = \sqrt{\left(\omega_e \psi_m + R i_q\right)^2 + \left(\omega_e L_q i_q\right)^2} \qquad (4\text{-}21)$$

By combing (4-20) and (4-21) and normalized by $2V_{dc}/\pi$, the modulation index in (4-18) can be obtained, which is a function of the operating point of the drive i.e. T_{em} and ω_e. Alternatively, the mechanical speed n can be employed with $\omega_e = \pi n/30$.

The pulse number in (4-18) can be readily determined by the motor speed n or ω_e, subjective to the constraint of the maximum permissible switching frequency. Fig. 4-22 illustrates the developed harmonic current prediction method, where the LUTs of the optimal distortion factor are acquired from the offline optimization of SOM.
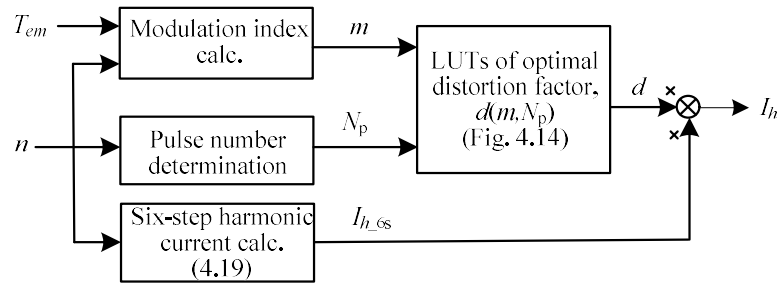
Fig. 4-22 Prediction of the harmonic current with SOM in steady states

The harmonic current predictions have been performed at the same conditions of the simulations in Fig. 4-21, where the modulation index and pulse number are varied. As evident in Fig. 4-21, the proposed prediction method can accurately predict the harmonic currents under SOM.

Further, the harmonic current prediction method can apply to the high-speed drive over a wide speed and torque range, where SOM is applied. Fig. 4-23 shows the operating torque and speed envelope and the modulation index contour of the prototype high-speed SPMSM as a starter and generator for aerospace gas turbine, with the DC-link voltage of 200V and without flux weakening. The motoring region is 0~30 krpm with the max torque of 3Nm and the generation region is 36~50 krpm with the required power of 5kW. As can be seen in Fig. 4-23, the modulation index at the highest speed is still below 0.8 thus a voltage margin for the prototype high-speed drive can be maintained with the DC-link voltage of 200V, ~75% of the nominal 270V.
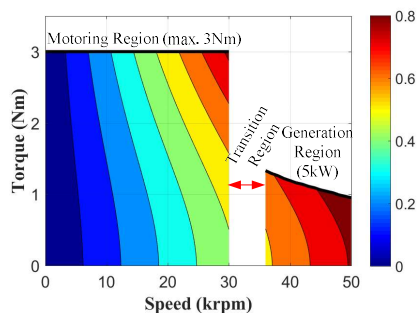
Fig. 4-23 Operation envelop and modulation index contour of the prototype high-speed drive
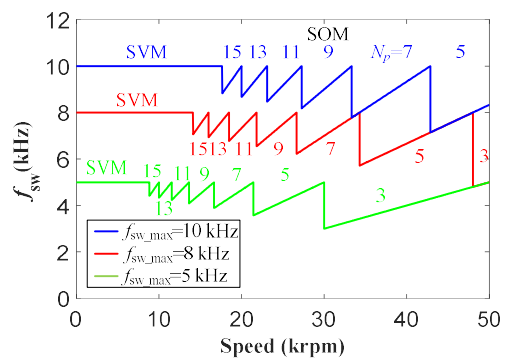
Fig. 4-24 PWM scheme and the associated switching frequency curves over the whole speed range under different switching frequency constraints.

Instead of using current THD, the figure of merit, TDD (total demand distortion) usually used in industry standard is employed. It is defined as the harmonic current normalized to the maximum current, i.e. 100 A for the prototype drive. With the PWM

schemes under the different switching frequency constraints shown in Fig. 4-24, the proposed method can quickly calculate the corresponding TDDs of the drive over the entire high-speed region with SOM, as shown in Fig. 4-25 respectively. With Fig. 4-25, both the worst scenario and the distribution of the TDDs can be known for a given switching frequency constraint. With the max switching frequencies of 5 kHz, 8 kHz and 10 kHz, the TDDs of the prototype drive in the high-speed region are around 4%~10%, 4%~6% and 4%~5%, respectively. For the convenience of visibility, the TDD contour can be plotted as well, e.g. Fig. 4-26 (a) for f_{sw_max}=8kHz.

(a)   (b)   (c)
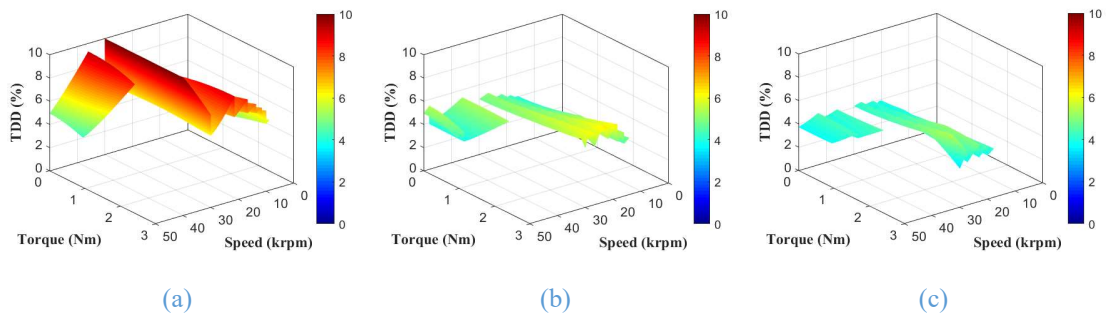
Fig. 4-25 TDD of the prototype high-speed drive over high-speed region with SOM (a) f_{sw_max}=5kHz (b) f_{sw_max}=8kHz (c) f_{sw_max}=10kHz

(a)   (b)

(c)
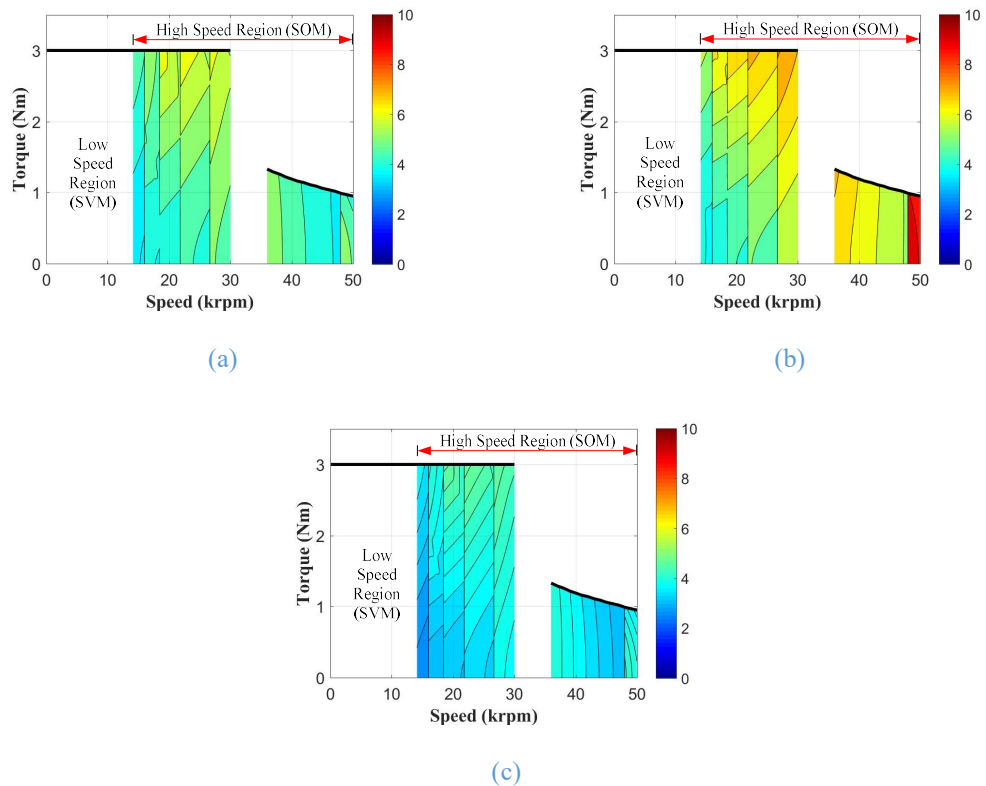
Fig. 4-26 TDD contours of the prototype high-speed drive over high-speed region with SOM (f_{sw_max}=8kHz) (a) 200VDC (b) 270VDC (c) 270VDC with increased winding turns

Fig. 4-26 (a) and (b) compare the TDD distribution with the DC-link voltages of 200V and 270V under the same max switching frequency of 8 kHz. As can be seen, if the original design voltage, i.e. 270VDC is employed, the TDDs over the high-speed region would increase to 4%~10%. This is because of the increase of the six-step current harmonics and the low operating modulation indices. The designed operating modulation index at 270V DC link voltage and the nominal maximum speed is only ~0.6. It can provide a large safe margin in the high speeds, since even at the 50% over-speed the inverter's diodes cannot be forward biased, avoiding uncontrollable rectification. However, this over designed voltage margin increases the current distortion. As shown in Fig. 4-26 (a), operation with reduced DC voltage such as 200V can reduced the current distortion if the motor can be safely disconnected when 13% over-speed occurs. On the other hand, it implies that the prototype high-speed motor design can be modified with increased winding turns. The resultant increases in the inductance and modulation index can both help to reduce current distortions. Fig. 4-26 (c) shows the TDD distribution of the modified design of the prototype high-speed motor, of which the winding turns increase from 16 to 21 and the highest modulation index becomes 0.8 at 50,000 rpm. As evident, the current TDD is reduced more than half to 3%~4.5% over the high-speed region. This is more effective than the operation with reduced DC voltage since the inductance rises proportionally to the square of the winding turns and consequently the six-step harmonic currents, I_{h_6S}, is also lower than that in Fig. 4-26 (a).

As demonstrated above, the proposed current harmonic prediction method based on the optimal current distortion factors can serve as a computationally efficient tool to assess the TDDs of high-speed drives with SOM over high-speed region.

4.2.8 Real-time HIL Testing and Experiment Results

In order to test the effectiveness of SOM and control strategies in real-time, a hardware-in-the-loop (HIL) model has been built for the prototype high-speed drive. According to the electromagnetic finite element (FE) simulation of the prototype motor, the inductance of the prototype high-speed motor is almost constant within the operating range, hence the conventional linear model of PMSM are employed. The permanent magnet flux linkage is obtained from the FE simulation but has been calibrated based on the measured back EMF. The measured phase inductance and resistance are used. The high-speed motor model are being implemented in the CPU of the real-time digital simulator, RT OPAL5600 by time-step of 25 μs. The inverter nonlinearity influence on

the high-speed drive is ignored and the average model of inverter is employed. The motor control algorithm is also running in the CPU while the signals between the motor emulator and controller are not interfaced directly as the delay effect is a critical factor in high-speed drives and should be correctly represented. The typical one time-step sampling and processing delay in an actual motor drive system has been considered and modelled.

Fig. 4-27 (a) shows the hardware of the HIL test rig. Fig. 4-27 (b) illustrates the layout of the developed real-time HIL testing program, which encompasses the motor emulator and the motor controller under testing. With the digital-to-analogue and digital output functions of RT OPAL5600, the signals including three-phase currents, motor position and PWM signals can also be physically output and captured in an oscilloscope for real-time observation. It should be noted that since the motor emulator is implemented in the CPU with the time-step of 25 μs (40 kHz), the relative data resolution of the output phase current signals with regards to the fundamental cycle of motor reduces as the motor speed increases. Implementing the motor emulator in the FPGA of OPAL 5600 can provide improved resolution of current data, which is only limited by the updating rate of DAC module, i.e. 2.5 μs for the present hardware. However, the developed CPU based HIL model suffices to verify the performance of the control algorithm as the accuracy of the current information at sampling instants can be guaranteed for the motor controller. Moreover, the dominated current harmonics are of low orders and the sampling frequency of 40 kHz is sufficient to capture these low order harmonics.

(a)   (b)
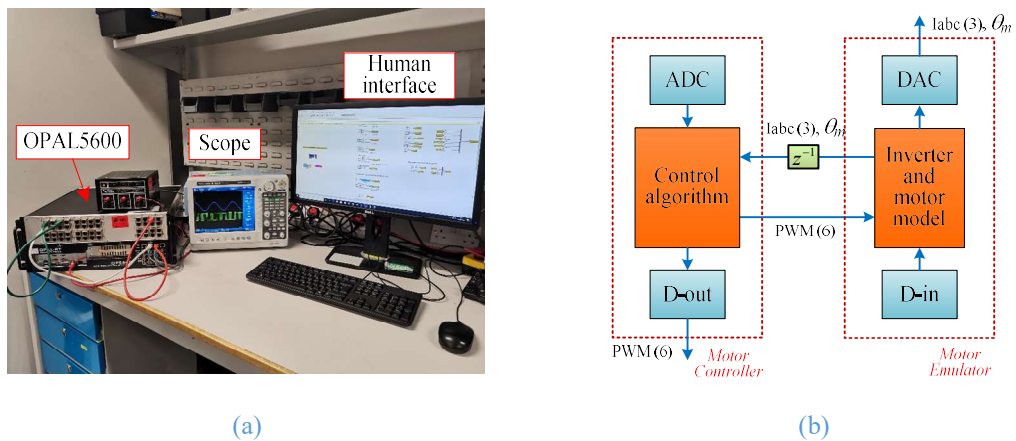
Fig. 4-27 The developed HIL test rig (a) the hardware (b) the software layout

Fig. 4-28 show the HIL testing results of the high-speed prototype motor with SOPWM in steady states at 30,000 rpm with pulse number of 7 and 15, respectively. As can be seen the phase voltage can be generated symmetrically and as a result, the phase currents exhibits the minimum current harmonic distortions for the given pulse numbers.

(a)   (b)
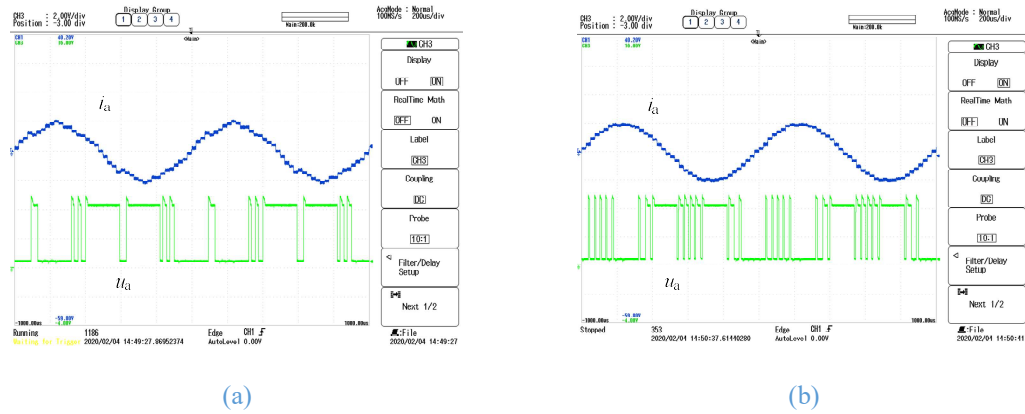
Fig. 4-28 The HIL testing results at 30,000 rpm (a) N_p=7 (b) N_p=15

Further, the experiments with SOPWM has been conducted on the prototype high-speed machine. In the testing, the DC-link is set to 100V and the high-speed machine is operated at the constant speed of 10,000 rpm. The q axis current reference is set to 25 A while d axis current reference is set to 0. The operating modulation index is 0.4.

Fig. 4-29 compares the phase currents in steady states and the current spectrum of phase A using SOPWM and SVM with N_p=15. As can be seen, SOPWM exhibits lower current THDs and the even switching harmonics i.e. 14th and 16th in the current spectrum of SVM can be eliminated.

(a)   (b)
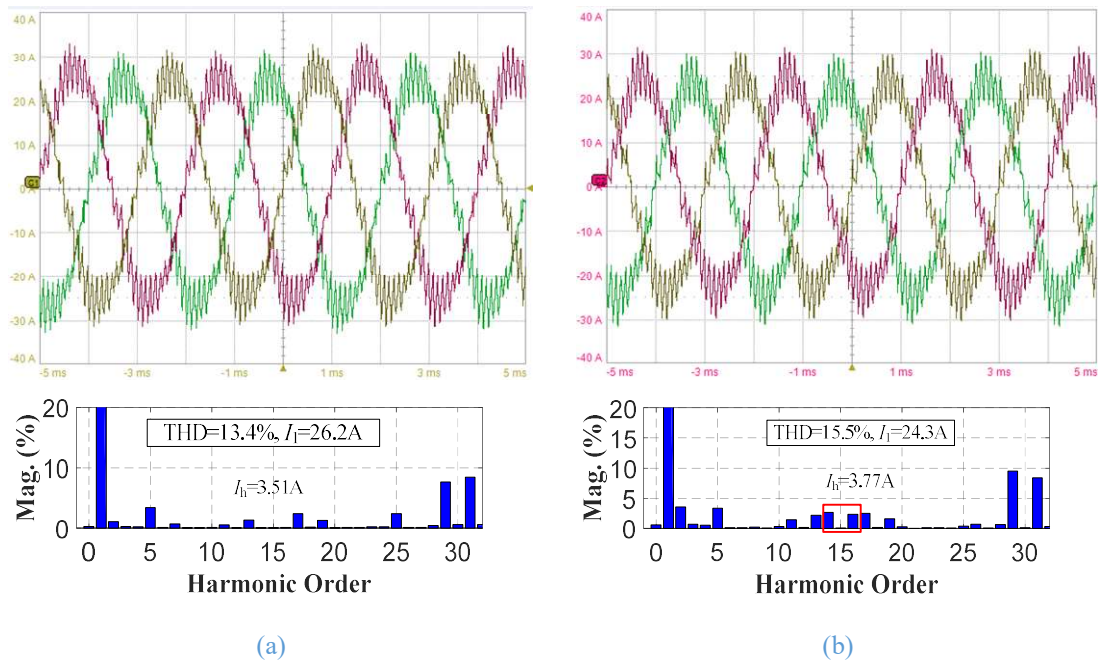
Fig. 4-29 Phase currents and current spectrum with Np=15 at 10,000 rpm (a) SOPWM (b) SVM

The experiment results of SOPWM with different pulse numbers at 10,000 rpm are shown in Fig. 4-30. As can be seen, the phase currents with SOPWM are always symmetric and only consist of non-triplen harmonics at all the pulse numbers due to the

161

synchronous and symmetric switching. The terminal phase voltages of SOPWM with N_p=15 and N_p=7 are plotted in Fig. 4-31 (a) and (b), respectively. The QWS, HWS and 3PS symmetries can be observed. Therefore, the effectiveness of SOPWM can be confirmed.

(a)

(b)

(c)

(d)

(e)   (f)
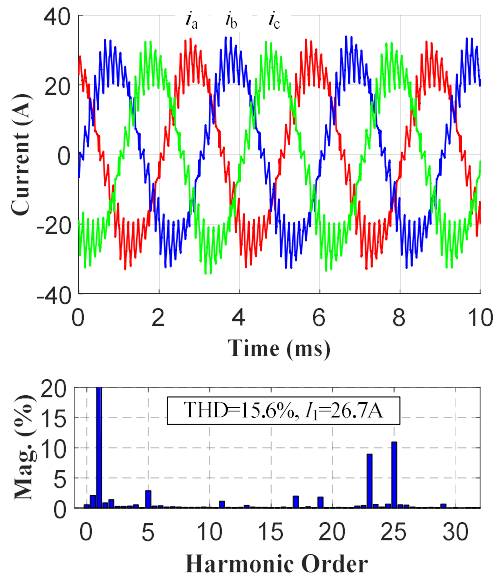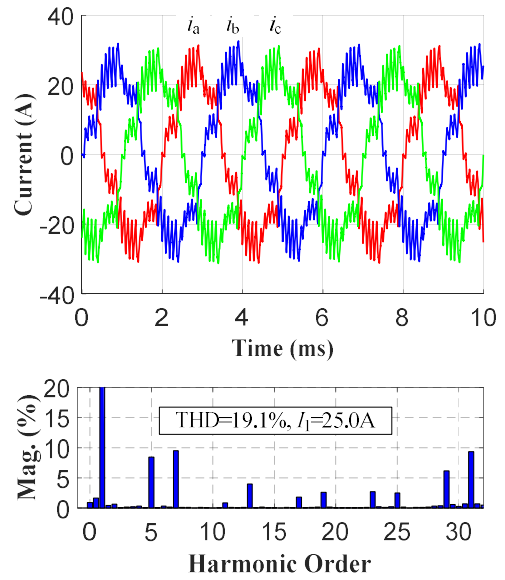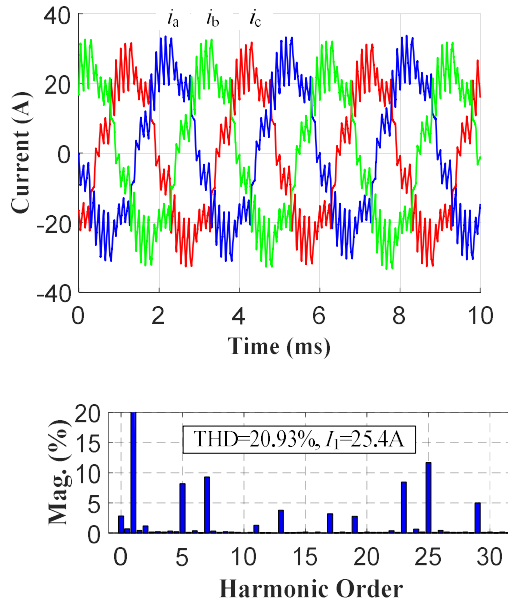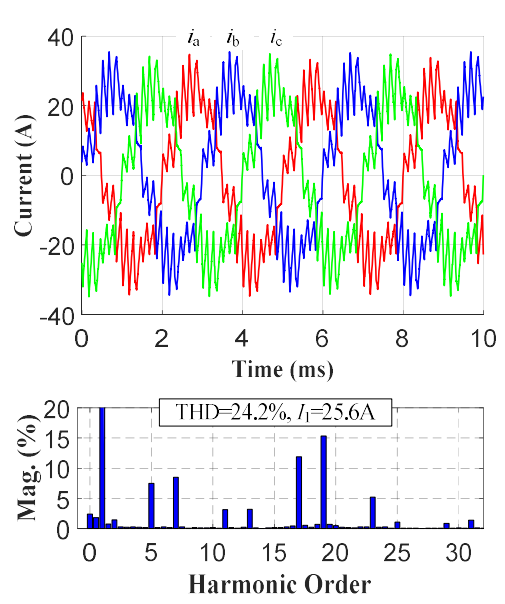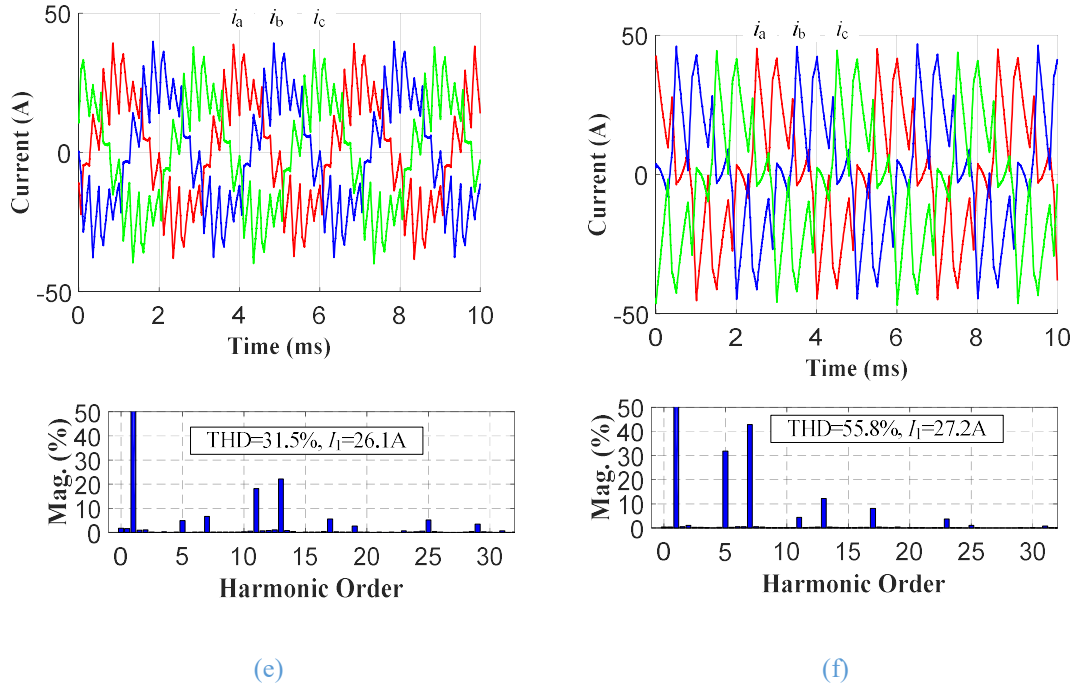
Fig. 4-30 Phase currents and current spectrum with different pulse numbers at 10,000 rpm (a) N_p=15. (b) N_p=13. (c) N_p=11. (d) N_p=9. (e) N_p=7. (f) N_p=3.

(a)   (b)
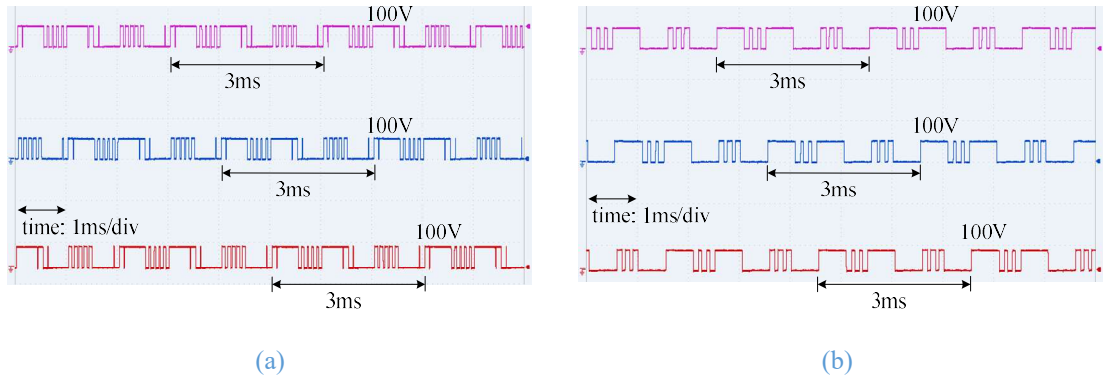
Fig. 4-31 Phase terminal voltages at 10,000 rpm (a) N_p=15. (b) N_p=7.

Fig. 4-32 plots the harmonic currents of SOPWM with different pulse numbers at 10,000 rpm, calculated from the current THD and fundamental current shown in Fig. 4-30 and Fig. 4-29. Meanwhile, the harmonic currents predicted by the proposed method in section 4.2.7 are also included in Fig. 4-32. As can be seen, the proposed harmonic current prediction method for SOPWM can give satisfactory accuracy. The small error between the experiment and prediction results can be attributed to that the inverter nonlinearity and back EMF harmonics caused current distortion are not accounted in the prediction. On the other hand, the consistency between the predicted and measured harmonic currents also verify the correctness of the simulation studies in section 4.2.6.
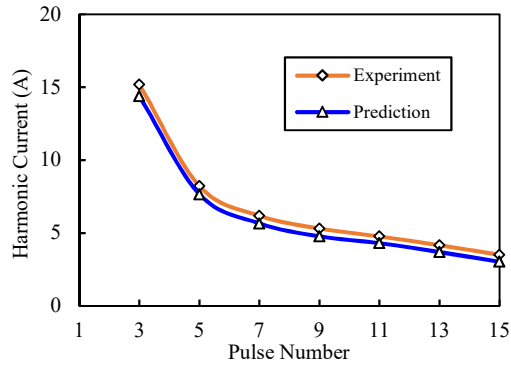
Fig. 4-32 Comparison of measured and predicted harmonic currents with SOPWM at 10,000 rpm (m=0.4)

4.3 Smooth and Fast Mode Transition Strategy for SOPWM

In this section, the SOPWM mode transition will be investigated. Firstly, the different modes of SOPWM is introduced. Secondly, the influence of the SOPWM mode transition, i.e. dynamic current errors are analysed. Subsequently, optimal switching vector patterns (OSVPs) and optimal flux trajectories (OFTs) associated with SOPWM are constructed and studied, based on which a smooth and fast mode transition method is then proposed. Finally, extensive simulation and experiment results validates the effectiveness of the propose method.

4.3.1 Different Modes of SOPWM
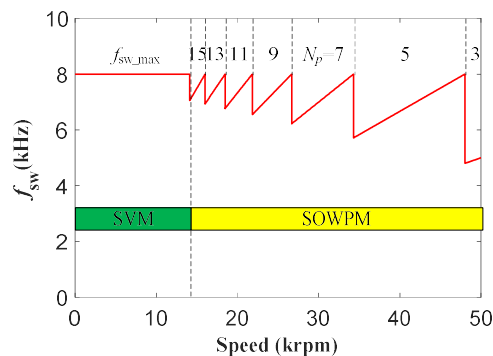
Fig. 4-33 PWM scheme over the entire speed range of a 4-pole high-speed PMSM drive

In variable-speed drives, the pulse number of SOPWM is determined by the switching frequency limitation and operating electrical speed. Fig. 4-33 gives an example of the pulse number variation scheme of a 4-pole high-speed PMSM drives with maximum switching frequency of 8 kHz. As can be seen, pulse number transition will inevitably occur at certain speeds.

In real-time control of electrical drives, the OPPs pertinent to different pulse numbers over the corresponding modulation range are being stored. Fig. 4-34 (a) shows the simplified diagram of SOPWM based on LUTs of OPPs, where m^* and φ_A^* are the reference modulation index and phase A voltage angle, calculated from the reference voltage vector, $\boldsymbol{u}_s^*$. The drive pulse generation for phases B and C are same. The continuity of the reference modulation index and phase angle are usually required so that the OPPs can be generated in real-time. For this purpose, SOPWM has been employed in conjunction with v/f control [139], FOC with limited bandwidth and reference voltage filtering [120], feedforward voltage control [140] and self-control [104]. Therefore, as can be seen in Fig. 4-34 (c), with the slowing changing reference voltage phase angle and OSAs, the generated drive pulse will always approach to the OPPs.

(a)   (b)   (c)
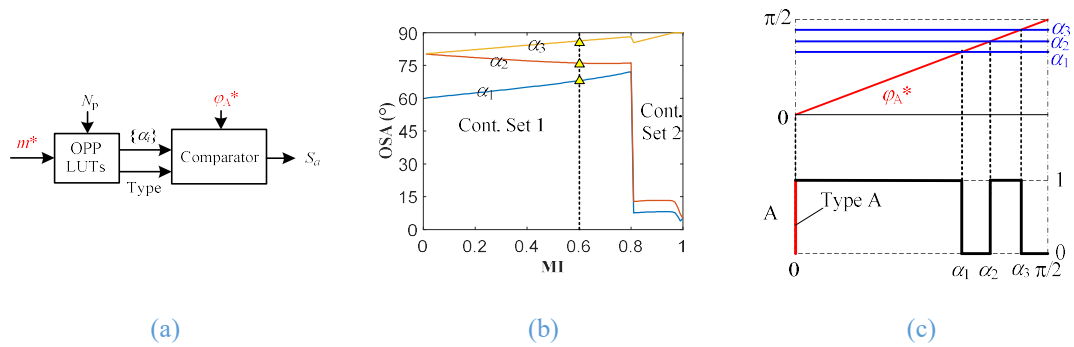
Fig. 4-34 Illustration of SOPWM implementation based on OPP LUTs (a) the block diagram (b) OSAs for N_P=7 (Type A) (b) the comparator to generate the drive signal

However, when the pulse number varies, the retrieved set of OSA will abruptly change and the output drive pulses will be altered accordingly. This undesired transient could cause large current error and may even trigger the current protection [105].The same problem will be expected when the OSAs switch from one continuous set to another at specific modulation indices, e.g. m=0.8 for N_P=7 (Type A) as shown in Fig. 4-34 (b). Moreover, the pulse type change will also lead to the abrupt change of drive pulses and transient current error. Therefore, the pulse number, the discontinuities of OSAs, and pulse type together define the mode of SOPWM. Change in any of these three parameters will lead to the mode transition and result in undesired transients.

Appropriate selection of the offline OPPs can reduce some mode transitions in real-time drive control. For example, in practice, usually only one pulse type, i.e. type A is employed [115] [139], since it leads to overall lower current distortions than type B. However, as evident in Fig. 4-33 and Fig. 4-35, mode transitions due to changes of the pulse number and the discontinuities of OSAs are often unavoidable in variable-speed

drives with SOPWM to obtain minimum current distortions. Therefore, analysis of the SOPWM mode transition influence become necessary and will be presented in the next section.

(a)　　　　　　　　　　(b)　　　　　　　　　　(c)

(d)　　　　　　　　　　(e)　　　　　　　　　　(f)
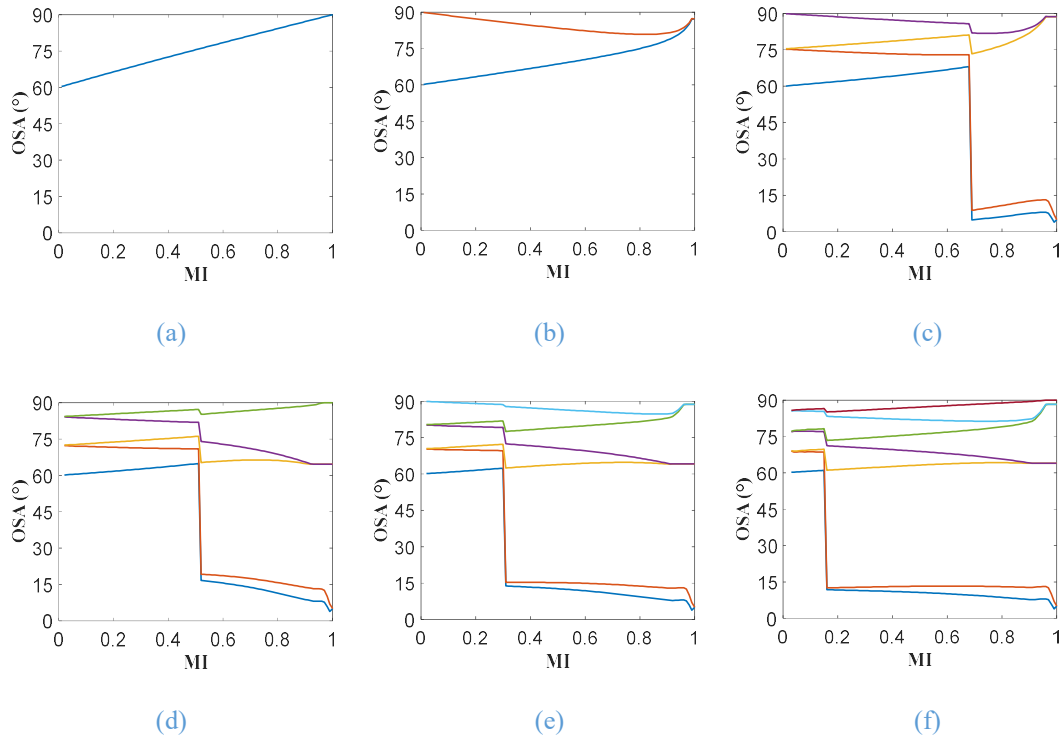
Fig. 4-35 The smoothed OSA solutions for SOPWM with only pulse type A (a) N_p=3 (b) N_p=5 (c) N_p=9 (d) N_p=11 (e) N_p=13 (f) N_p=15. The OSA smoothing methods are that 1) only use pulse type A; 2) employ smoothed OSAs when m>0.8 for Np>10, when m=0.95~1 for all the pulse numbers, and where the modulation index width of the continuous set of OSA is less than 0.1.

4.3.2 Dynamic Current Error Caused by SOPWM Mode Transition

In steady states, with the optimal voltage pulse pattern, the stator flux of PMSM will follow the associated optimal flux trajectory, which can be calculated from the integration of the optimal stator voltage and is a function of the modulation index and pulse number. According to the current-flux model of PMSM as illustrated in Fig. 4-36, the corresponding stator current will also track the optimal trajectory associated with the OPPs. However, as shown in Fig. 4-37 (a), the optimal stator fluxes and current trajectory which results with different modes can be very different even at the same modulation index.
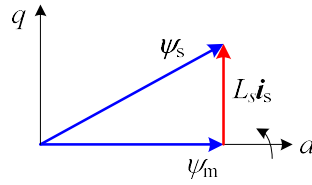
Fig. 4-36 Relationship between the stator flux vector and current vector

(a)

(b)
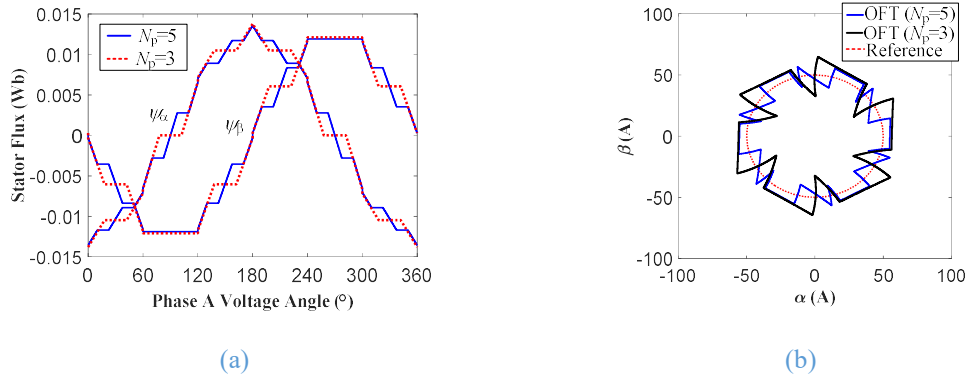
Fig. 4-37 The optimal flux and current with SOPWM in steady state at m=0.6 with different pulse numbers (a) stator flux traces (b) stator current trajectory

Assume that before the SOM mode transition the motor is operated at the steady state, being controlled by the optimal pulse pattern, $\boldsymbol{P}_1(m, N_{p1})$ and following the associated optimal trajectory, $\boldsymbol{\psi}_{ss1}(t)$. At the mode transition instant, t_k, the reference voltage and phase are kept the same, however, the pulse number changes from N_{p1} to N_{p2}. Consequently, a different optimal pulse pattern, denoted as $\boldsymbol{P}_2(m, N_{p2})$, will be employed and the resultant optimal flux trajectory, denoted as $\boldsymbol{\psi}_{ss}(t)$, will change. Taking the new optimal flux trajectory as reference, an dynamic flux error, $\boldsymbol{d}_\psi(t_k)$ is produced instantaneously by the SOM mode transition, which can be represented as

$$\boldsymbol{d}_\psi(t_k) = \boldsymbol{\psi}_{ss2}(t_k) - \boldsymbol{\psi}_{ss1}(t_k) \tag{4-22}$$

For a SPMSM, the corresponding dynamic current error can be derived as

$$\boldsymbol{d}_i(t_k) = \frac{\boldsymbol{\psi}_{ss2}(t_k) - \boldsymbol{\psi}_{ss1}(t_k)}{L_s} \tag{4-23}$$

From (4-23), large dynamic flux error at the transition instant will lead to high dynamic current error and it can be very large in high-speed PMSMs due to the low inductance.

This dynamic flux error caused by the SOPWM mode transition can be equivalently modelled as an impulse voltage disturbance input to the machine. Given the limited

167

current control bandwidth when SOPWM is employed, the drive control will not be able to regulate this dynamic current error. Hence, the voltage impulse response of the PSMM will be determined by the transfer function of PMSM in the stationary frame, i.e. $1/(L_s s + R)$. Therefore, the dynamic current error in the stationary frame caused by the mode transition will decay exponentially, governed by the machine electrical time constant, $\tau_e = L_s/R$.

However, due to the rotation of the motor, the dynamic error observed from the dq frame will exhibits oscillation. Denote the initial magnitude and phase of the dynamic current error, (4-23) in the dq frame as d_{i0} and φ_0, respectively. Assuming a transition takes place at $t_k = 0$, the dq axis current errors, d_{id} and d_{iq} after the mode transition can be obtained as

$$d_{id} = d_{i0} \cdot e^{-t/\tau_e} \cdot \cos(\omega_e t + \varphi_0) \tag{4-24}$$

$$d_{iq} = d_{i0} \cdot e^{-t/\tau_e} \cdot \sin(\omega_e t + \varphi_0) \tag{4-25}$$

where ω_e is the electrical angular speed of motor.

From (4-24) and (4-25), the magnitude of current errors in the dq frame will decay whilst the errors oscillate at the fundamental frequency, as shown in Fig. 4-40. As a result, the SOPWM mode transition can also give rise to increased torque ripples. Therefore, smooth mode transition scheme for SOPWM is required and important.
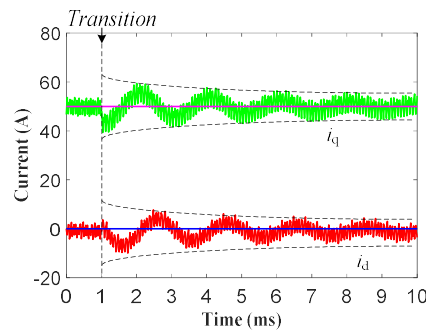
Fig. 4-38 dq axis current response at 15,000 rpm in the transient with pulse number of SOPWM change from 15 to 13 (simulation).

Further, as can be seen in Fig. 4-37 (a), the optimal flux difference due to mode transition is dependent on angular position of the reference voltage vector. Hence mode transition at different position will incur different dynamic current error magnitude, d_{i0}. Fig. 4-39 (a) plots the dynamic current error versus the transition position with respect to the phase A voltage angle, associated with Fig. 4-37 (a) for the prototype high-speed

PMSM with $L_s = 129.6 \, \mu$H. As can be observed, minimum current error can be achieved at the positions of $0° + k \cdot 60°$ and $30° + k \cdot 60°$, where k is an integer. Thus smooth transition can be realized at these positions. However, if a transition of switching modes does not take place at these positions, the resultant dynamic current error can be as high as 20A, accounting for 40% of the rated current of the prototype machine. Similarly, the dynamic current error magnitude as a function of transition position can be plotted for any mode transition, according the corresponding optimal flux trajectories obtained from the OPPs. Fig. 4-39 (b) shows the results with the transition from pulse numbers 7 to 9. The maximum current error magnitude is ~10A and still cannot be ignored. Moreover, as can be seen the width of the smooth transition range is very narrow at $30° + k \cdot 60°$ for any pulse number and the width at $0° + k \cdot 60°$ shrinks as the pulse number increases. Therefore, smooth transition schemes at specific positions may results in slow transition by waiting for these transition positions or require very high sampling frequencies in order to ensure a narrow period is not missed. The resultant sampling rate can be remarkably high for high-speed machines. To realize the smooth and fast mode transition for SOPWM, a simple yet effective method is proposed in the following section.

(a)   (b)
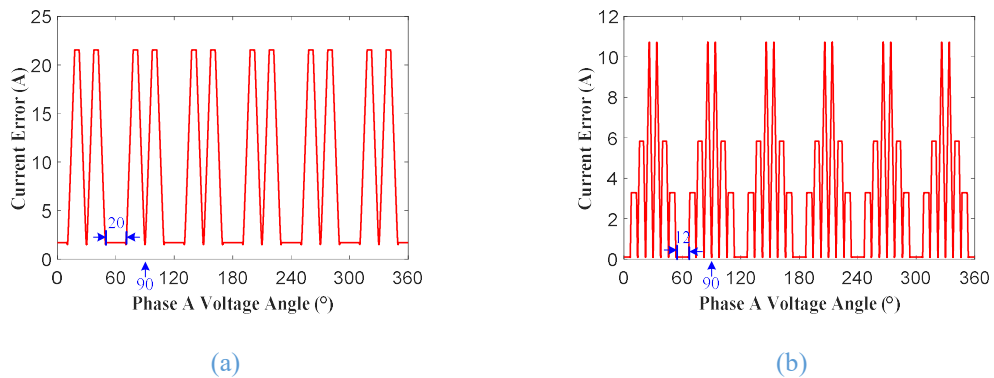
Fig. 4-39 Dynamic current error magnitude versus different transition position for pulse number change (a) from 5 to 3 (b) from 9 to 7

4.3.3 Proposed Fast and Smooth Transition Method

The proposed fast and smooth transition method is based on the general characteristics of the OSVPs and OFTs of SOWPM. Hence, in this section, the OSVPs and OFTs will be analysed firstly before the proposed method will be described and presented.

4.3.3.1 Properties of OSVPs and OFTs

According to the definition of switching vectors in Fig. 4-40, the optimal switching vector patterns can be alternatively employed to represent the three-phase OPPs, as shown in Fig. 4-41. Corresponding to the symmetry of three-phase voltage, the OSVP in the

whole cycle will also be symmetrical. It can be found that for the OPPs with QWS and 3PS, only the OSVP in the first half of voltage sector I, referred to as the prime OSVP is needed to characterize the whole-cycle OSVPs. It corresponds to the reference voltage vector over 0°~30° and reference flux vector over -90°~-60° as shown in Fig. 4-40. The OSPVs in the rest sectors can be constructed by mirroring and/or shifting.
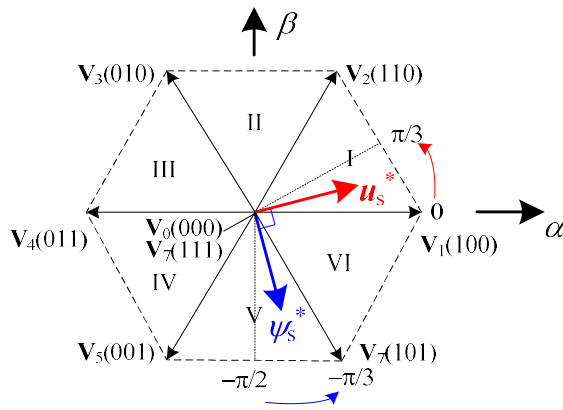
Fig. 4-40 Definition of the 8 switching vectors and the voltage sectors. The voltage vector angle is 90° ahead of the flux vector angle.
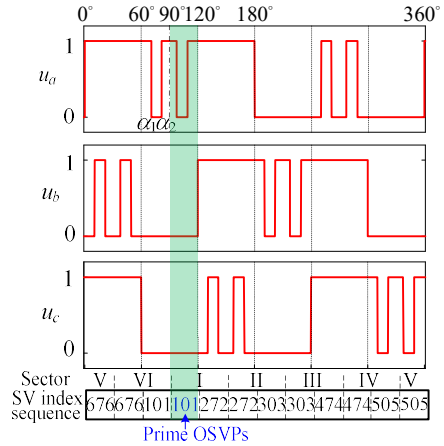
Fig. 4-41 Three-phase OPPs for N_p=5 (Type A) at m=0.6 and the associated OSVP. The angles in the figure are defined with respect to phase A voltage and thereby 90° ahead of the voltage vector angle.

As shown in Fig. 4-42, for a given OPP, the information of the voltage level sequence (determined by pulse type) and the optimal switching angles are needed. Similarly, the OSVPs are composed of two elements as well, i.e. the optimal switching vector sequence (OSVS) and optimal activating angle (OAA) of each switching vector. Fig. 4-38 shows the two representations of the optimal switching patterns of SOPWM.

(a)

(b)
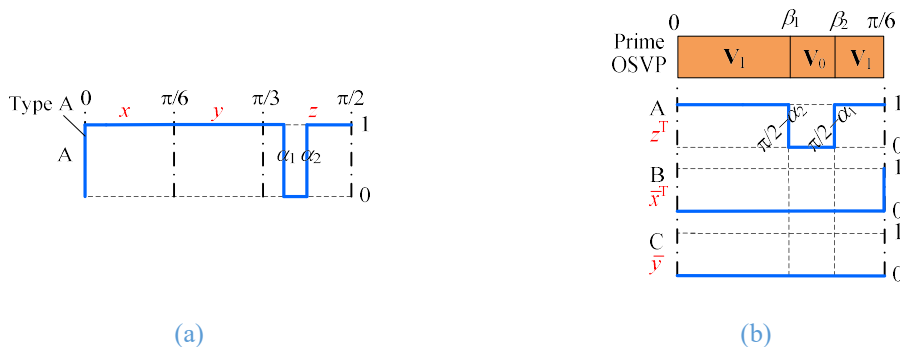
Fig. 4-42 Different representation manners of the optimal switching patterns of SOPWM with N_p=5 (Type A) (a) OPPs in the first quarter cycle (b) OSVPs in the first half of sector I and the associated three-phase voltages

Considering that the phase angle of the voltage vector is 90° lagging the phase A voltage angle, the prime OSVP corresponds to three-phase OPPs over 90°~120° is shown

in Fig. 4-40. Generally, denote the voltage sequence in each 30° region of the first quarter cycle of phase A as *x*, *y* and *z*, respectively, as shown in Fig. 4-42. According to the QWS and 3PS of OPPs, the voltage pulse sequences of the three phases in the first half of voltage sector can be derived as z^T, $\bar{x}^T$, $\bar{y}$, respectively, where the cap "-" denotes the level inversion operation and the superscript T denotes the sequence inversion operation. It indicates that the three-phase voltages in the first half of voltage sector I are determined by those over 60°~90°, 0°~30° and 30°~60° of the first-quarter OPP of phase A, respectively.

As can be seen from all the employed OPPs for SOPWM in Fig. 4-35, there is no switching angle located in the region of 30°~60°. Therefore, one important property of the prime OSVPs can be obtained, i.e. the switching state of phase C is clamped over the reference voltage vector angle of 0°~30°, i.e. over the reference flux vector angle of -90°~-60°. According to the waveform symmetry, i.e. QWS and 3PS, the clamping phase distribution over the whole cycle can be derived as shown in Fig. 4-43 with respect to the reference flux vector angle.

It is worth noting that for high pulse numbers, it is possible that the obtained OPPs have switching angles in 30°~60°. However this can be avoided by selection of an alternative continuous set of OSAs with no switching in 30°~60°. Such treatment will lead to negligible compromise in current distortions due to the high pulse number while being favourable to reduce the discontinuity of OSAs and simplify the implementation.
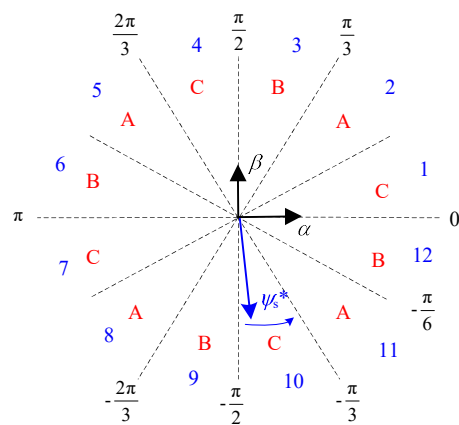
Fig. 4-43 The clamping phase distribution of SOPWM with respect to the reference flux vector angle.

Based on the OSVS, the corresponding OFT profile can be derived easily, as the switching of voltage vectors determines the change of direction of the flux trajectory while the angular duration of an applied voltage vector determines the length of the flux

171

trajectory variation. By way of example, the OFT profiles associated with the OSVPs for N_p =7 (Type A) are plotted in Fig. 4-44, where the small circles denote the positions where zero-vectors apply and the trajectory pauses. Corresponding to the two continuous set of OSAs in Fig. 4-34 (b), the OSVSs of the prime OSVPs are $\mathbf{V_0V_1V_0V_1}$ for m=0 ~0.8 and $\mathbf{V_0V_1V_2V_1}$ for m=0.8~1, respectively. Therefore, as can be seen in the OFT profile in Fig. 4-44, two different OFT profiles apply for the two modulation index ranges. The OFTs over -90°~-60° associated with the prime OSVPs is referred to as the prime OFTs. OFT profiles exhibit the same symmetrical property as OSVPs, which are visualized by the graphs of OFT in Fig. 4-44. Hence only the prime OFTs are required to construct the whole-cycle trajectories. Likewise, the OFT profiles for all the pulse numbers and pulse types can be obtained.
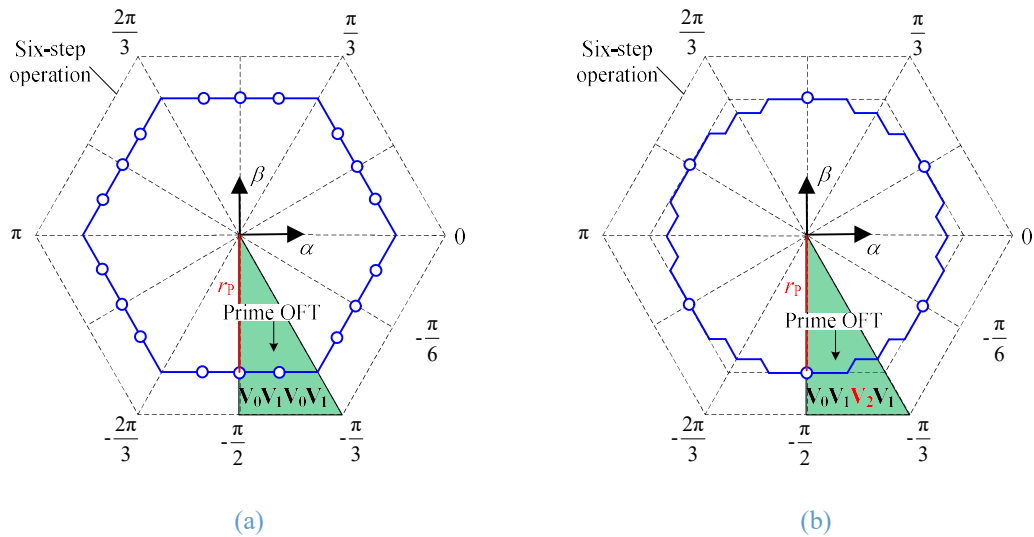
Fig. 4-44 The OFT profile under SOPWM with N_p =7 (Type A) (a) m=0~0.8 (b) m=0.8~1

As can be seen in Fig. 4-44, the OFT shape is a hexagon in the low modulation index range. This is reflecting the fact that only one active-vector i.e. $\mathbf{V_1}$ is employed in the prime OSVP. While at high modulation index, due to utilization of the other active-vector i.e. $\mathbf{V_2}$, the OFT shape exhibits more turns, resulting more corners than that of a hexagon. This is referred to as multiple-corner polygon. In the case of N_p=7 in Fig. 4-44 (b), the OFT shape is a 18-corner polygon. Generally, the corner number of an OFT shape, X, is determined by the number of switching vector transitions, denoted by $n_{V1\leftrightarrow V2}$, between $\mathbf{V_1}$ and $\mathbf{V_2}$ in the prime OSVP in (4-26).

$$X = 6 + 6 \cdot n_{V1\leftrightarrow V2} \tag{4-26}$$

Particularly, when there is no transition between $\mathbf{V}_1$ and $\mathbf{V}_2$, i.e. $n_{V1 \leftrightarrow V2} = 0$, it yields $X=6$, indicating the OFT shape is a hexagon.

In addition, the size of the OFT profiles can be measured by the apothem, r_p, of the hexagon envelop of the X-corner polygon, as shown in Fig. 4-44. According to the geometry relationship, the apothem of the OFT profile r_p can be generally obtained as

$$r_\mathrm{P} = \left(\frac{\pi}{6} - \sum \gamma_{0\_i}\right) \cdot r_\mathrm{P\_6s} \tag{4-27}$$

$$r_\mathrm{P\_6s} = \frac{\pi\sqrt{3}}{9} \cdot \frac{V_\mathrm{dc}}{\omega_e} \tag{4-28}$$

where γ_{0_i} is the duration angle in radian of the ith zero-vector in the prime OSVP, and $r_\mathrm{P\_6s}$ is the apothem of the hexagon OFT under six-step operation.

Therefore, with the OSVPs constructed from the OPPs available, the OFT apothems r_P normalised to $r_\mathrm{P\_6s}$ can be calculated for all the pulse number over the entire modulation index range. Fig. 4-45 plots the results associated with the OPPs with the smoothing OSAs given in Fig. 4-35 and Fig. 4-34 (b). As can be seen, the normalized apothem increases almost linearly with the modulation index. For different pulse numbers, only small differences will exist over high modulation index range. Considering that the high-modulation indices usually correspond to high-speeds, actually the absolute value of the OFT apothem difference will be reduced greatly at high-speeds as evident in (4-28) . Therefore, the OFT apothems of different SOPWM modes can be assumed to be identical.
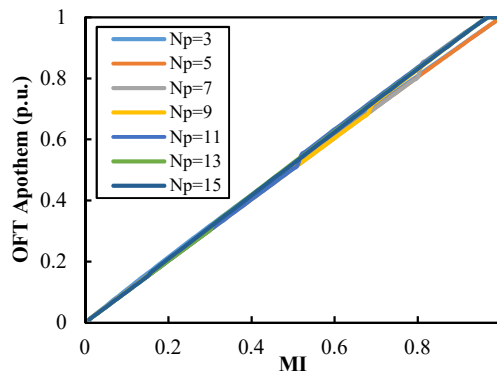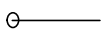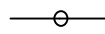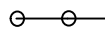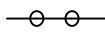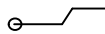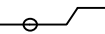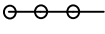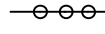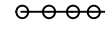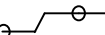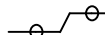
Fig. 4-45 The OFT apothem versus the modulation index for different pulse numbers, normalized by the value under six-step operation at the same speed.

The similar apothems indicates that switching SOPWM modes at the positions with the reference flux vector angle of -90° (or generally $k \cdot 60° - 90°$ due to the symmetry of OFT, where k is an integer) will lead to small dynamic current errors, i.e. smooth mode

transition. In addition, by (4-27), the similar apothems also imply that the sum of durations of zero-vectors or active-vectors in the OSVPs associated with different modes but the same modulation index are close.

Table 4-1 lists all the employed prime OFTs and OSVSs of the prime OSVPs. It can be seen that the OFT shape is hexagon for $N_p = 3$ and 5 in the whole modulation index range and for $N_p \geq 7$ when the modulation index is low. At high modulation index range with $N_p \geq 7$, the OFT shapes are all 18-corner polygon. It is worth noting that only two shapes of OFTs obtained in Table 4-1 are the outcomes of the selection of OPPs, i.e. the process of OSA smoothing. Other multiple-corner polygons such as 12-corner and 30 polygons are possible with differently selected OPPs, nevertheless the differences in the apothems are also small and the above analyses still apply.

Table 4-1 The employed prime OFTs and OSVSs for different pulse numbers

N_p	3	5	7	9
Pattern 1	01 (m=0~1)	101 (m=0~1)	0101 (m=0~0.8)	10101 (m=0~0.68)
Pattern 2	/	/	0121 (m=0.8~1)	10121 (m=0.68~1)
N_p	11	13	15	
Pattern 1	010101 (m=0~0.52)	1010101 (m=0~0.35)	01010101 (m=0~0.18)	
Pattern 2	012101 (m=0.52~1)	1012101 (m=0.35~1)	01012101 (m=0.18~1)	

4.3.3.2 Principle of Proposed Smooth and Fast Transition Method

Based on the general properties of different SOPWM mode described in the previous subsection, i.e. the clamping phase distribution property and the apothem similarity of the OFTs, a novel smooth and fast transition method is proposed.
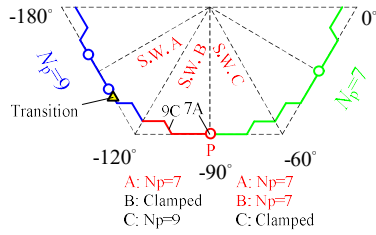
Fig. 4-46 The stator flux trajectory during the mode transition from N_p=9 to N_p=7 at high modulation index (m=0.8~1)
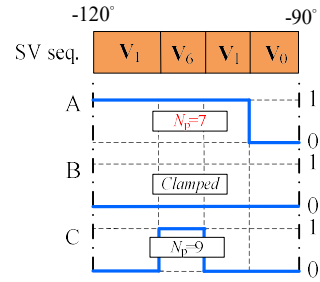
Fig. 4-47 The three-phase voltages and switching vector sequence during the mode transition from N_p=9 to N_p=7 at high modulation index

Without loss of generality, take pulse number transition from N_p=9 to 7 at high modulation index as an example to illustrate the principle of the proposed method. As shown in Fig. 4-46, the blue trace denotes the OFT associated with N_p=9, where small circles indicate that zero-vectors are applied and the trajectory is stationary. Assume that the mode transition demand occurs at an arbitrary instant between the flux vector angle of -150° and -120°. The instant of the corresponding position in the flux trajectory is marked by the yellow triangle as show in Fig. 4-46. Considering the phases A, B and C are clamped in the regions of -150°~-120°, -120°~-90° and -90°~-60° of flux vector angles, respectively, as can be seen in Fig. 4-43, the proposed smooth transition method is performed as follows. Firstly switching phase A to the new mode, i.e. N_p=7 and subsequently switching phases B and C, respectively, in the following 30° regions, i.e. -120°~-90° and -90°~-60°.

As illustrated in Fig. 4-46, the mode switching of phase A will not take effect until the flux angle reaches -120°. During the period of -120°~-90°, the voltage pulse pattern of phase A associated with the new mode, N_p=7 is effective while phase B is clamped and phase C still outputs the voltage pulse pattern of N_p=9. As a result, the actual stator flux will not follow either the OFTs of N_p=9 and N_p=7. However, at the end of this region, the stator flux will always reach point P as shown in Fig. 4-46, where the OFTs of two SOPWM modes are essentially identical. This can be attributed to the fact that in the period of -120°~-90°, the switching in phase A determines the duration of zero-vector, as shown in Fig. 4-47. Changing the mode leads to different pulse pattern in phase A, but the sum of the zero-vector duration will be similar to the old mode due to the similar apothems as analysed previously. Therefore, the mode transition can be completed at the flux angle of -90° and afterwards the stator flux will track the OFT associated with the new mode, by switching the modes of phases B and C sequentially.

The SOPWM mode transition at the other scenarios can be analysed exactly in the same manner as described above and hence omitted. It can be found for any mode transition, due to the properties of the clamping phase distribution and the apothem similarity of OFTs, the mode switchover can always be completed at the flux angle of -90° as shown in Fig. 4-46. Thus, the proposed transition method, sequentially switching the three-phase modes will lead to smooth transition.

Moreover, according to the symmetry of the OFTs and the clamping phase distribution in Fig. 4-43, the proposed transition method can start at any position. Table 4-2 gives the final scheme of the proposed method. The mode switchover for the 1st transition phase is conducted immediately at the required mode transition instant while the mode switchovers for the 2nd and 3rd transition phases are performed in the following 30° regions, respectively. As can be seen, the three phases are not switched at a specific position simultaneously but, instead, sequentially over 30° period. It imposes less requirement on the control updating frequency. However, the mode transition can always be achieved at the end of the next 30° region and the maximum transition delay is 60°, i.e. 1/6 cycle. Therefore, the proposed method can achieve smooth and fast mode transition for SOPWM while being very simple and adding no extra cost to both software and hardware.

Table 4-2 Phase transition sequence of the proposed smooth transition strategy

Reference voltage angel at the transition instant	30°~60°, 120°~150°, 210°~240°, 300°~330°	60°~90°, 150°~180°, 240°~270°, 330°~360°	0~30°, 90°~120°, 180°~210°, 270°~300°
1st transition phase	A	B	C
2nd transition phase	B	C	A
3rd transition phase	C	A	B

4.3.4 Simulation Study

Extensive simulations have been conducted in MATLAB/Simulink on the prototype high-speed machine. In the simulation, the sampling frequency is set to 10 kHz. As the dynamic response is not great concern in this section, the current control bandwidth of FOC with SOPWM is set to low value, i.e. 50 Hz in order to obtain slow smooth reference voltage vector in steady states. Otherwise, with high bandwidth the reference voltages may exhibit large ripples and increase the current distortions. This will be analysed in the next chapter.

Fig. 4-6 (a) shows the results during the SOPWM mode transition transient at 15,000 rpm (500Hz), where the pulse number is reduced from 5 to 3 at 65 ms and the proposed method is not applied. As evident, the mode transition gives rise to a large dynamic error in the dq axis currents. The current errors caused by mode transition takes ~5 fundamental cycles to disappear. However, with the proposed method, the mode transition at the same condition is smooth and fast, as shown in Fig. 4-6 (b).

(a)   (b)
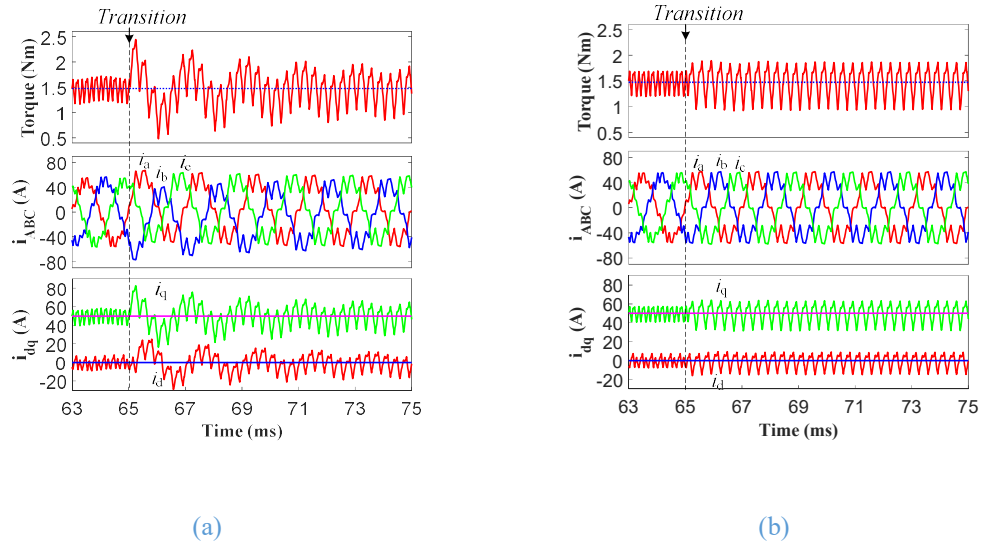
Fig. 4-48 The torque, phase currents and dq axis currents in the pulse number switching transient from N_p=5 to N_p =3 at 15,000 rpm (m= 0.59). (a) direct mode transition. (b) proposed method.

Fig. 4-49 and Fig. 4-50 plot the stator flux and current trajectories during the mode transition process, without and with the proposed method. The triangles denote the mode transition starting point, blue traces denote the trajectory in the half cycle before the transition, the red traces denote the trajectory in the half or one cycle after the transient and the green dotted traces denote the new optimal trajectory in steady states. Corresponding to the pulse number changes from 15 to 13, 11 to 9 and 5 to 3, the shapes of the OFTs switch from 18-corner polygon to 18-corner polygon, 18-corner polygon to hexagon, and hexagon to hexagon, respectively. As can be seen in Fig. 4-49 (a) when the proposed method is not applied, all the actual stator flux trajectories in red after the mode transition deviate from the new OFTs in green and the difference can be significant with low pulse numbers. However, as evident in Fig. 4-49 (b), the flux trajectories with the proposed method can well track the new OFT after the mode transition, for all the transition between the different OFT shapes.

(a)

(b)
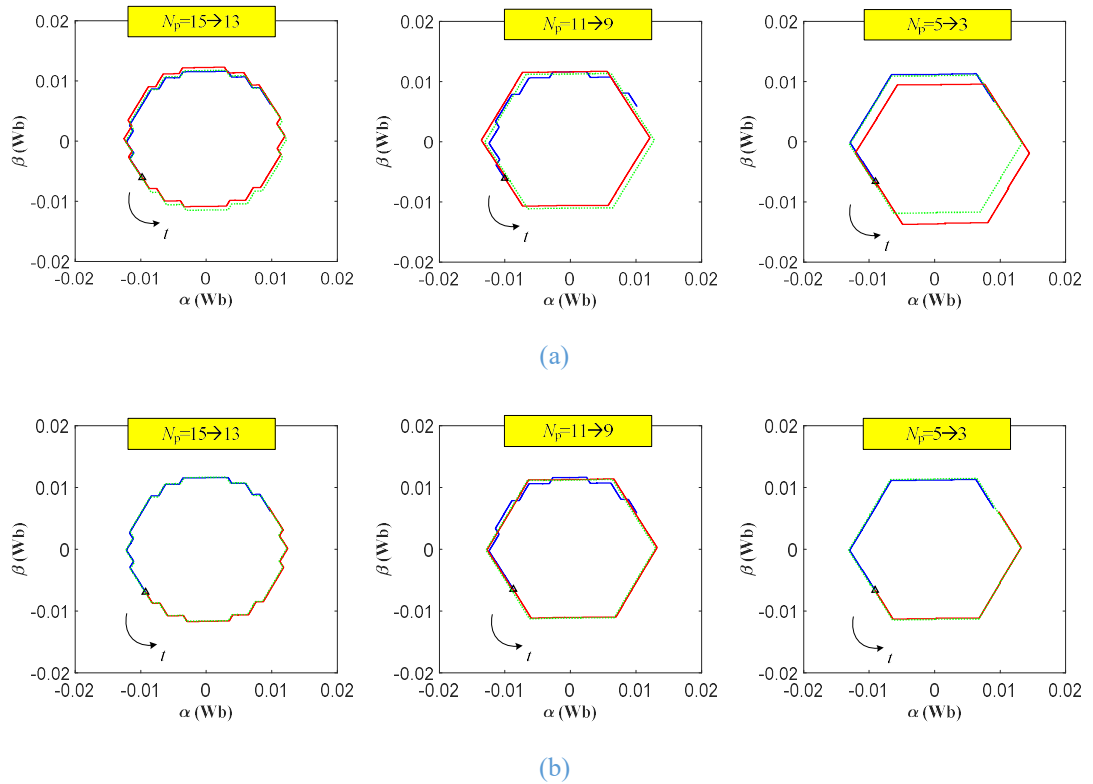
Fig. 4-49 The stator flux trajectories in the pulse number switching transients at 15,000 rpm (m= 0.59). (a) direct mode transition (b) proposed method.

(a)

(b)
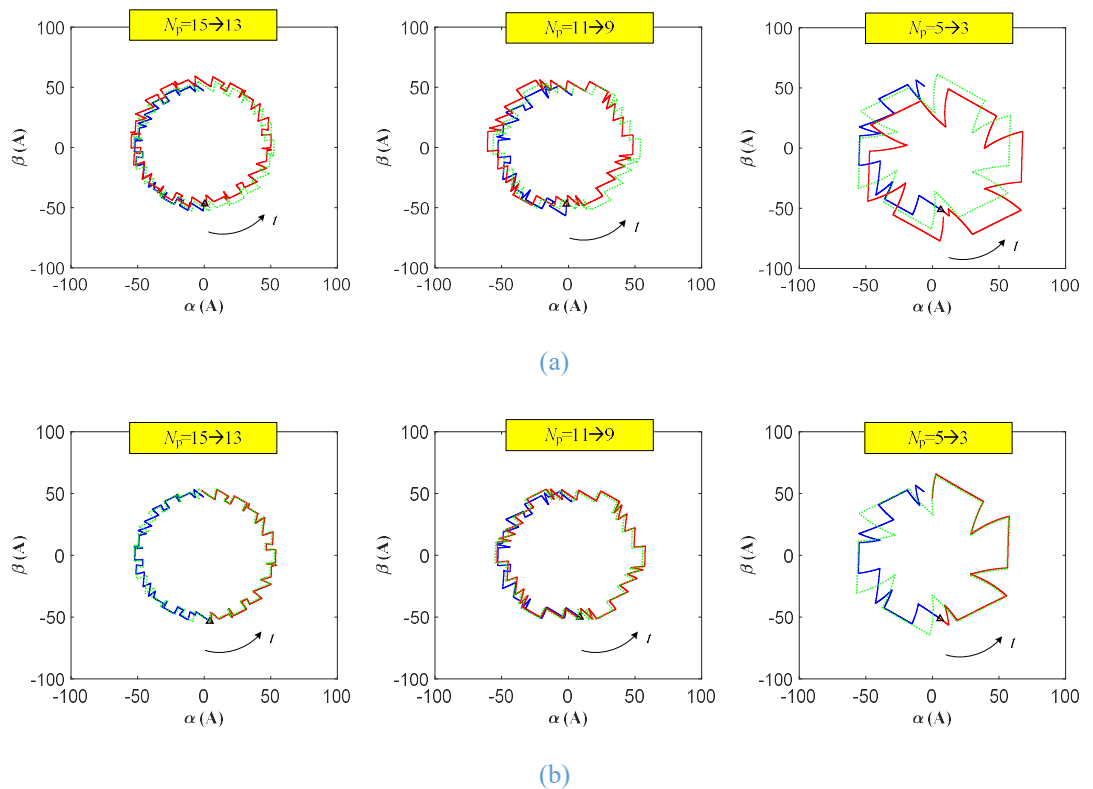
Fig. 4-50 The current flux trajectories in the pulse number switching transient from Np=15 to Np =13 at 15,000 rpm (m= 0.59). (a) direct mode transition (b) proposed method.

178

On the other hand, as can be more clearly seen form the current trajectories in Fig. 4-50, the optimal current trajectories for the two SOPWM modes in blue and green respectively are not identical. Mode transitions can cause current excursions, which is very remarkable in the low pulse number case. With the proposed transition method, the current trajectories can track the new optimal trajectories very quickly.

4.3.5 Experiment Results

In order to validate the effectiveness of the proposed method, extensive experiment tests have been performed on the high-speed prototype machine. In the tests, the machine is operated at the constant speed of 10,000 rpm and under current control mode. Firstly the SVM based FOC are employed and the dq axis currents are controlled at 0 and 25A respectively, with the operating modulation index of ~0.4. Then, it switches to SOPWM with different pulse numbers, following the profile shown in Fig. 4-51. As the dynamic current error in the transition transient will vary as the transition position change, the experiments have been repeated by many times.
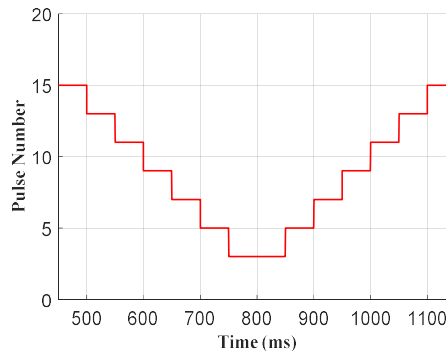
Fig. 4-51 Pulse number transition scheme in the testing

Fig. 4-52 (a) and (b) show the phase A currents without the proposed SOPWM mode transition method in two tests, where the top is the waveform over the long period and the bottom is zoom-in view of the certain pulse number transition transient. As can be seen, direct transition could cause large overshot current in transients, i.e. 12 A accounting for 48% of the q axis reference current of 25A. It increases the peak current requirement of the drive otherwise will trigger the overcurrent protection in the SOPWM mode transition. Moreover, it can be seen that the decay of the dynamic current error can take serval electric cycles and would increase the torque ripple in the transient according to the analysis in section 4.3.2.
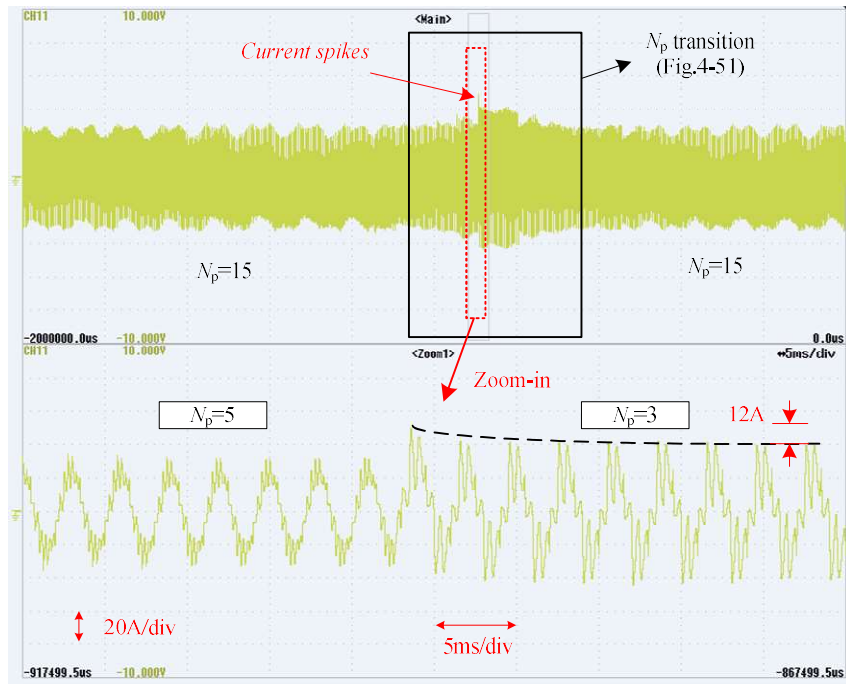
(a)
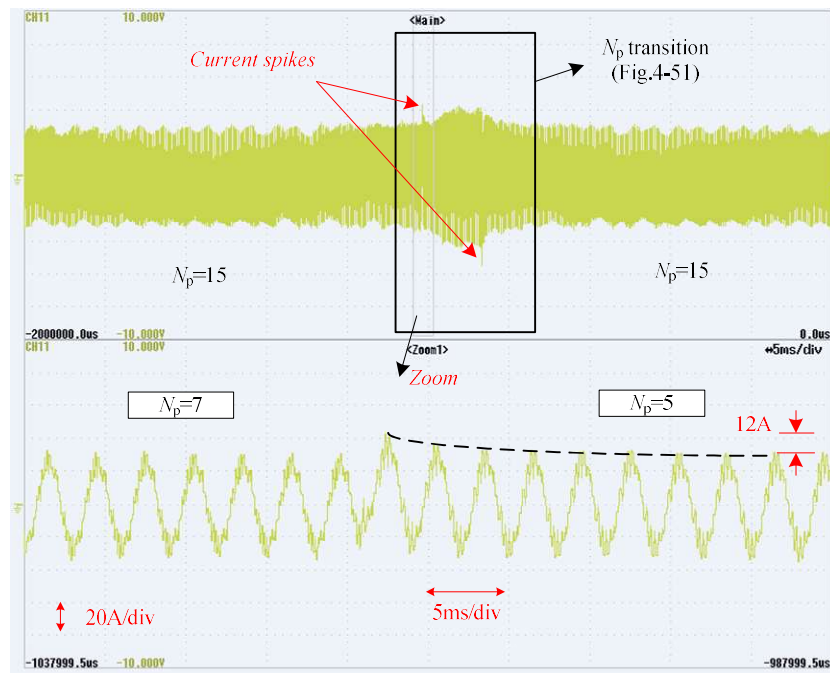
(b)

Fig. 4-52 Phase A current during SOPWM mode transition without proposed method.

However, as shown in Fig. 4-53, with the proposed method, no current spike is observed in the phase currents. As can be seen in the zoom-in view, very smooth transition can be realised when the pulse number switches from 5 to 3, which improves the performance greatly as compared to that in Fig. 4-52 (a) without the proposed method. Moreover, the experiments have been repeated by many times and no current spike is

180

noticed. Hence, it verifies that with the proposed method the smooth transition can be always achieved.
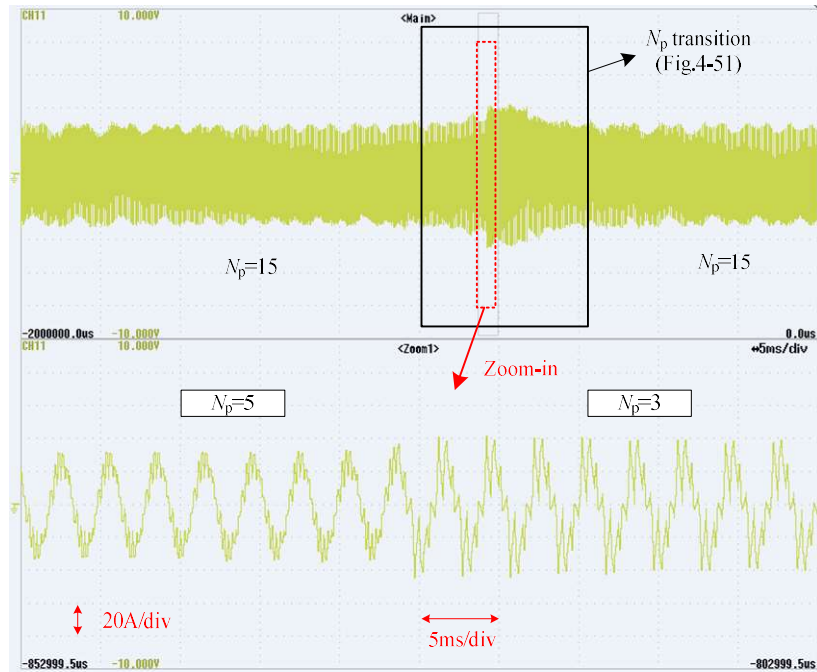
Fig. 4-53 Phase A current during SOPWM mode transition with proposed method.

The details of the sampled phase currents with the proposed method in the various pulse number transition transients are shown in Fig. 4-54. As can be seen, the fast and smooth SOPWM mode transition can be realised in all possible scenarios. It is worth noting that according to Table 4-1 at the modulation index of 0.4, the OFTs with N_p=13 and 15 are 18 corner polygons and those with N_p=3~11 are hexagons. Therefore, the SOPWM mode transitions from 18-corner polygon to 18-corner polygon, 18-corner polygon to hexagon, and hexagon to hexagon are all validated in the experiment tests.
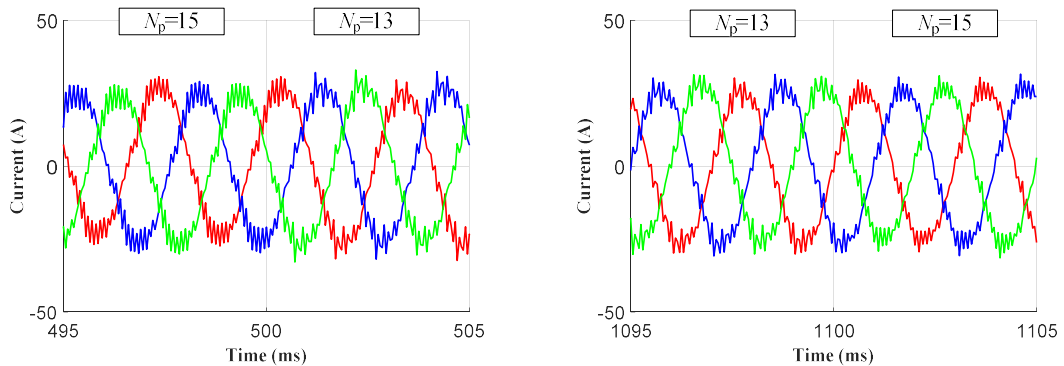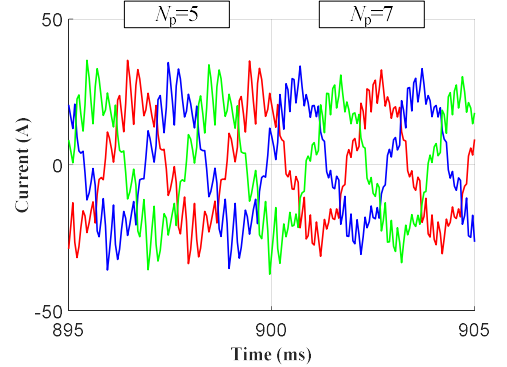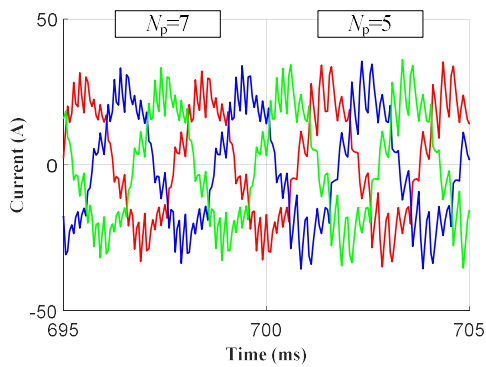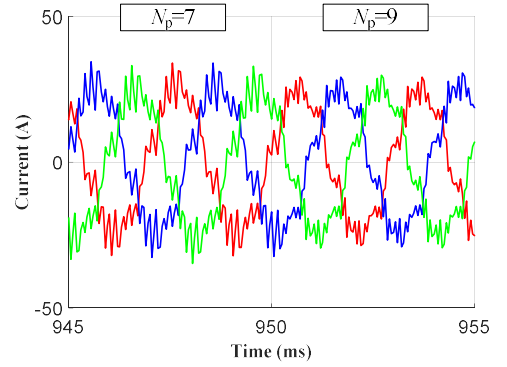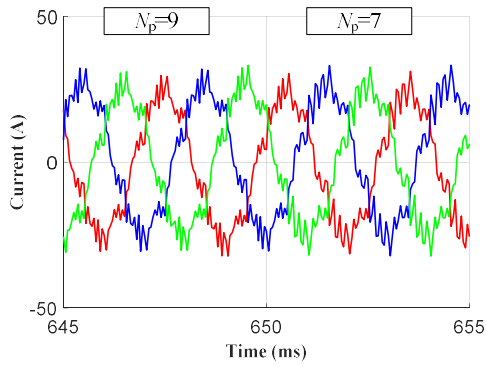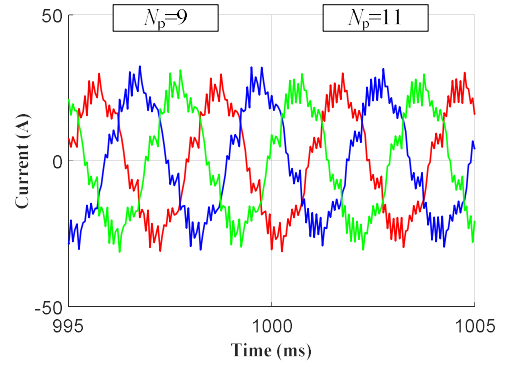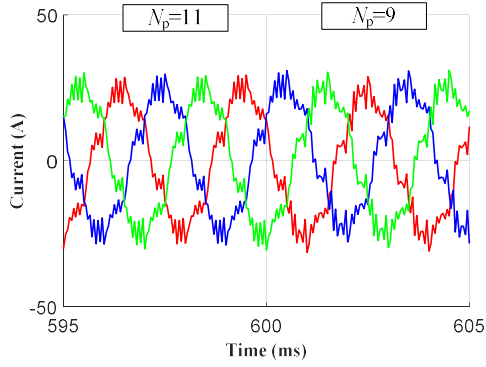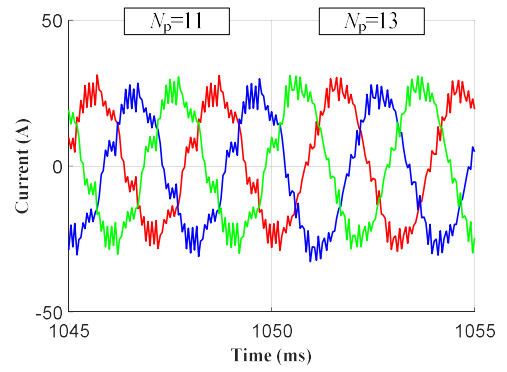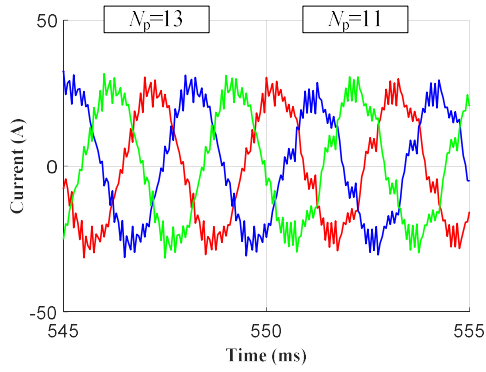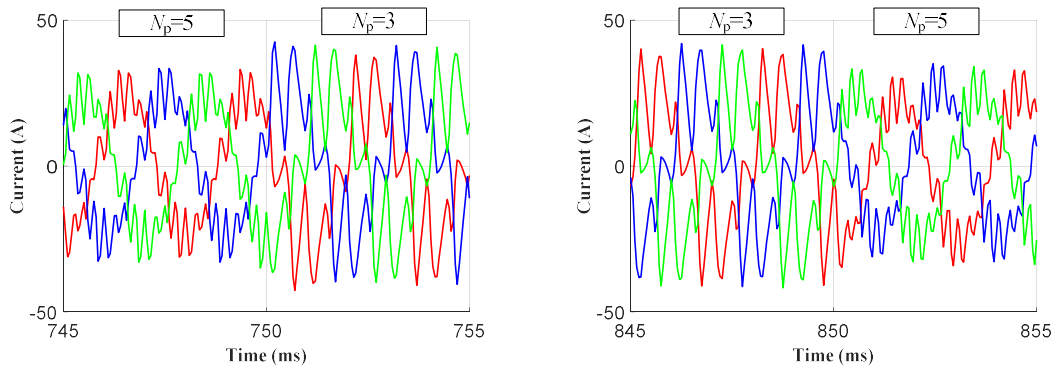
Fig. 4-54 Phase currents in the pulse number transition transients

4.4 Summary

In this chapter, the pulse pattern optimization problem of SOPWM has been analysed and a computationally efficient optimization procedure has been developed to derive all the optimal switching angles for different pulse numbers and pulse types. With the proposed optimization procedure, the trade-off between switching angle discontinuity and the current distortion can be flexibly made without need of tedious post-optimization and re-optimization. The real-time implementation of SOPWM for high-speed PMSM has been introduced as well. Additionally, a harmonic current prediction method based on the optimal current distortion factors of SOPWM have been proposed. The proposed method can accurately predict in a computationally efficient manner the actual current TDD of high-speed drives with SOM under limited switching frequencies. Extensive simulations HIL testing and experiments have been performed and confirmed that SOM based on the offline derived OPPs can contribute to minimized current harmonic distortions in real-time control of high-speed PMSMs with limited switching frequency.

Moreover, the SOPWM mode transition problem has been addressed and a novel smooth and fast mode transition method has been proposed. The SOPWM mode is defined by the pulse number, pulse type and the continuous set of OSA. The dynamic current error caused by the SOPWM mode transition has been analysed and the influence of mode transition has been derived. By representing the optimal patterns of SOPWM in the forms of OSVPs and OFTs, two general properties of SOPWM, i.e. clamping phase distribution and the apothem similarity of OFTs have been identified. Based on these two properties, the proposed method can realize the smooth and fast SOPWM mode transition with virtually no dynamic errors. Extensive simulations and experiments have validated the effectiveness of the proposed method.

CHAPTER 5 Fast Dynamic Control with Minimised Current Distortion

5.1 Introduction

The optimised pulse patterns of SOPWM can contribute to minimum current harmonics meanwhile the fundamental voltage is identical to the input reference voltage. However, it is based on steady state condition and requires steady-state or quasi steady-state operation of SOPWM in the real-time control of drives. The change of the reference voltage should be limited to obtain the output voltage close to the OPPs. Therefore, the v/f control [139] and low bandwidth FOC [120] are usually employed with SOPWM which results in slow dynamic response. It is acceptable in low-performance speed regulated drives such as fans and pumps. However, fast dynamic current or torque control is required for high-performance high-speed PMSM drives and control method which incorporates SOPWM with fast dynamic response will be investigated in this chapter.

To improve the dynamic performance of SOPWM based control, the optimal trajectory tracking technique has been extensively researched for high-power induction machines [141][121][104][105].The concept of this technique is based on real-time modification of the OPPs so that the optimal current or stator flux trajectory associated with OPPs in steady states can be tracked. Thereby in transients, the new optimal trajectory can be tracked quickly whereas in steady states, the OPPs can yield minimum current THDs. Compared with current trajectory tracking [121][122], stator flux trajectory tracking is not affected by the machine model accuracy [104][105] as the stator flux can be estimated by the voltage model at high modulation indices. Therefore, optimal flux trajectory (OFT) tracking is more favoured for fast dynamic control with SOPWM [100].

To compensate the dynamic flux error with respect to the OFT, the relationship between the stator flux variation and the angular displacement associated with a switching instant in OPPs can be established [104]. However, for a given required stator flux change determined by the dynamic flux error, the calculation of the OPP modification could be problematic depending on the switching numbers in each phase. Moreover, it requires complex observers [142] for the fundamental current and stator flux extraction to calculate the reference voltage and realize the stator flux vector control [105]. In [143], an improved method, called model predictive pulse pattern control was proposed. Instead

of modifying the OPPs to track the OFT in a deadbeat fashion, a cost function including the stator flux error and the OPP modification are formulated online to correct the switching instant. The complex fundamental flux observer was eliminated and a trade-off between the flux error reduction and OPP modification can be achieved. However, this method is very computationally intensive and additional scheme should be included at large transients [144], which makes the method more complicated. Additionally, SOPWM with the OFT tracking is mainly investigated for medium voltage high-power induction machines and that for high-speed PMSM drives is still lacking to the best knowledge of the author.

Therefore, in this chapter, a novel fast dynamic control method with SOPWM, referred to as pseudo six-step modulation (PSSM) is proposed. The proposed method tracks the OFT associated with the reference stator flux vector in six-steps per cycle. It is realised by employing a similar concept to the SVM method, where the calculated reference voltage vector is synthesized based on the optimized switching vector patterns (OSVPs) of SOPWM. As a result, the optimal stator flux can be tracked quickly in transients within one-sixth fundamental cycle, of which the time duration reduces as the machine speed increases. Meanwhile, the generated switching vector pattern will approach to the OSVP in steady states and lead to the minimum current THD for the given pulse number. Both excellent dynamic and steady state control performances can be achieved with the proposed PSSM. Moreover, the proposed PSSM does not require complex fundamental current and flux observers and the pulse numbers can be maintained or adjusted so that the associated switching frequencies are kept within the allowed range. The proposed PSSM can also be readily incorporated in the current vector control and speed control loops. The implementation of the proposed control method is simple and attractive for high-speed drives.

The rest of this chapter is arranged as follows. Section 5.2 analyses the problems of the SOPWM applied in the conventional FOC. Section 5.3 introduces fast dynamic current control with stator flux tracking and the real-time construction of OFTs. In Section 5.3, the principle and implementation of the proposed PSSM to track OFTs are presented. Finally, the simulation, HIL and experiment results are given in Sections 5.5, 5.6 and 5.7, respectively.

5.2 Analysis of SOPWM implemented in FOC

Fig. 5-1 shows the control block diagram of the SOPWM implemented in the conventional FOC. It shares the same structure as SVM based FOC. The dq axis reference voltage vector, $\boldsymbol{u}_{dq}^*$ is generated from the PI controller in the synchronous frame and then converted into the reference voltage vector, $\boldsymbol{u}_s^*$ in the stationary frame. Subsequently, the modulation index, m^* and the reference angle of each phase, φ_{abc}^* can be derived. The pulse number N_p is determined by the operating speed subject to the maximum switching frequency and can only be the odd number for two-level inverters. With the modulation index and pulse number as inputs to the OPP LUTs, the OPP associated with the reference voltage can be obtained and constructed as illustrated in Fig. 5-2. It can be inferred that if the reference dq axis reference voltage vector, $\boldsymbol{u}_{dq}^*$, is constant in steady states, the corresponding OPP will define the switching instants in an optimal manner, as the switching angles has been optimised offline to minimize the resultant current THD for the given pulse number.
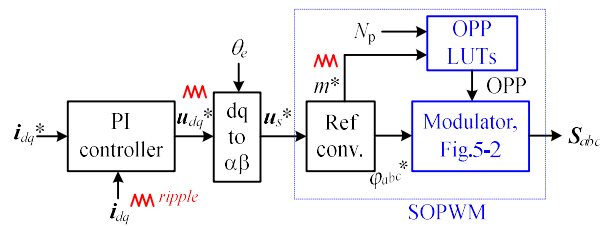
Fig. 5-1 Block diagram of FOC with SOPWM
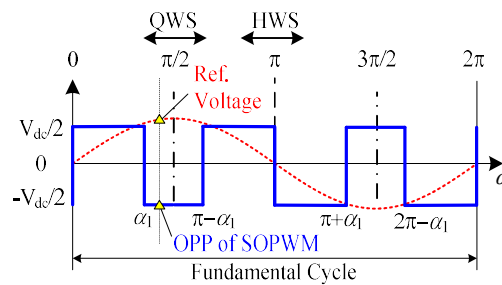
Fig. 5-2 The correlation between the reference phase voltage and the corresponding OPP of SOPWM (N_p=3)

However, when the SOWPM is employed in a current feedback control loop, the ripples in the reference dq axis voltages can be large and deteriorate the steady-state performance greatly. This is mainly because that the sampled currents in SOPWM based FOC can exhibit abundant harmonics especially at very low pulse numbers. These harmonics will excite large ripples in the reference dq axis voltages by the current PI controller. Fig. 5-3 shows the simulation results of the FOC with SOPWM (N_p=7). As

can be seen, the reference modulation index exhibits the ripple of about 18% due to the variation of the dq axis reference voltages. Consequently, the retrieved OPP varies accordingly which leads to asymmetry in the actual phase voltages and large distortion in the resultant three phase currents. Particularly, from the associated current spectrum of phase A shown in Fig. 5-3 (c), unexpected harmonics such as third harmonics occur can be noticed. Moreover, extra short pulses in the phase voltage can also be caused due to the ripples in the reference voltage and the persistent changing of OPP. It will increase the operating switching frequency, reduce the system efficiency and derate the maximum operating current of power electronic switches [100].
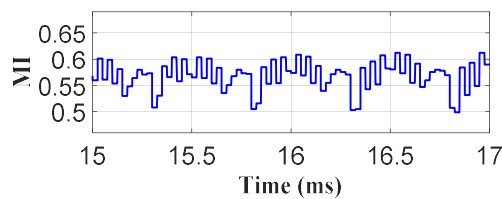
(a)
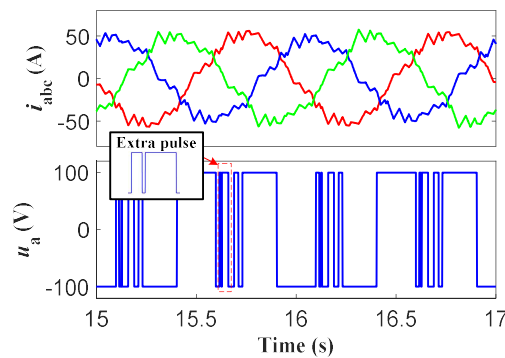
(b)
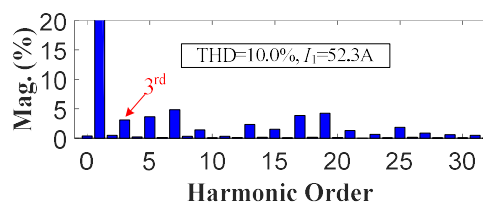
(c)

Fig. 5-3 The simulation results of FOC with SOPWM (N_P=7, control bandwidth of 1kHz) at 30,000 rpm (f_1=1kHz). (a) Reference modulation index. (b) Phase currents and phase A terminal voltage. (c) Phase A current spectrum.

High gains of the current controller could give rise to increased ripples in the dq axis reference voltages. Thereby, high control bandwidth of FOC is not favourable in order to maintain the steady-state performance of SOPWM. Moreover, employing filters for the feedback currents [120] can help reduce the reference ripples. However, as the low-order

current harmonics at low pulse numbers could be high, the introduced filters would again limit the dynamic response of the high-speed drive. In addition, it is worth noting that with conventional SVM, sampling at the beginning and middle of carrier cycles i.e. synchronous sampling scheme can intrinsically get rid of the switching harmonics [60]. Hence in principle, the conventional SVM does not pose such constraint on the control bandwidth.

On the other hand, during transients, SOPWM may not be able to produce the required reference voltage in average sense over the control step. This is because the equivalence of OPP to the reference voltage in the SOPWM is established in steady states over a fundamental period. This SOPWM property would result in poor transient performance since it can only cope with slow change of reference voltage. Therefore, based on the above analysis, low control bandwidth is essentially required when SOPWM is implemented in FOC.

5.3 Fast Dynamic Current Control with Optimal Stator Flux Trajectory Tracking

Alternatively to the conventional FOC, the stator flux tracking technique [104] can be employed for high-speed PMSM drives to enhance the dynamic control response. Fig. 5-4 shows the control diagram of the current control with stator flux tracking, which incorporates SVM and is essentially the deadbeat predictive current control (DBPCC) proposed in Chapter 2.
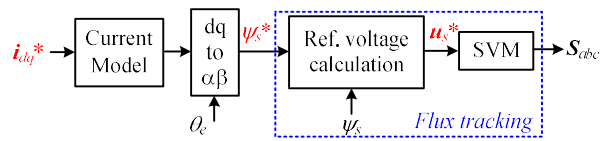
Fig. 5-4 current control with stator flux tracking based on SVM

In Fig. 5-4, the reference stator flux vector, $\boldsymbol{\psi}_s^*$ is derived from the reference dq axis currents, $\boldsymbol{i}_{dq}^*$, by the current model of high-speed SPMSMs expressed in (5-1) and the coordinate transformation from the dq frame to the stationary frame. The reference voltage $\boldsymbol{u}_s^*$ can be readily calculated from the difference of the reference flux, $\boldsymbol{\psi}_s^*$, and the actual stator flux, $\boldsymbol{\psi}_s$, divided by the time-step, T_s.

$$\boldsymbol{\psi}_{dq} = L_s \boldsymbol{i}_{dq} + \psi_m \tag{5-1}$$

As a result, fast dynamic response can be achieved by DBPCC in Fig. 5-4, when the reference voltage can be implemented by SVM and the reference flux can be realised in deadbeat fashion. It is worth noting that the control performance of DBPCC with stator flux tracking is dependent on accuracy of the machine parameters. However, highly accurate PMSM model can be acquired by the calibrated FEA results [130]. Hence, in this chapter, the machine parameters in the control are assumed obtained precisely unless otherwise stated.

Provided that the reference dq axis current is constant in steady states, the trajectory of a reference stator flux vector in the stationary frame will be circular. With sufficient high switching frequencies, the actual stator flux will follow the circular trajectory, which corresponds to low current THDs. However, at high speeds, the current distortions could be high as the circular trajectory cannot be closely tracked by low switching to fundamental frequency ratios.
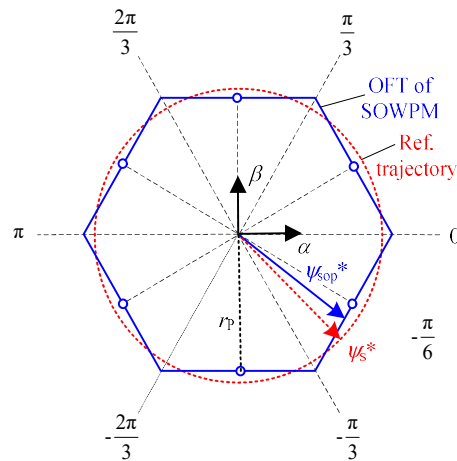
Fig. 5-5 The correlation between the reference flux trajectory and the corresponding OFT of SOPWM (N_p=3)

As analysed in the previous chapter, apart from OPP representation, SOPWM can also be characterized in the form of optimal flux trajectories (OFTs), which can be obtained by integration of applied voltage derived from three phase OPPs. Fig. 5-5 shows the reference flux trajectory and the OFT derived from SOPWM at N_p=3 in the stationary frame, where the small circles on the OFT represent the locations where zero-voltage vector is applied and hence the flux vector does not change. As can be seen, due to low pulse number, the circular trajectory of the reference flux is not possible to realise and the hexagon OFT is the best realisable flux trajectory with SOPWM (N_p=3). It should be noted that, for higher pulse numbers, the OFTs associated with SOPWM can be in

different profiles, e.g. 18-corner polygon for N_p=7 as shown in Fig. 4-44 (b) and described in section 4.3.3.1.

Therefore, in order to achieve minimum current THDs at high speeds with low pulse numbers, the OFTs associated with SOPWM instead of the circular trajectories should be the target for control to follow. To track an OFT, its real-time construction with respect to a given reference flux vector is needed first and this will be introduced next.

For simplicity and without loss of generality, take the case of N_p=3 in Fig. 5-5 as an example to illustrate the principle of real-time OFT construction. As shown in Fig. 5-5, the magnitude and phase angle of the reference stator flux vector, $\boldsymbol{\psi}_s^*$, are denoted as ψ_s^* and θ_{sf}^*, respectively. Assume at high operating speeds, the resistive voltage drops and the inverter nonlinear influence can be neglected. Thus, the magnitude u_s^* and phase θ_u^* of the reference voltage vector, $\boldsymbol{u}_s^*$, can be respectively obtained as

$$u_s^* = \omega_e \psi_s^* \tag{5-2}$$

$$\theta_u^* = \theta_{sf}^* + \frac{\pi}{2} \tag{5-3}$$

From (5-2), the reference modulation index, m^* can be known by normalizing to the fundamental voltage under six-step operation i.e. $2V_{dc}/\omega_e$. For a given pulse number, N_p, the employed optimal stator voltage vector sequence can be retrieved from the LUTs of OPPs, denoted as $\boldsymbol{P}(m^*, N_p)$. By integration of the optimal stator voltage vector sequence, the optimal stator flux vector, $\boldsymbol{\psi}_{sop}^*(\theta_{sf}^*)$, associated with the reference flux vector at θ_{sf}^*, i.e. $\boldsymbol{\psi}_s^*(\theta_{sf}^*)$ can calculated as

$$\boldsymbol{\psi}_{sop}^*(\theta_{sf}^*) = \boldsymbol{\psi}_{sop}^*(\theta_0) + \int_{\theta_0}^{\theta_{sf}^*} \boldsymbol{P}(m^*, N_p, \alpha)d\alpha \tag{5-4}$$

where $\boldsymbol{P}(m^*, N_p, \alpha)$ denotes the optimal stator voltage vector at the flux angel of α in $\boldsymbol{P}(m^*, N_p)$. The reference flux phase θ_{sf}^* determines the upper limit of the integral. The angle, θ_0, is the initial flux phase of the integral and can be set to $-\pi/2$. Thus as shown in Fig. 5-5, the coordinate of the initial flux vector in the stationary frame, $\boldsymbol{\psi}_{sop}^*(\theta_0)$ can be obtained as $(0, -r_\mathrm{P})$, where r_P is the apothem of the OFT, in unit of Wb or Vs. As already presented in section 4.3.3.1, the OFT apothem can be obtained as

$$r_{\mathrm{P}} = \frac{\pi\sqrt{3}}{9} \cdot \frac{V_{\mathrm{dc}}}{\omega_e} \cdot r_{\mathrm{P\_nor}}(m^*, N_p) \tag{5-5}$$

where $r_{\mathrm{P\_nor}}(m^*, N_p)$ is the normalised OFT apothem to that of six-step operation at the same speed, i.e. $\pi\sqrt{3}V_{\mathrm{dc}}/(9\omega_e)$ in (4-28), which can be expressed as a function of the modulation index and pulse number as plotted in Fig. 4-45 of section 4.3.3.1.

It is worthy noted that in order to reduce the integration length, the initial phase angle, θ_0 can be selected as the value close to $-\pi/2 + k \cdot \pi/3$ (k=0,1,···,5). The magnitude of the initial flux vector, $\boldsymbol{\psi}_{sop}^*(\theta_0)$ is same as r_{P} due to the symmetry of OFT, as shown in Fig. 5-5.

Therefore, with (5-2)~(5-5) and the LUTs of OPPs and the normalized OFT apothem, the optimal stator flux vector, $\boldsymbol{\psi}_{sop}^*$, associated with the OFT of SOPWM can be obtained in real-time according to the reference flux vector, $\boldsymbol{\psi}_s^*$. Fig. 5-6 shows the block diagram of the proposed OFT real-time construction process. In this chapter, the OPPs with OSAs shown in Fig. 4-35 are employed and the corresponding OSVSs and OFT profiles are shown in Table 4-1.
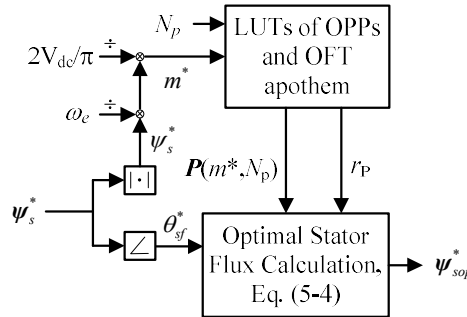
Fig. 5-6 Real-time OFT construction according to the reference flux vector

5.4 PSSM with Optimal Stator Flux Trajectory Tracking

According to the OFT real-time construction method described in the last section, the reference optimal stator flux vector can be calculated and obtained at each step from the reference stator flux. Regarding the real-time optimal flux tracking, the key requirements are summarized as follows.

1) The reference optimal stator flux vector should be reached quickly in transients;

2) In steady states, the OFT associated with SOPWM should be followed so that the minimum current THDs can be obtained with the low switching to fundamental frequency ratios.

The conventional SVM and SOPWM can stratify the requirement 1) and 2) respectively but not both. Therefore, the pseudo six-step modulation (PSSM) which combines SVM and SOWPM and exploits the general feature of OPPs, is proposed in this section.

5.4.1 Principle of Proposed PSSM

As shown in Fig. 5-7, $\boldsymbol{\psi}_{sop}^*(k)$ and $\boldsymbol{\psi}_{sop}^*(k+1)$ denote the constructed reference optimal stator flux vector from the reference flux by the process described in Fig. 5-6, at the kth and $k{+}1^{th}$ steps respectively.
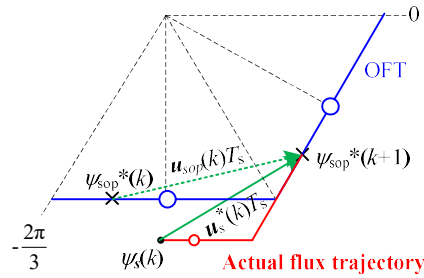
Fig. 5-7 Illustration of the optimal stator flux tracking using the proposed PSSM (N_{p}=3). Solid red line: the stator flux trajectory in transient, solid green arrow: the reference voltage vector in transient, dotted green arrow: the equivalent voltage vector of the associated OPP in the time-step, solid blue lines: the associated OFT over the 1/3 fundamental cycle, blue/red circles: zero vectors are applied and the flux vectors do not change.

The actual stator flux vector at the kth step is denoted as $\boldsymbol{\psi}_s(k)$ can be obtained from the current model expressed in (5-1). Therefore, the flux error at the kth step with respect to the optimal flux, $\boldsymbol{\psi}_{sop}^*(k)\boldsymbol{,}$ is given by

$$\boldsymbol{d}_\psi(k) = \boldsymbol{\psi}_{sop}^*(k) - \boldsymbol{\psi}_s(k) \tag{5-6}$$

The flux error in (5-6) cannot be eliminated by employing the OPP associated with the steady state condition. As already analysed in section 4.3.2, this dynamic error will only decay exponentially at a rate determined by the electrical time constant of the machine. It can last many electrical cycles before disappearing in high-speed drives and cause increased ripples in the dq axis currents and torque. Therefore, in order to realize fast tracking of the OFT, the reference voltage vector $\boldsymbol{u}_s^*$ for the kth step should be calculated by

$$\boldsymbol{u}_s^*(k) = \frac{\boldsymbol{\psi}_{sop}^*(k+1) - \boldsymbol{\psi}_s(k)}{T_s} \tag{5-7}$$

As can be seen in Fig. 5-7, this reference voltage vector differs from that associated with the OPP in steady state, i.e. $\boldsymbol{u}_{sop}(k)$, when the present stator flux, $\boldsymbol{\psi}_s(k)$, is not equal to the associated optimal flux, $\boldsymbol{\psi}_{sop}(k)$, on the OFT.

According to the principle of SVM, two active-vectors and zero-vectors can be employed to synthesize the derived reference voltage vector in (5-7). By way of example, for the reference voltage in voltage sector I as shown in Fig. 5-7, the two corresponding active-vectors can be derived as $\mathbf{V}_1$ and $\mathbf{V}_2$. The time durations of $\mathbf{V}_1$, $\mathbf{V}_2$ and zero-vector, t_1, t_2 and t_0 can be derived respectively as

$$t_1 = T_s \frac{\sqrt{3}u_s^*(k)}{V_{dc}} \cdot \sin\left[\frac{\pi}{3} - \theta_u^*(k)\right] \tag{5-8}$$

$$t_2 = T_s \frac{\sqrt{3}u_s^*(k)}{V_{dc}} \cdot \sin\theta_u^*(k) \tag{5-9}$$

$$t_0 = T_s - t_1 - t_2 \tag{5-10}$$

where, $u_s^*(k)$ and $\theta_u^*(k)$ are the magnitude and phase of the reference voltage vector, respectively. In the conventional SVM, the switching vector pattern (i.e. sequence and time duration), $\{\mathbf{V}_0,\mathbf{V}_1,\mathbf{V}_2,\mathbf{V}_7\}\&\{t_0/2, t_1, t_2, t_0/2\}$ (illustrated in Fig. 5-8 (a)) and $\{\mathbf{V}_7,\mathbf{V}_2,\mathbf{V}_1,\mathbf{V}_0\}\&\{t_z/2, t_2, t_1, t_z/2\}$ are employed alternately. They can bring the stator flux vector to the reference optimal flux vector at the end of the step.

Alternatively, the flux trajectory in the time-step can be decomposed into the components contributed by the two active voltage switching vectors with appropriate sequence and use of zero-voltage vectors. The direction and length of the stator flux variation determined by the voltage switching vectors and their time duration, respectively. When zero vectors apply, the movement of the flux trajectory stops. To realise the voltage reference vector $\boldsymbol{u}_s^*$ while following the switching pattern of the optimal flux trajectory, the actual flux trajectory in red shown in Fig. 5-7 should be achieved. The required switching sequence will be $\mathbf{V}_1$, $\mathbf{V}_0$, $\mathbf{V}_1$ and $\mathbf{V}_2$. However, this switching sequence is different from that of SVM. Therefore, the switching vector sequence of the conventional SVM will not follow the optimal switching vector patterns of the optimal flux trajectory and thus can result in increased current distortions.
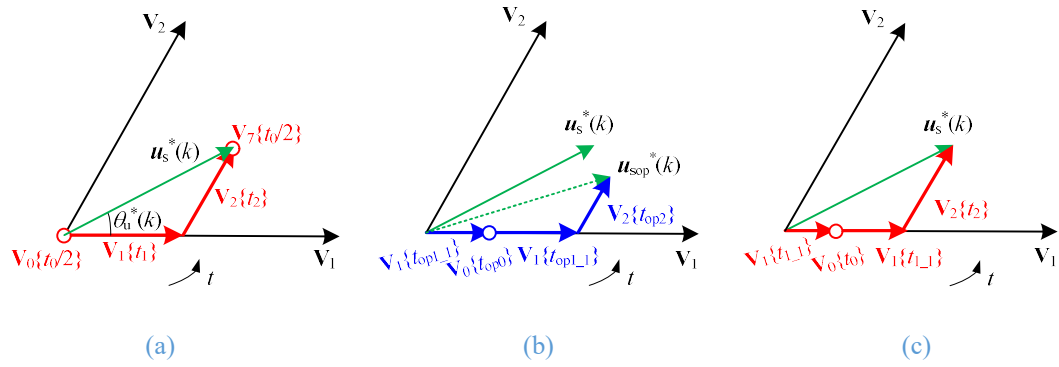
Fig. 5-8 Illustration of switching vector pattern with different methods (N_p=3). (a) SVM (b) SOPWM (c) Proposed PSSM. The arrow t indicates the direction of time progresses, the circle denotes the zero-vector and the length of the active switching vector denote the execution time duration.

In contrast, as described in section 4.3.3.1, the optimal switching vector patterns (OSVP) can be constructed from the three-phase OPPs. The corresponding OSVP at the kth step in Fig. 5-7 with N_p=3 is plotted in Fig. 5-8 (b). The switching sequence and time durations are given in $\{V_1, V_0, V_1, V_2\} \& \{t_{op\_1}, t_{1op}, t_{op1\_2}, t_{op}\}$. The time durations $(t_{op\_1}, t_{1op}, t_{op\_2}, t_{op})$ of the OSVP are derived from the optimal activating angles (OAAs) of OSVP divided by the electrical angular frequency. Hence, the resultant voltage vector of the OSVP, $\boldsymbol{u}_{sop}(k)$, indicated by the dotted green arrow in Fig. 5-7 and in Fig. 5-8(b) can be obtained. However, it differs from the reference voltage vector $\boldsymbol{u}_s^*$ when $\boldsymbol{\psi}_s(k)$ deviates from the optimal flux trajectory during a transient. That is, the OSVP can only track the OFT in steady states as shown in Fig. 5-7. To realise $\boldsymbol{u}_s^*$, the time durations of the OSVP should be modified to those shown in Fig. 5-8(c)

Therefore, in order to eliminate the dynamic flux error fast in transients and track the OFT in steady states, the reference vector synthesis scheme in the proposed PSSM is based on the following criteria:

1) The switching vector sequence of the OSVPs is employed.

2) In order to ensure that there are always at least two active-vectors and one zero-vector available in a time-step, the time-step is set to the 1/6 of the fundamental electric cycle.

3) The sum of the time durations of each voltage switching vectors stratifies (5-8)~(5-10), respectively.

4) The ratio of the time durations of a given voltage switching vector is equal to that of the OSVP.

194

The need for criterion 2 can be seen in Fig. 5-8 (b). If the time-step is too short, the OSVP in the time-step may only have one active voltage switching vector, e.g. $\{V_1,V_0,V_1\}\&\{t_{op\_1}, t_{1op0}, t_{op1\_2}\}$. This is not adequate to synthesize an arbitrary reference voltage vector. To realize the reference voltage vector, extra switching vector may be required in steady states and result in the increase of switching frequency. Alternatively short time-step may be implemented in such way that by defining a current error margin extra switching vector is only employed when the current error is larger than the defined margin. However, the vector synthesis in this method will be very complicated in order to cover all the possible scenarios and the setting of the current error margin is operating condition dependent. Setting the time-step to 1/6 cycle is sufficient for high-speed PMSMs because the control frequency will automatically increase with the rotational speed and variations in the reference stator flux or current vector can be always tracked in the one-sixth cycle by deadbeat control of the stator flux.

As the proposed method implements six-step control per fundamental cycle while use multiple switching vectors in a time-step, it is referred to as pseudo six-step modulation (PSSM). On the contrary, in the conventional six-step operation, only one active switching vector is available per step. The permissible switching frequency is more exploited and utilized in the proposed PSSM. Therefore, the superiority of the proposed PSSM against the six-step operation are twofold in terms of current distortion reduction, i.e. operating at the higher but permissible switching frequency and with optimized switching patterns.

With the proposed method, the optimal flux vector can be tracked at the next step in transients as shown in Fig. 5-7. While in steady states, as the reference voltage vector approaches to the resultant voltage vector associated with the OSVP, the derived switching vector pattern in Fig. 5-8 (c) will be close to that in Fig. 5-8 (b). This indicates that the flux trajectory will follow the OFT and lead to minimum current THDs of the SOPWM.

5.4.2 Reference Voltage Vector Synthesis in Proposed PSSM at Different Scenarios

The principle of the proposed PSSM has been described, which is to synthesize the reference voltage vector based on the OSVP six times per fundamental cycle. However, as the OSVP varies with sampling positions and pulse numbers, the synthesis procedure

of a reference voltage vector in the proposed PSSM may differ. According to the number of active vectors and the location of the reference voltage vector, the synthesis of reference voltage vector can be generally divided into three categories.

Fig. 5-8 (b) illustrates the most common case, referred to as normal case, where the OSVP exhibits two types of active vectors and the resultant voltage vector $\boldsymbol{u}_{sop}^*$ of OSVP are in the voltage sector of the actual reference $\boldsymbol{u}_s^*$. The voltage vector synthesis can be completed by following the four criteria listed previously. The other two different cases are represented in Fig. 5-9 and Fig. 5-10, respectively and will be elaborated next.

(a)	(b)
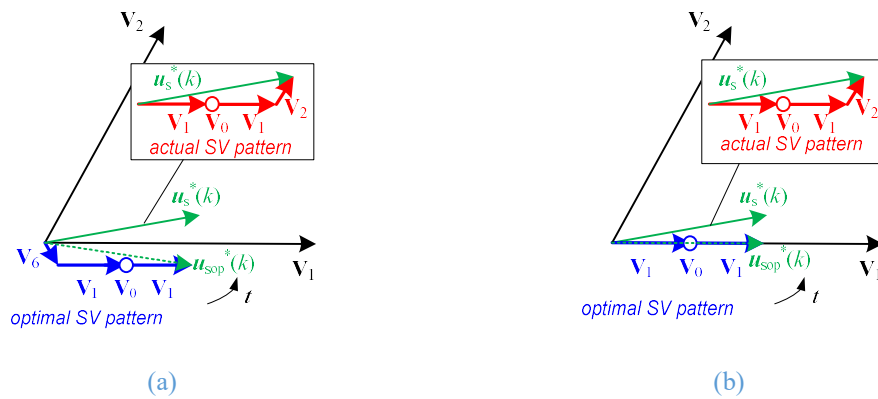
Fig. 5-9 Illustration of vector synthesis for special case 1 (a) reference vectors in the adjacent sectors (b) the resultant reference vector associated the OSVP at the sector edge

For special case 1 shown in Fig. 5-9 (a), the resultant voltage vector $\boldsymbol{u}_{sop}^*$ of an OSVP is not in the same sector of the actual reference, $\boldsymbol{u}_s^*$. To synthesize this reference voltage vector, the aforementioned criterion 1 needs to be modified. The actual switching vector sequence cannot be set exactly the same as the OSVP. Instead, a different active vector required by the reference vector synthesis, referred to as new active vector, $\mathbf{V}_2$, in Fig. 5-9 (a) is used at the end of the vector sequence of the OSVP while active vector, $\mathbf{V}_6$, is not used. Then by applying the criteria 2~4, the actual switching vector pattern can be derived as highlighted in red in Fig. 5-9 (a), where the sum of the time duration of the active vectors is determined by the synthesis of the reference voltage vector in (5-8) to (5-10) and the ratios of time durations of a voltage switching vectors in the sequence are determined from the OSVP.

Special case 1 also includes a particular scenario where the resultant voltage vector, $\boldsymbol{u}_{sop}^*$, of an OSVP locate at the edges of a voltage vector, as shown in Fig. 5-9 (b). In this case, the new active vector, $\mathbf{V}_2$, needs to be added as active vector, $\mathbf{V}_6$, is not required in the OSVP. Additionally, for a very large transient, $\boldsymbol{u}_s^*$ and $\boldsymbol{u}_{sop}^*$ may not locate

in two adjacent sections of the voltage hexagon. For these scenarios, in order to facilitate the implementation, the switching vector pattern of the conventional SVM can be employed to synthesize the reference, as the current distortion is not of great concern in transients.
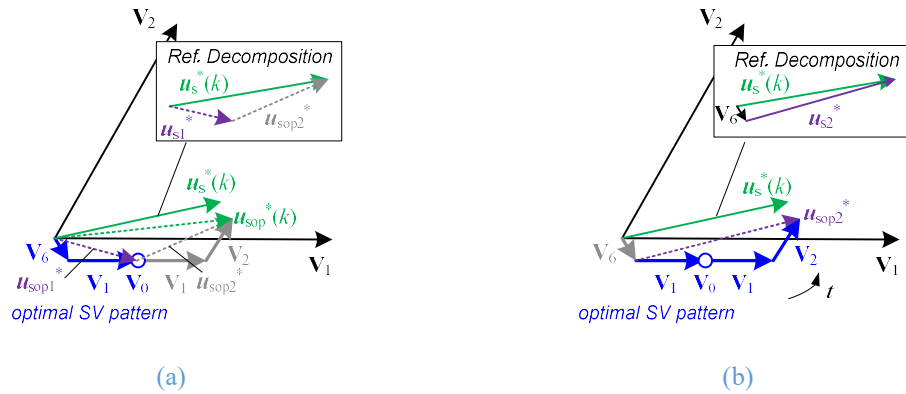
Fig. 5-10 Illustration of two-step vector synthesis for special case 2 (three types of active-vectors in the present OSVP) (a) 1st step, synthesize u_{s1}* with the OSVP associated with u_{sop1}* (b) 2nd step, synthesize u_{s2}* with the OSVP associated with u_{sop2}* where the time duration of the secondary switching vector, V_6 is determined in the 1st step synthesis.

For the special case 2 as shown in Fig. 5-10 (a), the OSVP in the time-step consists of three active vectors. This case usually occurs at high pulse numbers. The reference voltage vector $\boldsymbol{u}_s^*$ can be synthesized in two steps. Firstly, the switching vector sequence of OSVP is divided into two parts, where both parts exhibit two types of active vectors. Refer the same active vector in the two parts as the main active vector, i.e. V_1 in Fig. 5-10 (a) and the others as secondary active vectors, i.e. V_6 and V_2. Accordingly, the reference voltage vector $\boldsymbol{u}_s^*$ can be decomposed into two as illustrated in Fig. 5-10 (a), where the second one $\boldsymbol{u}_{sop2}^*$ is same as the resultant voltage vector of the second part of OSVP. By this means, the synthesis of the first reference voltage vector becomes similar to the aforementioned cases with two types of active vectors in the OSVP, i.e. the normal case and special case 1. The only difference is that when the special case 1 occurs, the new active vector doesn't need to added considering that the residual vector synthesis error can be addressed in the second step of the reference voltage vector synthesis. In the first step of vector synthesis, the time duration of the secondary active vector, i.e. V_6 can be derived and kept fixed in the following steps. Subtract it from the reference voltage vector yields a new reference, i.e. $\boldsymbol{u}_{s2}^*$ in Fig. 5-10 (b). Hence, based on the OSVP ruling out the fixed secondary active vector, i.e. V_6 the new reference can also be synthesized as similar to the normal case or the special case 1. Finally combining the derived switching vector

197

pattern in the second step synthesis with the fixed secondary active vector in the first step gives the final switching vector pattern for real-time drive control.

In summary, the three cases described above applied generally for all the pulse numbers and sampling instants. In all the three cases, the reference voltage vector can be synthesized. As a result, the optimal flux vector can be reached at the next step, indicating fast dynamic response. Moreover, in steady state, since the reference voltage vector in steady states is close to the resultant voltage vector of the OSVP, the actual switching vector pattern will approach the optimised one. Accordingly, the actual flux trajectory in the time-step will follow the optimal trajectory and lead to minimum current distortions. Therefore, both fast dynamic response and low current harmonic distortions in steady states can be achieved by the proposed method.

5.4.3 Implementation of Proposed PSSM

In this section, the implementation details of the proposed method are described. Firstly, the current sampling scheme and delay compensation method are introduced. Subsequently, the control diagram of the proposed PSSM are presented. Finally, the schematic diagram of the current and speed control with the proposed PSSM are given, where the current control error of the proposed PSSM caused by inaccurate machine model are addressed as well.

5.4.3.1 Current Sampling and Delay Compensation Scheme

Sampling and PWM delays can significantly affect the control performance of high-speed PMSM drives. If they are not addressed properly, the drive system would exhibit oscillations and even lose stability [31]. Hence, delay compensation is indispensable for control of high-speed machine drives. Fig. 5-11 shows the sampling and PWM updating timing sequence of the proposed method. The sampling of phase currents and the rotor position are executed in advance of step k by the time interval T_c, where T_c should be set large enough to complete the execution of the control program. The calculated stator voltages, effectively the PWM signals are updated at step k. The time interval of step k is set to one sixth of one electrical period. The corresponding sampling and calculation of the next step $k+1$ are triggered T_c time before the end of the current step. Therefore, the sampling time interval T_{sp} in the proposed method equals to one sixth of the electrical period and varies with the machine speed.
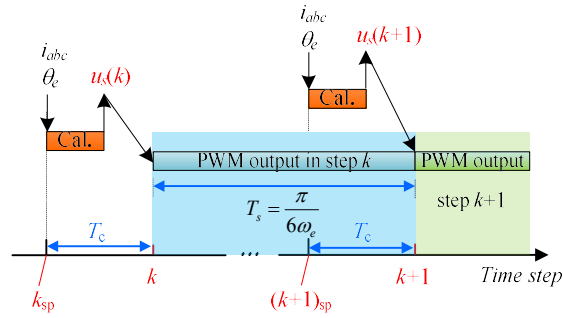
Fig. 5-11 Timing chart of sampling and PWM updating scheme for the proposed method
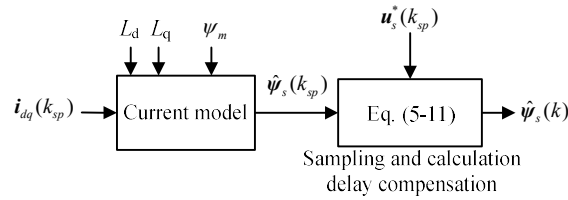
Fig. 5-12 Stator flux vector estimation with delay compensation

The sampling and calculation delay can be compensated by the prediction of the stator flux vector at step k, as shown in Fig. 5-12. The stator flux vector at the sampling instant, $\widehat{\boldsymbol{\psi}}_s(k_{sp})$, is estimated by the sampled dq axis currents, $\boldsymbol{i}_{dq}(k_{sp})$ and the current model expressed in (5-1).

Assuming that the inverter nonlinearity and resistive voltage drop is negligible at high speeds, the stator voltage at the time instant of step k_{sp} in Fig. 5-12 can be approximated by the corresponding reference stator voltage, $\boldsymbol{u}_s^*(k_{sp})$. Thereby the stator flux vector at step k can be obtained in (5-11), which compensates the sampling and calculation delay.

$$\boldsymbol{\psi}_s(k) = \boldsymbol{\psi}_s(k_{sp}) + \boldsymbol{u}_s^*(k_{sp}) \cdot T_c \tag{5-11}$$

Likewise the reference stator flux vector at the next step can be employed to compensate the PWM delay. Assume that the reference dq axis currents and the machine speed is kept constant during the control period, the reference flux vector at step $k+1$, $\boldsymbol{\psi}_s^*(k+1)$ can be obtained as

$$\boldsymbol{\psi}_s^*(k+1) = \boldsymbol{\psi}_{sdq}^*(k_{sp}) \cdot \boldsymbol{e}^{j\omega_e(T_c+T_s+\theta_e)} \tag{5-12}$$

where, $\boldsymbol{\psi}_{sdq}^*(k_{sp})$ is the reference stator vector in the dq frame at the sampling instant. $\boldsymbol{e}^{j \cdot x}$ denotes anti-clockwise vector rotation by the angle of x. By tracking the reference stator flux vector in (5-12), the PWM delay can then be compensated.

199

In addition, as can be seen in Fig. 5-11, variable time-step control is required when the operating speed varies. It can be realised in the processors e.g. DSP by event triggering function. However, it may not be able to be implemented in some processors employing model based programming, such as OPAL5600 used in this thesis, which only supports fixed time-step control. Nevertheless, with the sampling and delay compensation method described above, only slightly modification is needed to address this problem. With fixed time-step implementation, the time-step should be set small and the current sampling instants should be modified to the discrete time instants just before the one shown in Fig. 5-11. The advance time T_c will vary but can be easily calculated. The PWM signals calculated for the next step are being stored in the processor and the ones commencing in the present step are delivered to the FPGA at each time-step for PWM generation.

5.4.3.2 Control Diagram of Proposed PSSM
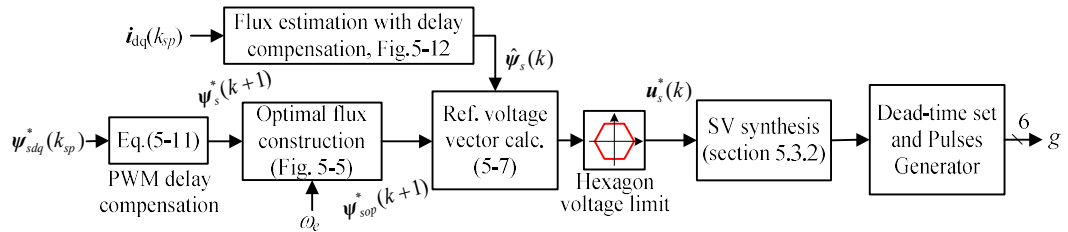
Fig. 5-13 Control diagram of the proposed method

The complete control diagram of the proposed PSSM is shown in Fig. 5-13. The input reference $\boldsymbol{\psi}^*_{sdq}(k_{sp})$ is the stator flux vector in the dq frame at the sampling instant. While the actual reference being tracked is the associated optimal stator flux, $\boldsymbol{\psi}^*_{sop}(k + 1)$, which is derived from the PWM delay compensation in (5-11) and the real-time optimal flux construction in Fig. 5-6. With the stator flux vector at step k obtained from Fig. 5-12, the reference voltage vector can be calculated and synthesized using the proposed PSSM. Finally, by inserting the dead-time, all the six drive signals for the two-level inverter can be obtained. It should be noted that the control algorithm is executed by the time step of one sixth of a fundamental period and the PWM signals are updated after T_c interval, as illustrated in Fig. 5-11.

5.4.3.3 Closed-loop Current and Speed Control with Proposed PSSM

As the stator flux vector can be directly regulated in the proposed PSSM, the conventional dq axis current control can be realised by converting the reference current vector to the reference stator flux vector based on the current model.

However, this reference conversion and the stator flux estimation in PSSM requires accurate machine model. The machine parameter mismatch and inverter nonlinearity will affect the current control accuracy. Since the current control is similar to that of DBPCC described in chapter 2, which tracks the stator flux to realise current control, the model error influence can be analysed in the same way and the similar conclusion as in section 2.3 can be drawn. The transient control performance of the proposed method is mainly affected by the inductance error while the steady state control accuracy is dependent on all the factors including the PM flux linkage, inductance and inverter nonlinearity. Therefore, in order to compensate the current control error in steady states, the adaptive reference correcting current injection (ARCCI) proposed in Chapter 3 can be included in the current control loop.
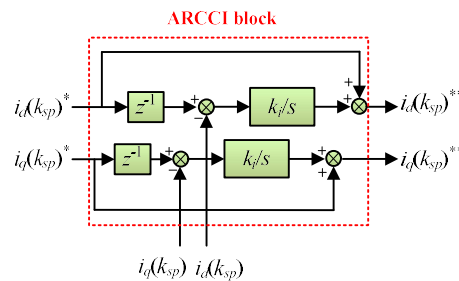
Fig. 5-14 Control diagram of ARCCI block to compensate the model errors

Fig. 5-14 shows the control diagram of the ARCCI, where the one-step delay blocks are incorporated due to the one-step tracking delay feature of the proposed method. The integral gain K_i is determined by the product of the adaptive rate, η, and the time-step which equals one sixth of the electrical period. In this chapter, the adaptive rate is set to 0.001.

Fig. 5-15 shows the control diagram of the closed-loop speed control with the proposed method which contains an inner current control loop. The pulse number of the proposed PSSM is determined by the machine speed and the max switching frequency. When the machine is operated at low speed with the corresponding pulse number higher than 15, the conventional SVM based FOC is employed. The control method transition can be realised quickly as both the control methods have good dynamic response during speed transient with relative high pulse number. Therefore, the proposed method can be applied over a whole speed range with transition to SVM mode at low speeds.
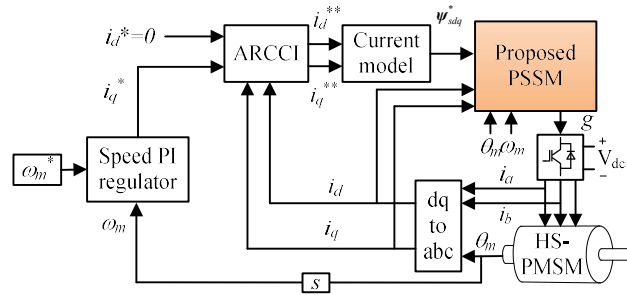
Fig. 5-15 Control diagram of the closed-loop speed control with the proposed method and model error compensation

5.5 Simulation Study

In this section, the performance the proposed method has been studied and verified by extensive simulations in MATLAM/SIMULNK. The same high-speed machine model as described in section 2.3 is employed. The maximum switching frequency is set to 8kHz. The advance sampling time T_c in Fig. 5-11 is set to 100us.

5.5.1.1 Transient and Steady-State Performance

The transient and steady state performance of the proposed method are studied by operating the machine in the current control mode at the constant speed of 30,000 rpm with the fundamental frequency of 1 kHz. Subject to the switching frequency limitation, the attainable pulse number is 7. The time-step i.e. one sixth of the fundamental period is 0.17 ms. The ideal inverter without dead-time is assumed.

Fig. 5-16 shows the torque, phase currents and dq axis current response when the q-axis current demand steps from 0 to 50A at t=2.17ms. As can be seen, very fast dynamic response can be achieved by the proposed method. The excellent transient performance is also evident in the corresponding current trajectory plotted in Fig. 5-17, where the new reference current trajectory can be followed quickly. Fig. 5-18 shows the dynamic flux error, i.e. the difference between the actual stator flux and the optimal stator flux in the steady states associated with OPPs. As can be seen, at the transient when the reference suddenly changes, a large dynamic flux error occurs. However, with the proposed method this dynamic flux error can be eliminated in one step, i.e. 0.17 ms, in the simulated scenario after the transient. Afterwards, the dynamic flux error is close to zero and indicates the actual stator flux is following the optimal flux trajectory. It is worth noting that as the control algorithm updates the PWM signals in every one sixth of the

fundamental period, if the reference changes during a time step, there will be an extra delay up to one time step.
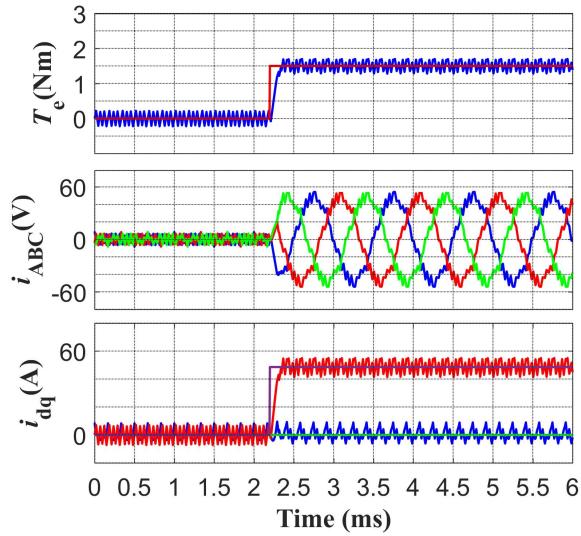
Fig. 5-16 Torque, phase currents and dq axis currents with the proposed PSSM (N_P=7) during the transient at 30,000 rpm
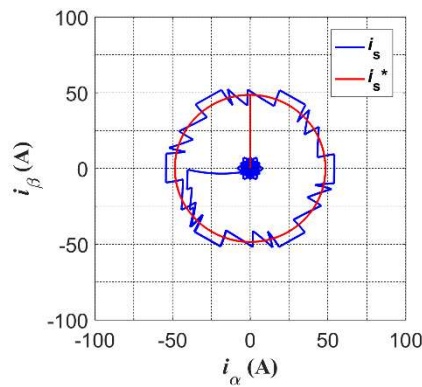
Fig. 5-17 Current trajectory in the stationary frame with the proposed PSSM (N_P=7) during the transient at 30,000 rpm
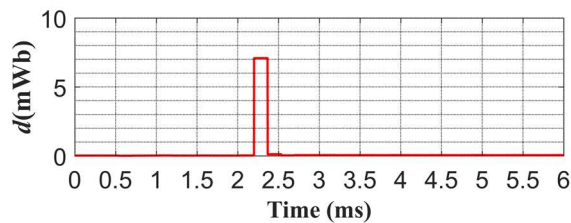
Fig. 5-18 Dynamic flux error magnitude with the proposed PSSM (N_P=7) during the transient 30,000 rpm

Fig. 5-19 (a) shows the phase A current and the resultant terminal voltage in the steady state at 30,000 rpm (1 kHz) with the q-axis current reference of 50A. The corresponding modulation index is 0.58. As can be seen, the voltage waveform is symmetric and consists of 7 pulses in a fundamental cycle, identical to the OPP with SOPWM. Consequently, the

phase current exhibits minimum THD, with only non-triplen order harmonics. The same observation can be made as the modulation index varies, such as that in Fig. 5-19 (b) when the q-axis current reference is increased to the maximum current, i.e. 100A and the resultant modulation index is 0.8. Fig. 5-20 plots the stator flux trajectories associated with the two steady states in Fig. 5-19, respectively. It can be seen that the optimal flux trajectory profile changes when the modulation index varies while the proposed method can always track the optimal flux trajectories, which contribute to the least current distortions.

(a)   (b)
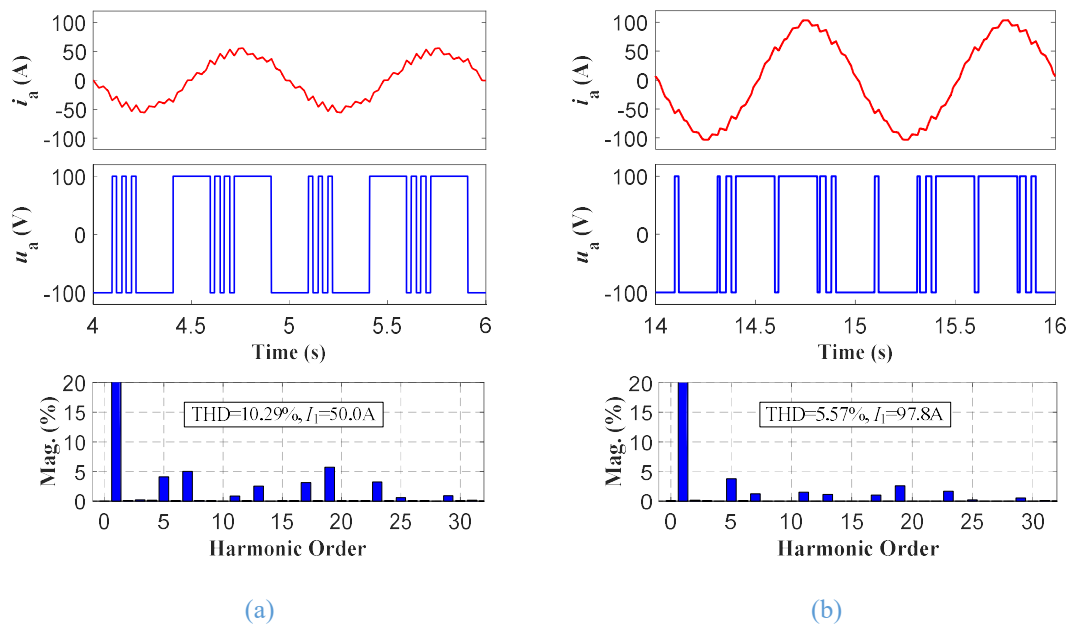
Fig. 5-19 Phase currents, terminal voltages and phase current spectrum with the proposed PSSM (N_P=7) in steady states at 30,000 rpm. (a) i_q*=50A (b) i_q*=100A
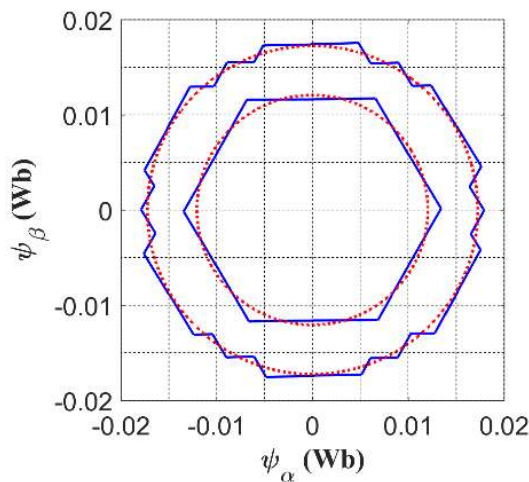
Fig. 5-20 Stator flux trajectories in steady states at 30,000 rpm

5.5.1.2 PWM Mode Transition

As has been discussed in section 4.3 of Chapter 4, the OPPs of SOPWM can exhibit multiple modes in the variable speeds, mainly due to the changes in the pulse number and the sets of optimal switching angles (OSAs). Similarly, for the proposed PSSM based on the OSVPs of SOPWM, the PWM mode transition is also inevitable. The PWM scheme in the whole speed range of the prototype high-speed PMSM is shown in Fig. 5-21, where the maximum switching frequency is set 8kHz. At the low speeds i.e. low fundamental frequencies, the conventional SVM is employed, whilst the proposed PSSM are used for high-speeds with the pulse number reduces as the speed increases.
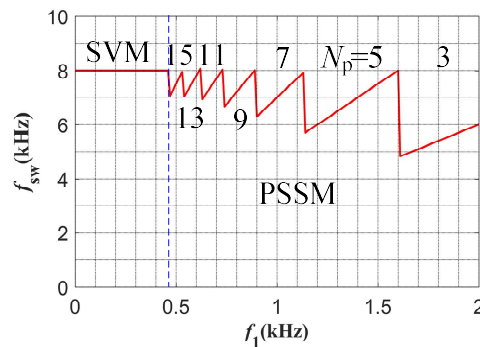
Fig. 5-21 PWM schemes over the whole speed range

Fig. 5-22 shows the simulation results of the speed control with the proposed method. The machine is accelerated from 14,000 rpm to 30,000 rpm with the maximum current of 100A. According to the PWM scheme illustrated in Fig. 5-21, the drive control undertakes several PWM mode transitions as the speed varies. Particularly, below the speed of the 14,120 rpm, the conventional SVM based FOC is employed. As can be seen from the machine waveforms in Fig. 5-22 , the proposed method can realize fast and smooth mode transition as the optimal stator flux are always being tracked.
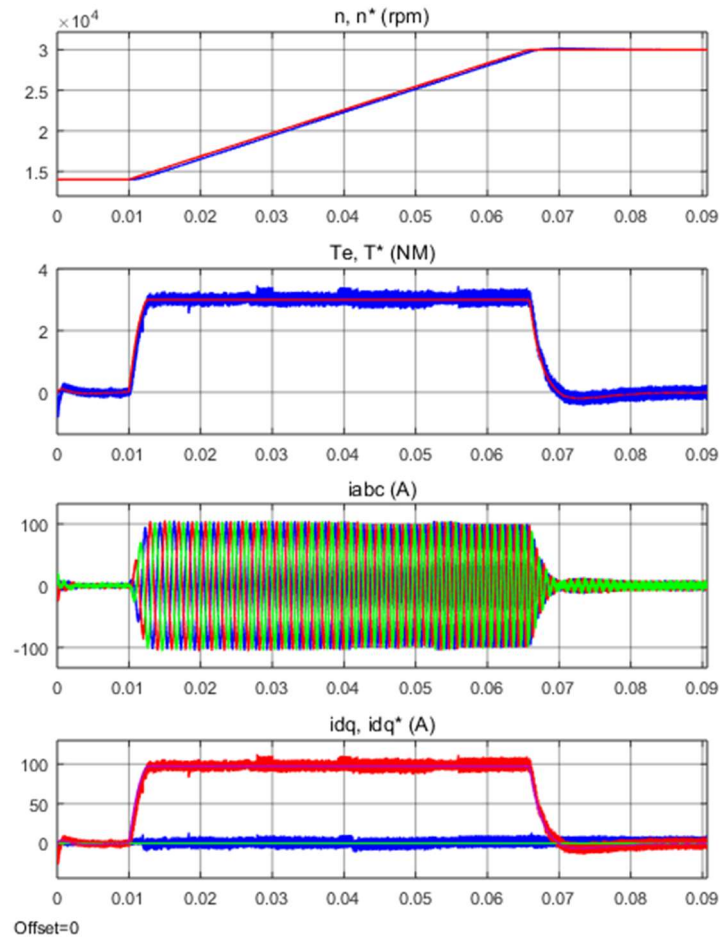
Fig. 5-22 Waveforms during the motor acceleration from 14,000 rpm to 30,000 rpm

The zoom-in view of the waveforms from t=0.027s to 0.033s in Fig. 5-22 are shown in Fig. 5-23 (a), where the bottom waveform is the mode transition indicator. Around t=0.028, the speed reaches the transition speed where the pulse number changes from N_p=13 to N_p =11 and around 0.031s, the modulation index reaches the point where the pulse pattern changes and the OSA discontinuity occurs at m=0.52 for N_p =11 as shown in Fig. 4-35. Hence, the pulse pattern with N_p =11 and m<0.52 is denoted as set 1 and that with N_p =11 and m> 0.52 as set 2 in Fig. 5-23(a). As evident in Fig. 5-23 (a), the proposed method manages the both types of PWM mode transitions quite well, the transition due to change in pulse number and the transition due to change in pulse pattern for a given pulse number. The resultant terminal voltages are shown in Fig. 5-23 (b). It can be seen that the terminal voltages can change to the required symmetric OPPs quickly as the operating point of the drive varies.

(a)

(b)
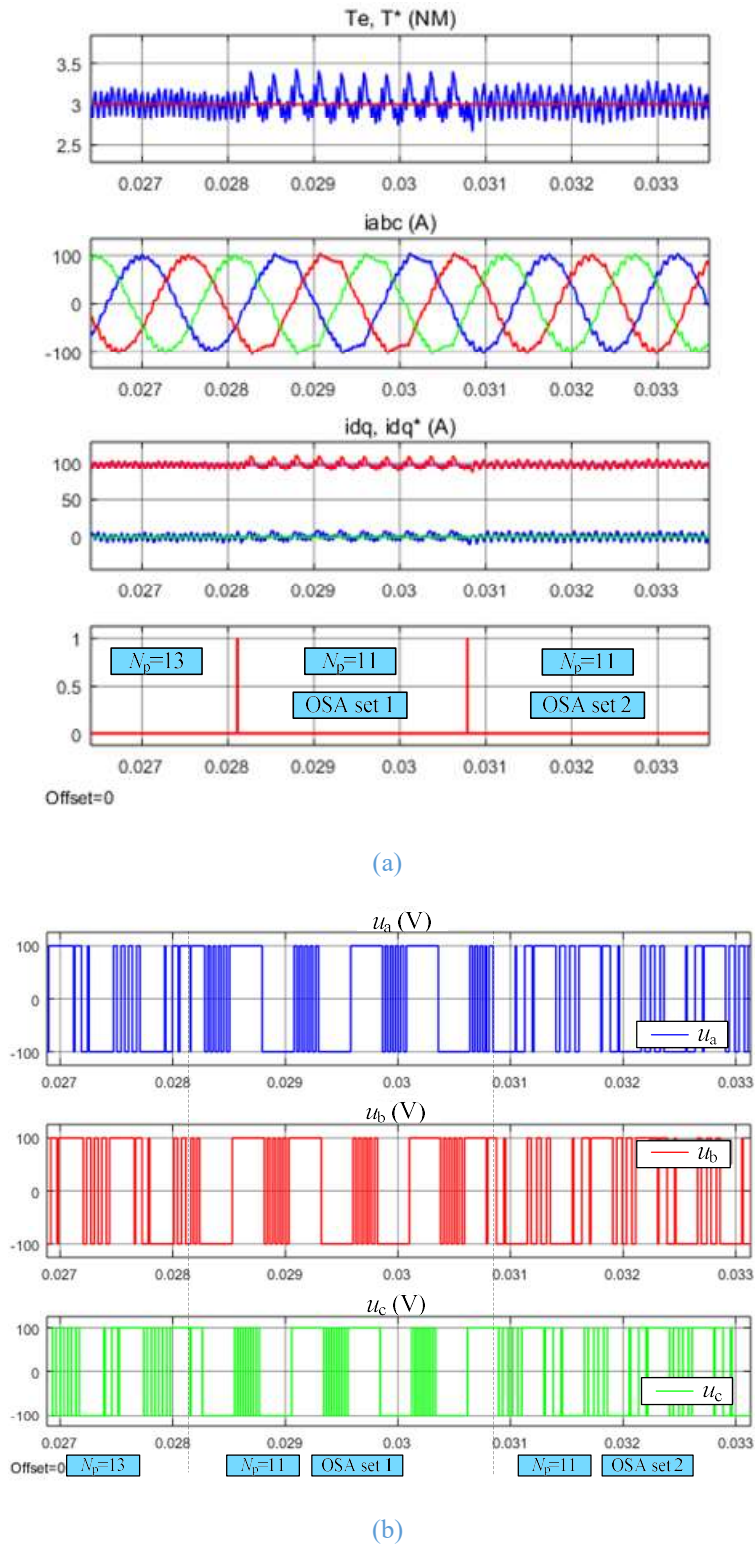
Fig. 5-23 Waveform during the mode transition transients. (a) torque, phase currents, dq axis currents and PWM mode transition indicating signal (b) the three-phase terminal voltages

5.5.1.3 Performance Sensitivity to Parameter Mismatch and Inverter Nonlinearity

To verify the performance of the proposed method under model errors, inaccurate machine parameters and inverter nonlinearity are deliberately included in the simulation.

207

The deadtime, t_{dd}, and the conducting voltage drop, V_{TD}, of the inverter is set to 2μs and 1V, respectively. 10% error of the estimated permanent flux linkage and inductance are considered.

The performance of the proposed PSSM without the model error compensation method, i.e. ARCCI are studied firstly and the simulation results are shown in Fig. 5-24. As can be seen, the inaccurate machine parameters would cause steady-state control error in the dq axis currents whilst they have little influence on the transient performance and the current ripples. With the inverter nonlinearity, the average q axis current is lower than the reference when the q axis current reference is not equal to zero. However, the d axis current is hardly affected. With the estimation error of permanent flux linkage, the d axis and q axis currents in steady states both exhibit offset control errors, which are independent of the magnitudes of dq axis current demands. When the inductance is incorrectly estimated, dq axis current control error can be both observed. It can be seen that even without any compensation, the proposed PSSM yield satisfactory control performance in the presence of inaccurate machine model.

(a)

(b)

(c)

(d)

(e)

(f)
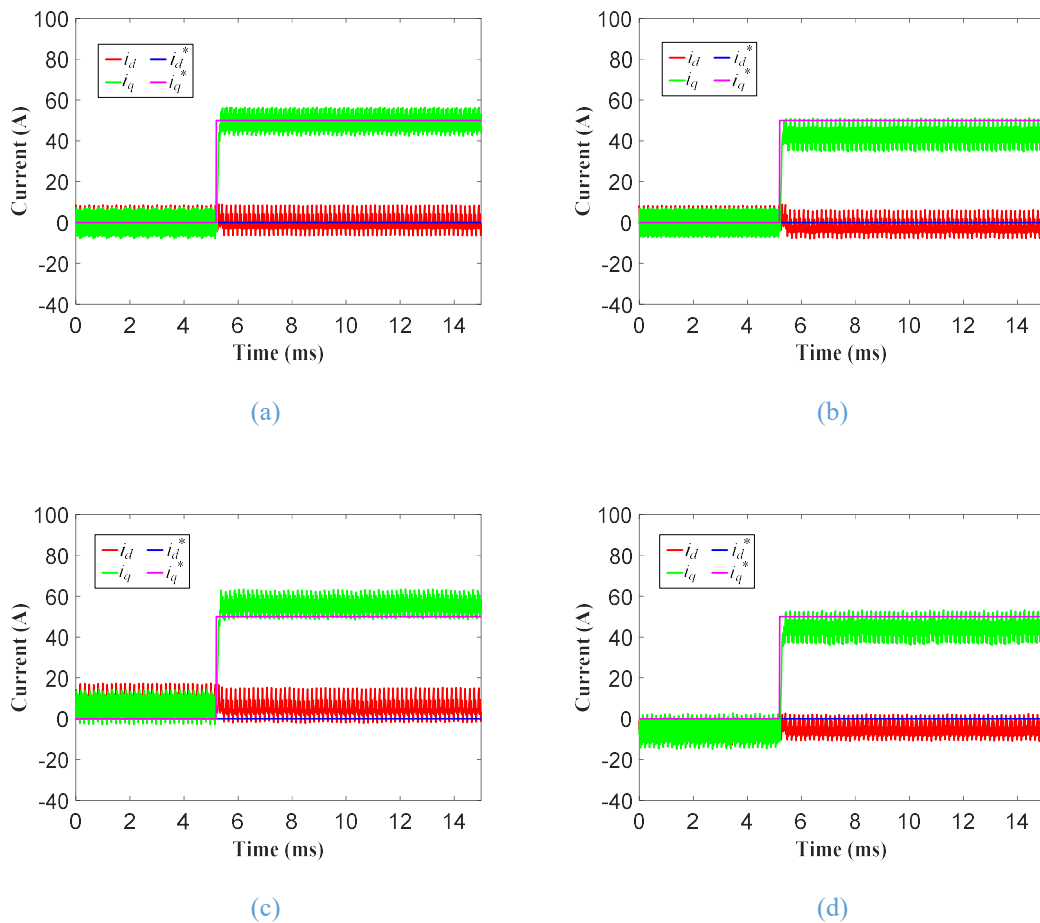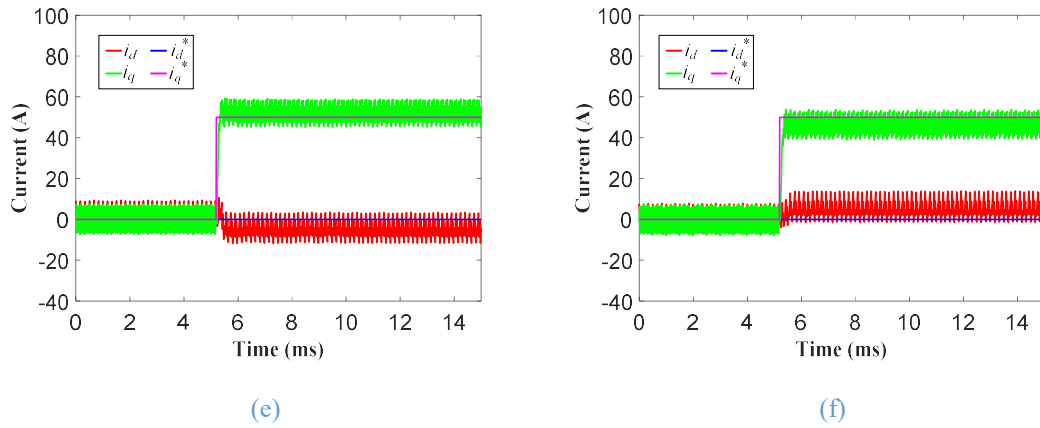
Fig. 5-24 The dq axis current response of the proposed PSSM (N_p=7) without ARCCI at 30,000 rpm. (a) Accurate model (b) Inverter nonlinearity (t_{dd}=2μs, V_{TD}=1V) (c) 10% overestimation in ψ_m (d) 10% underestimation in ψ_m (e) 10% overestimation in L_s (f) 10% underestimation in L_s

(a)

(b)
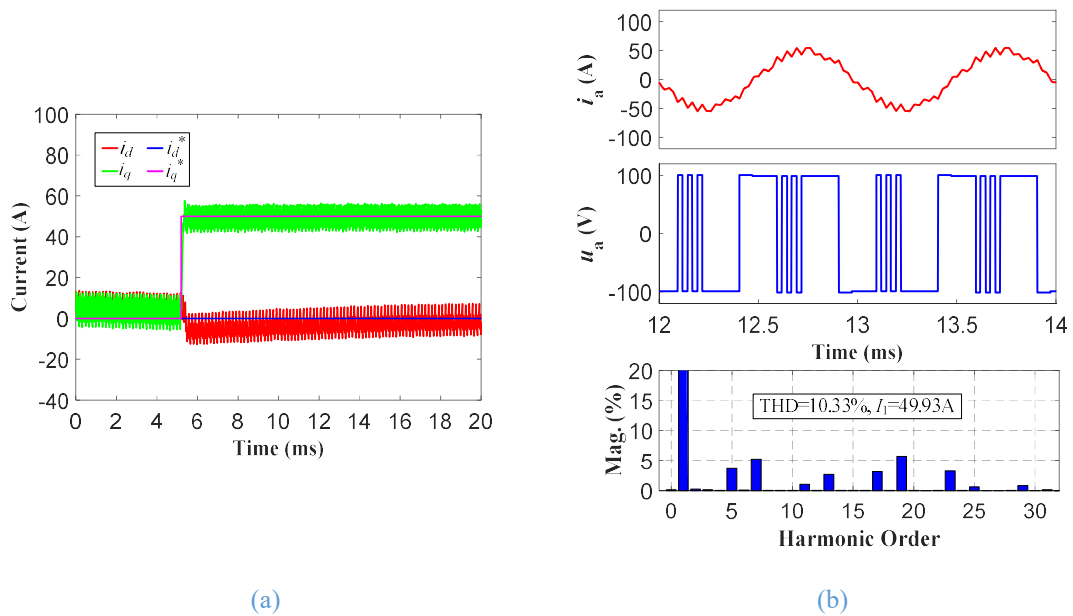
Fig. 5-25 Simulation results of the proposed PSSM (N_p=7) with ARCCI at 30,000 rpm and parameter mismatch and inverter nonlinearity. (a) dq axis current response (b) phase A current, terminal voltage and current spectrum (THD=10.5%, I_1=49.7A.)

Further, the control performance of the proposed PSSM with ARCCI are simulated with all the machine parameter mismatch accounted. Fig. 5-25 (a) shows the dq axis current response under inverter nonlinearity, 10% over-estimation in both permanent flux linkage and inductance and 50% under-estimation in phase resistance. As can be seen, with ARCCI, all the steady-state control errors caused by the model errors as shown in Fig. 5-24 can be compensated. Moreover, it can be seen in Fig. 5-25 (b) that the expected symmetric voltage phase waveform and current harmonic distribution can be still obtained with inaccurate machine model. The steady-state performance is close to the

results with accurate model in Fig. 5-19 (a). Therefore, the robustness of the proposed method against parameter mismatch and inverter nonlinearity has been verified.

5.6 HIL Testing Results

Before performing the experiment validation, the control performance of the proposed method has been tested in real-time on the HIL platform for the prototype high-speed machine. The same HIL test rig set-up as described in Chapter 4 is employed. Fig. 5-26 shows the HIL testing results of the proposed method with N_p=7 at 30,000 rpm, where the speed and current waveforms are generated by the DAC of the OPAL simulator and updated by the CPU time-step of 25μs. As can be seen in Fig. 5-26 (a), when the q axis current demand changes in step, the proposed method can track the reference quickly. From the switching signals in the steady state, the pulse pattern symmetries of SOPWM, i.e. QWS, HWS and 3PS can be observed. It verifies that the pulse pattern of the proposed method will approach to that associated with SOPWM in steady states and thus lead to the minimum current THD correspondingly. Therefore, both the excellent transient and steady state performance and the built program of the proposed control method in the OPAL have been confirmed by the HIL testing.

(a)   (b)
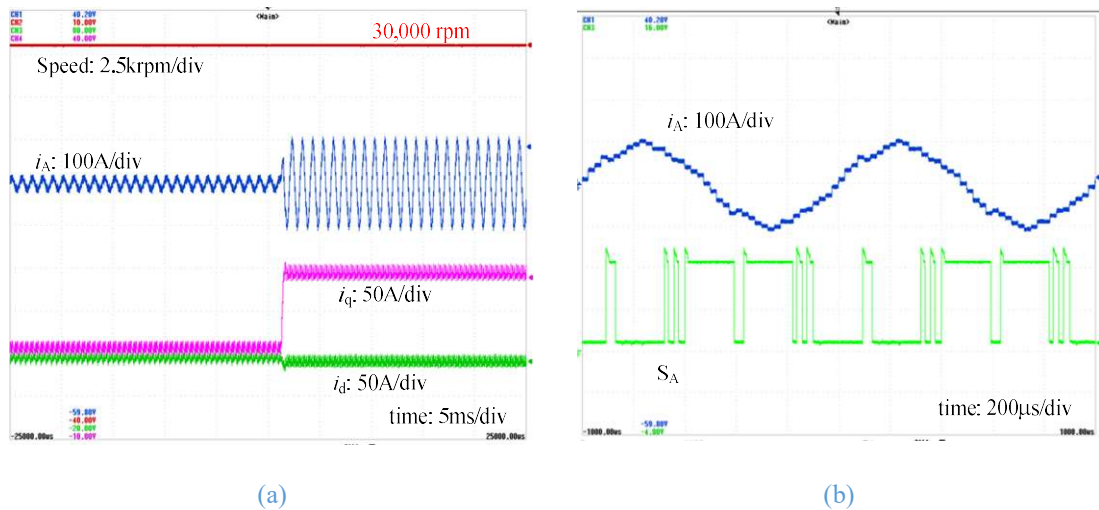
Fig. 5-26 HIL testing results of the proposed method with N_p=7 at 30,000 rpm (a) from top to bottom, speed, phase A current, q axis current, and d axis current. (b) phase A current and the associated switching signal.

5.7 Experiment Results

In this section, extensive experimental tests have been performed on the prototype high-speed machines. The same test rig as described in Chapter 2 is used. In order to the validate the performance of the proposed method with different pulse numbers ranging

from 3 to 15, the switching frequency of the inverter is not fixed in the testing and varies according to the operating speed and the employed pulse number. During the experiment, the high-speed prototype machine is under the current control mode and its speed is controlled by the high-speed dyno. Due to the computation limitation, the processor time-step is set to 50μs.

Firstly, the steady-state performance of the proposed method is studied. The high-speed machine drive is operating at 10,000rpm with N_p=15 i.e. the corresponding switching frequency of 5kHz. Fig. 5-27 shows the phase currents and the resultant current spectrum using the proposed method. As can be seen, with the proposed method, the current spectrum characteristic is similar to that of SOPWM in Fig. 4-29 (a), where the even and triplen switching harmonics can be eliminated. The current distortions of the proposed method and SOPWM are close and compared to the conventional SVM based FOC in Fig. 4-29 (b), the proposed method leads to a 6.1% reduction in the harmonic current, which reduces from 3.77 A to 3.54 A. This test validates the superiority of the proposed method in terms of steady-state performance.
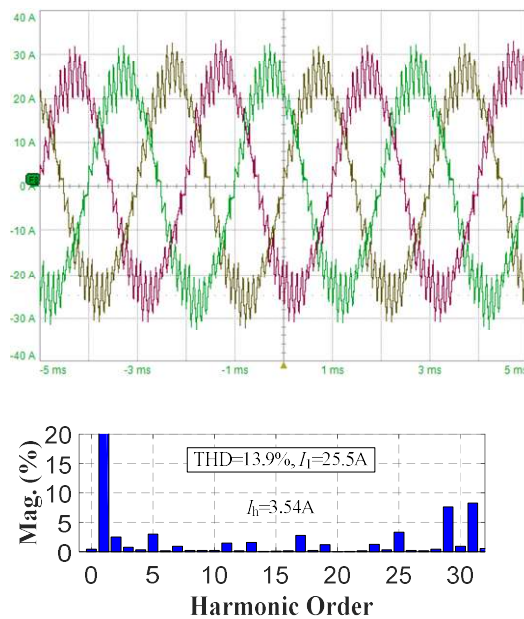
Fig. 5-27 Phase currents in steady states and current spectrum of phase A using the proposed PSSM at 10,000 rpm with N_p=15.

Secondly, the proposed method with different pulse numbers and pulse number transition performance are tested. In order to simplify the experiment testing, different pulse numbers are employed at the same speed, i.e. 10,000 rpm. The pulse number varies as time progresses, according to the profile defined in Fig. 5-28, where the pulse number gradually decrease from 15 to 3 and later increase from 3 to 15.
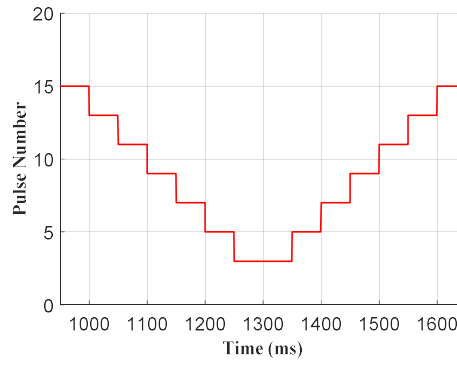
Fig. 5-28 Pulse number transition profile in the experiment.
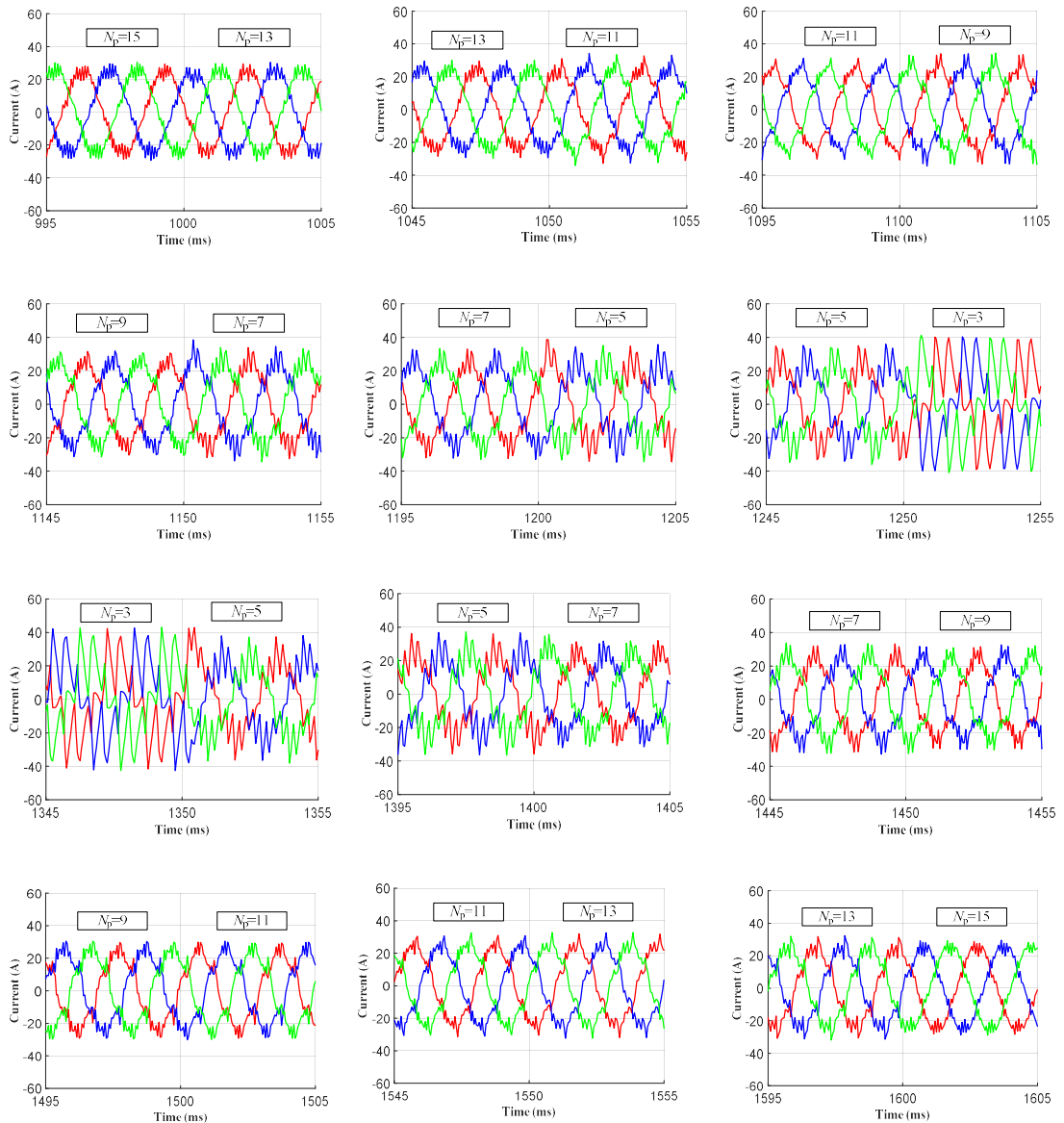
Fig. 5-29 Sampled dq axis currents during the pulse number transition transients using the proposed method at 10,000 rpm.

Fig. 5-29 shows the sampled phase currents during the various pulse number transition transients. As can be seen, fast and smooth transitions of PWM mode can be achieved by the proposed method as the corresponding OFT are being tracked.
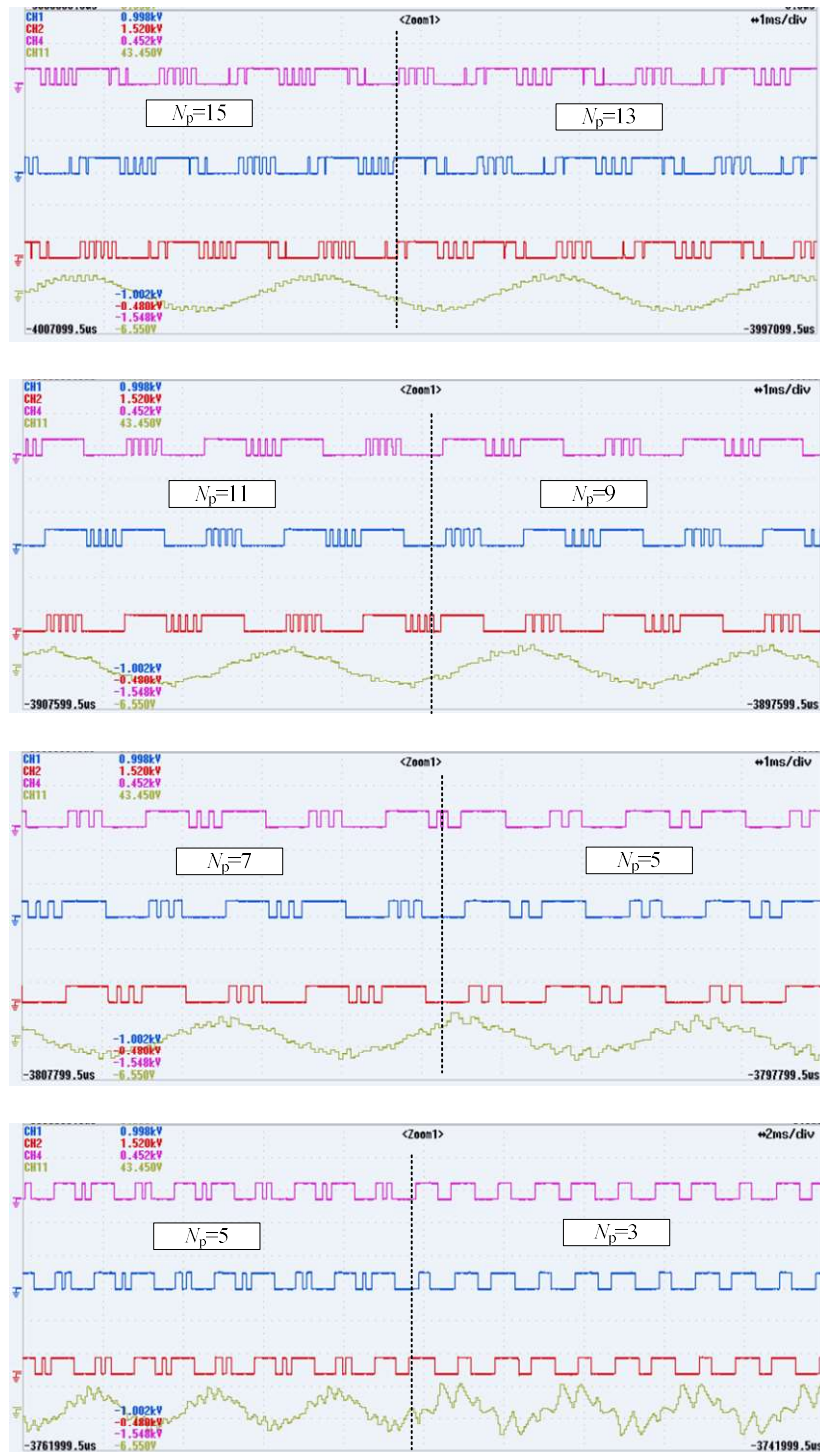
Fig. 5-30 Three-phase terminal voltages during the pulse number transition periods using the proposed method at 10,000 rpm. Purple/Blue/Red trace: terminal voltage of phase A/B/C; Yellow trace: phase A current.

Fig. 5-30 shows the three-phase terminal voltages and phase A current of the proposed method during the pulse number transition periods, where fast pulse number transition

can be seen. Moreover, before and after the transition, the voltage waveforms associated with the different pulse numbers in steady states can be obtained. It can be found that the symmetric voltage pulse patterns can be output by the proposed method, which is similar to SOPWM and consequently can lead to low current distortions.
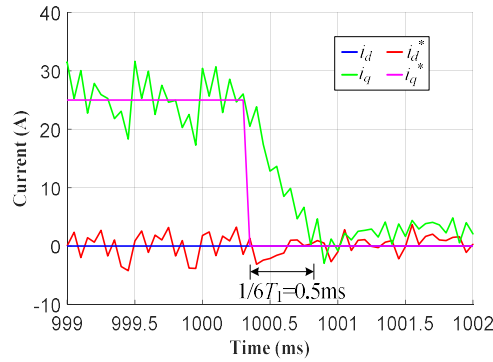
Fig. 5-31 Sampled dq axis currents of the proposed method (N_P=15) during the transient at 10,000 rpm.
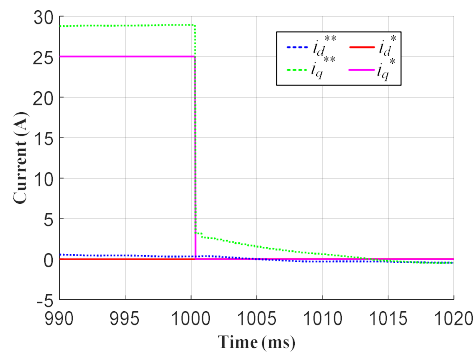
Fig. 5-32 Reference correcting currents in the proposed method (N_P=15) during the transient at 10,000 rpm.

Thirdly, the transient performance of the proposed method is validated by the q axis current step response testing. Fig. 5-31 shows the experiment results when the q axis current demand steps from 25 A to 0 A at 10,000 rpm. As can be seen, the actual q axis current can respond quickly and reach the new reference with a delay of only one sixth of the electrical period i.e. 0.5 ms at the operating speed of 10,000 rpm (the electrical period T_1=3ms). On the other hand, the average dq axis currents in the experiment is equal to the reference. Recalling the simulation result in Fig. 5-24 (b) without ARCCI under the inverter nonlinearity, the q axis current would exhibit control error. Therefore, the effectiveness of ARCCI regarding model error compensation can be verified as well. It is also evident in the recorded reference currents as shown in Fig. 5-32. The actual reference dq axis currents fed into the PSSM, i.e. i_d^{**} and i_q^{**} are different from the current demands,

i.e. i_d^* and i_q^* due to the injection of the correcting currents, which compensates the control error caused by the model error including the inverter nonlinearity.

(a)   (b)
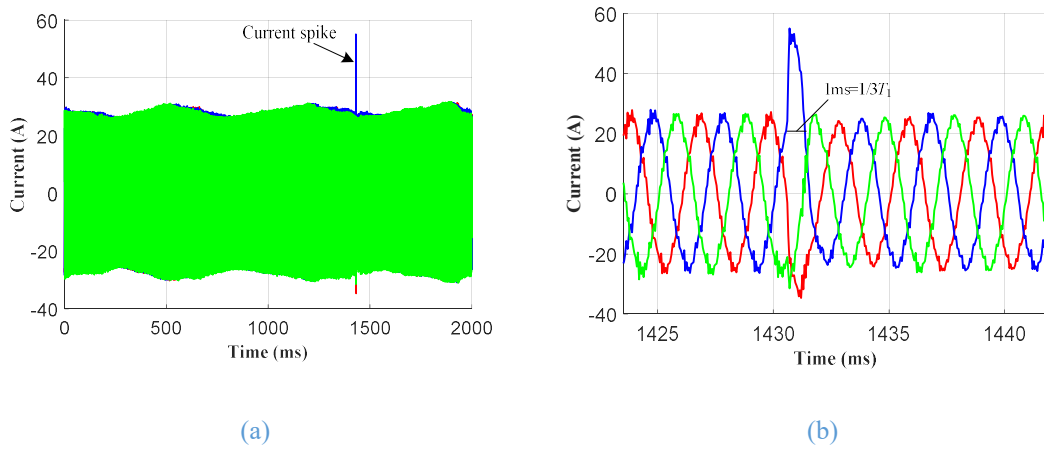
Fig. 5-33 Current spikes caused by inaccurate PWM signal generation at 10,000 rpm. (a) Phase currents over a long period. (b) Zoom-in view around the current spike
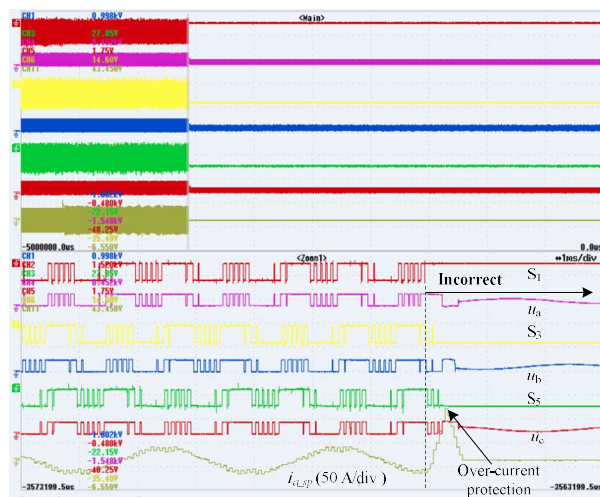
Fig. 5-34 Captured waveforms during the transient of over current protection at 10,000 rpm.

During the experiment tests, unexpected pulses are observed occasionally and randomly, which are accompanied with current spikes as shown in Fig. 5-33 and sometime will trigger the over-current protection (80 A) as shown in Fig. 5-34. This problem obstructs the further testing at higher speeds for safety reason. The cause of this problem has been figured out and it is because that the PWM signals cannot be fired out exactly as calculated by the processor, i.e. CPU. It may be because of the communication problem between the CPU and FPGA, such as memory leakage and requires further investigation into the FPGA implementation of PWM signal. Since the lab access is very limited during the period of Covid-19 and the lab reallocation and due to the timing reason, this implementation problem was found in the later stage of the PhD study, this problem have not yet been solved. However, as can be seen in Fig. 5-33 (b), the proposed method

215

can still effectively control the current back to the reference after 1/6 cycle (the total duration of abnormal current waveform lasts 1/3 cycle), demonstrating fast dynamic control capability. Therefore, the experiment results already obtained can confirms the effectiveness of the proposed method. The experiment test at higher speeds can be a future research work.

5.8 Summary

In this chapter, in order to improve the dynamic response of SOPWM based control, a novel method i.e. PSSM has been proposed. The proposed method tracks the optimal flux trajectory associated with SOPWM in every one sixth of a fundamental period based on the OSVPs of SOPWM. Both fast dynamic control of dq axis currents and low current distortions in steady states can be achieved. Moreover, the proposed method can realise fast and smooth pulse number transition and the steady-state current control error caused by the parameter mismatch and the inverter nonlinearity effects can be compensated. Extensive simulations and experiments have been performed and validated the effectiveness of the proposed method.

CHAPTER 6
Conclusions and Future Work

6.1 Work Summary

Due to high power density and efficiency, high-speed PMSM drives have been increasingly demanded in many applications such as electric vehicles and more electric aircrafts. However, since the switching frequency of the semiconductor switches is usually limited, high-speed PMSM drive which have high fundamental frequency would feature low SFRs. With low SFRs, both the dynamic response and the steady-state performance of high-speed PMSM drives will be deteriorated. Thus, in this thesis, advanced control and optimal PWM schemes have been investigated to address the low SFR problem of high-speed PMSM drives.

To achieve high bandwidth current control at high speeds with low SFRs, stationary frame based DBPCC is proposed in **Chapter 2**. By tracking the stator flux vector and considering the rotor movement during the control-time step precisely, the proposed DBPCC can realize very fast current control with only two time-step delays for the whole SFR range. The control performances under the conventional synchronous frame based DBPCC schemes with and without rotor movement compensation have also been analysed. It has been shown that to achieve similar control accuracy of the proposed method, the applicable SFRs for the conventional DBPCC without compensation and with rotor movement compensation should be higher than 50 and 20, respectively. In order to understand the influence of model inaccuracy on the performance of the proposed DBPCC deeply, the influence of the parameter mismatch and inverter nonlinearity in both the steady states and transients have been quantified analytically in **Chapter 2**. It has been shown that the steady state current errors caused by parametric mismatch increases as the speed rises while that caused by the inverter nonlinearity is nearly independent of the speed. The transient control performance is mainly affected by the inductance estimation accuracy and independent of the PM flux linkage. The numerical simulation results under various parametric mismatch scenarios matches exactly with the derived equations of the steady-state current errors. The experiment testing results further confirms the analytical predictions at various speeds.

To further improve the performance of the proposed DBPCC against the parameter mismatch and inverter nonlinearity, three novel methods have been proposed in **Chapter**

3 for DBPCC of high-speed PMSM drives. The proposed adaptive reference correcting current injection (ARCCI) method can effectively compensate the steady-state current errors caused by the inverter nonlinearity and parameter estimation errors of both the permanent magnet flux linkage and dq-axis inductances. The proposed adaptive harmonic reference correcting current injection (AHRCCI) method can suppress the current harmonics caused by the inverter nonlinearity and non-sinusoidal back EMFs. The proposed inductance identification method can significantly improve the transient performances when the inductance exhibits large estimation errors. All the proposed methods improve robustness of the DBPCC scheme and are valid for both low and high speeds. Employing the three proposed methods, ideal deadbeat current control can be achieved even though inaccurate machine parameters are used and the inverter nonlinearity and non-sinusoidal back EMF are significant in the PMSM drive. Experiments on the high-speed prototype PMSM drives have validated the effectiveness of all the three proposed methods.

To achieve minimised current THDs at high speeds with low SFRs, instead of the conventional SVM, SOPWM is employed and investigated for high-speed PMSM drives in **Chapter 4**. A computational efficient pulse pattern optimization procedure has been developed to obtain all the OPPs flexibly and quickly. Based on the offline OPPs, the minimised current THD can be obtained for a given pulse number per fundamental cycle. A fast harmonic current prediction for SOPWM based on the LUTs of optimal current distortion has been established. Both the simulation and experiment results have confirmed the accuracy of the harmonic current prediction. They also verify the effectiveness of SOPWM on producing the minimised current distortion as optimised offline. Moreover, in variable speed drives, SOPWM mode transition is inevitable, including the pulse number variation and change of continuous switching angle sets. The influence of SOPMW mode transition has been analysed and it is shown that a large transient current overshoot may occur. In order to address this problem, based on the general properties of optimal switching vector patterns and optimal stator flux trajectory patterns, a fast and smooth mode transition of SOPWM has been proposed for 2-level inverter fed high-speed PMSM drives. Extensive simulations and experiments have been conducted and confirm the effectiveness of the proposed method for all the possible mode transition scenarios.

Although SOPWM exhibits the optimised current distortion at high speeds with low pulse number in steady state, its dynamic response is undesirable. In order to address this dynamic problem of SOPWM, a novel and simple pseudo six-step modulation (PSSM) technique has been developed in **Chapter 5**. The proposed method tracks the OFT associated with the reference stator flux vector in six-steps per cycle based on the OSVPs of SOPWM. As a result, the proposed method can respond to the demand change within 1/6 fundamental cycle. Meanwhile the applied switching vectors would approach to the corresponding OSVP. It has been shown that the low current distortions close to the offline optimal results can be obtained in steady states. The effectiveness of the proposed method has been validated by extensive simulations and the experiment results at 10,000 rpm with various pulse numbers.

6.2 Future Work

Based on the research work of this PhD thesis, possible future work is listed below.

1) Experiment validation of proposed SOPWM mode transition scheme and PSSM at higher speeds

In this thesis, the experiments of the proposed SOM mode transition scheme and PSSM has been conducted on the prototype high-speed PMSM drives at 10,000 rpm for all possible low pulse numbers. Due to the FPGA implementation problem of PWM signals and potential risk at high speeds, the experiments at higher speeds have not yet been performed. Although the acquired experiment results have shown the effectiveness of the proposed method at 10000 rpm, the experiment testing of proposed methods at higher speeds is necessary in order to obtain more comprehensive validation and performance evaluation.

2) Extension of the proposed DBPCC methods to flux weakening operation region

In this thesis, the flux weakening operation is not considered since the prototype high-speed PMSM drive has a large voltage margin. While in a typical SPMSM drives, flux weakening operation is normally required when the speed is above the base speed due to the limitation of the DC-link voltage. Integration of the conventional flux weakening schemes to the proposed could be an effective solution. However, the transient performance of DBPCC may be deteriorated due to the voltage saturation and require

extra consideration of the voltage vector calculation. Alternatively, as the stator flux is used and tracked in the proposed DBPCC, it may be also possible to constrain the stator flux magnitude to realise the flux weakening. Additionally, flux weakening with six-step operation presents more challenges as there is virtually no voltage margin. Therefore, the proposed DBPCC operated in the flux weakening region requires further researches.

3) Extension of proposed DBPCC methods to IPMSM drives

The proposed DBPCC and the related performance improvement methods in this thesis have been developed and validated for SPMSM drives at both low speeds and high speeds. In theory, it is also applicable to IPMSM drives, which are widely employed in EVs. However, control of IPMSMs is more complex due to the magnetic saturation, inductance nonlinearity and MTPA operation. Hence, it is worthy of investigating the performance of the proposed DBPCC methods when applied to IPMSM drives.

4) Harmonic current injection to reduce torque ripples based on proposed DBPCC with AHRCCI

High torque ripples will lead to undesired large speed variation and noises of motor drives. Although this is not for high-speed drives which has large inertial damping against the torque ripples, it can be of particular concern in traction and servo drives. Harmonic current injection can effectively reduce the corresponding order of torque harmonics. However, as the dominant harmonic orders of the torque ripples are 6, 12, or higher, the harmonic current injection requires very high bandwidth control of current and low switching-to-harmonic frequency ratios (SHRs) at high speeds can bring about more challenges. As already demonstrated in this thesis, the proposed DBPCC also have a good harmonic current control capability at low SHRs and ARHCCI can effectively suppress the selective harmonic currents. Thus, the proposed ARHCCI could be an attractive solution for harmonic current injection to reduce the torque ripple and should be investigated further.

5) Hybrid PWM scheme with fast dynamic control and low steady-state harmonic distortion

Employing SVM and SOPWM in transients and steady states respectively can yield a hybrid PWM scheme. It can potentially realise the fast dynamic control and low steady-state harmonic distortion as well, but in a more straightforward manner compared to the

proposed PSSM. It does not require complex voltage vector synthesis process in the proposed PSSM. However, the determination of the transients and steady states requires proper setting of current error margin. It could be operating condition dependent and difficult to decide, as the harmonic currents in steady states are large at low pulse numbers and can hardly be predicted accurately. Moreover, the specific schemes should be developed to achieve smooth transition, avoid frequent transition and reduce the steady-state control error under SOPWM. Investigation of the hybrid PWM scheme may contribute to a simple method to realise fast dynamic control and low steady-state harmonic distortion.

References

[1]   H. Gavrila, V. M. (Paltanea), G. Paltanea, G. Scutaru, and I. Peter, "New Trends in Energy Efficient Electrical Machines," *Procedia Eng.*, vol. 181, pp. 568–574, 2017.

[2]   R. Abebe, M. Di Nardo, D. Gerada, G. Lo Calzo, L. Papini, and C. Gerada, "High speed drives review: Machines, converters and applications," *IECON Proc. (Industrial Electron. Conf.*, pp. 1675–1679, 2016.

[3]   M. A. Rahman, A. Chiba, and T. Fukao, "Super high speed electrical machines - summary," in *IEEE Power Engineering Society General Meeting, 2004.*, 2004, vol. 2, no. iii, pp. 1272–1275.

[4]   S. Silber, J. Sloupensky, P. Dirnberger, M. Moravec, W. Amrhein, and M. Reisinger, "High-speed drive for textile rotor spinning applications," *IEEE Trans. Ind. Electron.*, vol. 61, no. 6, pp. 2990–2997, 2014.

[5]   W. Feng, H. Ding, S. Lee, F. Chen, T. Jahns, and B. Sarlioglu, "Design of a 100 kW Surface Permanent Magnet Machine with Wide Constant Power Speed Ratio for Traction Applications," in *2020 IEEE Transportation Electrification Conference & Expo (ITEC)*, 2020, vol. 650, pp. 456–461.

[6]   S. Bozhko *et al.*, "Development of Aircraft Electric Starter–Generator System Based on Active Rectification Technology," *IEEE Trans. Transp. Electrif.*, vol. 4, no. 4, pp. 985–996, Dec. 2018.

[7]   A. Balachandran, M. Boden, Z. Sun, S. J. Forrest, J. D. Ede, and G. W. Jewell, "Design, construction, and testing of an aero-engine starter-generator for the more-electric aircraft," *J. Eng.*, vol. 2019, no. 17, pp. 3474–3478, Jun. 2019.

[8]   A. Binder and T. Schneider, "High-speed inverter-fed AC drives," in *2007 International Aegean Conference on Electrical Machines and Power Electronics*, 2007, pp. 9–16.

[9]   N. Bianchi, S. Bolognani, and F. Luise, "Potentials and Limits of High-Speed PM Motors," *IEEE Trans. Ind. Appl.*, vol. 40, no. 6, pp. 1570–1578, Nov. 2004.

[10]   D. Krahenbuhl, C. Zwyssig, H. Weser, and J. W. Kolar, "A Miniature 500 000-r/min Electrically Driven Turbocompressor," *IEEE Trans. Ind. Appl.*, vol. 46, no. 6, pp. 2459–2466, Nov. 2010.

[11]   T. Baumgartner, R. M. Burkart, and J. W. Kolar, "Analysis and Design of a 300-W 500 000-r/min Slotless Self-Bearing Permanent-Magnet Motor," *IEEE Trans. Ind. Electron.*, vol. 61, no. 8, pp. 4326–4336, Aug. 2014.

[12]   A. Borisavljevic, H. Polinder, and J. A. Ferreira, "On the speed limits of permanent-magnet machines," *IEEE Trans. Ind. Electron.*, vol. 57, no. 1, pp. 220–227, 2010.

[13]   M. T. Bartholet, T. Nussbaumer, S. Silber, and J. W. Kolar, "Comparative evaluation of polyphase bearingless slice motors for fluid-handling applications," *IEEE Trans. Ind. Appl.*, vol. 45, no. 5, pp. 1821–1830, 2009.

[14]   B. Warberger, R. Kaelin, T. Nussbaumer, and J. W. Kolar, "50-Nm/2500-W Bearingless Motor for High-Purity Pharmaceutical Mixing," *IEEE Trans. Ind. Electron.*, vol. 59, no. 5, pp. 2236–2247, May 2012.

[15]   J. Asama, Y. Hamasaki, T. Oiwa, and A. Chiba, "Proposal and Analysis of a Novel Single-Drive Bearingless Motor," *IEEE Trans. Ind. Electron.*, vol. 60, no. 1, pp. 129–138, Jan. 2013.

[16]   J. Rodríguez, J. S. Lai, and F. Z. Peng, "Multilevel inverters: A survey of topologies, controls, and applications," *IEEE Trans. Ind. Electron.*, vol. 49, no. 4, pp. 724–738, 2002.

[17]   J. Rodríguez, S. Bernet, B. Wu, J. O. Pontt, and S. Kouro, "Multilevel voltage-source-converter topologies for industrial medium-voltage drives," *IEEE Trans. Ind. Electron.*, vol. 54, no. 6, pp. 2930–2945, 2007.

[18]   C. Zwyssig, S. D. Round, and J. W. Kolar, "Power electronics interface for a 100 W, 500000 rpm gas turbine portable power unit," *Conf. Proc. - IEEE Appl. Power Electron. Conf. Expo. - APEC*,

vol. 2006, pp. 283–289, 2006.

[19]   I. Takahashi, G. Su, T. Koganezawa, and K. Ohyama, "A Super High Speed PM Motor Drive System by a Quasi Current Source Inverter," *IEEE Trans. Ind. Appl.*, vol. 30, no. 3, pp. 683–690, 1994.

[20]   X. Yuan, "Application of silicon carbide (SiC) power devices: Opportunities, challenges and potential solutions," *Proc. IECON 2017 - 43rd Annu. Conf. IEEE Ind. Electron. Soc.*, vol. 2017-Janua, pp. 893–900, 2017.

[21]   A. K. Morya *et al.*, "Wide bandgap devices in AC electric drives: Opportunities and challenges," *IEEE Trans. Transp. Electrif.*, vol. 5, no. 1, pp. 3–20, 2019.

[22]   T. Liu, T. T. Y. Wong, and Z. J. John Shen, "A Survey on Switching Oscillations in Power Converters," *IEEE J. Emerg. Sel. Top. Power Electron.*, vol. 8, no. 1, pp. 893–908, 2020.

[23]   J. Chen, X. Du, Q. Luo, X. Zhang, P. Sun, and L. Zhou, "A Review of Switching Oscillations of Wide Bandgap Semiconductor Devices," *IEEE Trans. Power Electron.*, vol. 35, no. 12, pp. 13182–13199, 2020.

[24]   B. Zhang and S. Wang, "A Survey of EMI Research in Power Electronics Systems with Wide-Bandgap Semiconductor Devices," *IEEE J. Emerg. Sel. Top. Power Electron.*, vol. 8, no. 1, pp. 626–643, 2020.

[25]   M. Ghassemi, "Accelerated insulation aging due to fast, repetitive voltages: A review identifying challenges and future research needs," *IEEE Trans. Dielectr. Electr. Insul.*, vol. 26, no. 5, pp. 1558–1568, 2019.

[26]   M. J. Corley and R. D. Lorenz, "Rotor position and velocity estimation for a salient-pole permanent magnet synchronous machine at standstill and high speeds," *IEEE Trans. Ind. Appl.*, vol. 34, no. 4, pp. 784–789, 1998.

[27]   B. H. Bae, S. K. Sul, J. H. Kwon, and J. S. Byeon, "Implementation of sensorless vector control for super-high-speed PMSM of turbo-compressor," *IEEE Trans. Ind. Appl.*, vol. 39, no. 3, pp. 811–818, 2003.

[28]   H. Kim, J. Son, and J. Lee, "A high-speed sliding-mode observer for the sensorless speed control of a PMSM," *IEEE Trans. Ind. Electron.*, vol. 58, no. 9, pp. 4069–4077, 2011.

[29]   G. Wang, R. Yang, and D. Xu, "DSP-based control of sensorless IPMSM drives for wide-speed-range operation," *IEEE Trans. Ind. Electron.*, vol. 60, no. 2, pp. 720–727, 2013.

[30]   LTN,   "RE   08,"   *Datasheet*.   [Online].   Available: https://www.ltn-servotechnik.com/fileadmin/imported/products/RE_08_EN_01.pdf.

[31]   Bon-Ho Bae and Seung-Ki Sul, "A compensation method for time delay of full-digital synchronous frame current regulator of pwm ac drives," *IEEE Trans. Ind. Appl.*, vol. 39, no. 3, pp. 802–810, May 2003.

[32]   J.-S. Yim, S.-K. Sul, B.-H. Bae, N. R. Patel, and S. Hiti, "Modified Current Control Schemes for High-Performance Permanent-Magnet AC Drives With Low Sampling to Operating Frequency Ratio," *IEEE Trans. Ind. Appl.*, vol. 45, no. 2, pp. 763–771, 2009.

[33]   J. Holtz, J. Quan, J. Pontt, J. Rodríguez, P. Newman, and H. Miranda, "Design of fast and robust current regulators for high-power drives based on complex state variables," *IEEE Trans. Ind. Appl.*, vol. 40, no. 5, pp. 1388–1397, Sep. 2004.

[34]   Hongrae Kim, M. W. Degner, J. M. Guerrero, F. Briz, and R. D. Lorenz, "Discrete-Time Current Regulator Design for AC Machine Drives," *IEEE Trans. Ind. Appl.*, vol. 46, no. 4, pp. 1425–1435, Jul. 2010.

[35]   M. Tang, A. Gaeta, A. Formentini, K. Ohyama, P. Zanchetta, and G. Asher, "Enhanced DBCC for high-speed permanent magnet synchronous motor drives," *IET Power Electron.*, vol. 9, no. 15, pp. 2880–2890, Dec. 2016.

[36]   A. D. Alexandrou, N. Adamopoulos, and A. Kladas, "Development of a Constant Switching Frequency Deadbeat Predictive Control Technique for Field-Oriented Synchronous Permanent-Magnet Motor Drive," *IEEE Trans. Ind. Electron.*, vol. 63, no. 8, pp. 5167–5175, Aug. 2016.

[37]   X. Zhang, B. Hou, and Y. Mei, "Deadbeat Predictive Current Control of Permanent-Magnet Synchronous Motors with Stator Current and Disturbance Observer," *IEEE Trans. Power Electron.*, vol. 32, no. 5, pp. 3818–3834, May 2017.

[38]   X. Zhang, L. Zhang, and Y. Zhang, "Model Predictive Current Control for PMSM Drives With Parameter Robustness Improvement," *IEEE Trans. Power Electron.*, vol. 34, no. 2, pp. 1645–1657, Feb. 2019.

[39]   J. Holtz, "Advanced PWM and Predictive Control-An Overview," *IEEE Trans. Ind. Electron.*, vol. 63, no. 6, pp. 3837–3844, Jun. 2016.

[40]   M. Preindl, E. Schaltz, and P. Thogersen, "Switching Frequency Reduction Using Model Predictive Direct Current Control for High-Power Voltage Source Inverters," *IEEE Trans. Ind. Electron.*, vol. 58, no. 7, pp. 2826–2835, Jul. 2011.

[41]   C. Bian, S. Ren, and L. Ma, "Study on Direct Torque Control of Super High-speed PMSM," in *2007 IEEE International Conference on Automation and Logistics*, 2007, pp. 2711–2715.

[42]   S. Konaka, Y. Inoue, S. Morimoto, and M. Sanada, "Comparative study of control characteristics in ultra-high-speed PMSM drives," in *2014 IEEE 5th International Symposium on Sensorless Control for Electrical Drives*, 2014, pp. 1–6.

[43]   M. Koc, J. Wang, and T. Sun, "Stator flux oriented control for high performance interior permanent magnet synchronous machine drives," *IET Conf. Publ.*, vol. 2016, no. CP684, pp. 6 .-6 ., 2016.

[44]   T. Sun, J. Wang, and M. Koc, "Virtual Signal Injection Based Direct Flux Vector Control of IPMSM Drives," *IEEE Trans. Ind. Electron.*, vol. 63, no. 8, pp. 1–1, 2016.

[45]   J. S. Lee, C. H. Choi, J. K. Seok, and R. D. Lorenz, "Deadbeat-direct torque and flux control of interior permanent magnet synchronous machines with discrete time stator current and stator flux linkage observer," *IEEE Trans. Ind. Appl.*, vol. 47, no. 4, pp. 1749–1758, 2011.

[46]   J. S. Lee and R. D. Lorenz, "Robustness Analysis of Deadbeat-Direct Torque and Flux Control for IPMSM Drives," *IEEE Trans. Ind. Electron.*, vol. 63, no. 5, pp. 2775–2784, May 2016.

[47]   Y. Wang, Y. Shi, Y. Xu, and R. D. Lorenz, "A comparative overview of indirect field oriented control (IFOC) and deadbeat-direct torque and flux control (DB-DTFC) for AC Motor Drives," *Chinese J. Electr. Eng.*, vol. 1, no. 1, pp. 9–20, 2019.

[48]   T. Geyer, G. Papafotiou, and M. Morari, "Model Predictive Direct Torque Control—Part I: Concept, Algorithm, and Analysis," *IEEE Trans. Ind. Electron.*, vol. 56, no. 6, pp. 1894–1905, Jun. 2009.

[49]   G. Papafotiou, J. Kley, K. G. Papadopoulos, P. Bohren, and M. Morari, "Model Predictive Direct Torque Control—Part II: Implementation and Experimental Evaluation," *IEEE Trans. Ind. Electron.*, vol. 56, no. 6, pp. 1906–1915, Jun. 2009.

[50]   W. Xie *et al.*, "Finite-control-set model predictive torque control with a deadbeat solution for PMSM drives," *IEEE Trans. Ind. Electron.*, vol. 62, no. 9, pp. 5402–5410, 2015.

[51]   S. R. Macminn and T. M. Jahns, "Control Techniques for Improved High-Speed Performance of Interior pm Synchronous Motor Drives," *IEEE Trans. Ind. Appl.*, vol. 27, no. 5, pp. 997–1004, 1991.

[52]   M. N. Uddin and M. A. Rahman, "High-speed control of IPMSM drives using improved fuzzy logic algorithms," *IEEE Trans. Ind. Electron.*, vol. 54, no. 1, pp. 190–199, 2007.

[53]   N. Bianchi, S. Bolognani, and M. Zigliotto, "High-performance PM synchronous motor drive for an electrical scooter," *IEEE Trans. Ind. Appl.*, vol. 37, no. 5, pp. 1348–1355, 2001.

[54]   T. S. Kwon and S. K. Sul, "Novel antiwindup of a current regulator of a surface-mounted permanent-magnet motor for flux-weakening control," *IEEE Trans. Ind. Appl.*, vol. 42, no. 5, pp.

1293–1300, 2006.

[55] K. D. Hoang, J. Wang, and H. Aorith, "Online feedback-based field weakening control of interior permanent magnet brushless AC drives for traction applications accounting for nonlinear inverter characteristics," *7th IET Int. Conf. Power Electron. Mach. Drives, PEMD 2014*, vol. 2, no. 4, pp. 3–8, 2014.

[56] T. S. Kwon, G. Y. Choi, M. S. Kwak, and S. K. Sul, "Novel flux-weakening control of an IPMSM for quasi-six-step operation," *IEEE Trans. Ind. Appl.*, vol. 44, no. 6, pp. 1722–1731, 2008.

[57] F. Briz, M. W. Degner, and R. D. Lorenz, "Analysis and design of current regulators using complex vectors," *IEEE Trans. Ind. Appl.*, vol. 36, no. 3, pp. 817–825, 2000.

[58] J. Holtz, "The Representation of AC Machine Dynamics by Complex Signal Flow Graphs," *IEEE Trans. Ind. Electron.*, vol. 42, no. 3, pp. 263–271, Jun. 1995.

[59] F. B. del Blanco, M. W. Degner, and R. D. Lorenz, "Dynamic analysis of current regulators for AC motors using complex vectors," *IEEE Trans. Ind. Appl.*, vol. 35, no. 6, pp. 1424–1432, 1999.

[60] J. Holtz, "Pulsewidth Modulation for Electronic Power Conversion," *Proc. IEEE*, vol. 82, no. 8, pp. 1194–1214, 1994.

[61] H. Kim, M. W. Degner, J. M. Guerrero, F. Briz, and R. D. Lorenz, "Discrete-time current regulator design for AC machine drives," *IEEE Trans. Ind. Appl.*, vol. 46, no. 4, pp. 1425–1435, 2010.

[62] G. Yuan, H. Liu, and X. Hou, "Synchronized PWM schemes for discrete-time complex vector current regulator of high power rectifiers," *2017 20th Int. Conf. Electr. Mach. Syst. ICEMS 2017*, no. 2, 2017.

[63] P. L. Jansen and R. D. Lorenz, "A Physically Insightful Approach to the Design and Accuracy Assessment of Flux Observers for Field Oriented Induction Machine Drives," *IEEE Trans. Ind. Appl.*, vol. 30, no. 1, pp. 101–110, 1993.

[64] M. Koc, T. Sun, and J. Wang, "Performance improvement of direct torque controlled interior mounted permanent magnet drives by employing a linear combination of current and voltage based flux observers," *IET Power Electron.*, vol. 9, no. 10, pp. 2052–2059, 2016.

[65] J. H. Kim, J. W. Choi, and S. K. Sul, "Novel rotor-flux observer using observer characteristic function in complex vector space for field-oriented induction motor drives," *IEEE Trans. Ind. Appl.*, vol. 38, no. 5, pp. 1334–1343, 2002.

[66] M. Koc, J. Wang, and T. Sun, "An Inverter Nonlinearity-Independent Flux Observer for Direct Torque-Controlled High-Performance Interior Permanent Magnet Brushless AC Drives," *IEEE Trans. Power Electron.*, vol. 32, no. 1, pp. 490–502, 2017.

[67] N. T. West and R. D. Lorenz, "Digital implementation of stator and rotor flux-linkage observers and a stator-current observer for deadbeat direct torque control of induction machines," *IEEE Trans. Ind. Appl.*, vol. 45, no. 2, pp. 729–736, 2009.

[68] A. E. N. Gaspar, Y. Xu, and R. D. Lorenz, "A simpler gopinath-style flux observer without a constant speed assumption for low and high sampling-to-fundamental frequency ratios for induction machines," *2019 IEEE Energy Convers. Congr. Expo. ECCE 2019*, pp. 1832–1839, 2019.

[69] W. Xu and R. D. Lorenz, "Low-Sampling-Frequency Stator Flux Linkage Observer for Interior Permanent-Magnet Synchronous Machines," *IEEE Trans. Ind. Appl.*, vol. 51, no. 5, pp. 3932–3942, Sep. 2015.

[70] A. Yoo and S. K. Sul, "Design of flux observer robust to interior permanent-magnet synchronous motor flux variation," *IEEE Trans. Ind. Appl.*, vol. 45, no. 5, pp. 1670–1677, 2009.

[71] W. Xu and R. D. Lorenz, "Reduced parameter sensitivity stator flux linkage observer in deadbeat-direct torque and flux control for IPMSMs," *IEEE Trans. Ind. Appl.*, vol. 50, no. 4, pp. 2626–2636, 2014.

[72] J. O. Krah and J. Holtz, "High-performance current regulation and efficient pwm implementation

for low-inductance servo motors," *IEEE Trans. Ind. Appl.*, vol. 35, no. 5, pp. 1039–1049, 1999.

[73]   Sheng-Ming Yang and Chen-Haur Lee, "A deadbeat current controller for field oriented induction motor drives," *IEEE Trans. Power Electron.*, vol. 17, no. 5, pp. 772–778, Sep. 2002.

[74]   Hoang Le-Huy, K. Slimani, and P. Viarouge, "Analysis and implementation of a real-time predictive current controller for permanent-magnet synchronous servo drives," *IEEE Trans. Ind. Electron.*, vol. 41, no. 1, pp. 110–117, 1994.

[75]   P. Wipasuramonton, Z. Q. Zhu, and D. Howe, "Predictive current control with current error correction for PM brushless AC drives," in *IEEE International Conference on Electric Machines and Drives, 2005.*, 2005, vol. 42, no. 4, pp. 558–564.

[76]   X. Yuan, S. Zhang, and C. Zhang, "Enhanced robust deadbeat predictive current control for PMSM drives," *IEEE Access*, vol. 7, pp. 148218–148230, 2019.

[77]   J. Rodriguez *et al.*, "State of the Art of Finite Control Set Model Predictive Control in Power Electronics," *IEEE Trans. Ind. Informatics*, vol. 9, no. 2, pp. 1003–1016, May 2013.

[78]   R. Kennel and A. Linder, "Predictive control of inverter supplied electrical drives," in *2000 IEEE 31st Annual Power Electronics Specialists Conference. Conference Proceedings (Cat. No.00CH37018)*, 2000, vol. 2, no. 9, pp. 761–766.

[79]   S. Vazquez, J. Rodriguez, M. Rivera, L. G. Franquelo, and M. Norambuena, "Model Predictive Control for Power Converters and Drives: Advances and Trends," *IEEE Trans. Ind. Electron.*, vol. 64, no. 2, pp. 935–947, Feb. 2017.

[80]   P. Cortes, M. P. Kazmierkowski, R. M. Kennel, D. E. Quevedo, and J. Rodriguez, "Predictive Control in Power Electronics and Drives," *IEEE Trans. Ind. Electron.*, vol. 55, no. 12, pp. 4312–4324, Dec. 2008.

[81]   M. Preindl and S. Bolognani, "Model Predictive Direct Torque Control With Finite Control Set for PMSM Drive Systems, Part 2: Field Weakening Operation," *IEEE Trans. Ind. Informatics*, vol. 9, no. 2, pp. 648–657, May 2013.

[82]   M. Preindl and S. Bolognani, "Model Predictive Direct Torque Control With Finite Control Set for PMSM Drive Systems, Part 1: Maximum Torque Per Ampere Operation," *IEEE Trans. Ind. Informatics*, vol. 9, no. 4, pp. 1912–1921, Nov. 2013.

[83]   Y. Zhang, Z. Li, Y. Zhang, W. Xie, Z. Piao, and C. Hu, "Performance improvement of direct power control of pwm rectifier with simple calculation," *IEEE Trans. Power Electron.*, vol. 28, no. 7, pp. 3428–3437, 2013.

[84]   Y. Zhang, J. Hu, and J. Zhu, "Three-vectors-based predictive direct power control of the doubly fed induction generator for wind energy applications," *IEEE Trans. Power Electron.*, vol. 29, no. 7, pp. 3485–3500, 2014.

[85]   Y. Wang *et al.*, "Deadbeat Model-Predictive Torque Control with Discrete Space-Vector Modulation for PMSM Drives," *IEEE Trans. Ind. Electron.*, vol. 64, no. 5, pp. 3537–3547, 2017.

[86]   T. Geyer and D. E. Quevedo, "Multistep Finite Control Set Model Predictive Control for Power Electronics," *IEEE Trans. Power Electron.*, vol. 29, no. 12, pp. 6836–6846, Dec. 2014.

[87]   T. Geyer and D. E. Quevedo, "Performance of Multistep Finite Control Set Model Predictive Control for Power Electronics," *IEEE Trans. Power Electron.*, vol. 30, no. 3, pp. 1633–1644, Mar. 2015.

[88]   T. Geyer, "Computationally Efficient Model Predictive Direct Torque Control," *IEEE Trans. Power Electron.*, vol. 26, no. 10, pp. 2804–2816, Oct. 2011.

[89]   J. W. Kolar, H. Ertl, and F. C. Zach, "Influence of the Modulation Method on the Conduction and Switching Losses of a PWM Converter System," *IEEE Trans. Ind. Appl.*, vol. 27, no. 6, pp. 1063–1075, 1991.

[90]   M. Cacciato, A. Consoli, G. Scarcella, and A. Testa, "Reduction of common-mode currents in

PWM inverter motor drives," *IEEE Trans. Ind. Appl.*, vol. 35, no. 2, pp. 469–476, 1999.

[91]   Lu Haifeng, C. Xiaomeng, Q. Wenlong, Z. Xing, and F. Yang, "A New PWM Strategy to Reduce the Common-Mode Voltage," in *TENCON 2006 - 2006 IEEE Region 10 Conference*, 2006, vol. 00, pp. 1–4.

[92]   H. Lu, W. Qu, X. Cheng, Y. Fan, and X. Zhang, "A Novel PWM Technique With Two-Phase Modulation," *IEEE Trans. Power Electron.*, vol. 22, no. 6, pp. 2403–2409, Nov. 2007.

[93]   G. Buja and G. Indri, "Improvement of pulse width modulation techniques," *Arch. f'ur Elektrotechnik*, vol. 57, no. 5, pp. 281–289, Sep. 1975.

[94]   S. Halász, S. R. Bowes, and A. Midoun, "Suboptimal switching strategies for microprocessor-controlled PWM inverter drives," *IEE Proc. B Electr. Power Appl.*, vol. 132, no. 6, p. 344, 1985.

[95]   A. M. Hava, R. J. Kerkman, and T. A. Lipo, "Simple analytical and graphical methods for carrier-based PWM-VSI drives," *IEEE Trans. Power Electron.*, vol. 14, no. 1, pp. 49–61, 1999.

[96]   E. R. da Silva, E. dos Santos, and C. Jacobina, "Pulsewidth Modulation Strategies," *IEEE Ind. Electron. Mag.*, vol. 5, no. 2, pp. 37–45, Jun. 2011.

[97]   A. M. Hava, R. J. Kerkman, and T. A. Lipo, "A high-performance generalized discontinuous PWM algorithm," *IEEE Trans. Ind. Appl.*, vol. 34, no. 5, pp. 1059–1071, 1998.

[98]   R. Jobing, F. S. van der Merwe, and M. J. Kamper, "Digital implementation of bus clamped space vector modulation," *IEEE Trans. Energy Convers.*, vol. 9, no. 2, pp. 344–348, Jun. 1994.

[99]   G. Narayanan and V. T. Ranganathan, "Two novel synchronized bus-clamping PWM strategies based on space vector approach for high power drives," *IEEE Trans. Power Electron.*, vol. 17, no. 1, pp. 84–93, 2002.

[100]   J. Holtz and X. Qi, "Optimal control of medium-voltage drives-an overview," *IEEE Trans. Ind. Electron.*, vol. 60, no. 12, pp. 5472–5481, Dec. 2013.

[101]   G. Narayanan and V. T. Ranganathan, "Synchronised bus-clamping PWM strategies based on space vector approach for modulation up to six-step mode," *PEDES 1998 - 1998 Int. Conf. Power Electron. Drives Energy Syst. Ind. Growth*, vol. 2, no. M, pp. 996–1001, 1998.

[102]   H. Yang, Y. Zhang, G. Yuan, P. D. Walker, and N. Zhang, "Hybrid Synchronized PWM Schemes for Closed-Loop Current Control of High-Power Motor Drives," *IEEE Trans. Ind. Electron.*, vol. 64, no. 9, pp. 6920–6929, 2017.

[103]   G. S. Buja and G. B. Indri, "Optimal Pulsewidth Modulation for Feeding AC Motors," *IEEE Trans. Ind. Appl.*, vol. IA-13, no. 1, pp. 38–44, 1977.

[104]   N. Oikonomou and J. Holtz, "Closed-Loop control of medium-voltage drives operated with synchronous optimal pulsewidth modulation," *IEEE Trans. Ind. Appl.*, vol. 44, no. 1, pp. 115–123, 2008.

[105]   J. Holtz and N. Oikonomou, "Synchronous optimal pulsewidth modulation and stator flux trajectory control for medium-voltage drives," *IEEE Trans. Ind. Appl.*, vol. 43, no. 2, pp. 600–608, 2007.

[106]   M. S. A. Dahidah, G. Konstantinou, and V. G. Agelidis, "A Review of Multilevel Selective Harmonic Elimination PWM: Formulations, Solving Algorithms, Implementation and Applications," *IEEE Trans. Power Electron.*, vol. 30, no. 8, pp. 4091–4106, 2015.

[107]   H. Zhang, W. Liu, Z. Chen, and N. Jiao, "Smooth Transition of Multimode Synchronous Modulation for IPMSM Sensorless Drives in Rail-Transit Applications," *IEEE Trans. Ind. Electron.*, vol. 68, no. 1, pp. 128–138, Jan. 2021.

[108]   M. Srndovic, A. Zhetessov, T. Alizadeh, Y. L. Familiant, G. Grandi, and A. Ruderman, "Simultaneous Selective Harmonic Elimination and THD Minimization for a Single-Phase Multilevel Inverter with Staircase Modulation," *IEEE Trans. Ind. Appl.*, vol. 54, no. 2, pp. 1532–1541, 2018.

[109] K. Peter, J. Böcker, F. Mink, and S. Beineke, "Comparison of quarter-wave with half-wave symmetrical pulse patterns applied in electrical high-speed drives," in *8th IET International Conference on Power Electronics, Machines and Drives (PEMD 2016)*, 2016, pp. 1–6.

[110] A. Khamitov and A. Ruderman, "Synchronous Optimal Modulation: Frequency or Time Domain, Global or Constrained Optimization? 40 Years to the First Formulation," *IEEE Trans. Ind. Electron.*, vol. 64, no. 11, pp. 8778–8781, 2017.

[111] A. K. Rathore, J. Holtz, and T. Boller, "Synchronous optimal pulsewidth modulation for low-switching-frequency control of medium-voltage multilevel inverters," *IEEE Trans. Ind. Electron.*, vol. 57, no. 7, pp. 2374–2381, 2010.

[112] B. J. Rabi, "Minimizing of Harmonics in PWM Inverters Based on Genetic Algorithms," *J. Appl. Sci.*, vol. 6, no. 9, pp. 2056–2059, 2006.

[113] S. M. Sadr, M. Monfared, and H. R. Mashhadi, "Application of PSO for selective harmonic elimination in a PWM AC/AC voltage regulator," *2012 2nd Int. eConference Comput. Knowl. Eng. ICCKE 2012*, vol. 2, pp. 62–65, 2012.

[114] P. Kshirsagar and R. Krishnan, "Implementation and experimental validation of efficiency improvement in PMSM drives through switching frequency reduction," *Conf. Proc. - IEEE Appl. Power Electron. Conf. Expo. - APEC*, vol. 2016-May, pp. 2027–2034, 2016.

[115] Z. Zhang, X. Feng, and J. Xu, "Closed-loop control of PMSM based on optimal synchronous pulse patterns," *Proc. - 2014 Int. Power Electron. Appl. Conf. Expo. IEEE PEAC 2014*, no. 2, pp. 687–692, 2014.

[116] A. Birth, T. Geyer, H. D. T. Mouton, and M. Dorfling, "Generalized Three-Level Optimal Pulse Patterns with Lower Harmonic Distortion," *IEEE Trans. Power Electron.*, vol. 35, no. 6, pp. 5741–5752, 2020.

[117] Rathore, Holtz, and Boller, "Generalized Optimal Pulsewidth Modulation of Multilevel Inverters for Low-Switching-Frequency Control of Medium-Voltage High-Power Industrial AC Drives," *IEEE Trans. Ind. Electron.*, vol. 60, no. 10, pp. 4215–4224, Oct. 2013.

[118] P. J. Torri, G. da Cunha, T. Boller, A. K. Rathore, J. Holtz, and N. Oikonomou, "Optimal pulse width modulation for multi-level inverter systems," EP2312739A1, 2009.

[119] M. Steczek, P. Chudzik, and A. Szelag, "Combination of SHE- and SHM-PWM Techniques for VSI DC-Link Current Harmonics Control in Railway Applications," *IEEE Trans. Ind. Electron.*, vol. 64, no. 10, pp. 7666–7678, 2017.

[120] F. Mink, K. Peter, H. Kasten, and S. Beineke, "Feedback control of high-speed PMSM with synchronous optimal PWM," in *2016 18th European Conference on Power Electronics and Applications (EPE'16 ECCE Europe)*, 2016, pp. 1–10.

[121] J. Holtz and B. Beyer, "The Trajectory Tracking Approach-A New Method for Minimum Distortion PWM in Dynamic High-Power Drives," *IEEE Trans. Ind. Appl.*, vol. 30, no. 4, pp. 1048–1057, 1994.

[122] J. Holtz and B. Beyer, "Fast Current Trajectory Tracking Control Based on Synchronous Optimal Pulsewidth Modulation," *IEEE Trans. Ind. Appl.*, vol. 31, no. 5, pp. 1110–1120, 1995.

[123] M. Marufuzzaman, M. B. I. Reaz, L. F. Rahman, and T. G. Chang, "High-Speed Current dq PI Controller for Vector Controlled PMSM Drive," *Sci. World J.*, vol. 2014, pp. 1–9, 2014.

[124] R. Togashi, Y. Inoue, S. Morimoto, and M. Sanada, "Performance improvement of ultra-high-speed PMSM drive system based on DTC by using SiC inverter," *2014 Int. Power Electron. Conf. IPEC-Hiroshima - ECCE Asia 2014*, pp. 356–362, 2014.

[125] L. Zhong, M. F. Rahman, W. Y. Hu, and K. W. Lim, "Analysis of direct torque control in permanent magnet synchronous motor drives," *IEEE Trans. Power Electron.*, vol. 12, no. 3, pp. 528–536, May 1997.

[126] Z. Zhang, H. Fang, F. Gao, J. Rodriguez, and R. Kennel, "Multiple-Vector Model Predictive Power

Control for Grid-Tied Wind Turbine System With Enhanced Steady-State Control Performance," *IEEE Trans. Ind. Electron.*, vol. 64, no. 8, pp. 6287–6298, Aug. 2017.

[127]   L. Springob and J. Holtz, "High-bandwidth current control for torque-ripple compensation in PM synchronous machines," *IEEE Trans. Ind. Electron.*, vol. 45, no. 5, pp. 713–721, 1998.

[128]   R. S. Dastjerdi, M. A. Abbasian, H. Saghafi, and M. H. Vafaie, "Performance Improvement of Permanent-Magnet Synchronous Motor Using a New Deadbeat-Direct Current Controller," *IEEE Trans. Power Electron.*, vol. 34, no. 4, pp. 3530–3543, Apr. 2019.

[129]   G.-K. Hung, C.-C. Chang, and C.-L. Chen, "Analysis and implementation of a delay-compensated deadbeat current controller for solar inverters," *IEE Proc. - Circuits, Devices Syst.*, vol. 148, no. 5, p. 279, 2001.

[130]   X. Chen, J. Wang, B. Sen, P. Lazari, and T. Sun, "A high-fidelity and computationally efficient model for interior permanent-magnet machines considering the magnetic saturation, spatial harmonics, and iron loss effect," *IEEE Trans. Ind. Electron.*, vol. 62, no. 7, pp. 4044–4055, 2015.

[131]   G. Pellegrino, B. Boazzo, and T. M. Jahns, "Magnetic Model Self-Identification for PM Synchronous Machine Drives," *IEEE Trans. Ind. Appl.*, vol. 51, no. 3, pp. 2246–2254, 2015.

[132]   L. Jarzebowicz, "Errors of a Linear Current Approximation in High-Speed PMSM Drives," *IEEE Trans. Power Electron.*, vol. 32, no. 11, pp. 8254–8257, 2017.

[133]   J. A. Haylock, B. C. Mecrow, A. G. Jack, and D. J. Atkinson, "Enhanced current control of high-speed PM machine drives through the use of flux controllers," *IEEE Trans. Ind. Appl.*, vol. 35, no. 5, pp. 1030–1038, 1999.

[134]   P. Mattavelli, "An Improved Deadbeat Control for UPS Using Disturbance Observers," *IEEE Trans. Ind. Electron.*, vol. 52, no. 1, pp. 206–212, Feb. 2005.

[135]   Y. Wang, S. Tobayashi, and R. D. Lorenz, "A Low-Switching-Frequency Flux Observer and Torque Model of Deadbeat-Direct Torque and Flux Control on Induction Machine Drives," *IEEE Trans. Ind. Appl.*, vol. 51, no. 3, pp. 2255–2267, 2015.

[136]   G. Liu, B. Chen, K. Wang, and X. Song, "Selective current harmonic suppression for high-speed PMSM Based on high-precision harmonic detection method," *IEEE Trans. Ind. Informatics*, vol. 15, no. 6, pp. 3457–3468, 2019.

[137]   L. Wang, Z. Q. Zhu, H. Bin, and L. M. Gong, "Current Harmonics Suppression Strategy for PMSM with Non-Sinusoidal Back-EMF Based on Adaptive Linear Neuron Method," *IEEE Trans. Ind. Electron.*, vol. PP, no. c, pp. 1–1, 2019.

[138]   K. Peter, S. Hanke, F. Mink, and J. Bocker, "Inverter loss management for an electrical high-speed drive system," in *2016 18th European Conference on Power Electronics and Applications (EPE'16 ECCE Europe)*, 2016, pp. 1–10.

[139]   A. Tripathi and G. Narayanan, "Investigations on optimal pulse width modulation to minimize total harmonic distortion in the line current," *IEEE Trans. Ind. Appl.*, vol. 53, no. 1, pp. 212–221, 2017.

[140]   H. Su *et al.*, "Stator Flux Trajectory Control with Optimized Pulse Patterns Based on Voltage Command Feed-Forward," in *2019 IEEE 3rd International Electrical and Energy Conference (CIEEC)*, 2019, pp. 662–667.

[141]   Z. Zhang, X. Ge, Z. Tian, X. Zhang, Q. Tang, and X. Feng, "A PWM for minimum current harmonic distortion in metro traction PMSM with saliency ratio and load angle constrains," *IEEE Trans. Power Electron.*, vol. 33, no. 5, pp. 4498–4511, 2018.

[142]   J. Holtz and N. Oikonomou, "Estimation of the fundamental current in low-switching-frequency high dynamic medium-voltage drives," *IEEE Trans. Ind. Appl.*, vol. 44, no. 5, pp. 1597–1605, 2008.

[143]   T. Geyer, N. Oikonomou, G. Papafotiou, and F. D. Kieferndorf, "Model predictive pulse pattern control," *IEEE Trans. Ind. Appl.*, vol. 48, no. 2, pp. 663–676, 2012.

[144]   T. Geyer and N. Oikonomou, "Model predictive pulse pattern control with very fast transient

responses," *2014 IEEE Energy Convers. Congr. Expo. ECCE 2014*, pp. 5518–5524, 2014.

List of Figures

233

234

235

238

List of Tables

APPENDIX A

Design and Construction of Prototype High-Speed PMSM Drive for Experiment Testing

This appendix presents the key works that have been done to build up a high-speed PMSM drive for experiment testing, which mainly consist of high-speed resolver mounting and the design and construction of the machine controller.

At the beginning of this project, the high-speed prototype machine has already been built. However, its shaft was too short for mounting a position sensor on. Hence, a new shaft with extended length has been rebuilt and a high-speed resolver has been mounted on the shaft and stator. The photos and drawing of machine assembly are shown below. The rebuilt rotor system has been balanced to Grade 2.5.

(a)

(b)
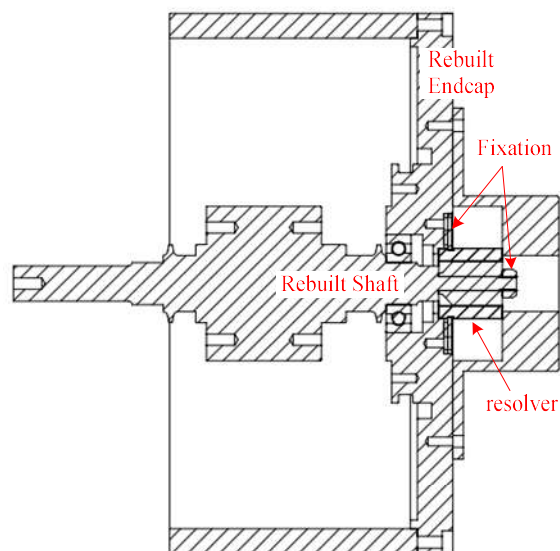
(c)

Fig. A-1 High-speed resolver mounting. (a) Resolve size. (b) Resolver mounted on the prototype high-speed machine. (c) Solidworks drawing of the machine assembly.

The overall structure of the high-speed PMSM drive is illustrated in Fig. A-2. Regarding the high-speed PMSM controller, the digital real-time simulator, OPAL5600 is selected as the core processor. The 3-phase inverter module (SKiM459GD12E4) and the commercial gate drive board (SKYPER 42 LJ R) both form SEMIKRON are employed. The interface boards for the inverter, OPAL simulator, resolver and current sensors have been designed, manufactured and enclosured in two boxes, as shown in Fig. A-3 and Fig. A-4. The PWM and enable signals generated from the OPAL simulator are transmitted to the OPAL interface board differentially by coaxial cables (DB cables) and later transmitted to the inverter boxes optically by fibre optic (FO) cables. The measured current and position signals in the inverter box are transmitted to the OPAL interface box differentially by coaxial cables as well. The low voltage side including OPAL simulator and OPAL interface box are isolated from the inverter box and machine.
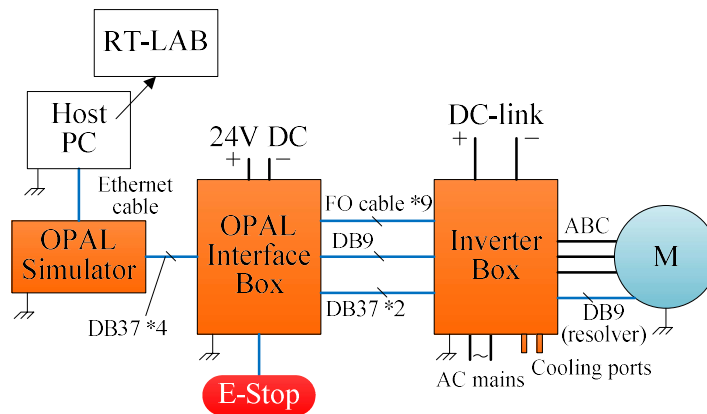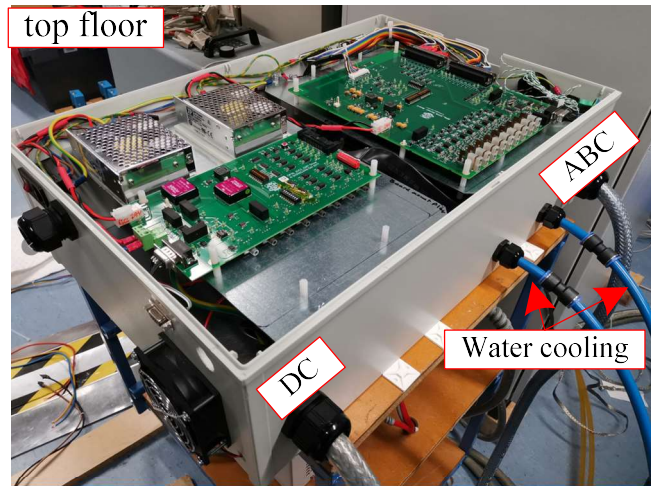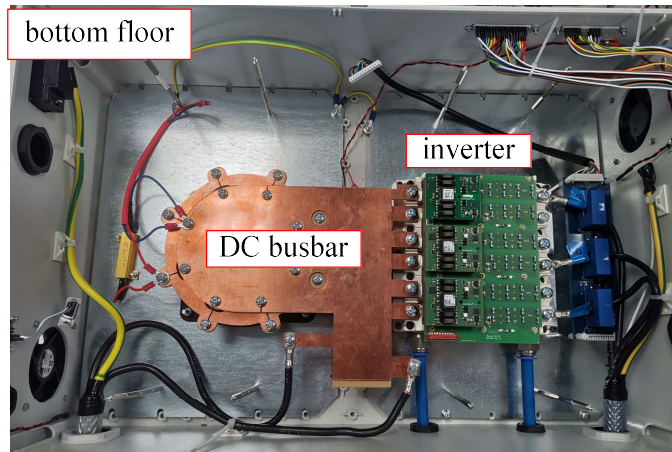

Fig. A-2 Schematic diagram of the OPAL based motor drive

Fig. A-3 OPAL interface board

(a)

(b)

Fig. A-4 Inverter box. (a) Top floor. (b) Bottom floor.

APPENDIX B
MATLAB Code for Pulse Pattern Optimisation of SOPWM

The pulse pattern optimisation code for SOPWM of two-level inverters are given as below. It is based on the algorithm developed in Chapter 4.

```matlab
%****************************** Main function **********************************
% constant
sigma_6step=sqrt(5/486*pi^4-1);
% current distortion factor tolerance, the difference within this range seen as same
diff_di_abs=0.001; % tolerance to accept a new global optimum
diff_di_abs_local=0.001; % tolerance to accept a new local optimum
%%% scenarios to optimize
Count_case=0;
for M=1:7 % switching angles' number
  for Type=[1 -1] % pulse type, 1 or -1 for Type A or B
    Count_case=Count_case+1; % the case index number
    index=0; % index number in the case with a given pulse number and type
    local_op_index=0; % element index of local optimal solution
    jj_0=0;
    for m=0.01:0.01:1 % 1st round optimization
      % initialization of optimization
      x_op=zeros(1,M);
      eflag_op=-100;
      f_op=10^5;
      index=index+1;
      time_start=tic;

      for count=1:10+5*M % optimization repeat time, or set as 100
        % one optimization routine starts
        n=M-1;% degree-of-freedoms to optimize
        %%% objective function, square of WTHD of phase voltage
        % use 5000 harmonics to approximate the WTHD0 of phase voltage
        objfun=@(x) obj_squareV_WTHD0_wGrad(x,5000,Type,M);
        %%% optimization parameters configuration, QWS
        % set the initial solution randomly, column vector
        if count==1 && index>1
          x0=x_op_pre; % the optimal solution at last modulation index
        else %first optimization
          x0=x_initial_random(M,1,m);
        end
        % linear ieq. cons., A*x<=B
        A=zeros(M,M);
        for p=1:M-1
          A(p,p)=1;
          A(p,p+1)=-1;
```

```
        end
        B=zeros(M,1); % linear ieq. cons., column vector
        Aeq=[]; % linear eq. cons., Aeq*x=Beq
        Beq=[]; % linear eq. cons., column vector
        LB=zeros(M,1); % low bound, column vector, 0
        UB=ones(M,1).*(pi/2); % upper bond, column vector, pi/2
        % nonlinear cons., c(x)<=0,ceq(x)=0
        NonlCon=@(x) NonlCons_wGrad(x,Type,M,m);%the fundament element constraint

        Options = optimoptions(@fmincon,'Algorithm','sqp','Display','iter');
        Options=
optimoptions(Options,'SpecifyObjectiveGradient',false,'SpecifyConstraintGradient',true);
        Options = optimoptions(Options,'MaxFunctionEvaluations', 200*M);%default is 100*Varibales'
Number

        %%% execute optimization
        % x is in rad
        [x,fval,eflag,output]=fmincon(objfun,x0,A,B,Aeq,Beq,LB,UB,NonlCon,Options);
        fval=sqrt(fval)/sigma_6step; % derive the distortion factor

        % update the solution
        if fval<f_op-diff_di_abs
            x_op=x;
            f_op=fval;
            eflag_op=eflag;
            rand_ini_index=count;
        end

        % save all the local optimal solution found
        if count==1
            local_op_index=local_op_index+1;
            x_local(local_op_index,1:M)=x;
            fval_local(local_op_index,1)=fval;
            eflag_local(local_op_index,1)=eflag;

di_local(local_op_index,1)=sqrt(obj_squareV_WTHD0_wGrad(x,10000,Type,M))/sigma_6step;
            m_local(local_op_index,1)=m;
        else
            for jj=jj_0+1:local_op_index
                if abs(fval-fval_local(jj,1))<=diff_di_abs_local
                    appear=1;
                    break;
                else
                    appear=0;
                end
            end
            if appear==0
                local_op_index=local_op_index+1;
                x_local(local_op_index,1:M)=x;
```

```
                fval_local(local_op_index,1)=fval;
                eflag_local(local_op_index,1)=eflag;

di_local(local_op_index,1)=sqrt(obj_squareV_WTHD0_wGrad(x,10000,Type,M))/sigma_6step;
                m_local(local_op_index,1)=m;
            end
        end
    end
    jj_0=local_op_index;
    Loop_Dur=toc(time_start);

    %%% save results
    clear x;
    x=x_op;
    % use harmonic orders up to 10000
    WTHD0=sqrt(obj_squareV_WTHD0_wGrad(x,10000,Type,M));
    F=F_Vn_nor(x,25,Type,M);
    % amplitude of each order harmonics, normalized by 2*Vdc/pi
    Vn_h(1,:)=F([1 5 7 11 13 17 19 23 25],1)';
    angles=x.*180/pi; % optimal switching angles in degree
    %save the solution as the initial point of next optimization at adjacent modulation index
    x_op_pre=x_op;

    % save the data output to a spreadsheet
    Sheet1(index,:)=[index m Type M fval eflag rand_ini_index WTHD0 Vn_h];
    Sheet2(index,1:M+2)=[index m angles'];
    Sheet3(index,1:M+2)=[index m x'];
    Sheet4(index,1:M+5)=[Vn_h(1,1) angles' WTHD0 WTHD0./sigma_6step eflag rand_ini_index];
end

%******************************** Sub function********************************
% random generation of initial solutions
function alph= x_initial_random(M,m)
% M, the number of switching angles
if m==0.01
    if rand>0.5
    A=sort(rand(M,1).*pi/6+ones(M,1).*pi/3);
    x=zeros(M,1);
    x(1:M,1)=A;
    alph=x;
    else
    A=sort(rand(M,1).*pi/3);
    x=zeros(M,1);
    x(1:M,1)=A;
    alph=x;
    end
else
    A=sort(rand(M,1).*pi/2);
    x=zeros(M,1);
```

```matlab
    x(1:M,1)=A;
    alph=x;
end
```

```matlab
%******************************* Sub function*******************************
% normalised magnitudes (referred to 2*Vdc/pi) of each order harmonics
% due to odd symmetric characteristic of the wave, magnitudes of even harmonics set as 0
function F = Vn_nor(x,n,Type,M)
% x,swithing angles vector, in radian
% n,order of the harmonic;
% Type, 1 or -1 for Type A and B respectively;
% M,the number of switching angles

if n==2*fix(n/2)
    F=0; % even harmonics equal to 0
else % odd harmonics
    sigma=0;% sum of trigonometric components
    for i=1:M
        if i~=2*fix(i/2)%odd
            sigma=sigma-cos(n*x(i,1));
        else
            sigma=sigma+cos(n*x(i,1));
        end
    end
    F=Type*(1+2*sigma)/n;
end
```

```matlab
%******************************* Sub function*******************************
% calculate the WTHD0 of phase voltage, maximum order of harmonics is n
function [f gradf] = obj_squareV_WTHD0_wGrad(x,n,Type,M)
% x,swithing angles vector, in radian
% n,order of the harmonic;
% Type, 1 or -1 for Type A and B respectively;
% M,the number of switching angles
WTHD0=0;
for i=2:n
    if i==fix(i/2)*2 || i==fix(i/3)*3
        WTHD0=WTHD0+0;% no even and triplen harmonics
    else
        WTHD0=WTHD0+(Vn_nor(x,i,Type,M)/i)^2;
    end
end
f=WTHD0;

if nargout>1
    for i=1:M
        Gi(i,1)=0;
        for j=2:n
            if j==fix(j/2)*2 || j==fix(j/3)*3
```

```matlab
            Gi(i,1)=Gi(i,1)+0;% no even and triplen harmonics
        else
            if i==fix(i/2)*2%even harmonics
                Gi(i,1)=Gi(i,1)-4*Vn_nor(x,j,Type,M)*sin(j*x(i,1))*Type;
            else%odd harmonics
                Gi(i,1)=Gi(i,1)+4*Vn_nor(x,j,Type,M)*sin(j*x(i,1))*Type;
            end
        end
    end
  end
 gradf=Gi;
end


%******************************* Sub function*******************************
% the nonlinear constraint
function [c,ceq,gradc,gradceq]=NonlCons_wGrad(x,Type,M,m)
% nonlinear cons.,c(x)<=0,ceq(x)=0
s=0; % sum of trigonometric components
for i=1:M
   if i==2*fix(i/2)% even
      s=s+cos(x(i,1));
   else % odd
      s=s-cos(x(i,1));
   end
end
c=[];
ceq=(1+2*s)*Type-m;

if nargout>1
   gradc=[];
   G=zeros(M,1);
   for i=1:M
      if i==2*fix(i/2) % even
         G(i,1)=-2*sin(x(i,1))*Type;
      else % odd
         G(i,1)=2*sin(x(i,1))*Type;
      end
      gradceq=G;
   end
end
```